

ECHO-1

TOWARDS THE BOUNDARIES OF E-FLIGHT



Towards the Boundaries of E-flight

Final Report

by

DSE Group 9

Name	Student number
Erik Regeling	4864794
Jurriën Kuin	4666461
Kian Heus	4876768
Leonardo Caranti	4796594
Maarten Beltman	4772350
Octavian Soare	4832701
Stein Munting	4837967
Thomas Riechelman	4859154
Tristan Bakker	4801482
Tudor Avarvarei	4822242

Supervisors: Dr. ir. F. Oliverio, F. Ascione, A. Choudhary
Date: June 22, 2021

Preface

This report was written by ten third-year Bachelor Aerospace Engineering students, studying at the Technical University of Delft. It was written as part of the AE3200 Design Synthesis Exercise (DSE) project. Over the course of ten weeks, an electric regional transporter called ECHO-1 was designed based on the requirements set by Venturi Aviation, a start-up company that the design was made for.

It is assumed that the reader has decent background knowledge in the field of aerospace engineering. However, it is not required to be an expert as the reasoning for design choices will be elaborated on in the different chapters of the report. For all the symbols and syntax that are used throughout the report, a nomenclature is created in the beginning of the report. Readers with particular interest in the design selection should read [chapter 4](#). Those with interest in the technical calculations should read [chapter 5](#) up until [chapter 12](#). Finally, readers with particular interest in the operational side of the aircraft as well as the cost aspect should read [chapter 13](#) up until [chapter 16](#).

Overall as a group we are really proud of what we achieved during this DSE. We managed to get very far in the design process and were able to obtain a converged design within our requirements. Not only that, but we also had a lot of fun doing it. Jokes were made, memes were sent and a lot of laughing has been done.

Finally, we would like to extend a gratuitous thank you to our tutor, Dr. ir. Fabrizio Oliviero, who assisted the group actively through the project. We would also like to thank the two coaches that assisted the group: Federica Ascione and Abhas Choudhary. Furthermore, we would like to thank our PM&SE Teaching Assistant Tristan Hamers for his help on the systems design aspect of the project. Additionally, we would like to thank Joost Dieben, Jan Willem Heinen and Frank Scholtens from Venturi Aviation for their support and expertise in the field of battery technology. Finally, we would like to thank some external experts that assisted the group throughout the ten weeks: Dr. ir. Tomas Sinnige, Dr. ir. Roeland de Breuker, Dr. ir. Maurice Hoogreef, Reynard de Vries, Daniel Juschus and Chizoba Ogugua.

Delft, 22/06/2021

Tudor Avarvarei, Tristan Bakker, Maarten Beltman, Leonardo Caranti, Kian Heus, Jurriën Kuin,
Stein Munting, Erik Regeling, Thomas Riechelman and Octavian Soare

Contents

Preface	i		
Nomenclature	iii		
List of Tables	vi		
List of Figures	vii		
1 Executive Overview	1		
2 Introduction	3		
3 Project Preparation	4		
3.1 Mission Analysis	4		
3.2 Functional Analysis	4		
3.3 Stakeholder Requirements	7		
3.4 Technical Risk Assessment	8		
3.5 Verification and Validation Plan	9		
4 Recap On Design Selection	10		
4.1 Design Options	10		
4.2 Design Trade-Off	11		
5 Performance Analysis	15		
5.1 Class II and Wing and Power Loading	16		
5.2 Performance Calculations Method	17		
5.3 Code Verification	21		
5.4 Results	22		
6 Propulsion Analysis	27		
6.1 Propeller Configuration	27		
6.2 Propeller Performance.	31		
6.3 Electric Propulsion	36		
6.4 Propulsion System Failure	39		
7 Aerodynamic Analysis	39		
7.1 Airfoil Design	40		
7.2 Wing Design	42		
7.3 Detailed Lift and Drag Estimation	45		
7.4 Verification and Validation	49		
8 Aircraft Geometry	50		
8.1 Fuselage Design	50		
8.2 Centre of Gravity Determination	55		
8.3 Horizontal Tail Sizing	57		
8.4 Vertical Tail Sizing	59		
8.5 Landing Gear Sizing.	60		
8.6 Control Surfaces.	61		
8.7 Verification and Validation	63		
8.8 Recommendations	65		
9 Dynamic Stability Analysis	65		
9.1 Dynamic Coefficients	65		
9.2 Eigenmodes Analysis	66		
9.3 Verification, Validation and Recommendations	68		
10 Structural Analysis	68		
10.1 Modelling Wing with Truss	68		
10.2 Material Selection for Wing Box	78		
10.3 Modelling Fuselage Structure for Battery Integration	80		
10.4 Vibrational Analysis.	83		
10.5 Verification and Validation	84		
11 Battery Integration	85		
11.1 Battery Architecture.	86		
11.2 Battery Packaging	87		
11.3 Thermal Management	89		
12 Converging to Final Design	94		
12.1 Iterative Process Description	94		
12.2 Final Design	97		
12.3 Compliance Matrix	100		
12.4 Final Design Sensitivity Analysis	102		
12.5 Resource Allocation and Class II Comparison	105		
13 Sustainability Analysis	106		
13.1 Methodology.	107		
13.2 Life-Cycle Analysis	107		
13.3 Further Use of Batteries	109		
13.4 Recommendations	110		
14 Operational Analysis	110		
14.1 Airport Infrastructure	110		
14.2 Ground Handling	114		
14.3 RAMS Characteristics.	118		
14.4 Recommendations	120		
15 Post-DSE Activities	121		
15.1 Project Design & Development Logic	121		
15.2 After DSE Project Gantt Chart	122		
15.3 Production Plan	124		
16 Economic Analysis	125		
16.1 Cost Break-Down Structure.	125		
16.2 Return on Investment and Operational Profit	128		
16.3 Market Analysis	128		
16.4 Business Case	129		
17 Conclusion and Recommendations	133		
17.1 Conclusion.	133		
17.2 Recommendations	133		
17.3 Errata.	135		
Bibliography	137		

Nomenclature

List of Abbreviations

<i>ADSEE</i>	Aircraft Design and System Engineering Elements–
<i>AEP</i>	Aircraft Estimated Price
<i>AF</i>	Activity Factor
<i>AHP</i>	Analytic Hierarchy Process
<i>AOA</i>	Angle of Attack
<i>BTMS</i>	Battery Thermal Management System
<i>CCS</i>	Connected Charging System
<i>CFRP</i>	Carbon Fibre Reinforced Polymer
<i>CG</i>	Centre of Gravity
<i>CO_{2e}</i>	Carbon Dioxide Equivalent
<i>CO₂</i>	Carbon Dioxide
<i>DOC</i>	Direct Operating Cost
<i>DOD</i>	Depth Of Discharge
<i>DSE</i>	Design Synthesis Exercise
<i>EASA</i>	European Union Aviation Safety Agency
<i>ECS</i>	Environment Control System
<i>EIS</i>	Entry Into Service
<i>EOL</i>	End of Life
<i>FBD</i>	Free Body Diagram
<i>FL170</i>	Flight Level 170
<i>FPMH</i>	Failures Per Million Flights
<i>HLD</i>	High Lift Devices
<i>ICAO</i>	International Civil Aviation Organization
<i>IOC</i>	Indirect Operating Cost
<i>LCN</i>	Load Classification Number
<i>LE</i>	Leading Edge
<i>MOI</i>	Moment of Inertia
<i>MSC</i>	Megawatt Charging System
<i>MTOW</i>	Maximum Take Off Weight
<i>NO_x</i>	Nitrogen Oxides
<i>OEI</i>	One Engine Inoperative
<i>OEW</i>	Operative Empty Weight
<i>PD&DL</i>	Project Design and Development Logic
<i>PERT</i>	Project Evaluation and Review Technique
<i>RAMS</i>	Reliability, Availability, Maintainability, and Safety
<i>RC</i>	Rate of Climb
<i>ROI</i>	Return on Investment
<i>RPM</i>	Rotations per Minute
<i>SHP</i>	Shaft Horsepower
<i>SOC</i>	State of Charge
<i>SOH</i>	State of Health
<i>VDC</i>	Volts of Direct Current
<i>VLM</i>	Vortex Lattice Method

List of Symbols

α_0	Zero Lift Angle of Attack	rad
α_{max}	Maximum Angle of Attack	rad
α	Angle of Attack	rad
α_{HE}	Heat Transfer Coefficient	–
\bar{c}	Length of MAC	m
\bar{x}_{ac}	Aircraft Aerodynamic Centre x-location	m
\bar{x}_{xg}	Centre of Gravity X-Location	m

β	Slide slip Angle	rad
β	Slipstream Correction Factor	–
χ	Ratio between two propulsion systems	–
$\dot{\theta}$	Aircraft Angular Acceleration	rad/s ²
δ_{flap}	Flap Deflection	deg
ΔAR	Change in Aspect Ratio	–
ΔC_L	Change in 3D Lift Coefficient	–
ΔC_l	Change in 2D Lift Coefficient	–
ΔC_{D_0}	Change in Parasite Drag Coefficient	–
ΔC_{D_i}	Change in Induced Drag Coefficient	–
$\Delta C_{D_{flap}}$	Change in Drag Coefficient due to Flap	–
$\Delta C_{L_{max}}$	Change in Maximum Lift Coefficient	–
$\Delta C_{L_{prop}}$	Change in Lift Coefficient due to Propulsion	–
ΔC_L	Change in Lift Coefficient	–
ΔT	Temperature Difference	K
ΔT_e	Differential Thrust	N
ΔY	Fraction of wingspan	–
δy	Distance between two propellers	–
δ	Displacement	m
δ_a	Aileron Deflection	deg
Δ_f	Flaps Influence of Aircraft Moment Coefficient	–
δ_r	Rudder Deflection	rad
$\delta_{e,max}$	Max Elevator Deflection	m
Δ_{fus}	Fuselage Influence of Aircraft Moment Coefficient	–
Δ_{nac}	Nacelle Influence of Aircraft Moment Coefficient	–
$\dot{m}_{coolant}$	Mass Flow Coolant	kg/s
$\dot{m}_{coolant}$	Mass Flow of Coolant	kg/s
\dot{m}_{tube}	Mass Flow Through Tube	kg/s
$\dot{Q}_{battery}$	Heat Flow of Battery	J/s
\dot{Q}_{cruise}	Heat Flow at Cruise	J/s
\dot{Q}_{motors}	Heat Flow of Motors	J/s
η_v	Airflow speed at vertical with respect to the wing	–
η_{deg}	Degradation Efficiency	–
$\eta_{dp,isolated}$	Propulsive Efficiency	–
η_{pack}	Pack Level Efficiency	–
η_{prop}	Propeller Efficiency	–
$\frac{t}{c}$	Thickness-to-Chord Ratio	–
Γ	Dihedral Angle	deg
Λ	Sweep Angle	rad
λ	Taper Ratio	–
$\lambda_c/2$	Sweep Angle at Half Chord	rad
$\Lambda_{0.5c}$	Sweep at Half Chord	rad
μ_d	Rolling Resistance Coefficient	–
ψ	Tip Over Angle	deg
ρ	Air Density	kg/m ³
ρ_{Al}	Density Aluminium	kg/m ³
$\rho_{coolant}$	Density Coolant	kg/m ³
σ_v	Sidewash Angle Vertical Tail	rad
σ_y	Yield Stress	Pa
σ_z	Stress in z-direction	Pa
σ_{axial}	Axial Stress	Pa
$\sigma_{bending}$	Bending Stress	Pa
$\sigma_{cc,panel}$	Crippling Stress Panel	Pa
σ_{cc}	Crippling Stress in Flange	Pa

σ_{cr}	Crippling Stress	Pa	$C_{n\beta}$	Directional Stability Coefficient aircraft	–
σ_{HE}	Geometrical Parameter	–	c_{root}	Root Chord	m
τ	Control Surface Effectiveness	–	$C_{y_{v\alpha}}$	Lift Slope of the Vertical tail	–
τ_v	Vertical effectiveness	–	$d\epsilon/d\alpha$	Downwash Gradient	–
τ_{cr}	Crippling Shear Stress	Pa	$d\sigma_v/d\beta$	Sidewash Gradient	–
A	Cross Sectional Area	m ²	$d\theta/dz$	Rate of Twist	1/m
a	Speed of sound maybe give a different symbol	m/s	D_p	Propeller diameter	–
a_p	Axial Induction Factor	–	d_{mlg}	Diameter of Main Landing Gear Wheels	m
a_w	Velocity Increase over Wing	–	d_{nlg}	Width of Nose Landing Gear Wheels	m
$A_{frontal}$	Frontal Area Radiator	m ²	D_{roll}	Rolling Drag	N
A_{LC}	Small Cable Cross-sectional Area	m ²	E^*	Battery Density	Wh/kg
A_{SC}	Large Cable Cross-sectional Area	m ²	E	Young's Modulus	Pa
AR	Aspect Ratio	–	e	Oswald Efficiency Factor	–
AR_h	Aspect Ratio Horizontal Tail	–	$E_{cell2035}^*$	Energy Density of Cell in 2035	Wh/kg
AR_{actual}	Geometric Aspect Ratio	–	$E_{cell2035}$	Energy Capacity of Cell in 2035	Wh
$AR_{effective}$	Effective Aspect Ratio	–	e_{HE}	Airflow Tube Perimeter	m
b	Wingspan	m	E_{tot}	Energy	J
c	Chord	m	F	Force	N
C_D	Aircraft Drag Coefficient	–	F_{axial}	Axial Force	N
c_f	Skin Friction Coefficient	–	F_{flap}	Flap Force	N
c_g	Geometric Chord	m	F_{size}	Safety Factor	–
C_L	Aircraft Lift Coefficient	–	FF_C	Component Form Factor	–
C_p	Power coefficient	–	G	Shear Modulus	GPA
C_t	Thrust coefficient	–	h_{cruise}	Cruise Altitude	m
$C_{coolant}$	Specific Heat Capacity	J/kg * K	h_{ground}	Fuselage Height From Ground	m
C_{D_0}	Zero Lift Drag Coefficient	–	h_h	Height Horizontal Tail	m
C_{Dblade}	Propeller Drag Coefficient	–	h_{pass}	Airflow Tube Height	m
C_{dmisc}	Miscellaneous Drag Coefficient Factor	–	$h_{tailcone_{end}}$	Height of End of Tailcone	m
C_d	Airfoil Drag Coefficient	–	$h_{winglet}$	Winglet Height	m
C_{f_c}	Flat Plate Skin Friction Coefficient	–	I	Moment of Inertia	m ⁴
C_f	Chord Length at Flap Location	m	i_h	Incidence Angle Horizontal Tail	deg
$C_{L\alpha_{A-h}}$	Lift Slope of Aircraft Without Tail	–	$I_{cell_{cruise}}$	Current Through Cell in Cruise	A
$C_{L\alpha_h}$	Lift Slope of Horizontal Tail	–	I_{yy}	Moment of inertia in y-direction	m ⁴
$C_{L\alpha_w}$	Lift Slope of Wing	–	IF_c	Interference Factor	–
C_{L_i}	Integrated Design Lift Coefficient	–	J	Advance Ratio	–
C_{l_p}	Rolling Moment Coefficient due to Roll Rate	–	k	Spring Stiffness	N/m
C_{L_0}	Lift Coefficient at Zero AOA	–	L/D	Lift over Drag	–
C_{l_α}	Lift Slope of the Airfoil	–	l_h	Distance between CG and Horizontal Tail	m
$C_{l_{\delta_a}}$	Rolling Moment Coefficient due to Aileron Deflection	–	l_v	Vertical Tail Arm	–
			$l_{business}$	Cabin Length Business Class	m
			l_{cabin}	Cabin Length	m
			l_{cables}	Cables Length	m
$C_{L_{A-h}}$	Lift Coefficient of Aircraft Without Tail	–	$l_{cockpit}$	Length of the Cockpit	m
$C_{L_{airframe}}$	Lift Coefficient of Full Aircraft	–	$l_{economy}$	Cabin Length Economy Class	m
$C_{L_{cruise}}$	Lift Coefficient in Cruise	–	l_{fn}	Distance Between Nose and LE of Wing	m
$C_{L_{design}}$	Wing Design Lift Coefficient	–	l_{galley}	Length of the Galley	m
$C_{l_{design}}$	Airfoil Design Lift Coefficient	–	$l_{lavatory}$	Length of the Lavatory	m
C_{L_h}	Lift Coefficient of Horizontal Tail	–	$l_{nosecone}$	Length of the Nosecone	m
$C_{L_{max, clean}}$	Max Lift Coefficient in Clean Configuration	–	$L_{tailcone}$	Length of the Tailcone	m
$C_{L_{max, landing}}$	Max Lift Coefficient in Landing Configuration	–	l_{tail}	Length of the Tail	m
$C_{L_{max}}$	Wing Maximum Lift Coefficient	–	l_{tubes}	Length of Tubes	m
$C_{l_{max}}$	Airfoil Maximum Lift Coefficient	–	$l_{type_{II}}$	Length of Type III Door	m
$C_{L_{opt}}$	Optimum Lift Coefficient	–	$l_{type_{I}}$	Length of Type I Door	m
$C_{m_0, airfoil}$	Zero Lift Moment Coefficient Airfoil	–	M	Mach Number	–
$C_{m_{acw}}$	Moment Coefficient of the Wing	–	M_x	Moment in x-direction	Nm
$C_{m_{ac}}$	Moment Coefficient of the Aircraft	–	m_{bat}	Battery Mass	kg
C_m	Airfoil Moment Coefficient	–	M_{bend}	Bending Moment	Nm
$C_{n_{\beta_{A-h}}}$	Directional Stability coefficient less horizontal tail	–	m_{cables}	Cables Mass	kg
			$m_{coolant-battery}$	Mass Coolant in Battery	kg

m_{HE}	Mass Heat Exchanger	kg	t_{Al}	Thickness Aluminium	m
M_{tip}	Mach Number at Tip of Propeller	–	$T_{c,max}$	Maximum Thrust Coefficient	–
$m_{winglet}$	Winglet Mass	kg	T_{cruise}	Cruise Thrust	N
M_{wing}	Moment of the Wing	Nm	T_{lift}	Torque due to Lift	Nm
M_W	Moment of the Weight	Nm	T_{loiter}	Loiter Time	min
MAC	Mean Aerodynamic Chord	m	t_{spar}	Thickness Spar	m
$MTOW$	Maximum Take Off Weight	kg	T_{static}	Static Thrust	N
N	Number of propellers	–	TR_{inv}	Investment Tax Rate	–
n	Revolutions per Second	RPS	TR_{rev}	Revenue Tax Rate	–
n_{blades}	Number of Propeller Blades	–	U	Voltage	V
N_{seat}	Number of Seats Abreast	m	U_{bl}	Annual Block Hours	hrs
n_{tubes}	Number of Tubes	–	V	Airspeed	m/s
P	Roll Rate	deg/s	ν	Poisson Ratio	–
P_a	Power Available	W	V_h	Airspeed at Horizontal Tail	m/s
P_p	Power per Propeller	kW	V_p	Propeller Disk Velocity	m/s
P_r	Power Required	W	V_{bl}	Block Velocity	m/s
P_{br}	Shaft Brake Power	kW	V_{cruise}	Cruise Velocity	m/s
P_{cruise}	Cruise Power	W	$V_{EAS_{climb}}$	Equivalent Climb Speed	–
$P_{required}$	Power Required	W	V_{LOF}	Lift Off Airspeed	m/s
q	Shear Flow	N/m	V_{shear}	Shear Force	N
Q_{engine}	Torque of Engine	Nm	W/P	Power Loading	N/W
R	Range	m	W/S	Wing Loading	N/m ²
R_w/R_p	Slipstream Contraction Ratio	–	W	Weight	N
$R_{business}$	Rows in Business Class	–	$W_{additionalcargo}$	Weight of the Additional Cargo	kg
$R_{cell-internal}$	Cell Internal Resistance	Ω	W_{aisle}	Width of the Aisle	m
$R_{cell_{int}}$	Internal Cell Resistance	Ω	W_{arm}	Width of the Arm Rest	m
$R_{diversion}$	Diversion Range	km	$W_{battery}$	Weight of the Fuselage	kg
$R_{economy}$	Rows in Economy Class	–	$W_{clearance}$	Clearance of the Cabin Width	m
$R_{nominal}$	Nominal Range	km	$W_{fuselage}$	Weight of the Fuselage	kg
RC	Rate of Climb	m/s	W_{ground}	Width of the Cabin at Cabin Floor	m
$RC_{max_{sl}}$	Maximum Rate of Climb at Sea Level	m/s	$W_{headroom}$	Width of the Cabin at Head Height	m
Re	Reynolds Number	–	w_{mlg}	Width of Main Landing Gear Wheels	m
Rev_{km}	Revenue per Kilometre	€	w_{nlg}	Width of Nose Landing Gear Wheels	m
S	Wing Area	m ²	$W_{passenger+luggage}$	Weight Passengers and Luggage	kg
S_h	Horizontal Tail Area	m ²	$W_{payloadtotal}$	Weight of the Total Payload	kg
S_v	Area of Vertical Tail	m ²	W_{seat}	Width of the Seat	m
S_{blade}	Area Propeller Blade	m ²	$W_{wingstructure}$	Weight of the Wing Structure	kg
$S_{landing}$	Landing Distance	m	x_p	Axial Position Propeller from Wing Leading Edge	m
S_{net}	Wing Area Without Projection of Fuselage	m ²	x_{ach}	Tail Aerodynamic Centre x-location	m
S_{ref}	Reference Area (Wing)	m ²	x_{LEMAC}	X-location of LE of MAC	m
$S_{take-off}$	Take-Off Distance	m	x_{mlg}	X-location of Main Landing Gear	m
S_{wet}	Wetted Area	m ²	x_{nlg}	X-location of Nose Landing Gear	m
T/W	Thrust over Weight	–	y	Distance to Neutral Line	m
T	Temperature	K	Y_e	Offset Engine in operative	–
t	Thickness	m	Y_{MAC}	Spanwise Location of MAC	m
T_c	Thrust coefficient	–	y_{mlg}	Y-location of Main Landing Gear	m

List of Tables

3.1	Explanation of the IDs used in Figure 3.1 . . .	4	9.1	Dynamic stability coefficients of ECHO-1 . . .	65
3.2	Stakeholder Requirements	7	9.2	Eigenvalues of the dynamic modes of ECHO-1	67
3.3	Changed Stakeholder Requirements	7	10.1	Dimensions of the wing box in terms of the chord	72
3.4	Design risks with their respective mitigation strategy	8	10.2	Optimization bounds on the inputs for the program	76
3.5	Operational risks with their respective mitigation strategy	8	10.3	Optimization program constraints. Note that here σ is the combination (addition) of axial and bending stresses (σ_{axial} and $\sigma_{bending}$). Moreover, τ is a combination of the shear stresses due to torque and the ones due to shear forces.	76
3.6	Different types of unit tests and their descriptions	9	10.4	Final wing dimensions and parameters.	77
4.1	Weight and symbol for each configuration trade-off criterion	10	10.5	Maximum allowable and actual stresses in the wing box.	78
4.2	Summarising values for each of the four design options from Midterm Report[1]	12	10.6	Materials Selected for Trade-Off	79
4.3	Final concept trade-off table	13	10.7	Materials with the related wing box weight	79
5.1	Performed Verification for Energy Calculations and Mission Profile Python Script	22	10.8	Life Cycle Assessment	80
6.1	Performed Unit Tests for Distributed Propulsion Python Scripts	31	10.9	The natural frequencies of the wing model	84
6.2	Performed Unit Tests for the Propeller Python Scripts	36	10.10	All the unit test performed on the python script for the structural analysis	84
6.3	The Characteristics of the 1.375 Scaled Base HPDM-250 Motor	37	10.11	Validation Results	85
6.4	H3X HPDM characteristics for the ECHO-1	37	11.1	The Number of Modules in Each of the Battery Compartments	88
6.5	Performed Unit Tests for the Cable Design Scripts	39	11.2	BTMS Parameters and Results Table	94
7.1	Airfoil Parameters From Xfoil	41	11.3	BTMS Components Mass Overview	94
7.2	Airfoil Scoring for Trade-Off	41	12.1	Performance Final Design Parameters	98
7.3	Airfoil Parameters From Xfoil	42	12.2	Structures/Weight Final Design Parameters	98
7.4	Airfoil Scoring for Trade-Off	42	12.3	Aerodynamics Final Design Parameters	98
7.5	High-Lift-Devices	44	12.4	Propulsion Final Design Parameters	98
7.6	Zero lift drag components of wing, fuselage, truss, horizontal tail and vertical tail	47	12.5	Geometry/Stability Final Design Parameters	98
7.7	Overview of all zero lift and total drag components	47	12.6	Compliance matrix	101
7.8	Performed Unit Tests for Aerodynamic Python Scripts	50	12.7	Contingency Check with Baseline Report Values	106
8.1	Dimensions for the fuselage sizing	51	13.1	Sustainability characteristics for production	108
8.2	Dimensions of the fuselage of ECHO-1[2]	53	13.2	Sustainability characteristics for use	108
8.3	Dimensions of the aircraft cargo-hold [2]	54	13.3	Sustainability characteristics for end-of-life	109
8.4	Centre of gravity and weight of the 5 main components that make up the operational empty weight	55	14.1	Time allocation of the activities performed during a turnaround	115
8.5	Centre of gravity (from nose of the aircraft) and weight of the battery and cargo compartments	56	14.2	The flights a day based on the battery replacement time	117
8.6	Centre of gravity ranges as percentage of MAC	56	14.3	"ABC" check interval and duration	119
8.7	Centre of gravity placement	57	16.1	Research and Development Cost	125
8.8	Final Horizontal Tail Value	59	16.2	Manufacturing and Acquisition Cost	126
8.9	The Required Surface Area for the Vertical Tail	60	16.3	Operating Cost	127
8.10	Dimensions for the landing gear sizing	61	16.4	A selection of top level requirements to be competitive in the regional market[3]	129
8.11	Performed Unit Tests for Geometry Scripts	64	16.5	Financial breakdown comparing ECHO-1 to main competitors	131
			16.6	Kerosene and electricity cost comparison	131

List of Figures

3.1	Mission profile of ECHO-1, explanation of the IDs can be found in Table 3.1	4	6.5	Hamilton Standard Propeller Static Thrust Chart For 4 Bladed 100 AF [6]	34
3.2	Functional Flow Diagram	5	6.6	Variation of thrust with Mach number [7]	34
3.3	Functional Breakdown Structure	6	6.7	Hamilton Standard Propeller Efficiency Chart for 4 Bladed 100 AF propeller [6]	35
3.4	Risk Map showing the risk rating of design and operational risks	9	6.8	Schematic of H3X HPDM-250 ¹	37
4.1	Prandtl-Box wing with aft wing mounted propellers.	11	6.9	Cable layout of single wing	38
4.2	Conventional high wing design with T-tail and two wing mounted propellers.	11	6.10	Temperature profile of power cable during the full mission	38
4.3	Blended wing body with aft-fuselage mounted distributed propulsion.	11	7.1	Top View of the Wing Planform of ECHO-1	43
4.4	Truss-braced wing with wing mounted distributed propulsion.	11	7.2	Sweep angle and cant angle of a winglet. [8]	45
4.5	A Figure showing the sensitivity analysis for the final trade-off	15	7.3	ECHO-1 spanwise lift distribution based on local lift coefficient	46
5.1	The Wing and Power Loading Diagram	16	7.4	Aerodynamic polars for ECHO-1 wing, only valid up to $C_{L_{max}}$. For values above $C_{L_{max}}$, the line is dotted.	48
5.2	Pie Chart Showing the Division of OEW	17	7.5	Comparison of XFOIL and JavaFoil data with respect to experimental data on NACA 4 and 5 series airfoils	49
5.3	Power required and power available (horizontal lines) for altitudes from $h = 0$ to $h = 6000$ [m]	18	8.1	Cross-sectional sketches for fuselage sizing	52
5.4	Battery Begin of Life versus End Of Life	23	8.2	Top view cabin layout of ECHO-1	53
5.5	Mission profile of altitude plotted against mission time, labels showing different flight phases	24	8.3	Sideview of the cargo hold of ECHO-1	54
5.6	Mission profile of true airspeed plotted against mission time, labels showing different flight phases	24	8.4	The 2 CG excursions drawings	56
5.7	Mission profile of propulsive power plotted against mission time, labels showing different flight phases	24	8.5	The two plots that were iterated to get the LEMAC, CG range and the tail sizing of the aircraft	58
5.8	Mission profile of battery energy spent plotted against mission time, labels showing different flight phases	25	9.1	Different parameters response to input for the dynamic eigenmodes of an aircraft	67
5.9	Mission profile of altitude plotted against ground distance, labels showing different flight phases	25	10.1	Geometric model of the wing and truss used in Anastruct	70
5.10	Mission profile of true airspeed plotted against ground distance, labels showing different flight phases	25	10.2	Free Body Diagram of the Wing with Truss for Load Case 1	71
5.11	Mission profile of propulsive power plotted against ground distance, labels showing different flight phases	26	10.3	Free Body Diagram of the Wing with Truss for Load Case 2	71
5.12	Mission profile of battery energy spent plotted against ground distance, labels showing different flight phases	26	10.4	Visualization of the wing box inside the NACA 43014	72
5.13	State of charge plotted against mission time for the design mission (battery EOL), red region showing SOC smaller than 20%	27	10.5	Torque distribution along the wingspan	73
5.14	State of charge plotted against ground distance for the design mission (battery EOL), red region showing SOC smaller than 20%	27	10.6	Twist angle along the wingspan	73
6.1	A visualisation of the three design parameters of the distributed propulsion array [4]	28	10.7	Allowed stress in the top and bottom skin before buckling	74
6.2	The effect of the distributed propulsion array in cruise conditions	31	10.8	Wing mass against truss-wing attachment location as a percentage of the total span.	76
6.3	The effect of the distributed propulsion array in landing conditions	31	10.9	Internal force diagrams for loading case one (flight with ultimate load factor).	77
6.4	A visualisation of the propeller [5]	33	10.10	Wing box stress diagrams for loading case one (flight with ultimate load factor).	78
			10.11	FBDD of the fuselage model	82
			10.12	Idealised cross section of the fuselage	82
			10.13	Vibrational model of the wing	83
			10.14	Deflection of the wing box tip with different meshes at load case 1	85
			11.1	The Two Types of Battery Modules	87
			11.2	The Battery Placement	88
			11.3	Heat Flow and Power Drawn Over the Mission Profile	89
			11.4	BTMS Architecture	90

11.5 Battery ΔT Over the Mission Profile	91	14.1 Charging performance of various charging setups	111
11.6 Heat Exchanger Frontal Geometry [9]	92	14.2 Power against State of Charge graphs	112
11.7 Heat Exchanger Frontal Area vs. Depth	93	14.3 Schematic overview of a possible aircraft stand for ECHO-1, icons coming from [10]	113
11.8 Heat Exchanger and Air Inlet in Fuselage Belly Fairing	93	14.4 Work Flow Diagram of the turnaround of ECHO-1	115
12.1 Design Process N2 Chart	95	14.5 The Respective ranges which can be achieved when charging for 29 min.	116
12.2 Iteration Process Flowchart	96	14.6 The ranges which can be reached when charging for 29 min at begin and end of life	117
12.3 Iteration and convergence overview for the MTOW, C_{Di} and wing weight fraction.	96	15.1 Project Design And Development Logic[1]	122
12.4 Effect of changing the initial MTOW estimate on the first outer iteration in Figure 12.3. For the red and purple lines, the iterations were truncated after 15.	97	15.2 Post DSE Gantt Chart	123
12.5 ECHO-1 Three-View	99	15.3 The Production Plan for ECHO-1	124
12.6 Design convergence sensitivity to various passenger and range combinations, with a 575 Wh/kg battery energy density.	103	16.1 Research, Development, Test and Evaluation Cost	126
12.7 Overview of the convergence boundaries for various battery energy densities.	103	16.2 Manufacturing and Acquisition Costs	127
12.8 MTOW of converged designs at energy density of 525 Wh/kg	104	16.3 Direct Operational Costs (left) and Indirect Operational Costs (right)	127
12.9 MTOW of converged designs at energy density of 575 Wh/kg	104	16.4 Break Even Point Point (left) and Break Even Analysis (right)	128
12.10 MTOW of converged designs at energy density of 625 Wh/kg	104	16.5 Distribution of flight distances worldwide[3]	130
12.11 Overview of the convergence boundaries for various landing and take-off distances.	105	16.6 US airports with runway length over 1500 m[11]	130
12.12 Overview of the convergence boundaries for various cruise speeds.	105	16.7 Feasible routes using ECHO-1	130
12.13 Payload-Range Diagram from Midterm Report Values	106	17.1 Final design convergence post-errata	135
		17.2 Final design sensitivity post-errata	136
		17.3 Comparison sensitivity pre-errata and post-errata	136

Executive Overview

The potential of electric transport innovations has been lighting up some of climate change's darkest corners in the last twenty years. For this Design Synthesis Exercise project, a team of young TU Delft Aerospace Engineering students has been contacted by Venturi Aviation with a challenging, yet highly innovative project: design a fully electric regional transport aircraft. In this report, the final stage of the conceptual design process is outlined, together with a summary of all the previous steps in the design process.

Mission Objective

The purpose of the project was to design a fully electric transport aircraft with entry into service by 2030, focused on achieving zero emission flight, flying at 500 km/h for 1000 km, whose payload volume can be easily reconfigured for both passenger transport (50 passengers) or cargo transport (6000 kg). These numbers were later revised to 48 passengers, 800 km, 5588 kg of cargo and entry into service by 2035. With this, and a number of other stakeholder requirements, it was possible to set up the design process, with the goal of evaluating the feasibility of the project.

Systems Design

After having performed preliminary performance calculations on four selected trade-off concepts, a truss-braced wing configuration stood out due to its extremely high lift-over-drag capabilities and propulsion integration capabilities. For each department or subsystem, more detailed calculations were performed and then combined in one larger iteration loop, which is run until a final design is obtained. Firstly, the performance department simulated the different flight phases of the aircraft to be able to estimate the mass of the batteries required, as well as a number of other performance-related parameters, such as the climb gradient and the power required at all flight phases. For the final design, a total of 6919 kg of batteries is required, which accounts for a total of approximately 33% of the maximum take-off weight. The power provided by the batteries, besides powering avionics and the thermal management system, also powers the propulsion system, which, due to the large wingspan, was chosen as distributed propulsion. For the final design, it comprises of 16 engines with four propellers each, mounted on the leading edge of the wing, and separated within the electric system into groups in a 3-3-2 configuration. Not only does this type of propulsion provide sufficient power and thrust for all phases of flight, but it even provides an increase of 0.3 in lift coefficient at landing, when atypically landing at 80% of the power available. However, this increase in lift coefficient is not sufficient to meet the total $C_{L_{max}}$ required at landing, and as such, the aerodynamics department also designed flaps to aid in this. Another interesting aspect which was modelled within the aerodynamics department was the estimation of the aerodynamic forces during flight: at cruise, a lift-over-drag of 28.24 is achieved for the final design, which is consistent with the numbers found in literature for the truss-braced wing. This high number truly is one of the reasons why ECHO-1 really makes the most out of the available design space for electric flight.

With propulsive, aerodynamic and performance attributes analysed, it was possible to start logistically organising the aircraft, within the geometry department. A 2-1 seating configuration was identified as most suitable for ECHO-1, which holds all cargo and batteries in the cargo compartment in the lower half of the cabin. Within this department, the landing gears were also sized, as well as the horizontal and vertical tail. With these it was possible for the stability and control department to analyse the stability of the aircraft, and the only (mildly) unstable eigenmode found was the spiral. Following this, a special note was payed to the batteries: due to this rare addition to aircraft, a whole

chapter was devoted to the design of the logistical implementation of the batteries in the fuselage, as well as the thermal management system. Due to the dense mass which the batteries have, the structures department computed a 4.19% increase in fuselage structural weight. The wing, wing box and truss were also designed: the chosen material was aluminium AL7068 T-6, which lead to a total wing weight of 1024.33 kg (both wings included). In comparison to other aircraft, the wing is about twice as light in percentage of maximum take-off weight: 4.9%, while typical numbers range between 8 to 13%. The reason for this is mainly due to the two trusses: one truss only weighs less than 50 kg but it can hold a tensile load of 1.2 MN, which equates to nearly two A320 at maximum take-off weight.

The final ECHO-1 design was obtained after 18 iterations, with a maximum take-off weight of 20937 kg and a wing surface area of 56.85 m², for a battery energy density of 575 Wh/kg. To see how this last value would affect the feasibility of the design, a sensitivity analysis was performed. Within this, a number of other parameters were also varied, such as the range, the number of passengers, amongst others. It was seen that in general, one row of passengers was equivalent to 73 km of range (in terms of limits of feasibility), and 1 additional Wh/kg was equivalent to 2 additional kilometers of range (at 575 Wh/kg). With this converged design, a number of other considerations were made: the first was the sustainability impact of ECHO-1. Throughout its life-cycle, ECHO-1 produces 87% less greenhouse gasses than comparable kerosene aircraft. It can thus be concluded that ECHO-1 complies with requirements set by Venturi Aviation. Moreover, in terms of operational characteristics, ECHO-1 is able to charge up to 94.1% state of charge using 4 Megawatt Charging System chargers, while still allowing for a 30 minute turn-around time. Furthermore, as ECHO-1 has electric distributed propulsion, the risk involved with engine failure is much lower compared to traditional propulsion options. Additionally, the operational costs for ECHO-1 are substantially lower due to 48% lower refuelling cost, allowing for more operational profit compared to existing similar aircraft. Lastly, due to the truss and simple engines, vibrations are considerably decreased, leading to lower maintenance cost.

For airlines, operating ECHO-1 is thus financially attractive and the required runway length of only 1500 meters allows ECHO-1 to operate from the vast majority of regional airports. In the near future, ECHO-1 will change regional air transport considerably. Although electric flight has room for improvement, it shows great potential. With continuous progress in battery energy density, ECHO-1 should be reconfigured in the future to make optimal use of these developments. However, for now, the boundaries of E-flight have been found.

Introduction

Over the last decades, a sustainable way of living has become more and more a topic of conversation. This comes at the same time the world is becoming more of a connected place, creating an ever increasing demand for transportation which is expected to continue after the COVID-19 pandemic. It is therefore that the transport industry has to make the transition to a more sustainable approach. In the past decade, the car industry has shown how electrification allowed for significant reduction in emission. It is up to the aircraft industry to follow this movement[12].

Venturi Aviation, a Delft-based start-up, has spotted this trend and aims to apply it to air transportation. Their goal is to develop an electric regional aircraft that is fully battery-powered, capable of transporting 50 passengers over 1000 kilometers at a flight velocity of 500 km/h. In order to fulfil this ambition, Venturi Aviation asked for assistance from DSE group 9 at the faculty of Aerospace Engineering at TU Delft. Combining the requirements from Venturi Aviation with those following from the DSE assignment, the objective statement reads: "Design a fully electric transport aircraft, focused on achieving zero emission flight, flying at 500 km/h for 1000 km, whose payload volume can be easily reconfigured for both passenger transport (50 passengers) or cargo transport (6000 kg), by ten students in ten weeks". Over the past ten weeks, ten third year BSc students have dedicated their time on this project. The final design is called ECHO-1.

Soon after the midterm report was handed in, following from preliminary calculations, it was deemed impossible to meet all initial stakeholder requirements. In consultation with Venturi Aviation, the new passenger requirement was set to 48 (total payload mass was set to 5588 kg), the new range requirement was set to 800 km and the new Entry Into Service (EIS) was set to 2035. Additionally, after completing the midterm report, a new requirement was added by Venturi: the wingspan shall not be larger than 36 meters. Therefore, for the final design, these were the driving requirements.

The main aim of this report is to describe the work performed over the past ten weeks, putting most of the emphasis on the final five weeks in which detailed calculations were performed. Throughout the midterm phase, a configuration had been chosen by means of a trade-off and initial calculations on that design option were performed. This yielded the starting point of the final design. To avoid ambiguity, only final results are presented throughout the report.

This report starts off by outlining the project preparation that was performed in the baseline report in [chapter 3](#). This is followed by [chapter 4](#) where the trade-off process in the midterm report is summarised. Then, in [chapter 5](#), ECHO-1 is analysed in terms of its performance. This is followed by a propulsion analysis in [chapter 6](#). The aerodynamic characteristics of ECHO-1 are presented in [chapter 7](#). Following from these analyses, the aircraft geometry sizing is performed in [chapter 8](#), also discussing the static stability of the aircraft. The dynamic stability is analysed in [chapter 9](#).

To continue, structural analysis was performed on ECHO-1, which is presented in [chapter 10](#). Having determined the geometry and structures, the integration of the batteries, something that distinguishes ECHO-1 from other aircraft, is explained in [chapter 11](#). Thereafter, in [chapter 12](#), it is explained how one integrated software tool was created, allowing for the design of an optimised aircraft.

Having finished the design of the aircraft, a sustainability analysis is performed in [chapter 13](#). Furthermore, an operational analysis is performed in [chapter 14](#). Thereafter, [chapter 15](#) outlines the activities that are to be performed after the DSE is over. Additionally, an economic analysis is performed in [chapter 16](#), outlining the cost breakdown as well as a business case for ECHO-1. The report is concluded in [chapter 17](#), where also a few recommendations for further work are presented, as well as a few errata that were found in the final design phase.

Project Preparation

This chapter aims to present the project preparation which was mainly determined throughout the first phases of the project. First, in [section 3.1](#), the mission profile of ECHO-1 is presented, after which the functional analysis on the aircraft is presented in [section 3.2](#). Afterwards, in [section 3.3](#), the requirements by Venturi are presented. Furthermore, in [section 3.4](#), the most important technical risks that were determined in the baseline report are presented[13]. Finally, in [section 3.5](#), an outline on the verification and validation procedures throughout the report is presented.

3.1 Mission Analysis

Given the objective of ECHO-1, the mission profile ([Figure 3.1](#)) of the aircraft can be constructed. Since the mission is very comparable to conventional aircraft, its mission profile is too. It consists out of flying to the destination aircraft, where a landing is attempted between point 6 and 7. If for any reason the aircraft should divert or loiter, reserves are accounted for which are identified by IDs 7 up until 10. It is very important to design for reserves as this will increase the range that the aircraft should be designed for significantly. Using the mission analysis, the functions of ECHO-1 can be determined based on the flight phases it will go through.

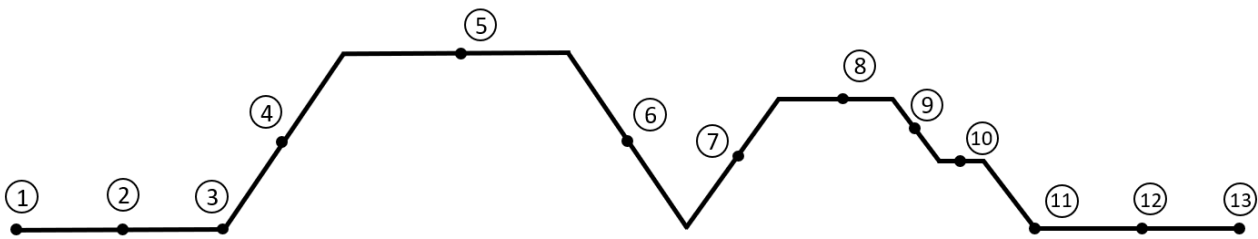


Figure 3.1: Mission profile of ECHO-1, explanation of the IDs can be found in [Table 3.1](#)

Table 3.1: Explanation of the IDs used in [Figure 3.1](#)

ID	Explanation	ID	Explanation
1	Engine Start	8	Diversion
2	Taxiing	9	Descent 2
3	Take-Off	10	Loiter
4	Climb 1	11	Landing
5	Cruise 1	12	Taxiing
6	Descent 1	13	Engine Shut-Down
7	Climb 2		

3.2 Functional Analysis

A functional analysis of ECHO-1 was performed in order to set up the requirements for the aircraft. This was done by making a functional flow diagram, which can be seen in [Figure 3.2](#). In this flow diagram, the functions of ECHO-1 are depicted in chronological order. Also, it is possible to see which functions are performed in parallel and which in series as well as dependencies which are indicated by dotted lines. Furthermore, the functional breakdown structure is shown in [Figure 3.3](#). This flow chart shows the five main phases ECHO-1 will go through during its life cycle: design, certify, produce, operate and retire.

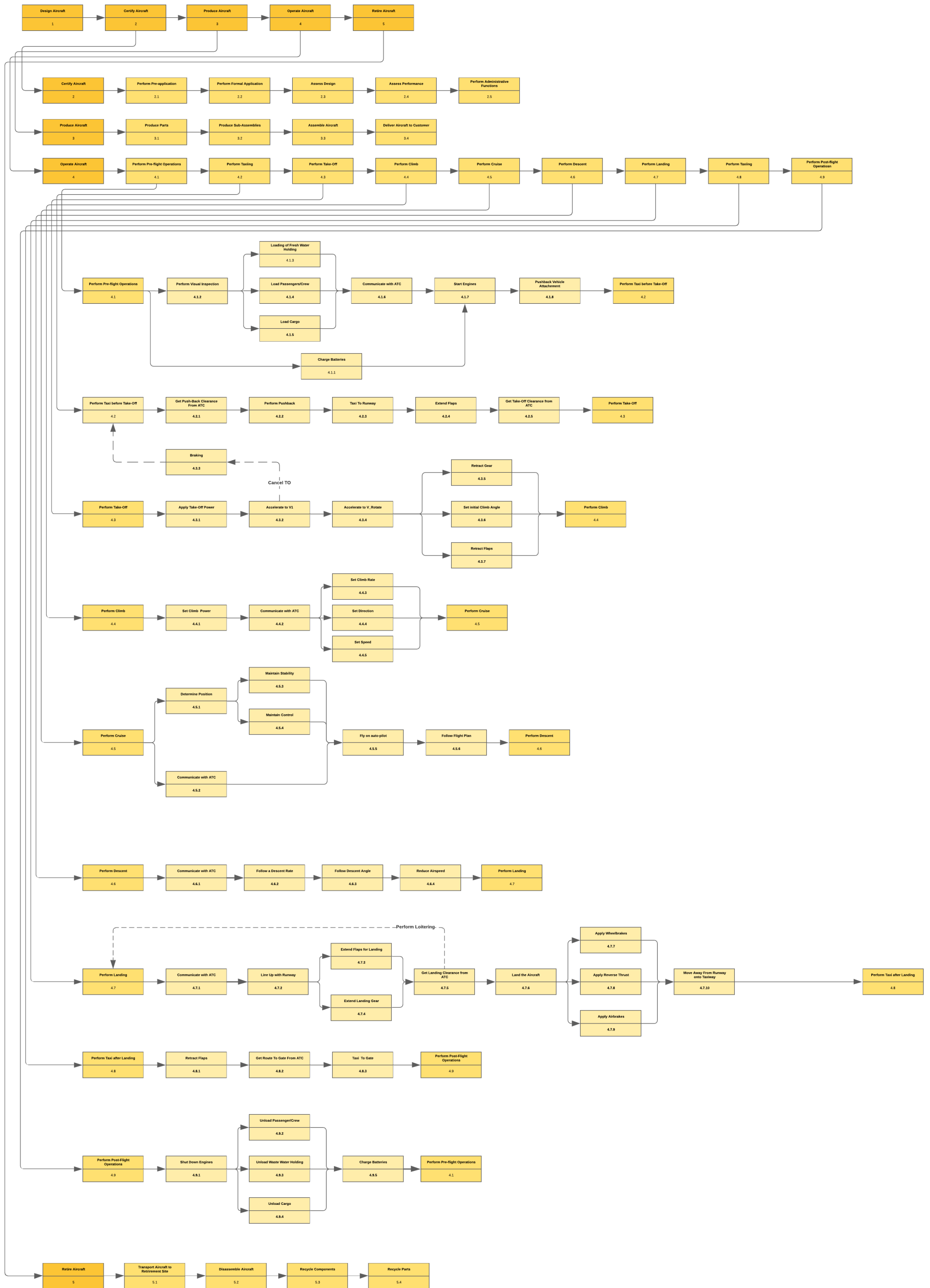


Figure 3.2: Functional Flow Diagram

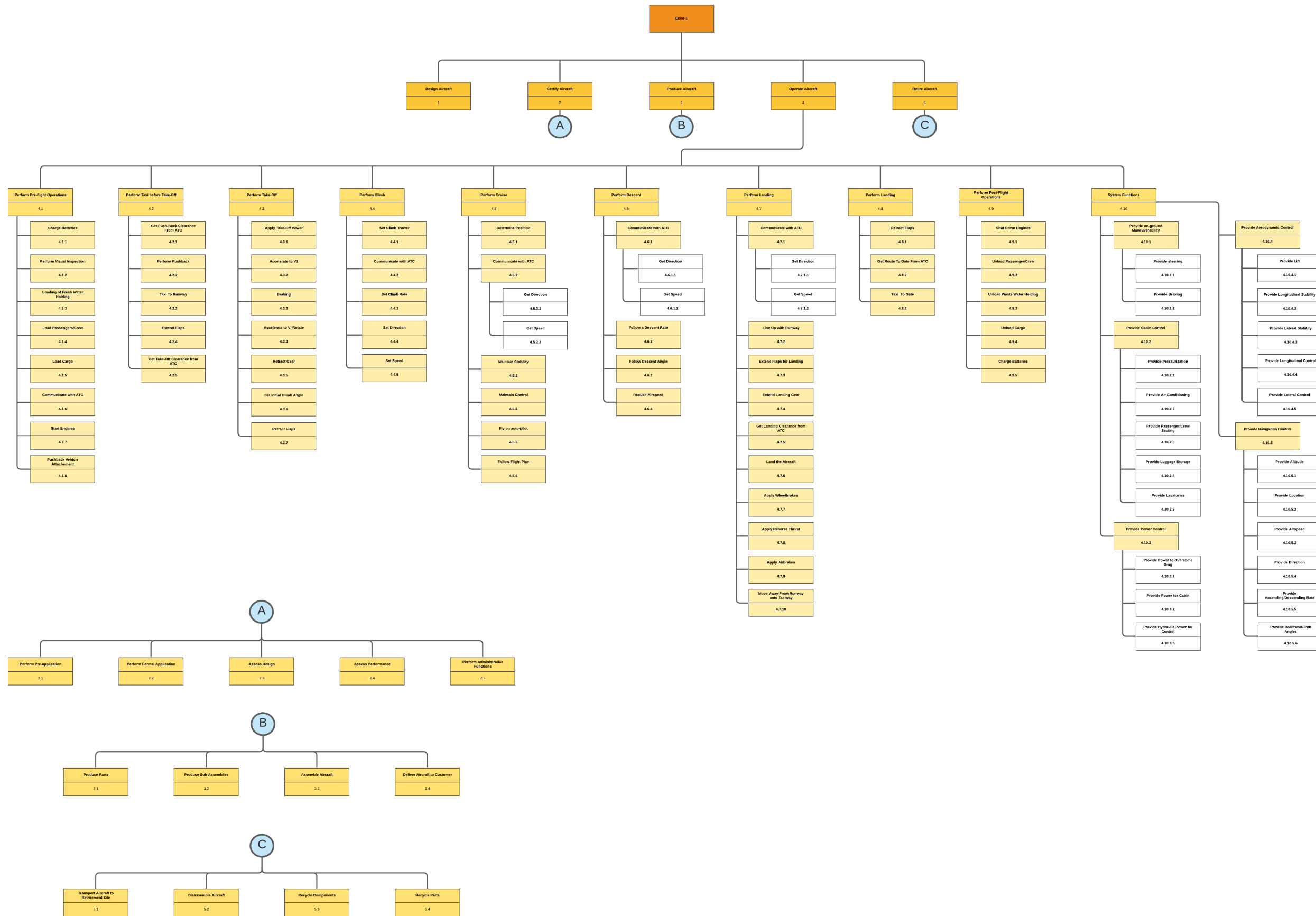


Figure 3.3: Functional Breakdown Structure

3.3 Stakeholder Requirements

This section will discuss the requirements set by Venturi. As these are requirements from the stakeholder, they are treated as top level system requirements or stakeholder requirements. Based on these requirements, initial sizing was performed. Using the top level requirements and the functional analysis of ECHO-1, subsystem requirements could be set up. These requirements are listed in the compliance matrix in [section 12.3](#). The stakeholder requirements are listed in [Table 3.2](#).

Table 3.2: Stakeholder Requirements

Requirement ID	Description
VEN-TOP-PERF-1	The aircraft shall be able to carry a payload of 50 passengers in passenger transport configuration.
VEN-TOP-PERF-2	The aircraft shall be able to carry 6000 kg of cargo in cargo configuration.
VEN-TOP-PERF-3	The aircraft shall have a range of 1000 km at maximum payload.
VEN-TOP-PERF-4	The aircraft shall have a cruise speed of 500 <i>km/h</i> .
VEN-TOP-PERF-5	The aircraft shall have a mission block time of 2.5 hours.
VEN-TOP-PERF-6	The aircraft's turnaround time shall be no more than 30 minutes.
VEN-TOP-SR-1	The aircraft shall be compliant with current EASA CS25 regulations.
VEN-TOP-SR-2	The arrangement and handling of batteries in the aircraft structure shall ensure operations as safe as the current conventional powertrains.
VEN-TOP-SR-3	The aircraft shall have an accessible battery storage space.
VEN-TOP-SUS-1	The aircraft shall be operated with zero emissions.
VEN-TOP-SUS-2	During the design process the cost for end-of-life shall be taken into account.
VEN-TOP-SUS-3	Electricity infrastructure shall be taken into account in terms of costs and emissions.
VEN-TOP-COST-1	The direct operating costs shall be competitive with respect to existing similar aircraft.
VEN-TOP-COST-2	A battery life-cycle financial plan shall be made when the battery life cycle is affecting the direct operating cost.
VEN-TOP-OTHER-1	Adequate technology parameters and technology readiness levels shall be considered to forecast an Entry Into Service in 2030.

As mentioned before, Venturi asked the group to do a feasibility study to see if their initial requirements can be met. After several meetings and some initial sizing, together with Venturi, it was decided to change some of the requirements in order to create an available design space. To add, an extra stakeholder requirement was added by Venturi which is a requirement on the wingspan. From [Table 3.2](#), requirements **VEN-TOP-PERF-1**, **VEN-TOP-PERF-2**, **VEN-TOP-PERF-3** and **VEN-TOP-OTHER-1** have been changed. The updated requirements (with a new ID) can be found in [Table 3.3](#).

Table 3.3: Changed Stakeholder Requirements

Requirement ID	Description
VEN-TOP-PERF-1.1	The aircraft shall be able to carry a payload of 48 passengers in passenger transport configuration.
VEN-TOP-PERF-2.1	The aircraft shall be able to carry 5588 kg of cargo in cargo configuration.
VEN-TOP-PERF-3.1	The aircraft shall have a range of 800 km at maximum payload.
VEN-TOP-OPS-1	The aircraft shall have a maximum wingspan of 36 m
VEN-TOP-OTHER-1.1	Adequate technology parameters and technology readiness levels shall be considered to forecast an Entry Into Service in 2035 .

3.4 Technical Risk Assessment

A technical risk analysis is very important for every project. For this project, technical risks have been identified in two different phases. First of all, design risks were identified. These risks can occur during the design phase of the project. Secondly, operational risks were identified. These risks can occur during the operational phase of ECHO-1 and therefore should be taken into account when designing the aircraft. For each of the identified risks, a risk rating was determined which is a multiplication of the likelihood and impact, both on a scale from 1-5. In order to reduce the risk rating, mitigation strategies were determined for each risk. Table 3.4 and Table 3.5 show ten design and operational risks with their planned mitigation strategy respectively. These tables show the ten most important risks with the highest risk rating, the complete tables can be found in the Baseline Report [13]. To add, the risk map before and after mitigation are shown in Figure 3.4. As can be seen in the right risk map, the maximum risk rating is only six on a scale of 25, which means the likelihood of occurrence and the impact is small.

Table 3.4: Design risks with their respective mitigation strategy

Risk ID	Event	Planned Prevention	Response
D1	Unachievable top level requirement	Allocate time for revising requirements and calculations	Revise requirements with Venturi
D2	Unachievable driving requirement	Allocate time for revising requirements and calculations	Revise requirements with Venturi
D3	Having a killer requirement, but classifying it as a normal one	Double check all requirements, predict impact on design space	Increase design space by changing requirements
D5	Battery energy density will not be as high as expected	Get information from both literature and market experts to perform better estimates	Redo the design calculations with the updated value
D6	Design is too complex which makes it hard to perform calculations	Give large weight to design complexity in trade-off, perform research on design process	Iterate a simplified version of the design, choose a different design
D7	No design convergence	Avoid design overconstraining, allocate time for revising requirements and calculations	Increase design space by changing requirements
D9	Wrong assumptions used during calculations	Prevent major simplifications, predict impact of simplifications, study literature, perform verification	Perform validation
D12	Missing design options	Spend extra time on determining every design option	Find missed options, enlarge DOT, re-iterate trade-off with new options
D17	Incorrect verification procedures	Set up detailed verification procedures and strictly adhere to them	Redo calculations
D18	Incorrect validation procedures	Set up detailed validation procedures and strictly adhere to them	Redo calculations

Table 3.5: Operational risks with their respective mitigation strategy

Risk ID	Event	Planned Prevention	Response
OP3	Due to a technical issue, one or more engines are inoperative	Aircraft is designed to fly with one or more engines inoperative	Aircraft will fly to the nearest airport with the available engines
OP4	During a storm the aircraft experiences strong gusts	Aircraft is designed to withstand higher loads due to gusts	Aircraft can continue its flight
OP5	Landing with strong crosswinds	Aircraft is designed to be able to land with strong cross winds	Aircraft can perform a go-around
OP6	The aircraft has to perform a go-around	During design, an energy reserve is accounted for	The aircraft will perform go-around since enough energy is available
OP15	Aircraft is overloaded	Maximum loading weight for the aircraft will be set by the manufacturer	Do not take-off
OP16	Aircraft is incorrectly loaded	Ground crew will be trained to load the aircraft correctly	Do not take-off
OP18	No battery power during flight	Batteries initially charged for reserves can be used	Check batteries to see what the problem is
OP21	During flight something catches fire	Fire protection taken into account when in detailed designing	Fire extinguishers on board
OP22	Flaps do not extend	Build in redundancy in the system	Divert to nearby airport with longer runway
OP23	Battery cooling system does not work	Build in redundancy in the cooling system of the batteries	Reduce thrust and land as quickly as possible

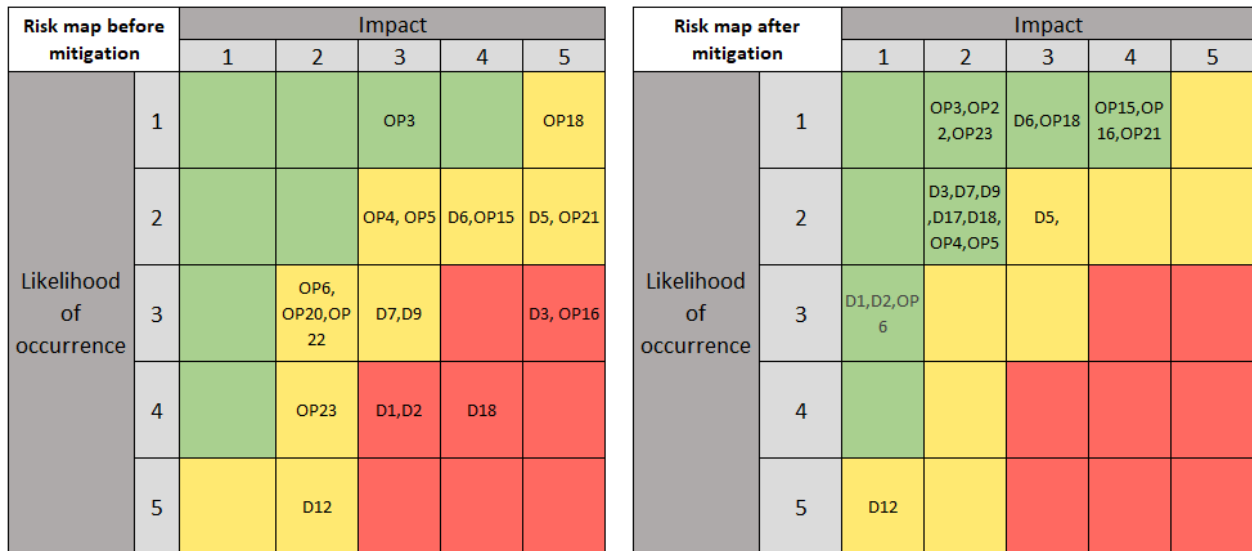


Figure 3.4: Risk Map showing the risk rating of design and operational risks

3.5 Verification and Validation Plan

Verification and validation of the written code is very important. Verification will determine if the simulation model accurately represents the physical problem and validation determines if the model represents the physical problem to be solved. A few ways of verifying code are visual walk-through, unit tests, integration tests and system tests. Model walk-through tests are performed while writing the code in order to correct obvious mistakes. There are a lot of different unit tests that can be performed. The unit tests that are performed are summarised in [Table 3.6](#). How to perform integration and system tests is highly dependent on the simulation to be tested. The tests performed in order to verify and validate the simulation models will be described in a separate section in [chapter 5 - chapter 12](#).

Table 3.6: Different types of unit tests and their descriptions

Name	Description
Check inputs	A unit test that checks in the inputs of a class or function are properly assigned.
Hand calculation	A unit test that checks the outputs of a class or function to a value calculated by hand
Excel test	A test that checks the outputs of a class or function by performing the same calculating in excel
Gradient test	A unit test that checks if the gradient of a curve or output of a class or function is as expected.
Zero test	A unit test that checks if the output of a class or function is as expected when an input parameter is set to zero.
One test	A unit test that checks if the output of a class or function is as expected when an input parameter is set to one.
Expected value test	A unit or system test that checks if a certain output value is as expected with the given input values.

Recap On Design Selection

This chapter aims to summarise the results of the Midterm Report. In this report, the configuration of the aircraft was decided upon. This chosen configuration is the starting point of all of the designs done in this report. [section 4.1](#) presents all of the configurations considered in the Midterm Report and [section 4.2](#) presents why and how the final design was chosen out of the configurations.

4.1 Design Options

The first step in designing an aircraft was deciding upon the concept or the general lay-out of the aircraft. In the Baseline Report[13], various design concept options were considered and evaluated. From this analysis, four different general aircraft concepts were chosen to be best and were investigated for further analysis. Initially, these four designs were: the conventional design, a partial redesign of an existing aircraft, the blended wing body and the truss-braced wing concept. After further reconsideration, the partial redesign was replaced with the Prandtl box wing because the redesign would perform the same or worse than the conventional concept and the potential of the Prandtl-box wing was overlooked.

In order to compare the different concepts at the highest level of accuracy, the best possible configuration for each concept must first be chosen for the final trade-off. This meant that before the final trade-off had started, separate configuration trade-offs were performed. For each concept, this configuration trade-off was performed based on the criteria and their weights seen in [Table 4.1](#). For some of the concepts, the configuration trade-off is split into two parts; one where the wing concept was chosen and one where the propulsion concept was chosen.

Table 4.1: Weight and symbol for each configuration trade-off criterion

Criteria	Aerodynamic Efficiency	Structural Efficiency	Airport Integration	Propulsive Efficiency & Integration	Technology Readiness Level	Stability
Weight	32.2%	26.5%	5.6%	7.7%	11.3%	16.7%
Symbol	A	B	C	D	E	F

The configuration trade-off for the conventional concept was split into two parts; the wing concept choice and the propulsion system choice. The different wing concepts were the high wing with T-tail, low wing with conventional tail, low wing with T-tail and low wing with box tail. From these different configurations, the best one was chosen to be the high wing with T-tail due to its excellent structural efficiency.

For the truss-braced concept, only one propulsion system trade-off was performed. This was because for the truss-braced concept, there is generally only one wing configuration viable, namely the high wing with T-tail. The different propulsion systems considered in this trade-off were boundary layer ingestion, distributed propulsion and two propellers on the wing. The last two can both be ducted or not. In the end, the non-ducted distributed propulsion was the winner because of its great aerodynamics.

The trade-off for the Prandtl-box wing also consisted of two parts. For the wing design there were three options considered; the conventional Prandtl-box wing, the inverted Prandtl-box wing and the Wolkovitch design. Furthermore, the propulsion system trade-off included the following options:

propeller engines mounted on the wing or fuselage, distributed propulsion, fuselage mounted push propellers and boundary layer ingestion. The final configuration for the Prandtl-box wing was the conventional wing with propellers mounted on the back wing, mainly because of its good aerodynamics and propulsive efficiency.

At last, the blended wing body trade-off was performed. This trade-off only consisted of one trade-off where the propulsion system was analysed. This is because the blended wing body concept does not have significantly different wing configurations. For the blended wing body the considered propulsion systems were distributed propulsion mounted on the wing or fuselage, boundary layer ingestion on the fuselage, two to four propellers both ducted and non-ducted mounted on wing or fuselage. From all of these options, the best configuration is the aft-fuselage mounted distributed propulsion due to its good aerodynamics and structural efficiency.



Figure 4.1: Prandtl-Box wing with aft wing mounted propellers.



Figure 4.2: Conventional high wing design with T-tail and two wing mounted propellers.



Figure 4.3: Blended wing body with aft-fuselage mounted distributed propulsion.



Figure 4.4: Truss-braced wing with wing mounted distributed propulsion.

All of the four configurations which were the best according to the configuration trade-offs are displayed in [Figure 4.1¹](#), [Figure 4.2²](#), [Figure 4.3³](#) and [Figure 4.4](#). The reason that different propulsion systems won for different concepts, was that the propulsion systems have interaction with the aircraft geometry. This interaction can counteract or amplify the positive or negative effects of the propulsion systems. In the end, these four designs were further analysed in the final trade-off.

4.2 Design Trade-Off

The design trade-off included a more detailed analysis of the four concepts. This analysis included an initial Class I Weight Estimation for each of the concepts which resulted in a estimate of MTOW. Together with the range equation, taken from literature[14], further insight on the effect of various parameters of the aircraft on the MTOW was obtained. These parameters included the payload mass,

¹<https://mmta.co.uk/2018/06/29/radical-closed-wing-aircraft-design-could-see-greener-skies-take-flight/> (accessed on 18 May 2021)

²<https://www.jetphotos.com/photo/6971104> (accessed on 18 May 2021)

³<https://www.airbus.com/newsroom/press-releases/en/2020/09/airbus-reveals-new-zeroemission-concept-aircraft.html> (accessed on 18 May 2021)

the lift-over-drag ratio, propulsive efficiency, battery energy density, the fraction of OEW over MTOW and the range[14].

For each of the concepts, a preliminary design point was chosen. These design points came from wing loading versus power loading graphs. These graphs were made by sizing for critical flight phases like take-off, landing and cruise. In these graphs, a certain wing loading and power loading was chosen for each concepts which resulted into wing areas, and power required. With these two known, further preliminary dimensions and performance parameters of each concept were computed, given in Table 4.2.

Table 4.2: Summarising values for each of the four design options from Midterm Report[1]

Parameter	Unit	Conventional	Prandtl	Truss Braced	Blended Wing Body
L/D	-	16	21.5	30	22
f_e	-	0.5	0.5	0.5	0.5
AR	-	12	9.7	21	6
W/S	N/m ²	3500	3500	3500	3500
W/P	N/W	0.051	0.044	0.067	0.029
$MTOW$	kg	178839	39247	23882	37322
S	m ²	501.09	109.97	66.92	104.57
P	MW	34.4	8.8	3.5	12.6
b	m	77.5	32.7	37.5	25.1

Once the detailed description and values for the four different concepts were known, the final concept trade-off was performed. The final trade-off was setup by first determining the trade-off criteria and their weights. This process was performed using the AHP method for determining trade-off weights. In short, the AHP works by giving a relative importance, rated from 1 to 9, between each set of criteria[15]. All of the criteria and their weights can be found in Table 4.3. In the concept trade-off, some important criterion were not considered for various reasons. Firstly, battery integration was left out because at that stage of the design, the battery integration was very difficult to assess and quantify. Including it in the trade-off would only lead to averaging out the scores. The stability was left out because all the designs need to have sufficient stability. However, some designs allow for less design penalties when reaching stability. This measure was taken into account in aerodynamic efficiency. Furthermore, sustainability was left out because sustainability would have been assessed in terms of carbon footprint, end of life costs and operational sustainability, which all was too difficult to quantify at this stage of the project. Finally, the costs were also left out because the designs are not detailed enough in order to estimate accurately the costs.

The final scores for the different configurations can all be found in Table 4.3. For each of the criterion, a brief reasoning for each concept is given. However, do note that all of these reasonings were done with all the information available up until the making of the Midterm Report. This means that not all values are fully up to date with respect to the final design values. The reasoning for the scores coming directly from the Midterm Report are:

“Aerodynamic efficiency is based on the approximate maximum L/D, the propulsion influence on the aerodynamics and the ease of designing stability. The conventional configuration scores the worst in this area because of its low L/D value of 16. The truss-braced design scores the best in this category because of its extremely high L/D of 30. The Prandtl box wing scores mediocre with a L/D of 21.5 but it has some complicated stability issues. The blended wing body scores slightly higher with a L/D of 22 and a some stability issues.” [1]

“Structural efficiency is based on the $\frac{OEW}{MTOW}$ of each design. This fraction is a good indication of the integrity of the structure. The $\frac{OEW}{MTOW}$ is computed by computing the wing weight fraction of each configuration by looking at reference aircraft. This is enough because the configurations of each

design are very similar except for the wing. Only the blended wing body is very different from the others so for this a method similar to the Class I Weight Estimation was performed by looking at reference aircraft.” [1]

“**Airport integration** takes into account how well the designs can be integrated into current airports and their operations. For this criterion the following aspects are taken into account: ease of maintenance, ground clearance, dimensions of the aircraft and ability to land at small airports. Logically, the conventional design can be integrated into airports very well. On the other hand, the aircraft will become extremely heavy and might destroy small runways. The truss-braced design scores the worst because of its large wingspan. The Prandtl-box wing scores the best because of its small size but the ease of maintenance is not optimal. Finally, the blended wing body has a mediocre score because even though it has a small wingspan, airport integration is hindered by its very unconventional shape.” [1]

“**Propulsion efficiency** is split into three subcriteria: integration of the engine (13%), efficiency (73%) and the sensitivity to design change (14%). With these criteria in mind, another propulsion efficiency trade-off is performed. The conventional design scores quite well because of good engine integration and relatively well efficiency and sensitivity. The truss-braced design also has a good score because of its high propulsion efficiency due to the many propellers. However, the distributed propulsion is more difficult to integrate compared to the other designs. The Prandtl-box wing has a similar score because of its good propulsion efficiency because a very large propeller diameter is possible. However, the design is susceptible to a shift in centre of gravity which makes the sensitivity score lower. The blended wing body scores the worst in this criterion. This is because of its bad efficiency due to the fact that less engines are possible for this distributed propulsion. Besides, the very aft position of the propulsion system results in a high sensitivity to design changes and thus the blended wing body score not well in this category.” [1]

“**Technology readiness level** represents the readiness and feasibility of the technology to be used in the near future and thus incorporates the available knowledge, projected timeline of reference aircraft and ease of certification. The conventional design scores the best in this criterion because this technology is already known for decades and a lot of reference aircraft and designs are available. The truss-braced design is similar to the technology of the conventional design. Only the braces are novel technology and thus it scores a bit worse than the conventional design. The Prandtl-box wing is somewhat similar to the conventional technology but the aerodynamics are new and complicated and only a few conceptual designs exists. The blended wing body technology is very unconventional and complex and they are new for airliners. However, there are some concepts and reference aircraft available and thus it has the worst score together with the Prandtl-box wing. Additionally, the ease of certification for both the blended wing body and the Prandtl-box wing is not great. The final scores of every configuration on each criterion is given in [Table 4.3](#).” [1]

Table 4.3: Final concept trade-off table

Configuration	A (36.1%)	B (26.4%)	C (7.1%)	D (26.4%)	E (4.0%)	Average
Truss-braced	9	7	5	7.47	7	7.70
Prandtl	6	5	8	7.59	4	6.22
Conventional	4	6	6	7.26	9	5.73
BWB	7	6	6	5	4	6.02

In the end, the winner of the design trade-off was the truss-braced wing design with non-ducted distributed propulsion. As seen in [Table 4.3](#), the truss-braced design won with a score of 7.70 out of 10.00 with the second place the Prandtl-box wing with a margin of 1.48. It was safe to say that the truss-braced configuration won comfortably. However, it was not known if results of the trade-off would be the same if some of the criteria weights or scorings would have been different. Therefore, to assess this, a sensitivity analysis on the concept trade-off was performed.

In the sensitivity analysis, the robustness of the trade-off is tested. This was done by changing the trade-off and if the truss-braced concept still came out on top, the results of the initial trade-off were valid. The sensitivity analysis consisted of two components: changing or removing the criteria weights and changing the initial design parameters.

First of all, the weights of the criteria were changed and the new results of the trade-off were analysed. In order to test one criterion, the new weight of that criteria varied between 50% and 150% of its original weight, while keeping proportions of the weights for the other criteria the same. This process was repeated for every criterion and the results can be seen in [Figure 4.5](#). All of the plots show that the truss-braced concept would have won comfortably for every criterion change. In order to remove a criterion, the same process was used as changing the weights but now the weight of the criterion in question was set to zero. This result is also given in [Figure 4.5](#) and it can be seen that again the truss-braced concept won convincingly. However, only if the aerodynamic efficiency criterion was removed, the margin of victory for the truss-braced design was insignificant. It can be argued that, because the aerodynamic efficiency is so critical for the performance, this would have never happened.

Secondly, the input parameters of the design were changed in order to have different designs values for each configuration. When changing the design parameters, the calculations will output a heavier and larger or lighter and smaller aircraft. This will effect all designs equally negatively or positively. In this case, the relative difference between the different concepts would not have changed, meaning that the outcome of the trade-off would have been the same. However, one thing that could have happened is that for one criterion all the designs scores would have been lowered because of the different design parameters. This would have affected the outcome of the trade-off, but this effect is the same as simply changing the weight of that criterion, which has already been done in the sensitivity analysis.

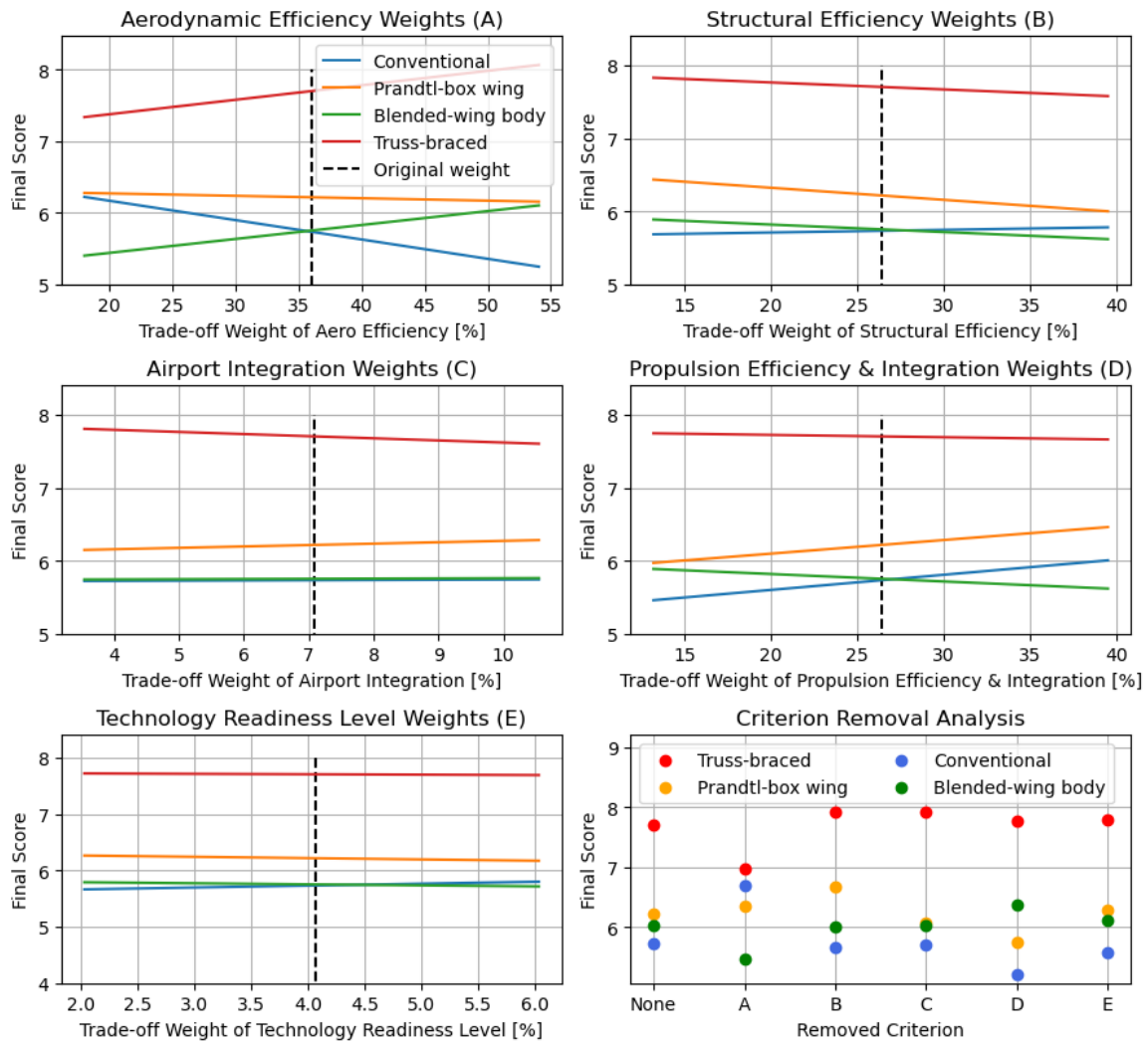


Figure 4.5: A Figure showing the sensitivity analysis for the final trade-off

To conclude, the final design chosen was the truss-braced design with distributed propulsion. The trade-off, which was used to determine the final design, showed very robust behaviour. This meant that the results of this trade-off were valid and thus it was highly likely that the truss-braced concept with distributed propulsion, is the best design choice for this specific design objective.

5

Performance Analysis

The performance analysis of an aircraft shows how it performs during all flight phases in the mission profile. The design mission at end of life of ECHO-1 has a range of 800 km, after which it needs to have enough battery energy left to perform a diversion of 185 km as well as 30 minutes of loitering. To enable the convergence of the design, accurate weight estimations are needed. This chapter will in [section 5.1](#) start by describing the weight estimation that was done with the wing- and power loading diagrams. This estimate was used as a starting point for the design and an initiation of the iteration loop. In this loop the battery weight is computed in a more accurate way by analysing the mission profile. The general mission profile has already been discussed in the previous reports[13][1], but now it will be discussed in more detail. [section 5.2](#) describes how the consumed energy is calculated for each flight phase. Subsequently [section 5.3](#) described how these calculations were verified. Finally the calculations lead to final estimations of the battery mass as well as plots of the flight profile, which

will be discussed in [section 5.4](#).

5.1 Class II and Wing and Power Loading

In order to be able to start with the performance analysis first a weight estimation needs to be performed. This weight estimation is done in two steps. First, initial sizing of the power required and wing area will be conducted which results in a wing and power loading diagram. The method to arrive at this weight and this diagram is presented in the Midterm report [1]. The resulting diagram can be seen in [Figure 5.1](#). From this figure the wing loading ($\frac{W}{S}$) equalled 3614 N/m² and the power loading 0.066 N/W.

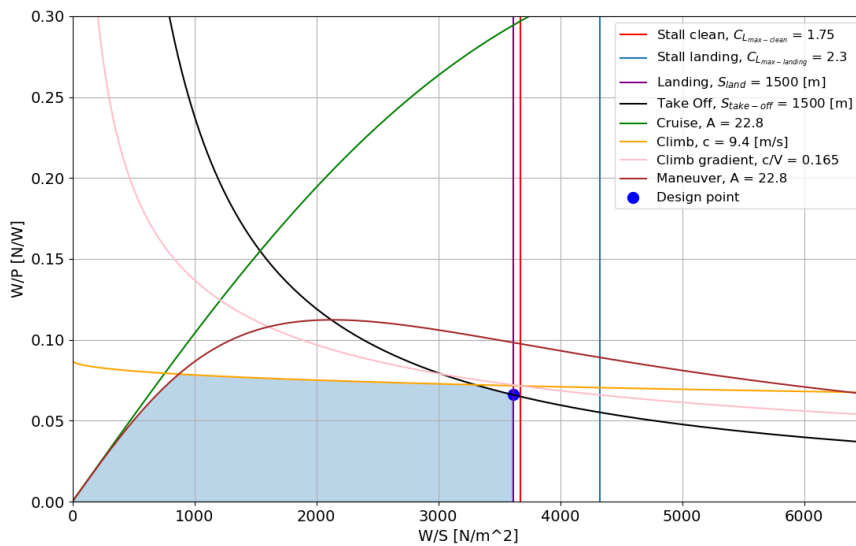


Figure 5.1: The Wing and Power Loading Diagram

With the wing and power loading, it is possible to make an initial estimate on the size of the wing and propulsion system. This can be done when knowing the MTOW of ECHO-1. A part of the MTOW is the OEW which can be estimated by the Class II weight estimation. In the Class II weight estimation the weight of all subsystems is estimated either using empirical data [16] or more accurate calculations when possible. The resulting weights of the subsystems can be seen in [Figure 5.2](#). Do note that these results are of the final converged design. The values were updated in each iteration as will be explained in [chapter 12](#). One part of the miscellaneous mass was attributed to the design of a future speed brake which would be necessary to generate enough drag during landing. Another part of the miscellaneous mass was attributed to unforeseen mass additions in future stages of the project.

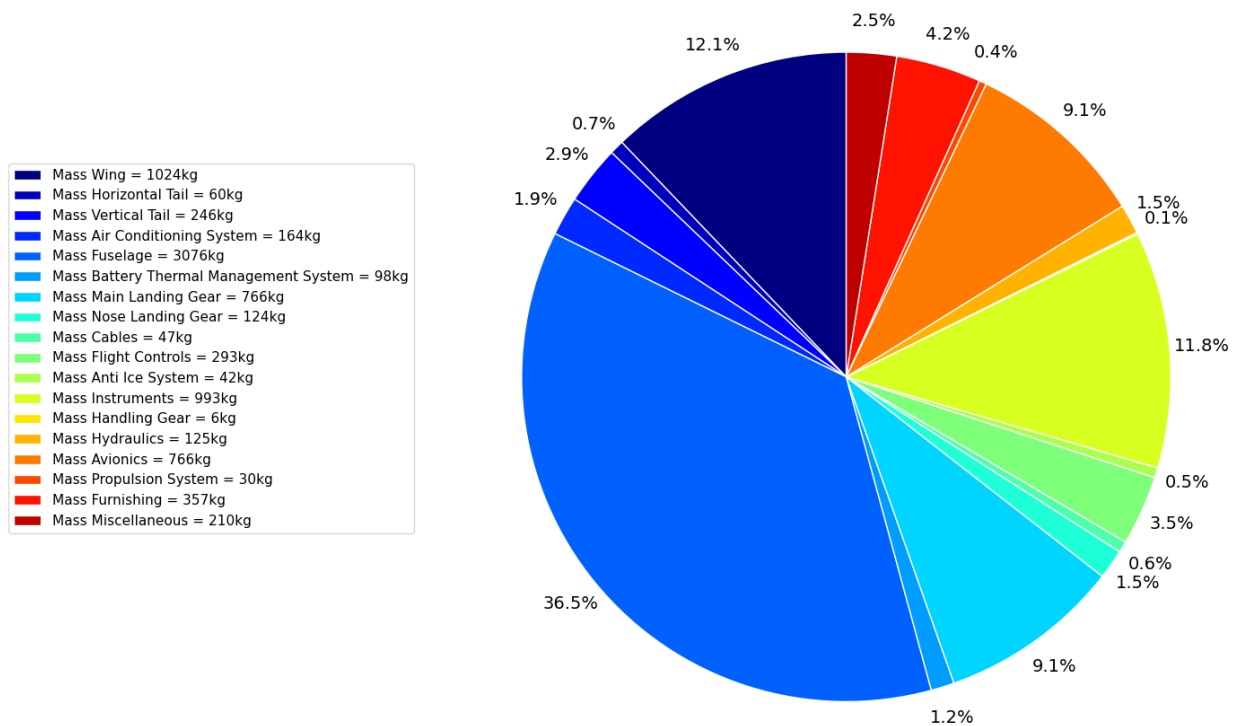


Figure 5.2: Pie Chart Showing the Division of OEW

5.2 Performance Calculations Method

The main goal of the performance analysis is to get an accurate description of the mission profile and subsequently the energy that is spent throughout the mission as described in [section 3.1](#). This energy can then be used to calculate the required battery mass. The battery mass is used as an input for the iteration loop instead of the Class I battery weight estimation. A python program was written to simulate the design mission by numerically integrating through each of the flight phases by calculating the aircraft performance in each point. The result is a complete mission profile including altitude, engine power, airspeed, ground distance and energy consumed at each point in time. The program calculates the above variables in each of the flight phases based on the way the specific flight phase is performed. There are however also some general assumptions that have been made regarding the mission profile calculations:

- Atmospheric properties like temperature and density are according to the ISA standard atmosphere with take-off and landing at sea level.
- The aircraft weight is constant throughout the flight and equal to the maximum take off weight (MTOW).
- The performance at a single point in flight during each of the flight phases, except for taxi and the take-off ground run, is calculated using the assumption that lift is equal to weight.
- Aerodynamic characteristics at points in the mission are calculated assuming a parabolic lift-drag polar. The parameters C_{D_0} , A_{eff} and e are estimated by the aerodynamics department to be 0.0165, 22.79675 and 0.93 respectively. Only for cruise a more accurate estimation of lift over drag is used since that one is available from the aerodynamics department.
- Since the aircraft uses variable pitch propeller propulsion it is assumed that power available for a given altitude is constant over airspeed. Furthermore it is assumed that power available scales inversely with density, resulting in lower power at higher altitude.
- Power required is obtained by multiplying the aircraft drag with the true airspeed. [Figure 5.3](#) shows the power required and power available for 4 altitudes from sea level to cruise. It can

be seen that the excess power gradually decreases when altitude increases. The lower bound of the power required curves is determined by the aircraft stall limit, at $C_{L_{max}}$.

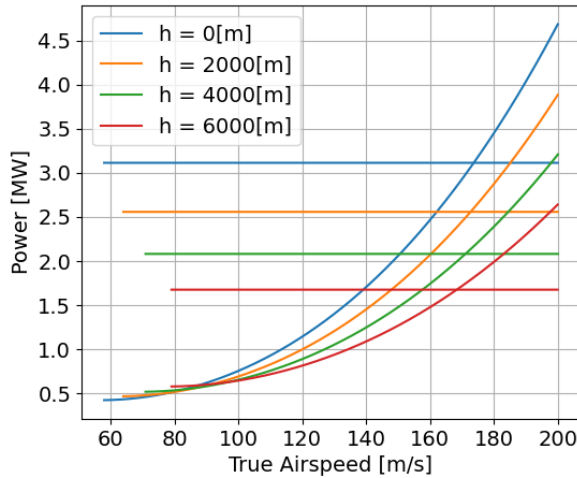


Figure 5.3: Power required and power available (horizontal lines) for altitudes from $h = 0$ to $h = 6000$ [m]

Using these assumptions and methods the performance at each point in flight can be calculated. Consumed energy follows from multiplying the propulsive power at a point with the time step dt and adding it to the total energy. Most of the parameters that influence the performance stem from the requirements as defined earlier. However some parameters had to be estimated or calculated separately, for those literature was used to support the assumptions. The sections below will describe the specifics regarding the method and assumptions for each of the flight phases within the mission profile. Starting with the taxi from the departure airport and moving through all mission phases, including diversion and loiter, until the arrival airport is reached.

5.2.1 Taxi

A flight mission always starts with a taxiing phase where the aircraft travels over the ground from the pier to the runway where it will take off. In this phase the propulsive power will be provided by the aircraft propellers. The power required is calculated by summing the drag due to aerodynamics with the rolling resistance from the tires and multiplying it with the velocity. The rolling resistance drag is given by the following formula:

$$D_{roll} = \mu_d * MTOW * g \quad (5.1)$$

Where μ_d is the rolling resistance coefficient, of which a conservative estimated value of 0.015 is taken [17]. For the aerodynamic drag only the zero lift drag is considered, since there is no lift produced during taxiing.

For the taxi speed and distance Amsterdam Airport Schiphol is taken as a reference. The maximum taxiing distance to the Polderbaan runway is one of the largest in the world at roughly 11 km, the maximum taxi speed at Schiphol is 14 m/s [18]. These values are again conservative to not underestimate the final energy requirements of the aircraft.

5.2.2 Take off and initial climb

After taxiing the aircraft takes off from the runway, this is done at full take off power to ensure a short take off distance. The time for the ground run, which is needed for the energy calculations, is obtained from the propulsion department as described in subsection 6.2.2.

The take off phase consists not only of a ground run, but also of an initial climb until a certain height

is reached. The objective of the initial climb is to gain as much height as possible in as short a distance as possible. Therefore the flaps are deflected in their take off setting to ensure a high lift coefficient and thus a high climb gradient. The flight at maximum climb gradient is obtained when the aircraft flies at full take off power at an equivalent airspeed equal to the lift off speed. This climb is maintained until an altitude of 1500 feet is obtained, after which the flaps are retracted and the normal climb phase is started. 1500 feet is chosen as it is a common starting point of the normal climb phase[19].

5.2.3 Climb

After the initial climb phase with the goal to climb as steeply as possible, it is important to climb as quickly as possible to cruise altitude. Therefore for the energy calculations it is assumed that the climb happens at the maximum steady rate of climb, again with maximum power available applied. The maximum steady rate of climb is obtained at a certain equivalent airspeed, $V_{EAS_{climb}}$, which for low subsonic aircraft is also approximately equal to the indicated airspeed. This equivalent airspeed for maximum steady rate of climb is constant over all altitudes. $V_{EAS_{climb}}$ is found at the point where the power required by the aircraft is minimal, since at this point the excess power is at maximum. However, as can be seen in Figure 5.3 the point for minimum power required is equal to or very close to the point where the aircraft stalls. Since this condition is clearly undesirable it is chosen to multiply the airspeed by a factor 1.1 to ensure a safety margin as well as higher speed stability [7]. With the airspeed found, the climb rate is calculated using the following equation:

$$RC = \frac{P_a - P_r}{MTOW * g} \quad (5.2)$$

As power available decreases and power required increases with increasing altitude, the rate of climb decreases as the aircraft goes higher. It is important that the aircraft still meets requirements **SUB-PERF-CL-1**, **SUB-PERF-CL-2**, **SUB-PERF-CL-1**. Therefore these are checked and the program returns a warning when they are not met. This would lead to a need for increase in power. However for the final design the values are: $RC_{max_{sl}} = 13.05$, RC_{max} at cruise altitude = 5.29 and time to climb to FL170 = 577 s, so it can be seen that these are well within the requirement limits.

The aircraft stops climbing when the cruise altitude of 6000 m is reached, after which it starts accelerating to cruise speed as the climb speed is not yet equal to the cruise speed.

5.2.4 Acceleration and Cruise

According to requirement **VEN-TOP-PERF-4** the aircraft needs to cruise at a true airspeed of 500 km/h, or equivalently, 138.88 m/s. Since the aircraft at the top of climb flies at an airspeed of around 87 m/s it first needs to accelerate to cruise speed. This is done at constant altitude, again with maximum power available.

As soon as the aircraft reaches cruise speed the power is reduced to the power required in cruise, such that the altitude and airspeed remain constant. The power required is again calculated with by multiplying the drag with the airspeed. However, the $\frac{C_L}{C_D}$ is in this instance not calculated from the parabolic lift-drag polar. A more accurate estimation of $\frac{C_L}{C_D}$ is available from the aerodynamics department for the cruise condition. The distance the aircraft needs to cover in cruise is obtained by subtracting the ground distance of all preceding phases, as well as the ground distance of the descent and approach phase from the nominal mission range. Which results in a nominal mission range that is equal the value that is used as input for the program. For the energy calculations this range value is set to the **VENT-TOP-PERF-3.1** requirement value of 800 km.

5.2.5 Deceleration and Gliding descent

It is chosen to model the descent phase of the mission as a gliding descent at maximum glide ratio with the power off, as this was determined to be the most energy efficient. The other considered option was to descent quicker than the gliding descent by increasing the drag of the aircraft. This

could be done by windmilling the propellers, which would increase drag but also allow the aircraft to regenerate a bit of the energy. However the aerodynamic efficiency of a windmilling propeller is very low, especially if it's not optimised for energy harvesting conditions [20]. The propeller could be designed with this in mind, as done for the Pipistrel Alpha Electro [21], where a large amount of energy spent in flight can be recuperated with this method. However, it should be noted that the Pipistrel Alpha is a trainer aircraft, which means it is specifically designed to fly short missions at low altitudes with a lot of ascending and descending. For ECHO-1 the mission objectives are very different, therefore a propeller optimised for cruise performance is preferred over a propeller designed for energy recuperation. The latter propeller would have the result that the energy it harvests from the flow does not weigh up to the extra drag it generates. Therefore it is chosen to descent with the propellers in feathering position, with the power off and the propellers in the pitch setting such that the chord is parallel to the airflow, resulting in minimal drag. The total feathered propeller drag is calculated with the following equation:

$$D_{feather} = C_{Dblade} * \frac{1}{2} * \rho * V^2 S_{blade} * N * n_{blades} \quad (5.3)$$

Where C_{Dblade} was conservatively estimated to be 0.02, as no specific data was available for the chosen propeller airfoil. The feather drag is added to the drag from the lift-drag polar for each point during the deceleration and descent phase. Before the actual gliding descent the aircraft first needs to decelerate to the speed that results in the optimal glide ratio. During deceleration, which happens at a constant altitude, the engines are turned off and the aircraft slows down due to its drag. When the aircraft reaches its optimal speed the gliding descent is initiated.

The optimal glide ratio of the aircraft is at the condition for maximum L/D . This maximum L/D value follows from the lift-drag polar and is calculated in the following way[7]:

$$\frac{C_L}{C_{Dmax}} = \frac{1}{2} \sqrt{\frac{\pi * AR * e}{C_{D0}}} \quad (5.4)$$

The maximum glide ratio is equal to the calculated $\frac{C_L}{C_{Dmax}}$. Using this formula, a maximum L/D value of 31.76 was found, but with the feathering drag added the gliding lift over drag becomes 27.40. Which equates to a glide angle of 2.09 degrees. With this ratio and the airspeed, the descent time and distance can be calculated. The airspeed that corresponds to this condition is calculated from the optimum C_L value, using that lift is equal to weight. The optimum C_L value is given by the following equation [7]:

$$C_{Lopt} = \sqrt{C_{D0} * \pi * AR * e} \quad (5.5)$$

As said before, the aircraft has to decelerate to the optimum glide velocity. This velocity is found by inputting the found C_{Lopt} into the lift formula. After the aircraft reaches this speed it starts gliding by keeping the indicated airspeed constant at the calculated value, in this case equal to 75.0 m/s. Which results in the desired glide at maximum lift over drag. When the aircraft reaches its approach altitude the approach phase is initiated. For the energy calculations the approach altitude is set to a fixed value of 1500 feet.

5.2.6 Approach

During approach the aircraft has its flaps deflected and it is assumed that it flies at a power equal to 0.8 times the take off power. This power is not needed to propel the aircraft, but it does increase the effective lift coefficient due to the blown wing effect. From requirement **VEN-PERF-APP-1** it follows that the aircraft needs to fly the approach at an airspeed of 72 m/s. For the energy calculations the approach is flown at the standard approach slope of 3 degrees [22]. This combination of airspeed,

approach angle and the applied thrust would result in an accelerating aircraft if no action is taken. Therefore the aircraft applies a speed brake to increase the drag, resulting in a steady approach until touchdown.

5.2.7 Diversion

According to requirement **SUB-PERF-RES-1** the aircraft needs to be able to fly its nominal mission range and have enough energy left to perform 185 km of diversion and 30 minutes of loiter. This is accounted for in the calculation of the total mission energy. The diversion phase starts directly after the approach by again having an initial climb at the steepest possible climb angle until an altitude of 1500 feet. This simulates a touch and go manoeuvre, which is deemed the most critical scenario in terms of energy required. After the initial climb the aircraft again climbs at the airspeed for maximum rate of climb. However, in this instance the aircraft does not climb all the way to cruise altitude, since the ground distance covered during climb + gliding descent would overshoot the 185 km. Therefore the diversion is simulated in such a way that the total distance of climb, glide and approach adds up to 185 km. At the maximum altitude reached during diversion the aircraft shortly accelerates to go from the optimal climb speed to optimal gliding descent airspeed. For our design mission this altitude is 5001 m.

5.2.8 Loiter

Finally the energy required for loitering for 30 minutes is also added to the total mission energy. It is important to know the altitude at which the loitering phase is performed to calculate the energy consumption. ICAO Annex 6 prescribes reserve fuel to be taken on a flight to allow for 30 minutes of holding at 1500 feet altitude [23]. Therefore this altitude is also taken as the loiter altitude for our energy calculations.

Loiter is ideally performed at the airspeed for maximum endurance, resulting in minimal energy consumption. This airspeed corresponds to the point where power required is minimal. Similar to the climb phase this airspeed is again multiplied by a factor of 1.1 to ensure a safety margin and speed stability [7]. After loitering for 30 minutes the aircraft performs its final approach, followed by another taxi run of 11 km, similar to the one at the start of the mission.

5.3 Code Verification

The performance calculations were verified by performing multiple unit- and system tests on the energy calculations python program. During this process several errors were found and fixed, in the end resulting in a program which was deemed verified.

Table 5.1: Performed Verification for Energy Calculations and Mission Profile Python Script

Nr.	Description	Type	Parameters	Passed
1	Check equivalence of $E_{totprop}$ and adding separate energies per phase	Expected test	value $E_{totprop}, E_{array}$	Yes
2	Same as 1 but for time	Expected test	value t, t_{array}	Yes
3	Same as 1 and 2 but for ground distance	Expected test	value $grounddist_{array},$ ground distance	Yes
4	Check if ground distance after nominal phases is 800 km	Expected test	value ground distance	Yes
5	Check visually if Energy only increases	Expected test	value E_{tot}	Yes
6	Check for multiple points if energy at that point is equal to the time integral of the power up until that point	Expected test	value $p_{array}, E_{totprop}$	Yes
7	Check max. and min. of p-, v- and h-array	Expected test	value $p_{array}, v_{array}, h_{array}$	Yes

5.4 Results

From numerically integrating through all the above flight phases the propulsive energy consumption in each flight phase is known. Moreover, at each point in time throughout the design mission the altitude, power, airspeed and ground distance covered are known. This section will provide all relevant results from these performance calculations, starting with the battery mass in [subsection 5.4.1](#) before moving on to the mission profile results in [subsection 5.4.2](#). It should be noted that all percentages of battery energy below correspond to the percentage at the end of the battery life, so with a battery energy density of 575 Wh/kg (2000 cycles, 15% degradation).

5.4.1 Battery Mass

To get from the total propulsive energy to the required battery mass some additional steps have to be taken. First the efficiencies in the power path from battery to propulsive power have to be taken into account. These include the following: Propeller efficiency, motor efficiency and electronics efficiency which includes the cables, battery and other components. The efficiencies were determined by the propulsion department to be the following values:

- Propeller efficiency: 0.82
- Motor efficiency: 0.93
- Electronics efficiency: 0.999

Dividing the total propulsive energy by these efficiencies gives the total battery energy that is spent by the propulsion during the design mission. However, there is also energy needed for the other aircraft systems such as: environmental control, avionics, de-icing and cooling. The power of these systems is estimated to be 150kW. This value is a conservative estimate based on literature. Half of this power is required by the Environmental Control System (ECS) to heat/cool or pressurise the cabin. Furthermore, 20kW is needed for flight systems and 5kW for the galleys[24]. Additionally another 50kW was added to account for other systems in the aircraft that require power throughout the flight. The 150kW power by these systems is assumed to be constant throughout the flight. This is a rough estimation, however due to time constraints and lack of literature it was deemed unfeasible

at this stage to more accurately predict the power in different flight phases by these systems. It is recommended to look deeper into in a subsequent design stage, as the energy requirements from these systems are significant with regards to the battery mass. Adding the energy spent by these power systems yields a total battery energy spent during the mission of 13.6 GJ.

However, this is still not everything needed to compute the battery mass, there are two more problems that have to be considered when calculating this number. Starting with the problem of a voltage (and thus power) drop from the batteries when operating at low State Of Charge (SOC). Venturi Aviation has supplied the knowledge that this voltage drop occurs roughly when the battery is below 5 % SOC. Since the aircraft uses high power during approach, it needs to have enough power available at this late point in flight. Therefore, it was decided to add 5% to the total battery energy to always have enough energy left to perform the final approach.

Secondly there is the problem of Depth of Discharge (DOD). For battery degradation it is important to not perform a full charge and discharge of 100% for each cycle. Together with Venturi Aviation it was determined that the battery under normal operations should not go below 20 percent state of charge. At the maximum nominal mission range of 800km, the 185km diversion and 30 minute loitering take 17.2 % and 9.2 % of the total battery energy respectively. When taking into account the 5 % SOC that is always left after a mission it becomes clear that loitering can in every scenario be performed in the 80% SOC that can always be used. For diversion that is a different story though. However, diversion happens only very rarely (it was necessary once every 333 flights in the US in 2020 [25]). Therefore it is assumed that this phase is allowed to take energy from the 20% SOC that not used under normal operation. So no additional margins on the battery mass are taken to account for the 20 percent depth of discharge.

A summary of what has been explained above can be seen in Figure 5.4. The left battery shows the status at the begin of life which shows that a total of 95% of the battery can be used during flight operations. The right battery is at the end of life after 2000 cycles when 15% of the battery has been degraded, as can be seen, the state of health is not equal to the state of charge anymore since 15% of the battery cannot be used anymore. Also, the Depth of Discharge is shown, as explained above under normal operations the state of charge should not drop below 20%. For the final design the nominal mission range that can be achieved at BOL is equal to 1035 km. The impact of battery degradation on range and charging time will be discussed in more detail in subsection 14.2.2.

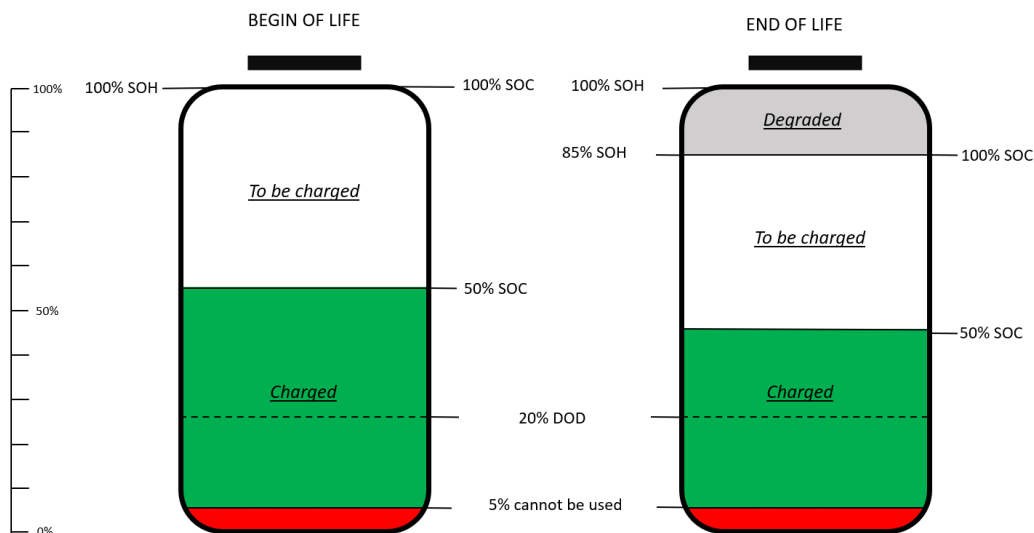


Figure 5.4: Battery Begin of Life versus End Of Life

Finally the battery mass is obtained by dividing the total battery energy with the end of battery life energy density of 575 Wh/kg. The final value of battery mass after design convergence becomes 6917 kg.

5.4.2 Mission Profile Results

The mission profile plots resulting from the energy calculations python program are described and shown in this section.

Plots against mission time

Figures 5.5, 5.6, 5.7 and 5.8 below show the altitude, velocity, power and consumed energy over the mission time. The labels in the plots indicate which parts belongs to which mission phase. Be aware that, for ease of readability, not all phase labels are shown in all plots. However all mission profiles do include all phases, even when not labelled.

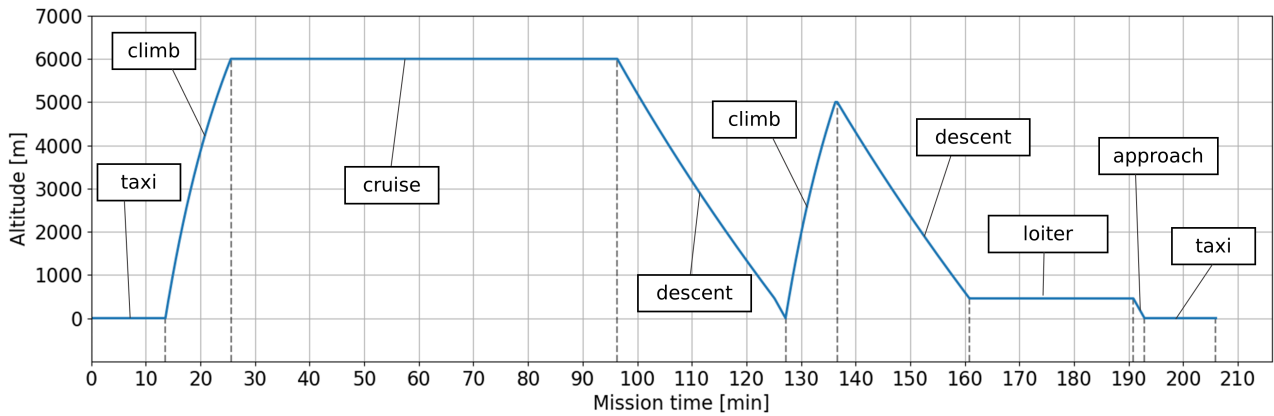


Figure 5.5: Mission profile of altitude plotted against mission time, labels showing different flight phases

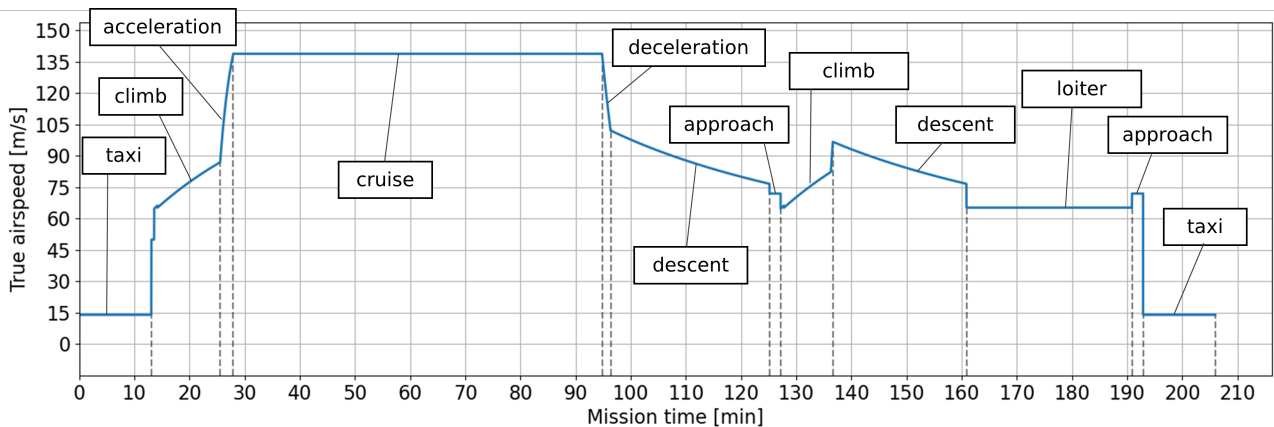


Figure 5.6: Mission profile of true airspeed plotted against mission time, labels showing different flight phases

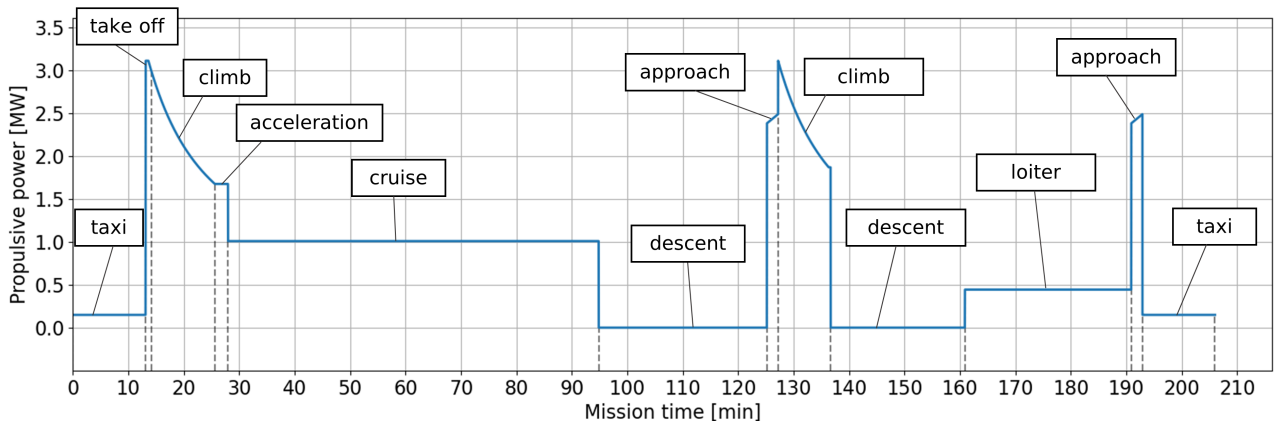


Figure 5.7: Mission profile of propulsive power plotted against mission time, labels showing different flight phases

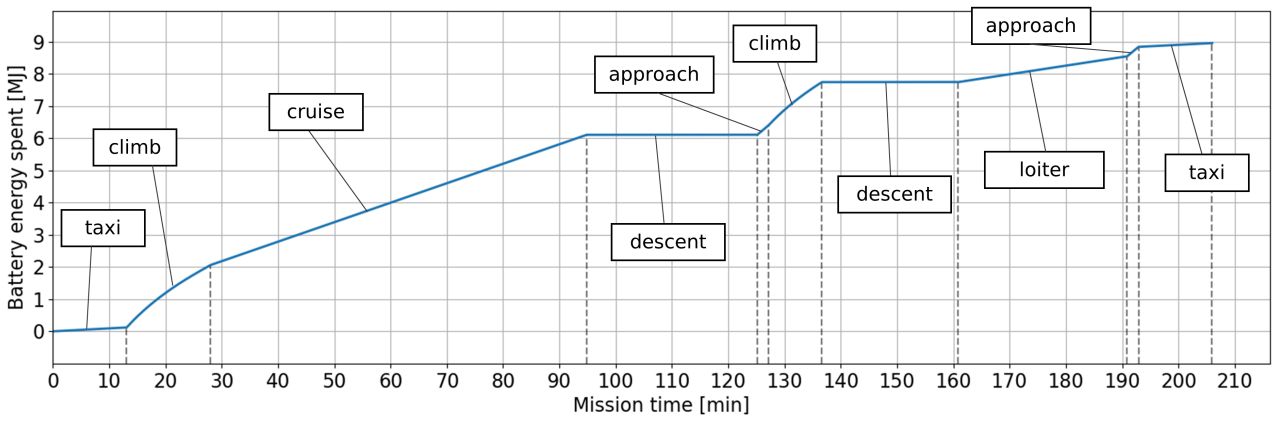


Figure 5.8: Mission profile of battery energy spent plotted against mission time, labels showing different flight phases

Plots vs. ground distance

Figures 5.9, 5.10, 5.11 and 5.12 below show the altitude, velocity, power and consumed energy over the covered ground distance. It can clearly be seen that, after the nominal mission 800 km has been covered, as prescribed by requirement **VEN-TOP-PERF-3.1**. Furthermore it should be noted that both taxi phases are not visible in these plots. That is correct as these phases do not count towards the ground distance covered in direction of the destination airport. It has been chosen to count ground distance from the moment the aircraft lifts off until the moment it touches down at the destination airport. Finally the loiter phase also does not show as a phase covering ground distance since it is performed circling around a constant location.

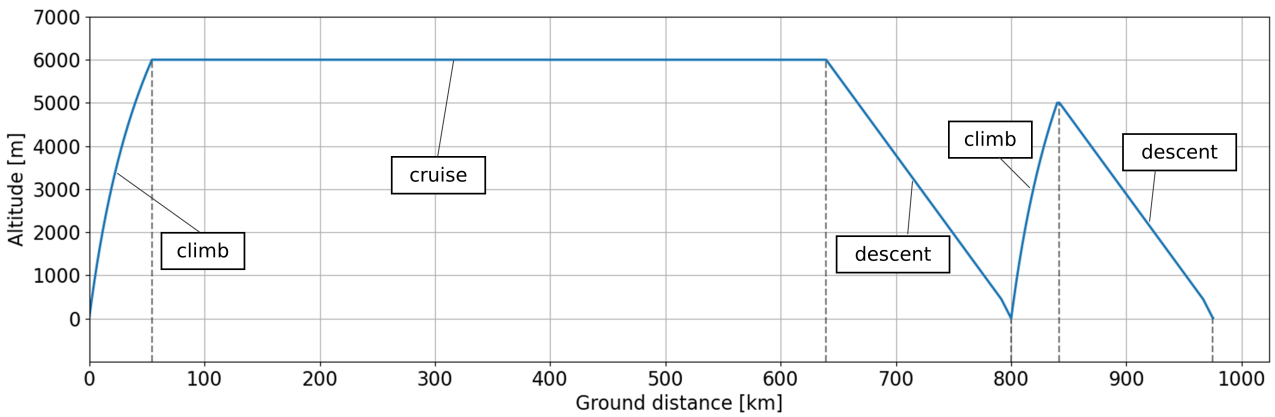


Figure 5.9: Mission profile of altitude plotted against ground distance, labels showing different flight phases

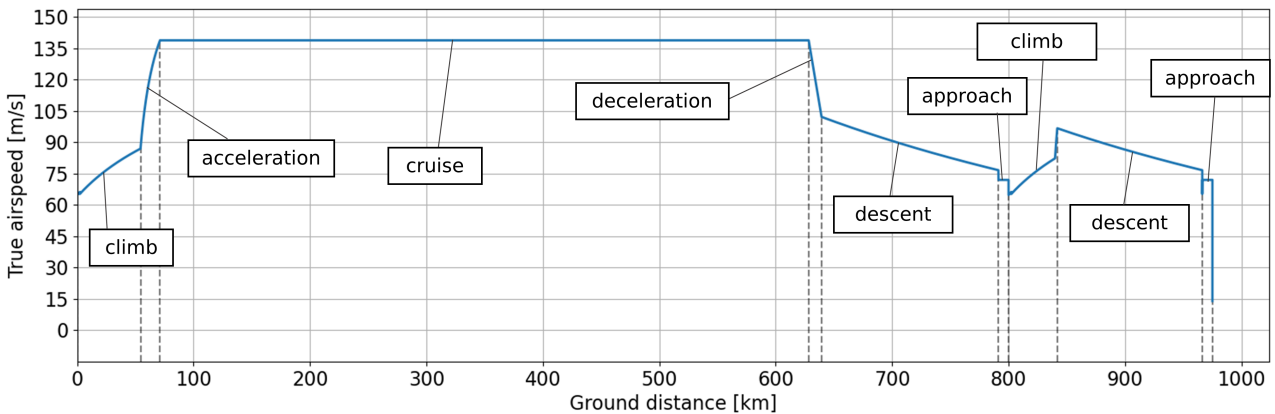


Figure 5.10: Mission profile of true airspeed plotted against ground distance, labels showing different flight phases

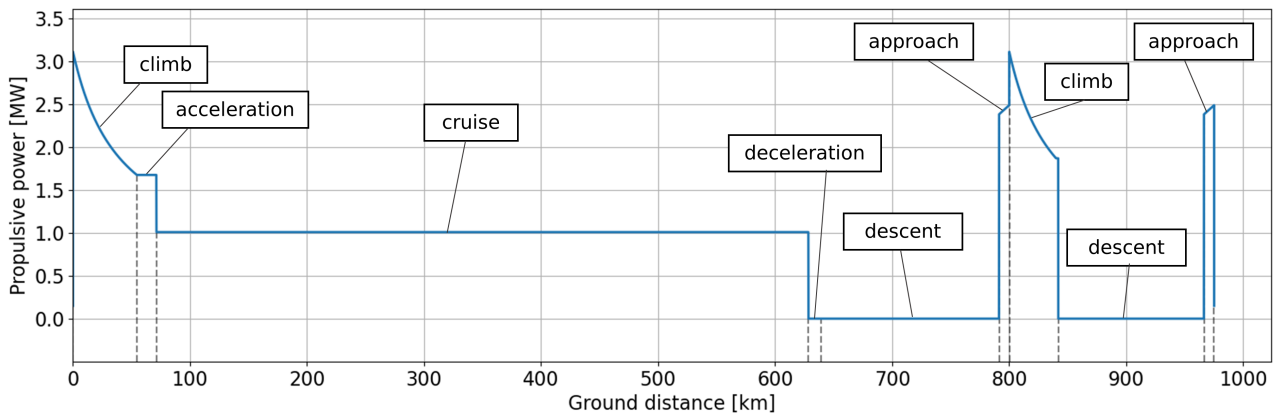


Figure 5.11: Mission profile of propulsive power plotted against ground distance, labels showing different flight phases

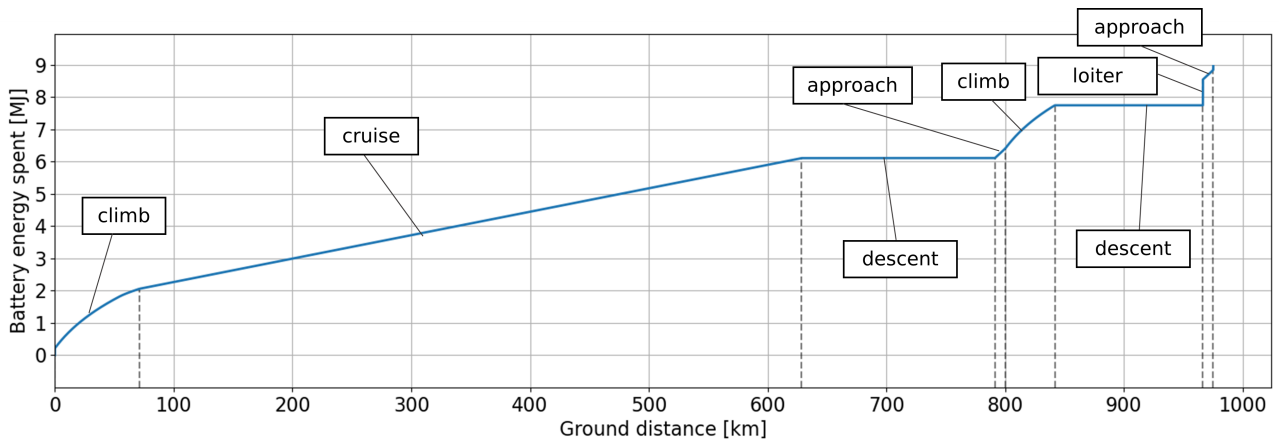


Figure 5.12: Mission profile of battery energy spent plotted against ground distance, labels showing different flight phases

State of Charge

One very important parameter for the aircraft operations is the battery state of charge. The state of charge needed for a mission determines to what extent the battery needs to be charged, which therefore has a very large influence on the turnaround time. It is also important to know at what point during the mission the aircraft goes below 20% SOC, as that is the determined threshold below which battery degradation becomes an issue. The 2 figures 5.13 and 5.14 below show the battery state of charge throughout the design mission at battery end of life. At the start of this mission the battery is charged to the full 100%, which results in a 5% state of charge at the end as explained in subsection 5.4.1. The region with state of charge below 20% is shown in red.

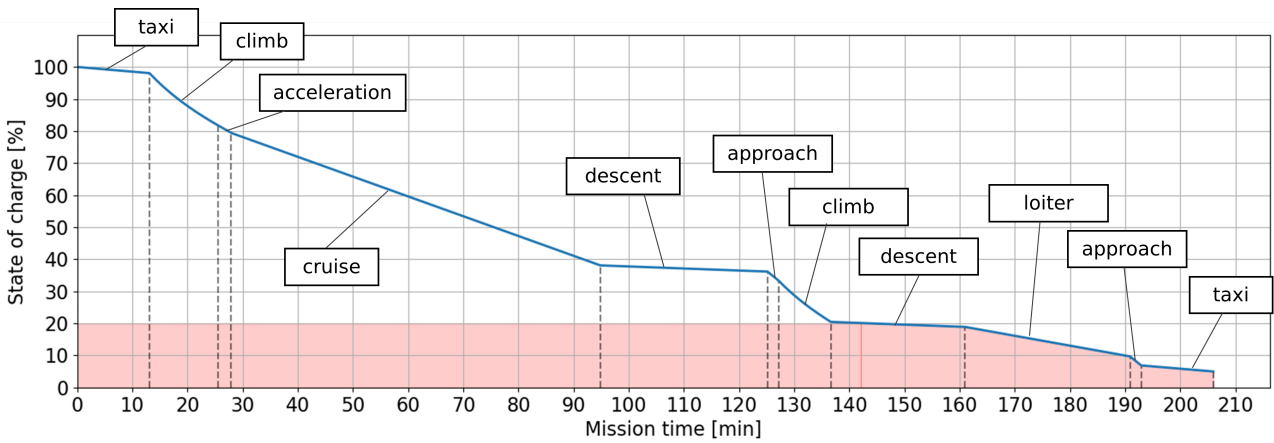


Figure 5.13: State of charge plotted against mission time for the design mission (battery EOL), red region showing SOC smaller than 20%

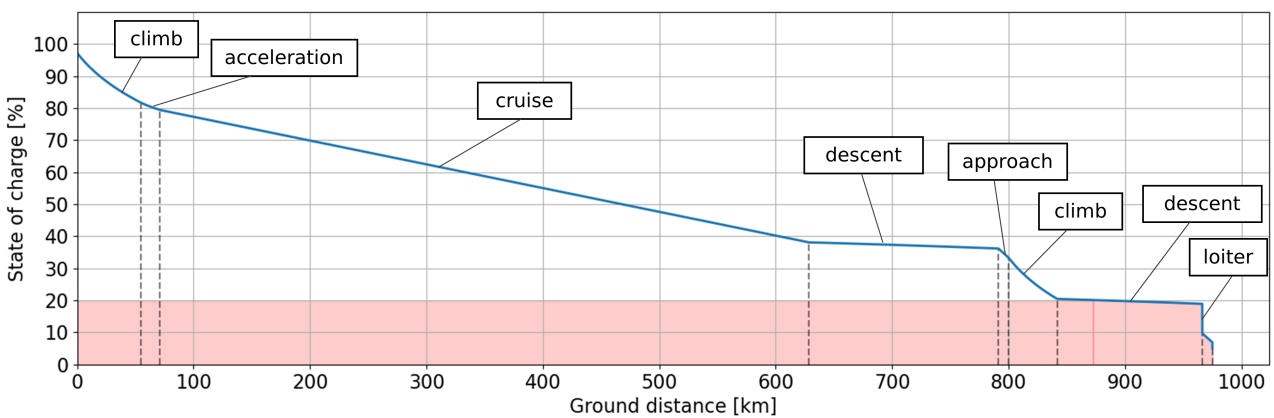


Figure 5.14: State of charge plotted against ground distance for the design mission (battery EOL), red region showing SOC smaller than 20%

6

Propulsion Analysis

The propulsion system of an aircraft greatly influences its flight performance and fuel efficiency. The ECHO-1 aircraft is powered by electric energy, and therefore uses electric motor powered propellers. Since electric motors are much lighter and more efficient compared to turboprop engines, the possibility arises to make use of distributed propulsion. This means that instead of using 2 large power full propellers, many smaller less powerful propellers are used which are distributed along the wingspan. Distributed propulsion is able to enhance the aerodynamic performance of the aircraft and achieve greater overall propulsive efficiency.

The selected propeller configuration is explained in [section 6.1](#). [section 6.2](#) describes the propeller performance in take-off and cruise. The electric motor design and power cable configuration are discussed in [section 6.3](#). Lastly, failure modes of the propulsion system are explained in [section 6.4](#).

6.1 Propeller Configuration

During the design trade off, it was decided upon using electric distributed propulsion as the main form of propulsion on ECHO-1. The distributed propulsion array will increase the dynamic pressure

over the wing, increasing both the lift- and drag coefficient of the aircraft. In order to estimate the performance improvement due to the use of the distributed propulsion system, the increases in lift- and drag coefficients need to be quantified. This section will describe the method used to quantify the increases in these coefficients.

The method used is a derivative of the method described in [4]. This method parametrises the distributed propulsion array in three main design parameters: the number of engines (N), the amount of wingspan occupied by the array (ΔY) and the distance between two propellers (Δy). These three design parameters can be seen in Figure 6.1 where b is the wingspan. The method will be converted into a python script such that it will be able to calculate the effects on the aerodynamic coefficients quickly for a wide range of number of propellers and fractions of span occupied. In the remainder of this section a combination of number of propellers and amount of wingspan occupied will be referred to as a propeller configuration.

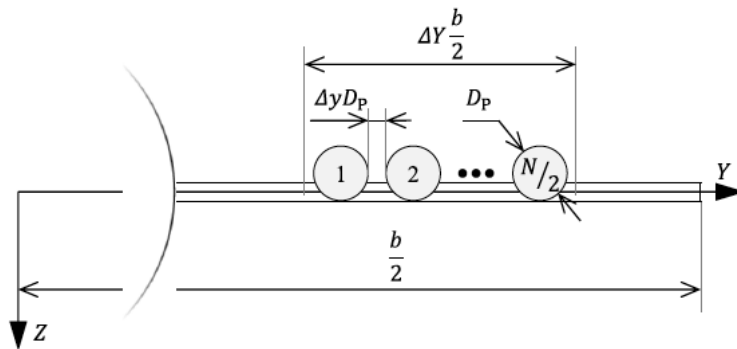


Figure 6.1: A visualisation of the three design parameters of the distributed propulsion array [4]

From Figure 6.1 the diameter of one propeller can be calculated as in Equation 6.1. Since b is an extensive parameter and unknown at the beginning of the sizing process it is important that the propeller diameter will be normalised. The propeller diameter can be normalised using Equation 6.2.

$$D_p = \frac{\Delta Y}{N(1 + \Delta y)} b \quad (6.1)$$

$$\frac{D_p^2}{W} = \frac{\Delta Y^2}{N^2(1 + \Delta y)^2} \frac{A}{(W/S)} \quad (6.2)$$

It is important to ensure that the obtained propeller is able to efficiently provide the required thrust with the available disk area. First the thrust coefficient of the of the distributed propulsion array (DP array) can be calculated using Equation 6.3. In this equation, the term $\frac{T}{W}$ appears, which is the thrust loading of the aircraft. Since ECHO-1 will use propellers, the propulsion system is sized using the power loading. The power loading can be converted to thrust to weight ratio with the use of Equation 6.4, where in this case V is the airspeed in cruise.

$$T_c = \frac{1}{N} \frac{\chi(T_{cruise}/W)}{\rho V^2 (D_p^2/W)} \quad (6.3)$$

$$\frac{W}{P_p} = \frac{1}{V(T_{cruise}/W)} \quad (6.4)$$

The propulsive efficiency can then be calculated by rewriting Equation 6.5 which gives the theoretical maximum propulsive efficiency. To account for practical losses in efficiency, a factor of 0.85 was applied to the theoretical maximum efficiency. This value was decided upon in a meeting with Reynard de Vries on propellers and distributed propulsion. From the equations it can be seen that if N tends to infinity the propulsive efficiency will tend to zero. Since this method will be used in Python to do the calculations for a variety of propeller configurations, a lower limit on the calculated propulsive

efficiency was required. The value on the lower limit on the propulsive efficiency was set to 0.7 since this is was found to be the minimum propulsive efficiency that would still be able to meet the performance requirements.

$$T_{c,max} = \frac{\pi}{8} \left[\left(\frac{2}{\eta_{dp, isolated}} - 1 \right)^2 - 1 \right] \quad (6.5)$$

With the thrust coefficient of the DP array known the effects on the aerodynamic coefficients can be estimated. This step involves calculating the axial induction factor of the propeller disk, using Equation 6.6. The axial induction factor is a measure of how much the propeller disk increases the speed of the airflow compared to the free stream velocity. With the axial induction factor the contraction ratio of the slipstream at the wing leading edge can be expressed as in Equation 6.7, obtained from a derivation of [26]. In Equation 6.7 the term x_p references to the axial position of the propeller relative to the wing leading edge. This value was set to 0.15 times the MAC which was again decided upon with Reynard de Vries as for the propulsive efficiency.

$$a_p = \frac{V_p - V}{V} = \frac{1}{2} \left(\sqrt{1 + \frac{8}{\pi} T_c} - 1 \right) \quad (6.6)$$

$$\frac{R_w}{R_p} = \sqrt{\frac{1 + a_p}{1 + a_p \left(1 + (x_p/R_p) / \sqrt{(x_p/R_p)^2 + 1} \right)}} \quad (6.7)$$

From the conservation of mass in compressible flow it follows that the velocity increase over the wing can be calculated as in Equation 6.8. With the increase in velocity due to the thrust by the propellers known, the increase in lift coefficient (Δc_l) per section of wingspan can be calculated by using Equation 6.9 as found in [27]. In Equation 6.9, β is the finite slipstream correction factor, α_w is the wing geometric angle of attack, to be calculated with the use of Equation 6.10, and α_p is the propeller incidence angle. Equation 6.9 assumes a symmetric wing airfoil, whereas ECHO-1 will use a cambered airfoil as described in section 7.1. In order to account for the change to this assumption a small propeller incidence angle of -2° [4] will be used to simulate this cambered effect.

$$a_w = \frac{a_p + 1}{(R_w/R_p)^2} - 1 \quad (6.8)$$

$$\Delta c_l = 2\pi \left[(\sin \alpha_w - a_w \beta \sin(\alpha_p - \alpha_w)) \sqrt{(a_w \beta)^2 + 2a_w \beta \cos \alpha_p + 1} - \sin \alpha_w \right] \quad (6.9)$$

$$\alpha_w \approx \frac{C_{L,airframe}}{2\pi A} \left[2 + \sqrt{A^2 (1 - M^2) \left(1 + \frac{\tan^2 \Lambda_{0.5c}}{1 - M^2} \right) + 4} \right] \quad (6.10)$$

Since c_l as calculated in Equation 6.9 is only the sectional increase in lift coefficient in 2D, in order to convert this increase in c_l to a 3D wing it has to be multiplied with the fraction of wingspan occupied by the DP array as seen in Equation 6.11.

$$\Delta C_L = \Delta c_l * \Delta Y \quad (6.11)$$

Along with an increase in lift coefficient there is also an increase in drag coefficient. This consists of two parts: first, an increase in zero lift drag coefficient C_{D_0} caused by the larger friction drag of the

wing surface due to the higher dynamic pressure. Second an increase in induced drag coefficient due to the increase in C_L . The enlargement of C_{D_0} was calculated using Equation 6.12. In Equation 6.12, c_f is the skin friction coefficient which has a typical value of 0.009 [4]. The contribution to C_{d_i} can be estimated using Equation 6.13 whilst assuming a parabolic drag polar and expanding it.

$$\Delta C_{D_0} = \Delta Y a_w^2 c_f \quad (6.12) \quad \Delta C_{D_i} = \frac{\Delta C_L^2 + 2C_{L, \text{airframe}} \Delta C_L}{\pi A e} \quad (6.13)$$

With the complete method of calculating the effects of the DP array on the aerodynamic coefficients known, it is possible to produce a number of plots which show the effect of the DP array for various numbers of propellers and fractions of span occupied. Plots like these can be seen in Figure 6.2 and Figure 6.3. These figures show the effects of the distributed propulsion array on the C_L and C_D in cruise conditions ($V = 500$ m/s and $h = 6000$ m) in the top left and right hand corner. The bottom left plot shows the product of the propulsive efficiency and the new lift- over drag ratio. This product is important to the design since these two parameters have a strong influence on the range of the aircraft through the Breguet range equation Equation 6.14. The general trend that can be observed in Figure 6.2 and Figure 6.3 is that with more engines on the same amount of span a higher ΔC_L can be achieved but this comes at the cost of a lower $\eta_{prop} * \frac{L}{D}$. This means that finding the best propeller configuration becomes a balancing act of achieving the required ΔC_L whilst also maintaining a sufficient propeller efficiency times lift over drag product.

$$R = E^* \cdot \eta_{tot} \cdot \frac{1}{g} \cdot \frac{L}{D} \cdot \frac{m_{bat}}{MTOW} \quad (6.14)$$

In order to find this optimum configuration a number of additional constraints need to be applied. The first constraint is imposed on the minimum increase in ΔC_L . Since the DP array enhances the lift in landing conditions it can be used as a sort of high lift device (HLD). The total required ΔC_L in landing configuration is 0.55 as stated in [1]. Since some redundancy will be required to achieve this ΔC_L not all of this 0.55 increase will be achieved with the use of the DP array. A design decision was made that at least 0.3 of the ΔC_L will be achieved with the DP array and the additional 0.3 will be achieved with the use of simple flaps. Since the loss of a motor does not only decrease thrust but also an amount of ΔC_L , the flaps will add a layer of redundancy by being able to compensate for this loss by being set at a higher flap angle. This does however require the flaps to be over-designed in normal operating conditions. The full design of the HLD's will be presented in subsection 7.2.2.

The second constraint that was imposed on the propeller configuration was the maximum number of engines. The maximum number of engines was set at a maximum of 24 engines. This number was obtained by practical limitations such as engine maintenance, reliability and inspection. It was decided that with an engine number greater than 24, the impracticality of maintenance and inspection would be higher than the possible gain in efficiency. Furthermore, the decision was made to group all engines together in groups of 2 to 3 for the reasons listed in subsection 6.3.2. Going higher than 24 engines would mean that an additional group of engines and corresponding wiring would be necessary which would result in excessive complexity of the system.

The last constraint imposed on the propeller configuration was the maximum amount of span available for the DP array. It is physically impossible to occupy 100% of the wingspan with the DP array since the fuselage is in the middle. Placing propellers at this location would mean that they would cut into the fuselage, which is undesirable. To account for this, a check was performed to see if the occupied space by the DP array would not exceed the space available. This can be seen in Figure 6.2 and Figure 6.3 by the fact that there are no lines for (ΔY) equal to one.

After running the iteration and optimisation script for the complete design a final propeller configuration of 16 propellers with a diameter of 1.907 m on 0.89 if the span was found to be the most optimal. This configuration is able to achieve a maximum ΔC_L in landing conditions of the required 0.3. The estimated practical propulsive efficiency for this configuration was found to equal 0.815.

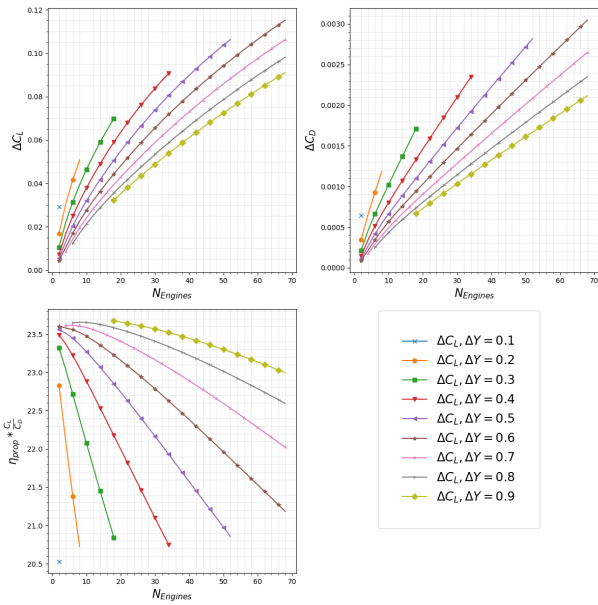


Figure 6.2: The effect of the distributed propulsion array in cruise conditions

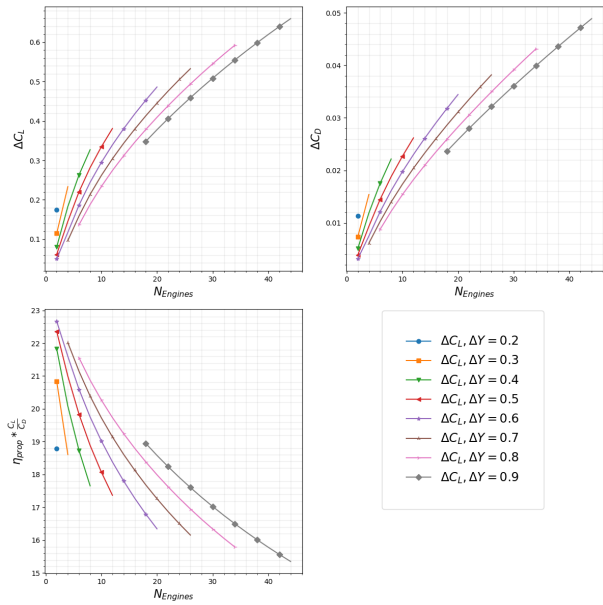


Figure 6.3: The effect of the distributed propulsion array in landing conditions

6.1.1 Verification and Validation

Since the methods to analyse the distributed propulsion system described in section 6.1 were put into python some verification of the code is necessary. This verification was done with a number of unit tests. A table with the different unit test performed is provided in Table 6.1. Since the DP technology is quite novel not a lot of data or reference aircraft using this technology are available. To still be able to validate the results of the model used, a meeting with Reynard de Vries was held where the results of the conducted analysis were discussed and properly validated. For the propeller performance, the graphs that were used to determine this performance were based on real world testing. This means that by using these plots, the propeller design will automatically be validated since the data that is used to estimate the performance is not from a theoretical approximation but from real world tests.

Table 6.1: Performed Unit Tests for Distributed Propulsion Python Scripts

Nr.	Name	Type	Parameters	Passed
1	Input Assign	Check Inputs	$N, \Delta Y, b, A, W/S, W/P, V, alt, C_L$	Yes
2	Calc Conditions	Hand Calculation	M, ρ	Yes
3	Calc Conditions Standard Input	Zero Test	M, ρ	Yes
4	Geometric Description	Hand Calculation	$D_{prop}, T/W, T_c, \eta$	Yes
5	Geometric Description Standard Inputs	One Test	$D_{prop}, T/W, T_c, \eta$	Yes
6	Delta Aero Perform	Hand Calculation	a_p, V_j, a_w	Yes
7	Plot Func	Gradient Test	-	Yes
8	Draw Func	Gradient Test	-	Yes

6.2 Propeller Performance

In section 6.1, the method to calculate the most optimum propeller configuration was described and the optimum configuration was mentioned. It was found that the optimum configuration uses 16 propellers with a diameter of 1.907 m. For this configuration a propulsive efficiency of 0.815 was calculated. With the configuration known it is now necessary to find a propeller type which is able

to provide both enough power and thrust whilst still maintaining the required propulsive efficiency in cruise conditions. First in [subsection 6.2.1](#), the reasoning behind the choice of propeller type will be presented. After this [subsection 6.2.2](#) will present the static and take off performance which will be analysed, whereas in [subsection 6.2.3](#) the cruise performance will be examined.

6.2.1 Propeller Type

For the propeller type it was chosen to use a four-bladed Hamilton standard propeller with an activity factor (AF), a measure of how well a propeller can absorb power, of 100 and an integrated design lift coefficient (C_{L_i}), the lift coefficient of the propeller blades, of 0.5. The choice to use a Hamilton Standard propeller was made since a lot of data on the performance of these types of propellers is available in [6]. This makes the analysis easier since real world data can be used in the form of graphs. This type of analysis was preferred over more detailed types of analyses such as blade element theory since those types of analysis would be too detailed and opens up a lot of new variables to be considered. These variables are, but not limited to blade twist, blade airfoil, blade chord distribution etc. It was decided that this type of analysis would be outside the scope of this DSE.

The choice for a 4 bladed propeller comes from [5] which show that this is the optimal number of blades for an aircraft with a cruise Mach number of around 0.4. The AF is a measure of how well a propeller can absorb power and can be calculated using [Equation 6.15](#). In [Equation 6.15](#)[6], c is the chord of the propeller and D is the propeller diameter. By making the approximation that the propeller blade shape can be approximated as a rectangle and keeping the AF fixed at the chosen 100, the average chord of the propeller blade can be calculated for the found diameter. The average chord of the propeller was found to be equal to 0.122 m. The choice for AF of 100 was made using [5] where it is stated that the range of AF for 3 or 4 bladed propellers is between $100 \leq AF \leq 120$. Since there was no data available on a 4 bladed propeller with 120 AF, the AF of 100 was chosen. A C_{L_i} of 0.5 was chosen since the ECHO-1 has both a short take off and landing requirement but it also needs to be efficient in cruise. C_{L_i} is the integrated design lift coefficient and can also be interpreted as the lift coefficient of the complete propeller blade. In general a higher C_{L_i} will result in a higher thrust coefficient (C_T) for the same power coefficient (C_P), as can be seen in [Figure 6.5](#), but it will have a lower propulsive efficiency at cruise. For a Hamilton Standard propeller the options for C_{L_i} are 0.15, 0.3, 0.5, 0.7 [6]. A design for 0.5 was chosen since this would provide a good balance between thrust at take off conditions and propulsive efficiency at cruise conditions.

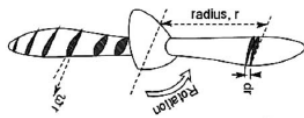
$$AF = \frac{100,000}{16} \int_{.15}^{1.0} \left(\frac{c}{D_p} \right) x^3 dx \quad (6.15)$$

6.2.2 Take Off Performance

With the type of propeller, number of blades, activity factor and C_{L_i} known it is possible to analyse the take off performance of the propulsion system and see if it meets the requirements. The first parameter that needs to be calculated is the maximum RPM setting of the propeller. The faster the propeller is able to rotate, the more thrust can be produced. This is due to the fact that the propeller blades are shaped as airfoils, as can be seen in [Figure 6.4](#) and thus for a higher velocity more lift or in this case thrust will be produced.

However, there is a limit to how fast the propellers can spin. This limit lies in the fact that there cannot be supersonic airflow anywhere on the propeller blades. Supersonic airflow over the blades would not only produce a large amount of drag, which translates to a large torque required to spin the propeller, but would also cause a lot of noise. To prevent the occurrence of supersonic or transonic flow over the propeller the Mach number at the tip needs to be kept below 0.72 [28]. The maximum RPM can be calculated using [Equation 6.16](#) [28], rewriting for n which is the revolutions per second (rps). From [Equation 6.16](#) it can be noted that the cruise conditions will result in the lowest allowable rps setting since at these conditions, the free stream Mach number (M) is 0.43 whereas at take off and landing conditions this will be lower. This resulted in a maximum propeller RPM of 1808.

The argument could be made to use different rpm settings at various flight phases to achieve maximum thrust for each flight phase. Instead, it was decided to use a constant speed variable pitch propeller. The constant speed allows the electric motors to spin at the same rpm for almost the entire flight. This is beneficial since now the electric motors can be specifically designed to provide the required power and torque at a small rpm range. This would in turn mean that the electric motor only has to be designed to be efficient for a small rpm range opposed to being efficient at a large rpm range which would increase the complexity and costs of the electric motors. The variable pitch control mechanism will ensure that the pitch angle of the propeller blades is altered according to the desired thrust setting. If more thrust is required the electric motor will provide more torque to the propeller shaft. If the pitch is left unchanged this would cause the propeller to start spinning faster, but by increasing the propeller pitch the propeller blades will produce more lift (thrust) and thus also more drag (torque). This increase in torque counters the extra applied torque from the motor such that the rpm remains constant.



$$D = \sqrt{\frac{a^2}{\pi^2 n^2} (M_{tip}^2 - M^2)} \quad (6.16)$$

Figure 6.4: A visualisation of the propeller [5]

The next step in calculating the take off performance of the propeller is finding the power coefficient (C_p) at take off conditions. From [1] the power loading ($\frac{W}{P}$) is known to be equal to 0.066 N/W. The critical sizing condition for the power loading was take-off, so the take off power can be calculated by dividing MTOW by $\frac{W}{P}$. This resulted in a power required of 3.11 MW. Since ECHO-1 will use multiple motors, the power required per motor can be calculated by dividing the total power required by the number of motors. The C_p for each propeller can now be calculated using Equation 6.17 from [5]. In Equation 6.17 the power is given in Shaft Horse power. The power required per engine is given in kW and thus a conversion factor of 0.000133 to convert to SHP needs to be applied. With the C_p known, the ratio between C_T/C_p can be found from Figure 6.5. With the C_T/C_p , the static thrust can be calculated using Equation 6.18. Along with the power and thrust, the torque required to be provided by the engine is an important parameter to quantify. This torque can be calculated using Equation 6.19 resulting in a torque required at take off of 1024.89 Nm. Do note that these equations can give values in Imperial units, a conversion to metric might be necessary.

$$C_p = (550 \times SHP) / (\rho * n^3 * D^5) \quad (6.17) \quad T_{static} = \left(\frac{C_T}{C_p}\right) (33,000 \times SHP) / ND \quad (6.18)$$

$$Q = \frac{C_p}{2\pi} \rho n^3 D^5 \quad (6.19)$$

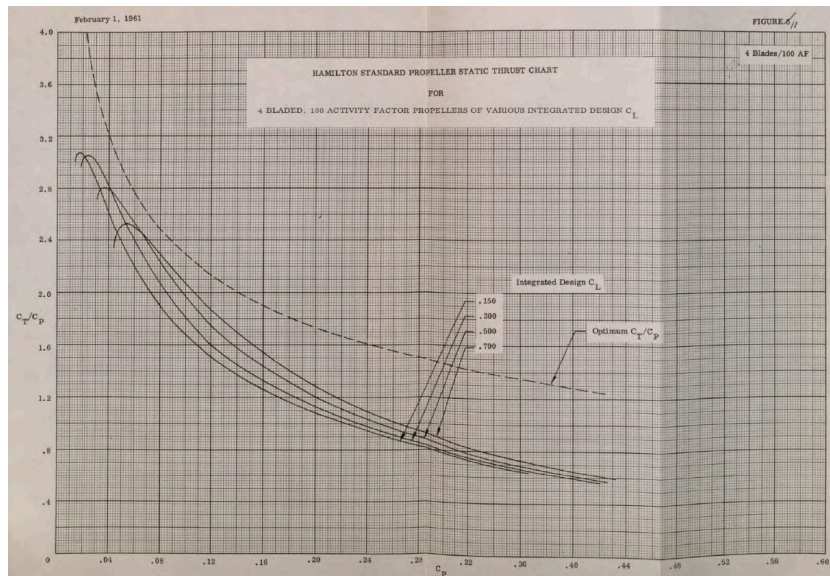


Figure 6.5: Hamilton Standard Propeller Static Thrust Chart For 4 Bladed 100 AF [6]

Using the static thrust it is possible to determine the take off distance required to lift off. To calculate this, it is required to determine the thrust at each moment of time during the take off run. Since the aircraft will immediately start moving once the brakes are released, the thrust will not be constant at the static thrust but it will vary with airspeed. In [7] a relationship between the ratio of $\frac{T}{T_S}$ and Mach number can be found. The relationship can be seen in Figure 6.6. Figure 6.6 was digitalised in python such that it could be turned into a function which provides the thrust ratio for a given mach number. With the thrust known at each airspeed, the acceleration at each instance of time can be calculated by subtracting the aircraft drag from the thrust. With the acceleration, both the velocity and distance covered along the runway could be calculated. The result of this calculation was a take off run in a standard sea level day of 1101.4 m and a take off time of 28 seconds. The static thrust per propeller at take off was equal to 3600 N which resulted in a total take off static thrust 57.6 kN which is comparable to aircraft of similar size and weight.

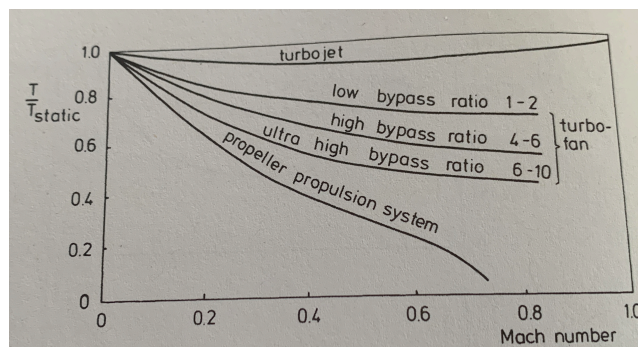


Figure 6.6: Variation of thrust with Mach number [7]

6.2.3 Cruise Performance

Next to the take off performance of the propeller, it is important to analyse if the given propeller is able to efficiently provide the required thrust at cruise conditions. A propulsive efficiency was already found in section 6.1 but this was just a theoretical estimation of the efficiency. In this section the analysis will show if the chosen propeller is able to actually meet this efficiency requirement.

The first step in finding the efficiency in cruise is determining the power required to be delivered by the engines in cruise conditions. Realising that in cruise the drag is equal to the thrust and thus power required is equal to the power available, the power required can be calculated using Equation 6.20.

This is the total power required in cruise; in order to find the power required per engine this power has to be divided by the number of engines. Similar to the method in subsection 6.2.2, the power coefficient in cruise can be calculated using Equation 6.17 where the power is used in SHP so a conversion factor of 0.0013 to the previously found power in must be applied. The power required per engine was found to equal 60.4 kW which is a total of 0.966 MW for all 16 engines together. The shaft brake power can be calculated using Equation 6.21 with the initial estimation of η_{prop} equals 0.815. This resulted in a required P_{br} of 74.4 kW per engine.

$$P_r = \frac{\frac{1}{2}C_D\rho SV^3}{\eta_{prop}} \quad (6.20) \quad P_{br} = \frac{P_a}{\eta_j} \quad (6.21)$$

Next to the C_p in cruise the advance ratio (J) is needed to determine the efficiency. The advance ratio can be calculated using Equation 6.22. J is the ratio between the free stream velocity and the propeller tip speed. With the C_p and J known, the propeller efficiency can be determined using Figure 6.7. This resulted in a final propulsive efficiency of 0.82 which is close to the theoretical estimation of 0.815.

$$J = V/nD \quad (6.22)$$

Just as in subsection 6.2.2 the thrust at cruise conditions can be calculated. This can be done using Equation 6.23. This resulted in a cruise thrust of 434N per engine, which results in a total power available equal to the power required. This was to be expected from the original assumption that power required equalled power available.

$$T_{cruise} = \frac{P_{br} * \eta_{prop}}{V} \quad (6.23)$$

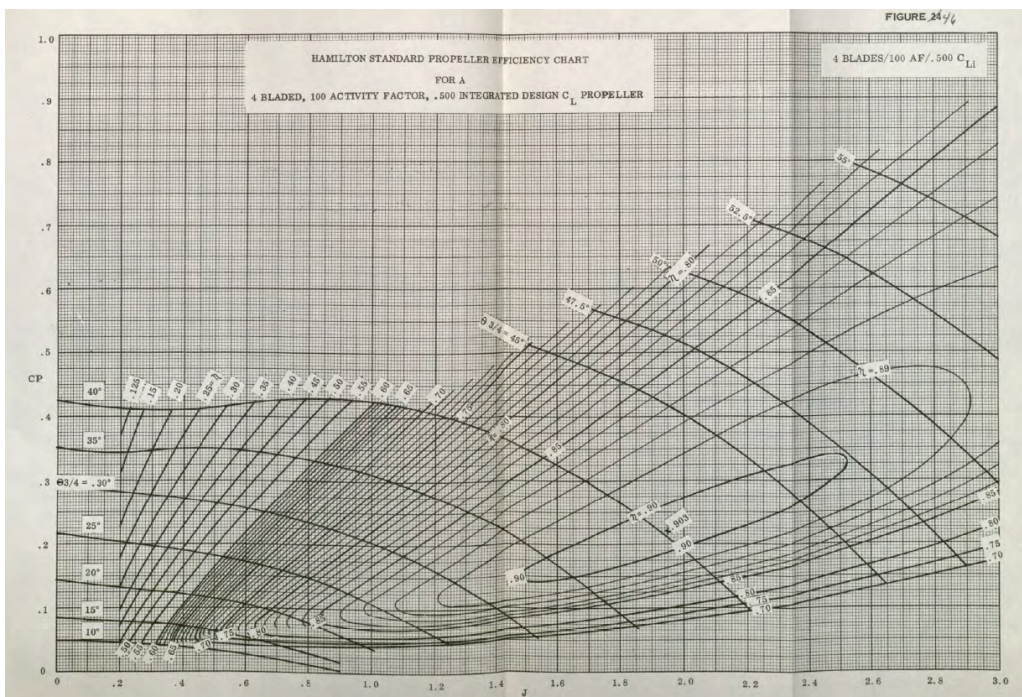


Figure 6.7: Hamilton Standard Propeller Efficiency Chart for 4 Bladed 100 AF propeller [6]

As a recommendation for future work, it would be worthwhile to conduct a blade element theory analysis on the propeller. This type of analysis splits the propeller blade in small blade sections and is able to calculate the thrust, power and torque on each of these sections. This type of analysis would

thus result in a more accurate estimation of the propeller performance. The blade element theory method can also be used to optimise the propeller on more parameters such as blade twist angle, blade airfoil, blade chord distribution and geometric pitch angle. All of these parameters were not fully or not at all taken into account in the propeller analysis in this report.

6.2.4 Verification and Validation

Just as in [section 6.1](#), the methods in [section 6.2](#) were put into a python script. Just like any piece of code this required verification. The verification was done with a number of unit tests which can be seen in [Table 6.2](#). Since the data used from [6] is obtained from real world experiments the propeller performance the performance of the propeller is automatically validated since from this data the actual performance in the real world can be derived.

Table 6.2: Performed Unit Tests for the Propeller Python Scripts

Nr.	Name	Type	Parameters	Passed
1	Propeller Pre Calc	Hand Calculation	ρ, a, rps	Yes
2	Propeller Take Off Calc	Hand Calculation	P_{tot} , Take Off Run	Yes
3	Propeller Take Off Input Check	Check Inputs	P_{tot}	Yes
4	Propeller Cruise Calc	Hand Calculation	η_{prop}	Yes

6.3 Electric Propulsion

After selecting a propeller configuration and a fitting Hamilton propeller, the remaining components of the propulsion subsystem must be sized. The selection of an electric motor is described in [subsection 6.3.1](#). The power cable design is explained in [subsection 6.3.2](#) and [subsection 6.3.3](#), and their verification & validation is explained in [Table 6.5](#). Lastly, design for subsystem failure is discussed in [section 6.4](#).

6.3.1 Electric Motors

For the sizing of the electric motor, existing motors as well as motors that are still in development were considered. It was decided to design the propulsion system for the H3X HPDM-250, an electric motor capable of delivering 200kW of continuous power and continuous torque of 95 Nm without a gearbox at 800 VDC ¹. The motor is shown in [Figure 6.8](#). The motor has a hexagonal shape and room for a planetary gearbox which allows for an increase in torque at the cost of RPM. Even though this motor is still in development, it was selected because of the appropriate power capability and high efficiency. And since ECHO-1 will be designed to enter into service in 2035 it is expected that this motor will have transition from the development to the production phase.

Because ECHO-1 is designed for entry into service in 2035, a 10% technology improvement factor was applied to the motor power density and torque output. Since the motor on ECHO-1 will use 1200 V instead of 800 V the power and torque delivered by the base motor will be scaled by 1.5. This comes on top of the 10% technology increase resulting in a scaling factor of 1.65 on the performance parameters. This resulted in a motor with the characteristic as in [Table 6.3](#).

¹<https://www.h3x.tech/>

Table 6.3: The Characteristics of the 1.375 Scaled Base HPDM-250 Motor

Parameter	Value	Unit
Continuous power	275	kW
Efficiency	93	%
Speed range	0 - 20000	RPM
DC bus voltage	200 - 1200	VDC
Mass	13.1	kg
Volume	8.25	L

For the remainder of this section it will be assumed that the motor is able to scale linearly with the maximum continuous power that is required and that the torque required at take off can be achieved by applying a planetary gearbox to increase the torque at the cost of RPM. The maximum continuous power is the power required at take off which equalled 194.4 kW and the torque at take off of 1025 Nm. Both these numbers are the values per engine. The results of this power scaling can be seen in Table 6.4. The assumption was made that the packaging of the engine does not scale with the power and torque requirements such that the motor dimensions remain the same as the original motor. In Table 6.4, it can be seen that the maximum achievable RPM with the gear ratio is 3058. Since the maximum allowable RPM for the propeller was 1808 the motor will easily be able to spin the propeller at the correct RPM.

For future work it would be recommended to dive deeper into the electric motor design to see in more detail how the electric motor can be designed to tailor to the specific required power and torque by ECHO-1. It is also recommended to perform this design by getting into contact with a company that specialises in electric motor design, since this is more of an electrical engineering task than aerospace engineering related.

Table 6.4: H3X HPDM characteristics for the ECHO-1

Parameter	Value	Unit
Continuous power	194.4	kW
Cruise efficiency	0.929	-
Gear ratio	6.54 : 1	-
Speed range (motor)	0 - 20000	RPM
Speed range (propeller)	0 - 3058	RPM
DC bus voltage	200 - 1200	VDC
Mass	15.92	kg
Volume	8.25	L
Diameter	0.2074	m

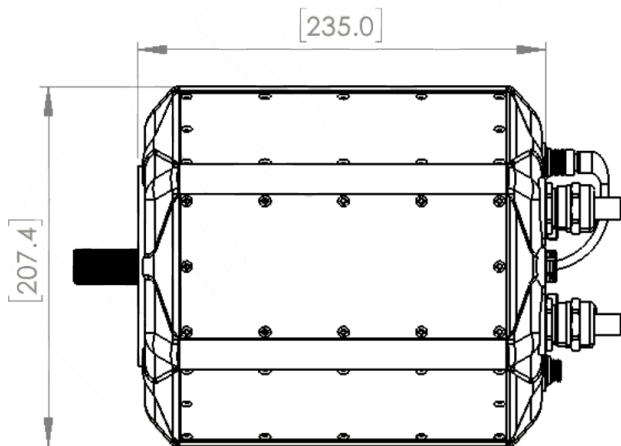


Figure 6.8: Schematic of H3X HPDM-250²

6.3.2 Cable Layout

The final components in the propulsion subsystem are the power cables, which connect the batteries to the propellers. These cables are distributed in groups to allow for redundancy in the propulsion system. The distribution of cables and the grouping of electric motors for one wing is shown in Figure 6.9. It can be seen that the eight motors per wing are divided in three groups, containing 3, 3 and 2 motors, respectively.

²<https://www.h3x.tech/>

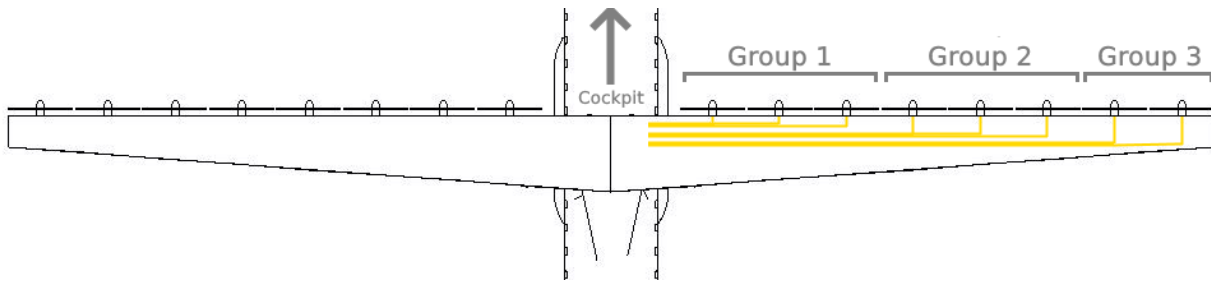


Figure 6.9: Cable layout of single wing

One large power cable runs to the first motor of each group, after which the cable splits into smaller ones to the individual motors. The large power cables for the most inboard motors run along the fuselage skin, whereas the other large cables are placed inside the truss. This decreases the total required cable length, compared to passing all cables through the fuselage or truss. This decreases the power loss and the required area, and thus the weight of the cable. Both the large and small cables deliver direct current power to the motors, and therefore require a pair of cables to complete the electric circuit.

6.3.3 Cable Sizing

The materials used for the power cables consist of an aluminium conductor core with a silicone elastomer insulator. Although aluminium has a worse conductivity than the more conventional copper, this is made up for by its low density and low cost [29]. The maximum allowable temperature of aluminium and copper are similar, at 90 degrees Celsius³. The choice of insulator was made based on the good material properties of silicone elastomers, combined with their relatively high thermal conductivity.

Each small cable has a conductor cross-sectional area of 27 mm², to prevent overheating, which is explained in the next section. For the larger cables the cross-sectional area was determined using the following equation:

$$A_{LC} = 1.2N_{motors}A_{SC} \quad (6.24)$$

6.3.4 Thermal Management

In order to ensure that the cables do not overheat during any part of the flight envelope, a thermal model was created. This model shows the temperature of cable components as a function of time. The results of this simulation are shown in Figure 6.10.

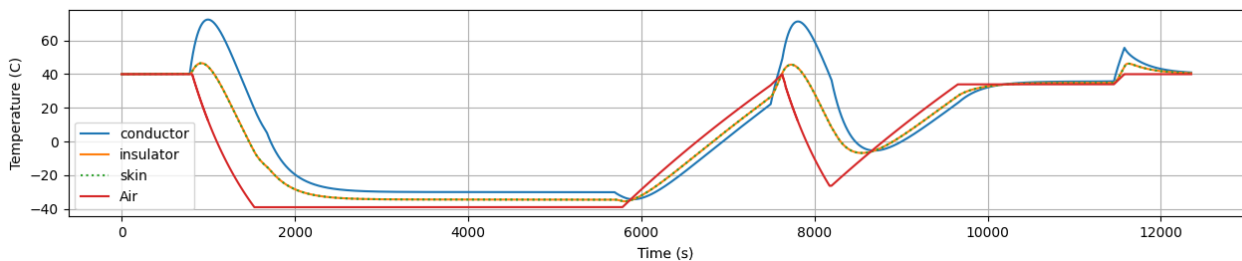


Figure 6.10: Temperature profile of power cable during the full mission

It is clearly visible that the temperature of the cables peaks at take-off, reaching around 75 degrees Celsius. All cables are sized to follow the same temperature profile and never exceed a temperature of 75 degrees. Since this is below the 90 degrees threshold, the cables are sufficiently sized.

³[https://media.distributordatasolutions.com/ThomasAndBetts/v2/part2/files/File_7437_emAlbumalbumsOcal20\(USA\)oc_1_g_nec31016p](https://media.distributordatasolutions.com/ThomasAndBetts/v2/part2/files/File_7437_emAlbumalbumsOcal20(USA)oc_1_g_nec31016p)

The conductive core of the cable reached the highest temperatures, whereas the insulator and aircraft skin temperature were very close due to the high thermal conductivity of the aluminium skin. The air temperature was assumed to be 40 degrees Celsius at sea level, to ensure safe operation even when taking off in extreme conditions. The mass of the power cables was found to be 23 kilograms per wing, which leads to a final mass of 47 kilograms.

6.3.5 Verification & Validation

The calculations for cable layout and sizing were verified using multiple different methods. The types of verification and their result are displayed in [Table 6.5](#).

Table 6.5: Performed Unit Tests for the Cable Design Scripts

Nr.	Name	Type	Parameters	Passed
1	Cable Layout Input Check	Check inputs	P_{engine} , η_{prop} , engine positions	Yes
2	Thermal Simulation Single Time-Step	Hand Calculation	$T_{conductor}$, T_{skin} , T_{air} , $T_{insulator}$	Yes
3	Cable Sizing Input Check	Check Inputs	U , ρ , t_{skin} , A_{SC} , A_{LC}	Yes
4	Cable Sizing Calculation Check	Hand Calculation	m_{cables} , l_{cables}	Yes

Validation of the power cable system is difficult, because information about electric aircraft power systems is speculative and hard to come by. In order to substantiate the found cable mass, an expert on electric aircraft design, Maurice Hoogreef, was contacted. This allowed for a comparison of the cable mass with empirical methods, which corresponded well.

6.4 Propulsion System Failure

In order to guarantee safe operations of the aircraft, sufficient performance must be ensured even in the case that components of the propulsion system fail. For traditional aircraft, the most severe case that must be designed for is the one-engine-inoperative (OEI) condition. There are currently no regulations for distributed propulsion aircraft, but it is safe to assume that simply designing for OEI is not sufficient.

Instead, the failure of a battery, and thus the failure of a set of engines is considered for the critical flight condition. When one or more engines fail, this leads to a decrease in power and a moment around the aircraft z-axis. Failure of the most outboard propeller group is studied, since their large moment arm causes the most significant moment. Since the propellers are also used for lift augmentation, a decrease in lift must not be considered during this analysis.

The induced moment around the z-axis is compensated for in the design of the vertical tail wing, as shown in [section 8.4](#). In order to ensure sufficient lift generation, a safety margin was included while sizing the high lift devices, which is described in [subsection 7.2.2](#).

7

Aerodynamic Analysis

This chapter presents the aerodynamic analysis that was performed on ECHO-1. This chapter first illustrates how the wing airfoil was chosen and verified in [section 7.1](#). Afterwards, in [section 7.2](#), the analysis is translated from 2D to 3D. Furthermore, the effects of a winglet and the truss are discussed, as well as simple high lift devices. Additionally, for the final design, a detailed drag estimation and aerodynamic polars are presented in [section 7.3](#). Finally, the verification and validation outcomes for

the aerodynamics calculations are presented in [section 7.4](#).

7.1 Airfoil Design

The preliminary aerodynamic analysis involves determining the required lift coefficient for the wing and for the airfoil, followed by choosing a suitable airfoil. This is all complemented by 2D and 3D CFD simulations.

7.1.1 Root Airfoil Selection

The aerodynamic sizing begins with the airfoil selection. When choosing the airfoil, the following issues should be targeted, in order of importance:

- For a certain $C_{l_{design}}$, look for the airfoil with the minimum C_d ;
- Look for the largest $C_{l_{max}}$ possible;
- Look for the lowest C_m (most negative) possible at the $C_{l_{design}}$;
- Larger t/c is beneficial for structural weight, especially for high wingspan aircraft, like ECHO-1.

The airfoil selection then relies heavily on determining the $C_{l_{design}}$. The procedure for this is the following: as the aircraft optimization is performed for cruise conditions, we determine the $C_{L_{design}}$ of the wing using equation [Equation 7.1](#). In this equation, the multiplication with a 1.1 factor is meant to account for 10% losses in lift due to the horizontal tail. The distributed propulsion helps mitigate this by providing a $\Delta C_{L_{prop}}$ of approximately 0.03 in cruise conditions.

$$C_{L_{design}} = \frac{1.1 * MTOW}{\frac{1}{2} * \rho * V^2 * S} - \Delta C_{L_{prop}} \quad (7.1)$$

The transformation from wing lift coefficient to airfoil lift coefficient at the design point is performed using the DATCOM method [30]. By definition, the α_0 of both the airfoil and wing coincide. The slope of the C_l - α - curve for an airfoil is always 2π and the slope for the wing's linear C_L - α - curve is computed using DATCOM and is influenced by airfoil effectiveness, by wing sweep and by the effective aspect ratio. The $C_{l_{design}}$ value that comes out is 0.6.

In order to select the very best airfoil for the design, an airfoil trade-off is performed. In this airfoil trade-off, multiple airfoils are considered:

- Airfoils from similar aircraft: the ATR-72 airfoil and the Bombardier Dash 8-Q400 airfoil (NACA 63412);
- NACA 5-series: relatively high $C_{L_{max}}$, designed for speeds which close to the cruise speed of ECHO-1 and are used by similar turboprop or regional commuter aircraft.

From the NACA 5-series, two existing airfoils with large amount of experimental data are considered: NACA 23012 and the NACA 23018. NACA 5-series airfoils also have the advantage that they can be specifically generated using tools such as Javafoil for the a specific C_l value, which is equal to 0.15 times the first integer digit of the airfoil designation. Using this method, four new airfoils are created that are designed for the C_l needed in cruise condition: NACA 43014, NACA 43012, NACA 45014, NACA 45012. To sum up, the airfoils used in the trade-off are shown in [Table 7.1](#).

Selection Criteria and Weighting

For the root airfoil selection, 4 criteria were selected in order to asses the performance of all the airfoils:

- A - $C_{l_{max}}$ (to be maximised): 55%
- B - C_d at $C_{l_{design}}$ (to be minimised):30%
- C - C_m at $C_{l_{design}}$ (to be minimised): 7.5%

- D - α_{max} (to be maximised): 7.5%

Scores and Results

The results from Xfoil of the 2D airfoils can be seen in Table 7.1. This tables gives the values for $C_{l_{max}}$ and $\frac{t}{c}$ which are just characteristics of each airfoil. Furthermore, the C_d and the C_m are taken when $C_l = C_{l_{design}}$. The scores for each criteria and airfoil are given in Table 7.2. These scores are again on the 1-10 scale. The scoring in each criteria is purely based on the values in Table 7.1. As seen by the sum of each airfoil, the final chosen airfoil is the NACA 43014.

Table 7.1: Airfoil Parameters From Xfoil

Contenders	$C_{l_{max}}$	C_d	C_m	α_{max} [deg]
ATR72	1.726	0.00581	-0.037	14
NACA 63412	1.495	0.00505	-0.093	13
NACA 43012	1.84	0.0068	-0.016	14
NACA 43014	1.94	0.0071	-0.013	14.5
NACA 45012	1.775	0.0060	-0.044	13.7
NACA 45014	1.76	0.0062	-0.041	13.7

Table 7.2: Airfoil Scoring for Trade-Off

Contenders	A	B	C	D	SUM
ATR72	6	9	6	6	690
NACA 63412	4	10	9	5	625
NACA 43012	8	6	6	8	725
NACA 43014	10	4	5	10	812.5
NACA 45012	6	8	10	7	697.5
NACA 45014	6	7	9	7	660

7.1.2 Tip Airfoil Selection

Despite the high $C_{l_{max}}$, the stall behaviour of NACA 5-digit airfoils is very abrupt. This does not make them suitable for the wing tip sections where stall behaviour needs to be delayed and progressive. The delay will be later addressed using wing twist. A more predictable stall can be achieved by using NACA 4-series airfoils near the wing tips. [31] ¹ In order to keep a constant t/c ratio, several airfoil with the last 2 digits 14 were tried: NACA 4414, NACA 5414, NACA 6414. These are more cambered airfoils that have very high $C_{l_{max}}$ and gradual stall, at the cost of higher drag. For these airfoils, another trade-off is set up.

Selection criteria and Weighting

For the tip airfoil selection, 4 criteria were selected in order to asses the performance of all the airfoils:

- A - $C_{l_{max}}$ (to be maximised): 37%
- B - C_d at $C_{l_{design}}$ (to be minimised):16%
- C - C_M at $C_{l_{design}}$ (to be minimised): 7%
- D - α_{max} (to be maximised): 39%

¹https://web.stanford.edu/~cantwell/AA200_Course_Material/The%20NACA%20airfoil%20series.pdf

Scores and Results

The results from Xfoil of the 2D airfoils can be seen in [Table 7.3](#). This tables gives the values for $C_{l_{max}}$ and $\frac{t}{c}$ which are just characteristics of each airfoil. Furthermore, the C_d and the C_m are taken when $C_l = C_{l_{design}}$. The scores for each criteria and airfoil are given in [Table 7.4](#). These scores are again on the 1-10 scale. The scoring in each criteria is purely based on the values in [Table 7.3](#). As seen by the sum of each airfoil, the final chosen airfoil for the tip is the NACA 4414.

Table 7.3: Airfoil Parameters From Xfoil

Contenders	$C_{l_{max}}$	C_d	C_m	α_{max} [deg]
NACA 3414	1.98	0.0054	-0.156	20
NACA 4414	2.00	0.0053	-0.130	19.5
NACA 5414	2.01	0.0055	-0.104	19
NACA 6414	2.02	0.0057	-0.078	19

Table 7.4: Airfoil Scoring for Trade-Off

Contenders	A	B	C	D	SUM
NACA 3414	7	8	10	10	847
NACA 4414	8	10	9	9	1479
NACA 5414	9	7	7	8	974
NACA 6414	10	6	6	8	1039

7.2 Wing Design

This section presents the final wing planform design, as well as some of its features including high lift devices, twist and the option of having winglets. Furthermore, the aerodynamic consequences of the trusses on ECHO-1 are discussed in this sections.

7.2.1 Wing Planform

The wing planform was designed based on a number of parameters. Following from the design point selected in [chapter 5](#), a value for the wing loading (W/S) of 3614 N/m^2 was obtained. Given the Maximum Take-Off Weight (MTOW) of 20937 kg, the wing area was determined to be 56.85 m^2 . Furthermore, in order to be allowed to land at a International Civil Aviation Organisation (ICAO) Code C airport, a wingspan of 36 meters is designed for. In order to achieve the highest Oswald efficiency factor possible, as suggested in the ADSEE-I course [32], the taper ratio was set to 0.4. Following from this wing area and taper ratio, the root chord can be calculated, using [Equation 7.2](#), after which the tip chord can be calculated by multiplying the root chord with the taper ratio. This yields a root chord of 2.26 m and a tip chord of 0.90 m. Additionally, for stability reasons, the high-wing configuration will have an anhedral angle of 1 degree (i.e. $\Gamma = -1$).[30]

$$c_{root} = \frac{2 * S}{b * (1 + \lambda)} \quad (7.2) \quad AR_{actual} = \frac{b^2}{S} \quad (7.3)$$

Furthermore, it was chosen to have zero degrees of sweep at the Leading Edge (LE) of the wing. From the ADSEE course, it is suggested for aircraft that fly at a Mach number smaller than 0.7 to have zero sweep at quarter chord [32]. This would yield a sweep at LE of 0.82 degrees, a very small difference. Having zero sweep at LE, however, allows for easier integration of the distributed propellers. It was therefore chosen to have zero sweep at LE and a small negative sweep angle at quarter chord.

Following from the root chord, the wingspan, and the taper ratio, it is possible to determine the length of the Mean Aerodynamic Chord (MAC) and the spanwise location of this MAC (YMAC). Using [Equation 7.4](#), the length of the MAC was determined to be 1.68 m and using [Equation 7.5](#), the spanwise location of the MAC was determined to be 7.71 m.

$$MAC = \left(\frac{2}{3}\right) c_{root} \left(\frac{1 + \lambda + \lambda^2}{1 + \lambda}\right) \quad (7.4)$$

$$y_{MAC} = \left(\frac{b}{6}\right) \left(\frac{1 + 2\lambda}{1 + \lambda}\right) \quad (7.5)$$

Furthermore, from the wingspan and the surface area, the aspect ratio can be calculated. As for this report, the effect of winglets is also investigated, a distinction will be made between the actual aspect ratio (following from the wingspan and the wing area) and the effective aspect ratio which includes the effect of the winglet. The actual aspect ratio is found using Equation 7.3 and was found to be 22.8. Since for such high geometric aspect ratio it was decided not to have winglets, the effective aspect ratio also equals 22.8. The top view of the wing planform is shown in Figure 7.1. The high lift devices (HLD) in this image are explained in more detail in subsection 7.2.2.

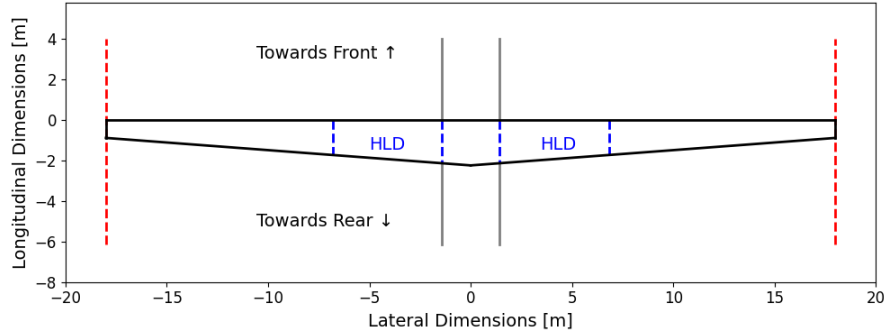


Figure 7.1: Top View of the Wing Planform of ECHO-1

7.2.2 High Lift Devices

The distributed propulsion can provide a significant ΔC_L of 0.3 over the $C_{L_{max}}$ of the clean wing, as was found in section 6.1. Regardless, for the required landing $C_{L_{max}} = 2.3$ another small boost of 0.3 is needed. For that purpose, a simple flaps system is required. Also, flaps will help with providing an additional ΔCd to aid in bleeding speed before landing, since the electric motors need to be run at full thrust to provide the previously mentioned ΔC_L .

Since the ΔC_L requirement is small, the added drag is beneficial, the wing chord is small and the mechanism needs to be kept as simple and light as possible, plain, trailing edge flaps were opted for. For sizing the following formula from ADSEE was used[32]:

$$\Delta C_{L_{max}} = 0.9 * \Delta C_{l_{max}} * \frac{S_{wetflaps}}{S_{wing}} * \cos(\Lambda_{hingeline}) \quad (7.6)$$

Plugging in the $\Delta C_{L_{max}} = 0.3$, the wetted area of the flaps $S_{wetflaps}$ is obtained. For plain flaps, the $\Delta C_{l_{max}} = 0.9$. Also, the hinging line is considered to be straight, parallel with the leading edge of the wing. The wetted area is presented in Figure 7.1.

For the drag contribution estimation of the flaps, the following equation was used[32]:

$$\Delta C_{D_{flap}} = F_{flap} * \frac{c_f}{c} * \frac{S_{wetflaps}}{S_{wing}} * (\delta_{flap} - 10) \quad (7.7)$$

For both the sizing and the drag estimation, the parameters and results are presented in Table 7.5, below. It should be noted that the $S_{wetflaps}$ is the total wetted area of the flaps, on both sides of the wing. Also, the $\Delta C_{D_{flap}}$ is offered for landing configuration.

Table 7.5: High-Lift-Devices

Parameter	Value	Unit
$\Delta C_{L_{max}}$	0.3	-
$\Delta C_{l_{max}}$	0.9	-
$S_{wet\ flaps}$	21.04	m²
$\frac{c_f}{c}$	0.25	-
δ_{land}	20	deg
$\delta_{takeoff}$	60	deg
F_{flap}	0.0144	-
$\Delta C_{D_{flap}}$	0.066	-

7.2.3 Wing Twist

As mentioned in the airfoil selection, the NACA 5-series airfoils have poor stall behaviour, meaning that there is a sudden drop after $C_{l_{max}}$. For this reason, the NACA4414 airfoil was selected for the tip section of the wing, where stall needs to be postponed and predictable in order to maintain aileron effectiveness even at large angles of attack. The wingtip airfoil will be used for the section of the wing that is included in the area affected by the ailerons. In order to optimise the wing for cruise, the wingtip airfoil needs to be set at the value of angle of attack where it produces the least drag, which in this case is 1.15 deg. The root airfoil produces its $C_{l_{design}}$ at 3.9 deg. Therefore, there needs to be a twist angle of 2.75 degrees (pointing downwards) from root to tip and the twist will be constant from root to tip.

This has the added benefit that when the root airfoil reaches its $C_{l_{max}}$ at 14.5 deg, the tip airfoil is at an angle of attack of just 11.25 deg, which judging by the α_{max} of the tip airfoil of 19.5 deg, means that there is absolutely no risk of the wing tip section stalling before the root, ensuring the desired controllability and predictability of inputs. However, there is a slight drag penalty that is associated with the introduction of this twist, whose value is shown in [section 7.3](#).

7.2.4 Winglet Design

In order to achieve the most efficient wing possible in terms of lift over drag (L/D), one option is to install a winglet at the wingtip. This increases the effective aspect ratio by ΔAR as indicated in [Equation 7.8](#), which is a function of the height of the winglet, as well as the actual aspect ratio and the wing span [30]. Increasing the effective aspect ratio decreases the induced drag, hence increases the lift over drag ratio, which allows for a lighter aircraft. On the other side, installing a winglet itself causes a weight penalty. Not only does the winglet add weight, the wing itself will also become heavier to transfer the loads from the wingtip to the fuselage. From data on the Boeing 737-800, a relationship was set up linking the height of the winglet to the additional mass added to the aircraft, including both the mass of the winglet itself as well as the mass of the structural reinforcement². This relationship is highlighted in [Equation 7.9](#). Here, the 2.49-term is the height of the Boeing 737-800 winglet and the 217.72-term is the additional mass due to the winglet. It was decided that installing a winglet on ECHO-1 would only be beneficial if the geometric aspect ratio AR_{actual} would be below 22. The method of sizing the winglet is described below, even though in the final design, AR_{actual} already exceeded 22 and thus ECHO-1 does not have a winglet.

$$AR_{effective} = AR_{actual} + \Delta AR = AR_{actual} + \frac{h_{winglet}}{b} * 1.9 * AR_{actual} \quad (7.8)$$

$$m_{winglet} = \frac{h_{winglet}}{2.49} * 217.72 \quad (7.9)$$

²<http://www.b737.org.uk/winglets.htm>

From literature, it was found that two aspects can play a role in the effectiveness of the winglet: the sweep angle and the cant angle. These two angles are illustrated in [Figure 7.2](#). It was found that when shifting the winglet longitudinally, there is no effect on the induced drag reduction [33]. Therefore, for the conceptual design, only the height, cant angle and twist of the winglet was designed for. Different cant angles were considered and tested in XFLR5. Since the aircraft should not have a wingspan larger than 36 meters, any cant angle smaller than 90 degrees would result in a decrease in the original wingspan, leaving less space for the placement of propellers. It is therefore that only large cant angles were tested. In the end, XFLR5 presents that a cant angle of 90 degrees will generate the best performance in terms of induced drag.

Additionally, a 5 percent twist was applied to the winglet as this reduces the induced drag when running simulations in XFLR5. This phenomenon is confirmed by a study conducted by T.T. Moore, which shows a reduced induced drag when applying wash-in twist for high aspect ratio wings, like ECHO-1[34].

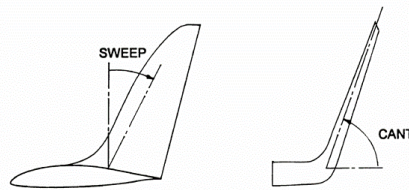


Figure 7.2: Sweep angle and cant angle of a winglet. [8]

Concluding, should ECHO-1 see an increase in MTOW, this will cause a larger required wing area for the same wing loading, hence a smaller geometric aspect ratio. If that would be the case, the winglet height could be designed for. The cant angle of the winglet would be 90 degrees and there would be a 5 percent twist on the winglet. For now however, there is no winglet installed.

7.2.5 Truss Sizing

One of the components that distinguishes ECHO-1 from other aircraft is its truss. The truss will be designed structurally in [chapter 10](#), however in this section, it is explained what was done to minimise the aerodynamic drag resulting from the truss. Two inputs determine the size of the truss: the cross-sectional area of the truss that is required in order to withstand the axial force running through the truss as well as the cross-sectional area that is required for cables to run through. The latter of which arrives from [chapter 6](#). A NACA0024 with a 24% thickness to chord ratio was chosen to accommodate the required cross-sectional area while minimising the wetted area and thus drag. Given the geometry of the airfoil, it was calculated that the truss would have a chord of 0.27 meters.

From the structural department, it was found that connecting the truss at 30% of the half wingspan would yield the optimal bending relief. Furthermore, in the vertical direction, the truss has to be connected from the bottom of the fuselage to the bottom of the wing, which is more or less equal to the diameter of the fuselage. This is illustrated in [Figure 7.3](#). In the end, the required truss length was calculated to be 6.18 meters, and in total two trusses have to be installed; one on each side.

To model the drag of the truss, since the truss has an airfoil as cross-sectional area, the same method will be applied as for a regular wing using the Class I Drag Estimation method. More on this will be presented in [section 7.3](#).

7.3 Detailed Lift and Drag Estimation

After having determined the 2D and 3D characteristics of the wing, the aerodynamic behaviour can be determined by making use of XFLR5. For running this analysis, a number of inputs have to be given. The model that is used is a horseshoe vortex method (VLM1). Furthermore, the free-stream velocity (138.89 m/s) and Reynolds number ($10 * 10^6$) are required by XFLR5. Additionally, the wing

planform parameters and the winglet parameters that were discussed in [section 7.2](#) serve as inputs to the simulation. The results of the simulations are presented below.

7.3.1 Spanwise Lift Distribution

One of the outputs that XFLR5 presents is the lift distribution over the span of the aircraft at the design lift coefficient of 0.5955. This distribution is illustrated in [Figure 7.3](#), where the local lift coefficient is plotted. It should be noted that this does not automatically translate into total lift as the wing has a smaller chord near the tip. This lift distribution will be used in [chapter 10](#) to determine the aerodynamic loads that the wing should be able to withstand.

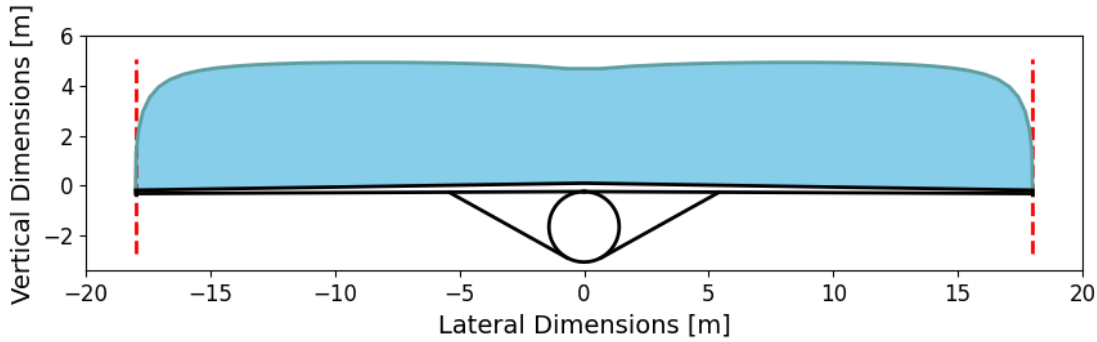


Figure 7.3: ECHO-1 spanwise lift distribution based on local lift coefficient

7.3.2 Viscous Drag Estimation

Multiple methods exist to determine the viscous drag of the aircraft. A paper by Gur et al. investigates differences between the Class I Drag Estimation model and methods developed by Shevell, Hoerner and Jobe/Nicolai/Raymer[35]. The paper concludes that, especially for high lift over drag aircraft, the differences between the methods are small, hence it does not make a large difference which method is used. It is therefore that it was chosen to make use of the Class I Drag Estimation, which calculates a viscous drag component for the wing, fuselage, horizontal tail, vertical tail and truss, using [Equation 7.10](#) for the computation of said contributions.

$$C_{D_0} = \frac{1}{S_{ref}} \sum_c C_{f_c} * FF_c * IF_c * S_{wet_c} + C_{d_{misc}} \quad (7.10)$$

In [Equation 7.10](#), C_{f_c} is flat plate skin friction coefficient and estimates the skin friction drag based on what type of boundary layer surrounds the component. In the calculation of the C_{f_c} it is important to establish the ratio of laminar flow from the total flow over the respective component. For the fuselage which in the current design has a conventional shape, as well as for the horizontal and vertical tail, the ratio was taken from statistical data. For the wing and truss, the 0.45 value of this ratio is closer to the 0.5 value that advanced aircraft such as the Piaggio GP180 have. FF_c is the component form factor which estimates the pressure drag due to viscous separation. IF_c is the interference factor that estimates the increase in drag due to the interference between different components. The S_{wet_c} is the wetted area of each component, or the area which comes in contact with the flow. In the calculation of the C_{f_c} it is important to establish the laminar to turbulent flow on the respective component.

Table 7.6: Zero lift drag components of wing, fuselage, truss, horizontal tail and vertical tail

Components	Lam/Tot Ratio	C_{fc}	FF_c	IF_c	Wetted Area	C_D Component
Wing	0.45	0.00181	1.52333	1.00	125.35067	0.00569
Fuselage	0.25	0.00232	1.09488	1.00	180.97139	0.00756
Horizontal Tail	0.45	0.00181	1.34135	1.04	11.77214	0.00049
Vertical Tail	0.45	0.00181	1.30848	1.04	27.69197	0.00112
Truss	0.45	0.00181	2.09338	1.00	7.07186	0.00044

Furthermore, to estimate the viscous drag due to the wing twist, it was found that a wing with 2.75 degrees of wing twist would result into a zero lift drag increase of 9.2×10^{-5} [30].

Finally, it was aimed to determine the drag as a result of the fairing that houses the landing gear. From a paper by van Oene, a method was found to compute this[36]. This paper illustrates two test cases of the method, one of which determines the C_{D_0} counts for a fuselage-connected fairing for different dihedral angles. Since ECHO-1 has an anhedral angle of 1 degree, it follows that the viscous drag component of the fairing is equal to 0.0008.

7.3.3 Total Drag Estimation

Following from the viscous drag estimation presented in the previous section, the zero lift drag components of the wing, fuselage, horizontal tail, vertical tail and truss in Table 7.6 were summed and equal to 0.01531. In order to account for unforeseen drag components, a 2% miscellaneous drag factor on these five components was taken into account. Next, to find the total zero lift drag, the components of the fairing and the wing twist were added. This results in a total C_{D_0} of 0.0165 as can be seen in Table 7.7. Additionally, a drag component from the distributed propulsion and the induced drag need to be added to arrive at the total drag coefficient of ECHO-1. From XFLR5, running the VLM1 analysis, the induced drag coefficient for the design lift coefficient was found to be 0.00475. This yields a total drag coefficient of 0.02213 for the final design. Finally, the lift-over-drag ratio of the aircraft can be found by dividing the lift coefficient in cruise by the drag coefficient in cruise. The lift coefficient in cruise is equal to the sum of the design lift coefficient (0.5955) and the lift coefficient increase due to the distributed propulsion (0.029). This yields a lift-over-drag ratio of 28.24.

Table 7.7: Overview of all zero lift and total drag components

Component	C_D Component
C_{D_0} 5 Main Components	0.01531
Misc. Factor on 5 Main Components	1.02
Sum 5 Main Components	0.01561
C_{D_0} Fairing	0.00080
C_{D_0} Twist	0.00009
Total C_{D_0}	0.01650
C_D from Propulsion	0.00088
C_D induced	0.00475
Total C_D	0.02213

To conclude, an approach was made to determine the drag that would be caused by propellers if inoperative. Two cases were distinguished here. In one case, the propellers would be unfeathered. In this case, the propeller was modelled as a flat plate. In the other case, the propeller would be feathered, hence it would be in its minimal drag position. For the latter case, a drag coefficient of 0.02

was assumed³, for the first case a drag coefficient of a flat plate of 1.28 was assumed⁴. Assuming cruise conditions ($V_{cruise} = 500$ km/h at 6000 m altitude) this yields a feathered propeller drag of 29.6 N and an unfeathered propeller drag of 1895N. This difference was to be expected since the drag coefficient of the flat plate is also 64 times larger than that of the propeller in minimum drag condition. This difference clearly shows the benefit of feathering the propeller if inoperative.

7.3.4 Aerodynamic Polars

From the VLM1-analysis that was described in the beginning of this section, the aerodynamic wing behaviour was extracted and plotted in Figure 7.4. It should be noted that each of these plots is only valid up until a maximum lift coefficient $C_{L,max}$ of 1.75 or equivalently an angle of attack α of 15 degrees. After this, the aerodynamic performance will drastically worsen, ultimately leading to stall. Since the XFLR5 software only allows to run a VLM1-analysis, it is not possible to take this phenomenon into account for angles of attack larger than 15 degrees. From the upper-left graph, it can be seen that the lift varies linearly with the angle of attack, with an offset α_0 of approximately 2.5 degrees left from the origin. Additionally, the lift slope is equal to approximately 0.1 deg^{-1} . For the upper-right and lower-right graphs, XFLR5 did not provide the zero-lift drag. This was computed using the method that was described in section 7.3 and added manually to the equation. This explains the offset upwards in the upper-right graph and the offset to the right in the lower-right graph. Finally, in the lower-left graph, the moment curve is plotted as a function of the angle of attack. Clearly, it is visible that the moment coefficient C_m becomes more negative as the angle of attack increases. This is beneficial for the aircraft stability. More on the aircraft stability will be presented in chapter 9.

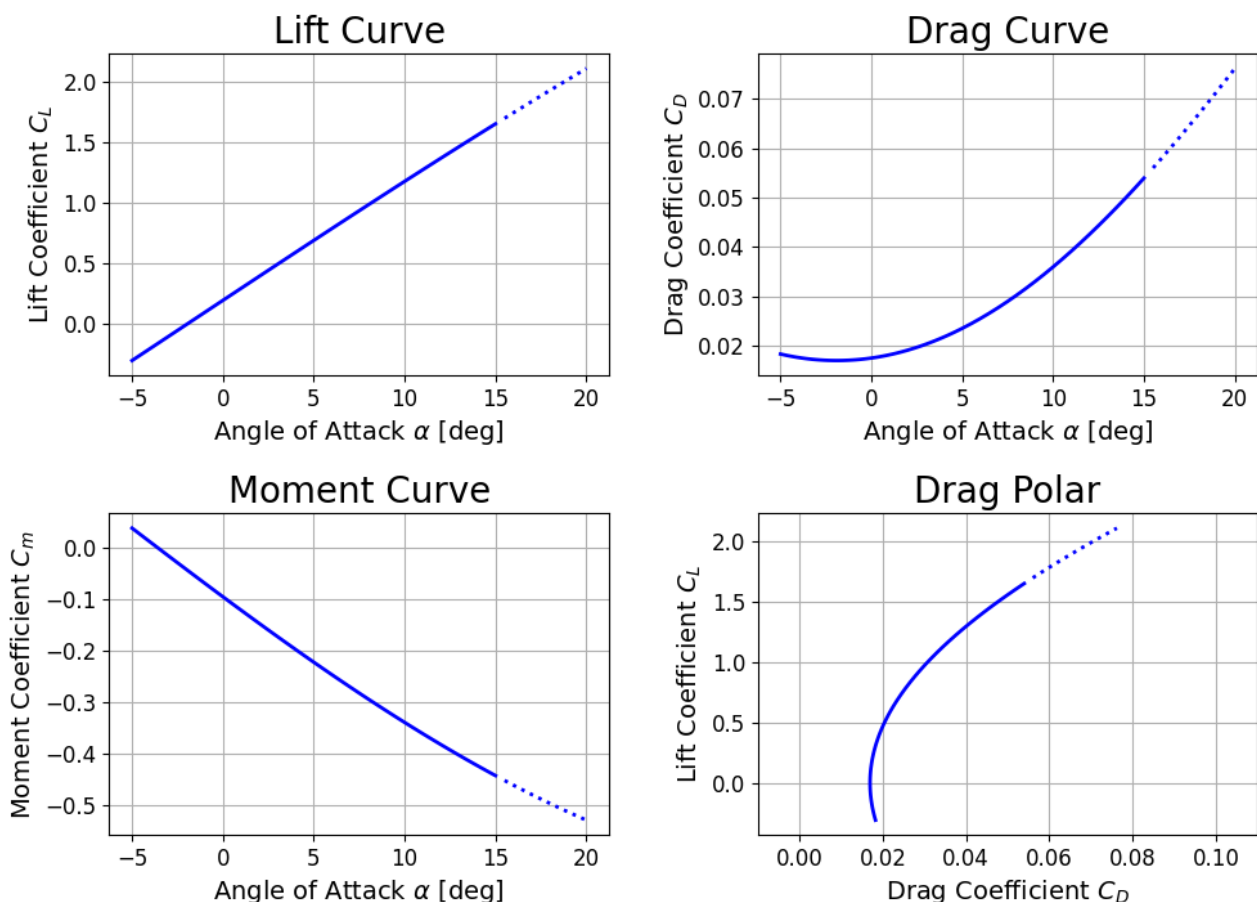


Figure 7.4: Aerodynamic polars for ECHO-1 wing, only valid up to $C_{L,max}$. For values above $C_{L,max}$, the line is dotted.

³<http://airfoiltools.com/>

⁴<https://www.grc.nasa.gov/www/k-12/airplane/shaped.html>

7.4 Verification and Validation

This section presents the verification and validation that was performed on the aerodynamics calculations as well as the software that was used to determine the aerodynamic behaviour of ECHO-1.

7.4.1 Aerodynamic Software Verification and Validation

The aerodynamic parameters that were used in the previously-presented trade-offs are results of the CFD software Xfoil which is subject to errors. In order to ensure the robustness of these results, the software will be verified by comparison with another one, such as JavaFoil. The validation will consist in comparison between the Xfoil results and experimental data on the respective airfoils and conditions. The 2 airfoils that will be used for the comparison are the two chosen ones:

- NACA 43014 at $Re = 10 * 10^6$
- NACA 4415 at $Re = 9 * 10^6$; this was chosen instead of the actual chosen NACA 4414 because only for the 4415 experimental data was found.

The airfoil's lift coefficient from both softwares and from the experimental data was plotted against the angle of attack, shown in Figure 7.5a and Figure 7.5b. Experimental data was obtained from "The Theory of Wing Sections" [37] and from the "Riegels Aerofoil Sections" [38]. Analysing the root airfoil (NACA 43014) plot it becomes apparent that the $C_{L_{max}}$ is accurately predicted by XFOIL, but neither software accurately models the sudden stall behaviour that is typical for the NACA 5-series airfoils. For the NACA 4-series that is used as the tip airfoil, the stall behaviour is more accurately predicted by the viscous models used by the 2 softwares, but the $C_{L_{max}}$ is significantly overpredicted by both, although the angle of attack where it occurs is predicted correctly. For the rest of the design, Xfoil and its 3D version, XFLR5, are used since their results are reliably the closest to experimental data. That being said, more detailed CFD analysis and wind-tunnel testing should be implemented further down the design process for a more accurate estimation of all aerodynamic parameters.

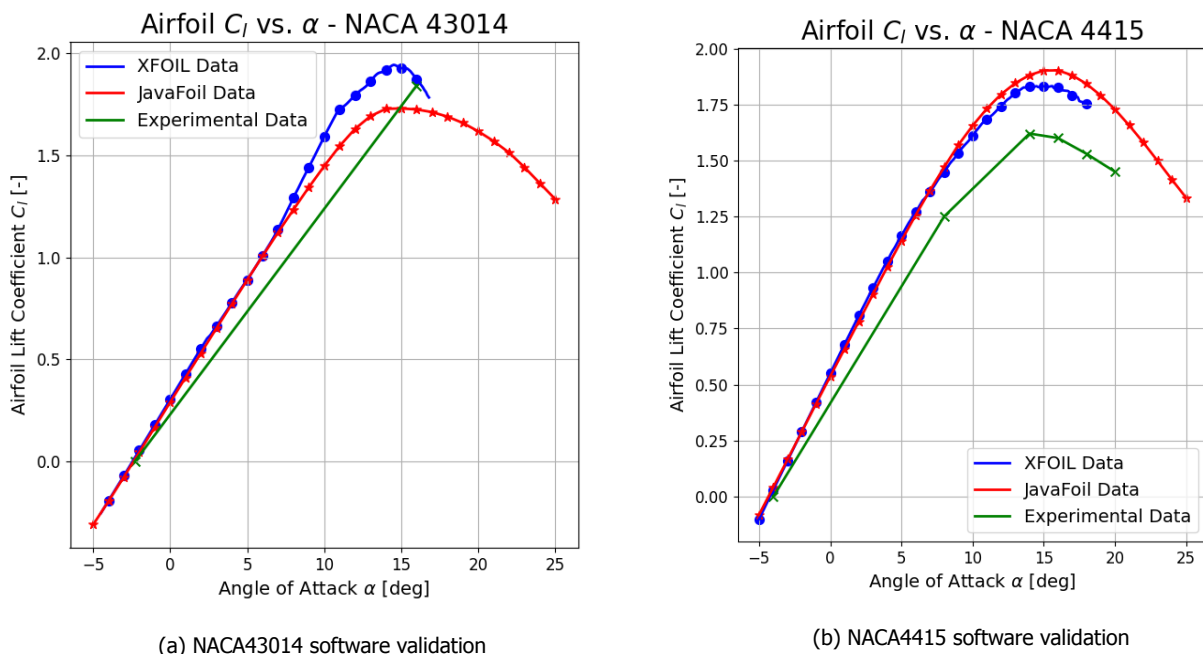


Figure 7.5: Comparison of XFOIL and JavaFoil data with respect to experimental data on NACA 4 and 5 series airfoils

7.4.2 Code Verification and Validation

Each of the single unit tests that were performed to verify the code that was written for the aerodynamic analysis is presented in Table 7.8. The process of verifying the code has been done in two ways. Each function was checked by means of hand calculations. Additionally, an excel tool was built to calculate the same parameters and hence served as a second means of back-up. The excel tool

allowed to check also how all functions work together, therefore it could be seen as a system test. Based on a number of inputs, the outputs of the entire system were checked and passed. Seeing that each of the unit and system tests passed, it is safe to conclude that the code has been verified.

Table 7.8: Performed Unit Tests for Aerodynamic Python Scripts

Nr.	Name	Type	Parameters	Passed
1	Airfoil Calculations	Hand calculation, Excel test	$\rho, T, M, A_{actual}, c_{root},$ CL_{cruise}, MAC	Yes
2	Truss Calculations	Hand calculation, Excel test	$l_{truss}, S_{wettruss}$	Yes
3	Winglet Calculations	Hand calculation, Excel test	$h_{winglet}$	Yes
4	HLD Calculations	Hand calculation, Excel test	$S_{wetflaps}$	Yes
5	Form Factor	Hand calculation, Excel test	$CF_{fus/wing/truss/vtail/htail},$ $FF_{fus/wing/truss/vtail/htail}$	Yes
6	Wet Surfaces	Hand calculation, Excel test	$S_{wetfus/wing/truss/vtail/htail}$	Yes
7	CD0 Calculations	Hand calculation, Excel test	$CD_{0fus/wing/truss/vtail/htail/twist},$ $CD_{total}, L/D$	Yes
8	Propeller Drag Calculations	Hand calculation, Excel test	$D_{propfeathered},$ $D_{propunfeathered}$	Yes

8

Aircraft Geometry

In this chapter the geometry of the aircraft is determined. The aircraft geometry is mainly depended on the aircraft configuration which was selected in the Midterm Report[1]. In the Midterm report a truss-braced wing was selected. Therefore, the aircraft will definitely have high-wing configuration. The sizing of the fuselage, tail, landing gear and control surfaces is performed in this chapter.

This chapter is divided into the following sections. In [section 8.1](#), the design of the fuselage is discussed. The centre of gravity of the aircraft is determined in [section 8.2](#). The sizing of the horizontal is performed in [section 8.3](#). In [section 8.4](#), the vertical tail will be sized. The control surfaces of the aircraft are designed in [section 8.6](#). In [section 8.5](#), the sizing and the placement of the landing gear is performed. Next, the verification and validation procedures are presented in [section 8.7](#) and some future recommendations will be summarised in [section 8.8](#)

8.1 Fuselage Design

The size of the fuselage is mainly dependent on the amount of passengers the aircraft should be carrying. Initially Venturi Aviation asked DSE Group 9 to design an electric battery powered aircraft, which could carry 50 passengers. However, Over the course of the Design Synthesis Exercises, this requirement ought to be unachievable. Therefore, Venturi Aviation has set a new requirement, "ECHO-1 shall at least accommodate 48 passengers".

The length of the aircraft is mainly dependant on the numbers of seats abreast and the amount of passengers. When using empirical formulas for the sizing of the aircraft it was determined that 4 seats abreast is required. However, the number of seats abreast was reassessed, because for aerodynamic performances a smaller frontal area is more beneficial than a shorter fuselage length. For this reason

it was chosen to design the fuselage for a 3 seats abreast configuration to decrease the diameter of the fuselage.

During the cross-sectional design of the aircraft the key is to minimise the inner diameter of the fuselage in order to decrease the frontal area as specified before. To size the cross-sectional area of the aircraft a sketch is made, whereby the regulations for the sizing are taken into account, such as the width of the seats, clearances, aisle, armrest. The width of the ground, which is the distance between most left passenger shoulder to the most right passenger shoulder, is given by [Equation 8.1](#). The headroom width, which is the distance between most left passenger head to the most right passenger head, is calculated with [Equation 8.2](#). The dimensions which are used to calculate these parameters can be found in [Table 8.1](#).

$$W_{ground} = N_{seat} \cdot W_{seat} + W_{aisle} + 2 \cdot W_{clearance} + N_{arm} \cdot W_{arm} \quad (8.1)$$

$$W_{headroom} = W_{ground} - W_{seat} - 2 \cdot W_{arm} - 2 \cdot W_{clearance} \quad (8.2)$$

Table 8.1: Dimensions for the fuselage sizing

Parameter	Width in m	Parameter	Height in m	Parameter	Length in m
W_{seat}	0.49	$H_{shoulder}$	1.05	Lavatory	0.9144
W_{aisle}	0.51	H_{head}	1.42	Galley	0.762
W_{arm}	0.06	H_{aisle}	1.90	Business seat	0.889
$W_{clearance}$	0.02	H_{floor}	0.10	Economy seat	0.8128

Furthermore, to determine the inner fuselage diameter a sketch of cross-section of the fuselage is made. In this sketch, the internal layout of the fuselage is drawn. To minimise the inner fuselage diameter, the circle around the internal layout was drawn such that it is not allowed to cross any of the inner passenger blocks as seen in [Figure 8.1a](#). The smallest diameter is determined via python optimisation program. Resulting into the sketch given in [Figure 8.1a](#). Moreover, the internal layout of the fuselage is presented in [Figure 8.1b](#).

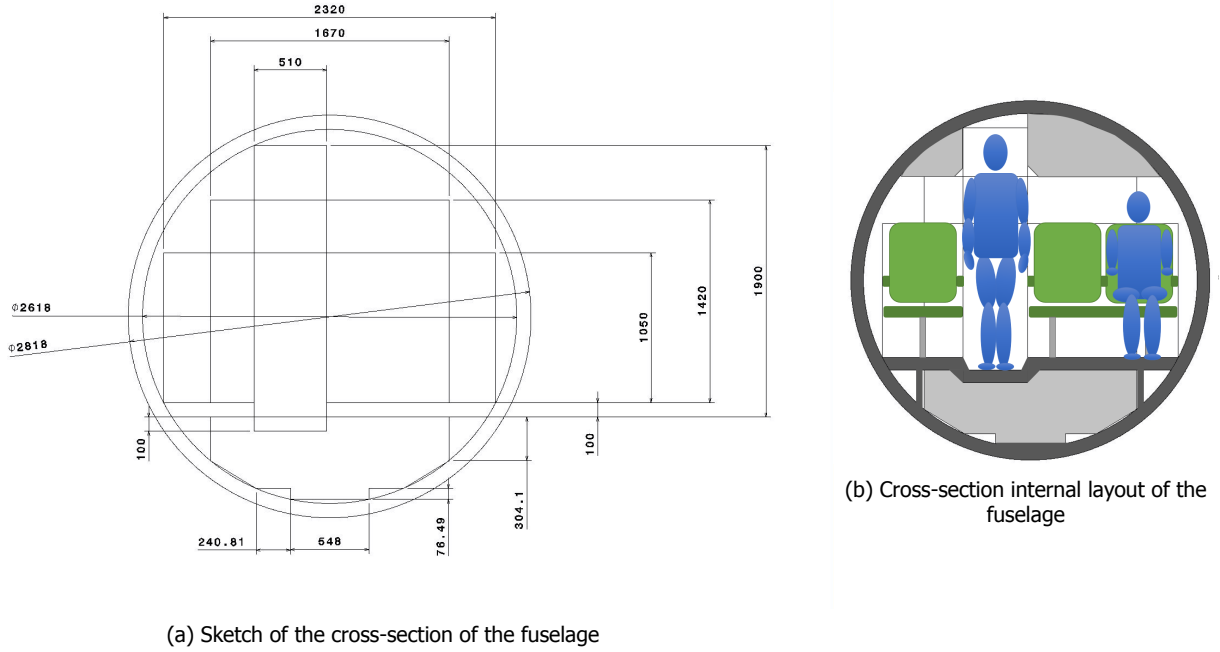


Figure 8.1: Cross-sectional sketches for fuselage sizing

The length of the cabin is dependant on the number of cross aisle, lavatories, galleys and number of passengers rows. Furthermore, the seat pitch is not constant since Venturi Aviation is aiming to design a cabin with a business class and a economy class. This results into a configuration where 20% of seats should be business class and 80% economy class. Moreover, it was decided that a row of seats only could consist of one type of class. In the end this resulted in 3 rows of business class and 13 rows of of economy class. In addition, it was chosen to design the cabin with 2 lavatories in the front of the aircraft and 1 galley in the back of the aircraft. From safety regulations it was determined that the aircraft should have at least one type I and one type III or type IV exit.

To calculate the length of the cabin Equation 8.3 can be used. The total fuselage length is then calculated by Equation 8.4.

$$l_{Cabin} = R_{Business} \cdot l_{Business} + R_{Economy} \cdot l_{Economy} + l_{Galley} + l_{Lavatory} + l_{TypeI} + l_{TypeIII} \quad (8.3)$$

$$l_{Fuselage} = l_{Cockpit} + l_{Cabin} + l_{Tail} \quad (8.4)$$

Furthermore, it was required to determine the length of the nosecone, length of the tailcone and constant diameter fuselage length, to model the aircraft in XFLR5. The nosecone and tailcone lengths are determined by multiplying the outer diameter of the fuselage with the ratio's $\frac{L_{Nosecone}}{D_{fus-outer}}$ and $\frac{L_{Tailcone}}{D_{fus-outer}}$. When those lengths are determined the length where the fuselage has a constant diameter can then be calculated with Equation 8.5.

$$l_2 = l_{Fuselage} - l_{Nosecone} - l_{Tailcone} \quad (8.5)$$

After all dimensions were determined, a top-view drawing of the aircraft is made and shown in Figure 8.2. The dimensions of the aircraft are given in Table 8.2. The next step in the fuselage design process, is the space allocation of the cargo-holds, overhead storage spaces, and the battery packages. Since the cabin has a three seats abreast configuration, there is only room for one overhead storage bin as can be obtained on the right side from Figure 8.1b. The overhead storage bin will run

over the entire length of the passenger seats. However, the overhead storage bin will be interrupted at the location where the wing is fixed to the fuselage, to take into account that extra structure is required to fix the wing onto the fuselage.

Table 8.2: Dimensions of the fuselage of ECHO-1[2]

Parameter	Length in m	Parameter	Length in m	Parameter	Width in m
$l_{cockpit}$	4	$l_{nosecone}$	4.51	W_{ground}	2.32
l_{cabin}	16.0274	l_2	14.79	W_{head}	1.67
l_{tail}	6.6	$l_{tailcone}$	7.33	$D_{fus-inner}$	2.62
$l_{fuselage}$	26.6274	l_{pax}	13.23	$D_{fus-outer}$	2.82

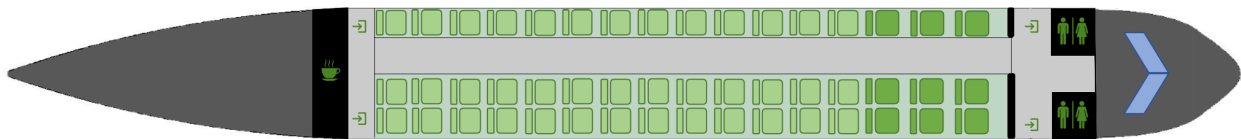


Figure 8.2: Top view cabin layout of ECHO-1

During the belly design, it should be taken into account that it is not possible to utilise the total length of the fuselage. Only the cabin length can be used as effective space due to its cylindrical shape. The cargo-hold is designed in such a way that it can hold 500 kg of cargo and is able to store the battery package. Moreover, the landing gear, a water tank and cooling- and avionics systems are stored in the belly of the fuselage. Resulting in that 72 % of the cabin length is utilised for the storage of cargo and batteries, and as a consequence 28% of the cabin length is used for the rest. To store the main landing gear a fairing is also required.

The location of the battery package is most critical, after all it has the greatest influence on centre of gravity shifts. Therefore, it was decided to place the battery package as close to OEW centre of gravity as possible. To achieve this goal, the battery package is subdivided into 2 storage places, where 64% of the total batteries is placed in front of the location where the truss is fixed to the fuselage and the second battery package is stored aft the storage of the main landing gear. The second battery package contains 36% of total battery package. These values are obtained from a python optimisation program. Due to the placement of the batteries two cargo holds are designed, one in front of the first battery package and one behind the second battery package. Between the cargo holds and the battery packages fire walls are placed to not spread the fire outside the battery packages. Each cargo-hold will have his own cargo hold door. Moreover, the battery packages will be accessible from the side, via two cargo hold doors such that each battery module can be switched easily when defect. The size of of cargo compartments and battery packages are given in Table 8.3. A side view of ECHO-1 will be given in Figure 8.3, on this side view the exact locations of the battery package and cargo compartments can be visualised.

To store avionics systems and the nose landing gear 10% of the cabin length is utilised (box_1). To store the cooling system, main landing gear and extra structure for the truss, 18% of the cabin length is utilised, which is given by box_2 in The Respective ranges which can be achieved when having charging for 30 min and presented in Figure 8.3.

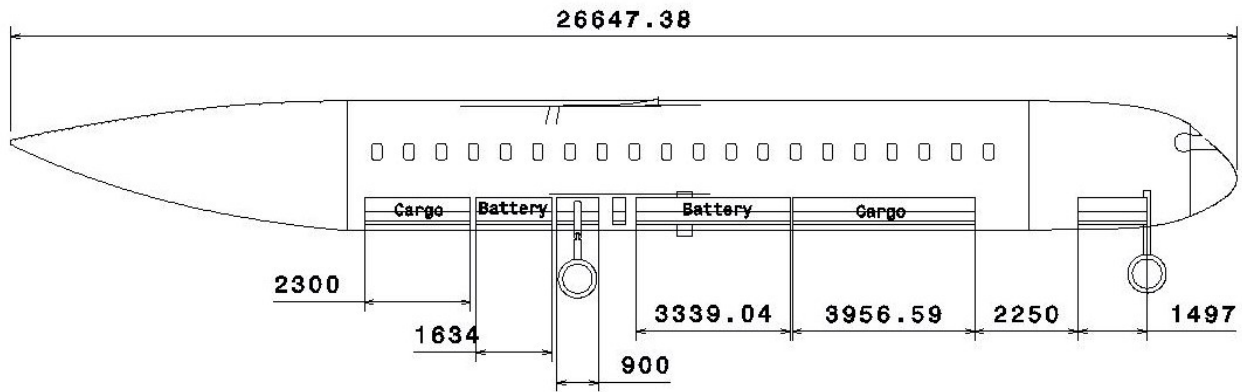


Figure 8.3: Sideview of the cargo hold of ECHO-1

Table 8.3: Dimensions of the aircraft cargo-hold [2]

Parameter	Volume	Parameter	Volume
Total Cargo-hold Storage	8.22 m ³	Hand Luggage	3.95 m ³
Front Cargo-hold Storage	2.06 m ³	Cargo volume	3.13 m ³
Aft Cargo-hold Storage	1.64 m ³	Total Battery volume	3.05 m ³
Front Battery Pack Storage	1.51 m ³		
Aft Battery Pack Storage	0.71 m ³	Box ₁	0.82 m ³
Overhead Luggage Storage	3.08 m ³	Box ₂	1.48 m ³
Free Storage Volume	1.18 m ³		

8.1.1 Cargo Configuration

The ECHO-1 aircraft should also be designed as a cargo aircraft. The cargo configuration of ECHO-1 shall be able transport 5588 kg of cargo. However, over the course of the project an emphasis was put on the design of a passenger transport configuration of ECHO-1. Nonetheless, the passenger transport configuration can easily be transformed into a cargo configuration storage wise. Resulting into the removal of the entire passenger cabin configuration and creating a large cargo storage space over the length of the cabin, allowing to store large containers in the cabin. Since the fuselage of the aircraft in passenger transport configuration is quite long, 5588 kg of cargo will fit without any problem. For the cargo configuration a cabin length of only 11 m is required, which is only 68.65% of the cabin in passenger transport configuration.

To prevent any alterations of the passenger transport configuration of ECHO-1, a cargo loading plan should be made such that the centre of gravity range will stay within the boundaries of the passenger transport configuration. In such way you can potentially operate an cargo configuration aircraft. However, more detailed calculations on the cargo configuration of ECHO-1 have to be performed to see if an transformation is possible.

When it is not possible to simply load the cabin with cargo containers a partial redesign of the aircraft need to be performed. Since loading the cargo containers into the aircraft will shift the centre of gravity. Therefore, the centre of gravity range in the potato plot diagram will probably increase, which in return will result in a increase of horizontal tail area and will have an effect on the longitudinal stability of the aircraft. Furthermore, the centre of gravity shift will result in a redesign of the landing gear. To conclude further analysis on the cargo configuration of ECHO-1 should be performed to determine the possibility's.

8.2 Centre of Gravity Determination

The centre of gravity is a parameter that has to be updated at any step in the design. Thus, because of its complexity and necessity for iteration, values are required for its components. The aircraft was divided in five main components each with its own weight and centre of gravity location:

- **Wing** which includes the structures of the wing;
- **Fuselage** which includes the structures of the fuselage but also of the landing gear;
- **Propulsion** which includes the propulsion system with its propellers and nacelles;
- **Empennage** which includes the vertical and horizontal tail areas;
- **Fixed Equipment** which includes all the other components or systems that were ignored in the operational empty weight (e.g.: avionics, cables etc.);

The weights were estimated using Class-II weight estimation methods which were presented in [chapter 5](#). Meanwhile, for most of the components, the centre of gravity was estimated using statistics. The only component whose centre of gravity was calculated was the wing which will be also iterated in [chapter 12](#). All those parameters are summarised in [Table 8.4](#):

Table 8.4: Centre of gravity and weight of the 5 main components that make up the operational empty weight

Component	Centre of gravity	Weight in % of MTOW
Wing	30% of MAC	0.04891
Fuselage	42% of Fuselage Length	0.14697
Propulsion	0% of MAC	0.04
Empennage	90% of Fuselage Length	0.0276
Fixed Equipment	42% of Fuselage Length	0.13912

The centre of gravity of the fuselage was taken from Roskam's empirical estimations[16]. The CG of the fixed equipment component was assumed to be the same as the fuselage component. For the wing CG, the value was determined using the weight calculations in [chapter 10](#), after the necessary structure was determined during the final iteration. Meanwhile, for the propulsion system, as the distributed propulsion acts at the leading edge of the wing and there is no sweep, a CG value equal to the leading edge of the wing was chosen. Last but not the least, the centre of gravity of the empennage was approximated at 90% of the fuselage length which coincides with the ATR-72.

The weights of the components were determined both statistically but also through iteration. First, the ratio between OEW and MTOW (f_e) was found to be 0.4026 using class II weight estimation in [section 5.4](#). Similarly, after iteration, the wing weight fraction and the fuselage weight fraction were calculated for the aircraft's structure. The wing weight was found to be so low compared to usual percentages of 10-15% of MTOW[16] because of the truss which releases a lot of stress in the wing while the fuselage weight was found higher than usual because the batteries were placed in the belly where a lot more reinforcement was needed for its very high density. Next, using Roskam's empirical estimations[16], the empennage weight was considered to be 0.0276, while the remaining weight of 0.13912 remained for fixed equipment. This remaining part complies with other similar MTOW aircraft fixed equipment weight like Fokker F27-500 (0.144), Fokker F27-100 (0.151), Convair 240 (0.102).

Regarding the batteries, those were not included in the OEW. On the other hand, their centre of gravity was calculated based on the placement established in the previous section. Thus, two battery compartments were considered, one in front and one aft the wing. For both of them, their centre of gravity was assumed to act at the half of the compartment. The exact same procedure was done for the two cargo compartments whose position, similar to batteries, was explained in the previous section as well. The weights and CG's of the batteries and cargo will be summarised in [Table 8.5](#):

Table 8.5: Centre of gravity (from nose of the aircraft) and weight of the battery and cargo compartments

Component	CG in m	Weight in kg
Battery front	11.08411	4715.79829
Battery back	16.13274	2204.12311
Cargo front	7.606165	651.11111
Cargo back	18.42466	520.88889

In order to find the centre of gravity of the passengers, the layout as presented in the [section 8.1](#) will be used. The passenger centre of gravity was assumed to be placed at 70% of the seat pitch[39]. With this information in mind, the centre of gravity of the passengers was found to be at 12.399 m from the nose of the aircraft while keeping in account they account for 5088 kg of the MTOW.

With all the information gathered, the centre of gravity for the MTOW can be determined. However, this centre of gravity might be shifted because of the different placement of the passengers or the way the cargo is loaded in the aircraft. Also, the batteries can be shifted which might lead to a change in the centre of gravity. However, the batteries are almost never moved or shifted, especially not during a flight, and for this reason, in some cases, they can be assumed as a part of the OEW. Only when replacing the battery package the CG shift needs to be taken into account. For example, for tail sizing, as the batteries will not be moved during flight, the batteries will be considered as part of the OEW. On the other hand, for landing gear sizing, the shift in centre of gravity caused by batteries might cause the tip back of the aircraft. Thus, for this case, the batteries will be considered separately from OEW. With these considerations in mind, the CG excursion plot could be drawn for both cases as seen in [Figure 8.4](#) which will lead to 2 CG ranges summarised in [Table 8.6](#):

Table 8.6: Centre of gravity ranges as percentage of MAC

Case	Most forward CG	Most aft CG
Batteries included in OEW	-0.10616	0.25364
Batteries not included in OEW	-0.22143	0.33964

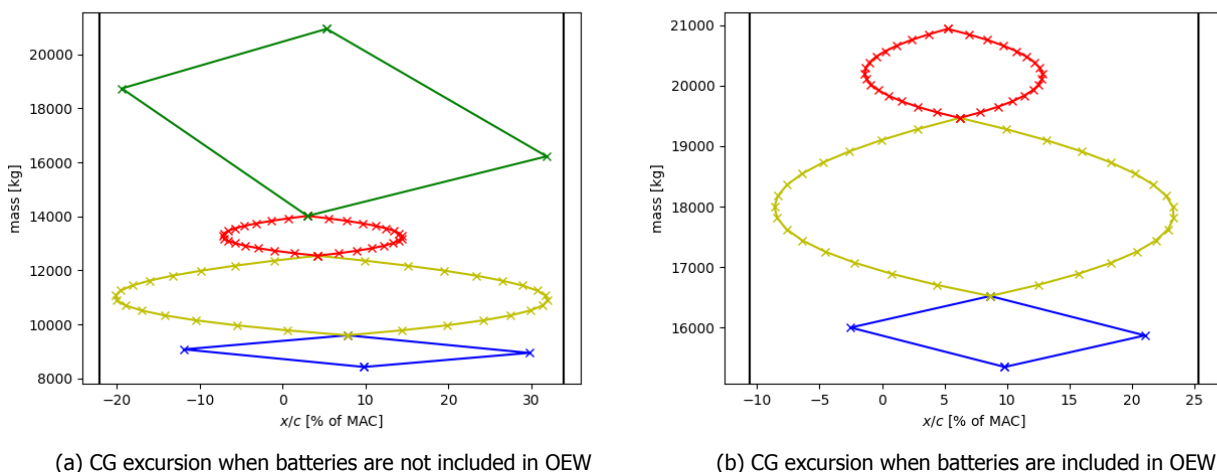


Figure 8.4: The 2 CG excursions drawings

For the landing gear sizing which will be performed later on, also the z-position of CG was calculated. The final results along with the component position will be presented in [Table 8.7](#) as a percentage of the aircraft outer diameter. Some values were introduced using common sense and engineering judgement while others used empirical formulas (empennage). For example, the fuselage along with

its fixed equipment was assumed to have the CG in the middle while the wing and its propulsion system would have the CG at the very top of fuselage because it is a high wing aircraft. The z-location of the CG of the cargo and batteries was calculated by finding the centre of area of the compartment. Lastly, the passengers centre of gravity was assumed to be 0.8 m above the floor[39].

Table 8.7: Centre of gravity placement

Component	CG in % of diameter	Component	CG in % of diameter	Component	CG in % of diameter
Wing	100	Empennage	211[40]	Passengers	57
Fuselage	50	Fixed Equip-ment	50	Battery	16.1
Propulsion	100	Cargo	16.1	Total	48.2

8.3 Horizontal Tail Sizing

With the centre of gravity found, the design of the tail could start. The tail has the purpose to assure both the stability and the controllability of the aircraft. For pitch, the horizontal tail is the determining factor. Thus, to determine the required area, the following equation is used:

$$S_h/S = \frac{\bar{x}_{cg}}{\frac{C_{L\alpha_h}}{C_{L\alpha_{A-h}}} \left(1 - \frac{d\epsilon}{d\alpha}\right) \frac{l_h}{\bar{c}} \left(\frac{V_h}{V}\right)^2} - \frac{\bar{x}_{ac}}{\frac{C_{L\alpha_h}}{C_{L\alpha_{A-h}}} \left(1 - \frac{d\epsilon}{d\alpha}\right) \frac{l_h}{\bar{c}} \left(\frac{V_h}{V}\right)^2} \quad (8.6)$$

Moreover, the horizontal tail area given by the controllability requirements is found using:

$$S_h/S = \frac{\bar{x}_{cg}}{\frac{C_{L_h}}{C_{L_{A-h}}} \frac{l_h}{\bar{c}} \left(\frac{V_h}{V}\right)^2} + \frac{\frac{C_{m_{ac}}}{C_{L_{A-h}}} - \bar{x}_{ac}}{\frac{C_{L_h}}{C_{L_{A-h}}} \frac{l_h}{\bar{c}} \left(\frac{V_h}{V}\right)^2} \quad (8.7)$$

In both Equation 8.6 and Equation 8.7, there are parameters which are not known yet. Fortunately, some parameters were already found like the centre of gravity position \bar{x}_{cg} and MAC which was fixed already to 1.685 m. For the unknown values, empirical formulas, or statistical values exists and will be used to estimate the horizontal tail area. The tail lift slope $C_{L\alpha_h}$ was found using the DATCOM method[30] to be 4.327. This uses an AR_h of 5 as found from statistics[41]. β was taken from cruise conditions as that is the most critical phase for stability and inputted as 0.8985. Similarly, η was initialised from statistics[30] at 0.95 and $\Lambda_{0.5c}$ was found to be -1.076° . $C_{L\alpha_{A-h}}$ was found with empirical equations to be 6.5. This is different than the lift coefficient of the wing $C_{L\alpha_w}$ shown in chapter 7 as it does not include also the effect of the fuselage. Moreover, in the empirical equation, S_{net} is set equal to 50.46. Also the downwash $\frac{d\epsilon}{d\alpha}$ is calculated empirically[30] and found to be equal to 0.15567.

With all the equations inputted in the program, only the l_h and h_h should be found. For the l_h , the horizontal tail was assumed to be placed at 0.95 of the fuselage length. This value was verified statistically with similar regional aircraft that have a T-tail. Thus, this led to a value of 12.7584 m and for the r to be 0.7088. On the other hand, the h_h was a parameter that was more difficult to calculate. One first assumption made in its determination was neglecting the incidence angle of the wing and of the horizontal tail. This can be done as the assumption is conservative. A second assumption done was to assume the distance between wing on z-direction simply equal to the height of the vertical tail. Again this one is conservative. Thus, the h_h was considered to be equal to the height of the vertical tail which, after the sizing of the vertical tail is done, is equal to 4.5 that leads to a m_{tv} of 0.25.

One parameter that is present in both the controllability and stability equations is V_h/V . As the horizontal tail is positioned up on the vertical tail, its flow is not greatly affected by the wing. Thus V_h/V

can be assumed simply to 1. C_{L_h} was calculated again with an empirical formula and set to -0.5833. Similarly, $C_{L_{A-h}}$ is simply found by subtracting C_{L_h} from the required lift coefficient $C_{L_{max,landing}}$. Landing was chosen because this is the most critical phase during a flight for controllability. Thus, for a necessary $C_{L_{max,landing}}$ of 2.3 taken from chapter 7, a $C_{L_{A-h}}$ of 2.8833 is needed.

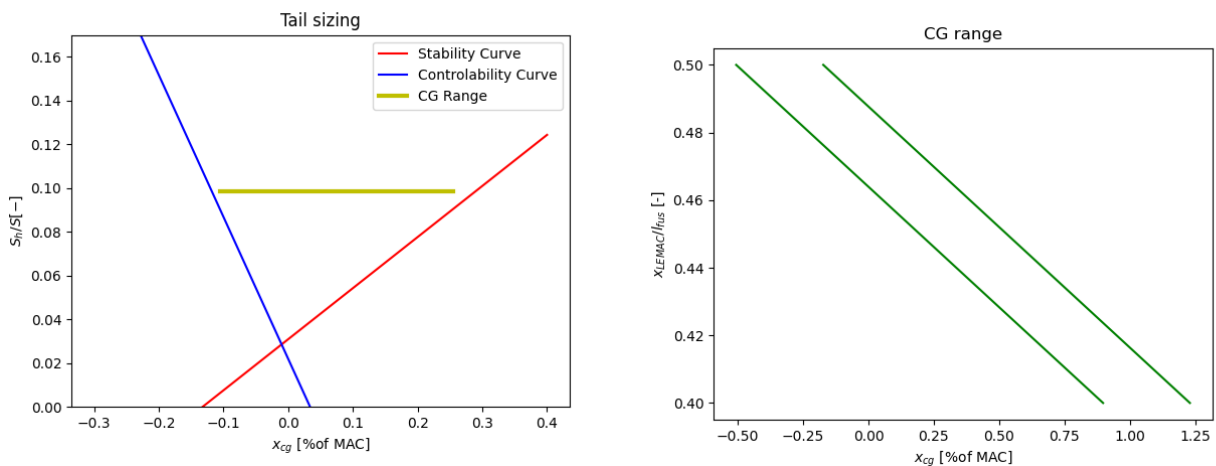
The aircraft moment coefficient $C_{m_{ac}}$ is affected by multiple parameters as follows:

$$C_{m_{ac}} = C_{m_{ac_w}} + \Delta_f C_{m_{ac}} + \Delta_{fus} C_{m_{ac}} + \Delta_{nac} C_{m_{ac}} \quad (8.8)$$

First, the wing influence will be considered using an empirical equation[42]. All the required parameters in this equation were already determined in chapter 7. Thus, for a $C_{m_{oairfoil}}$ of -0.04, AR of 22.79675 and Λ of -0.53816° , an influence of the wing towards the aircraft moment coefficient of -0.03677 is found. Next, the fuselage influence was found in the same way[42]. In its equation, $C_{L_{\alpha_{A-h}}}$ is different than the one calculated for stability as, now, landing is the critical phase. Lastly, C_{L_0} was again found from chapter 7 to be 0.33. All those values lead to a fuselage influence towards the aircraft moment coefficient of -0.12632. One last influence that has to be account is due to flaps. This was taken from an empirical estimation[42] for a necessary additional lift coefficient of 0.3 found in chapter 7. Thus, the flaps influence was found to be -0.09. Lastly, as the nacelles are very small and their estimation is very complicated, their effect is neglected. Concluding, the final moment coefficient found was -0.253087 which complies with the requirement as it is negative.

Last but not the least, the aerodynamic centre position \bar{x}_{ac} is required for both stability and control. The value for both conditions will be different as for control, landing is the critical situation while for stability, cruise is the critical situation. However, the same empirical formula will be used for both cases[43]. In this formula, the nacelles contribution and the windmilling propeller will be neglected as the propulsion system size is very small and thus their influence as well. In order to validate this assumption, a small test was done during the building of the program with preliminary values to quantify the actual influence. Fortunately, it was found that those changes affected the centre of gravity range very little. Moreover, the assumption is conservative so, with the help of the assumption, the horizontal tail area is slightly oversized. The wing influence $(\frac{\bar{x}_{ac}}{\bar{c}})_w$ was found from chapter 7 to be 0.25 of the MAC. Moreover, the fuselage contribution is given by another empirical formula[43]. With the parameters inputted, a fuselage influence for controllability of 0.2778 and for stability of 0.2993 which further gives an x_{ac} for controllability of -0.0324 and for stability of -0.0539.

With all the variables found, both curves can be plotted which will lead to an S_h/S value acceptable for the centre of gravity range previously found as can be seen in Figure 8.5a. In this graph, the wing was already placed after an intensive iteration process which will be explained more extensively later in its own subsection.



(a) Tail sizing graph for stability (red) and controllability (blue); the yellow line shows the CG range

(b) CG range as a function of LEMAC position

Figure 8.5: The two plots that were iterated to get the LEMAC, CG range and the tail sizing of the aircraft

8.3.1 Wing Placement

For the wing placement, the horizontal tail area calculations along with the centre of gravity placement had to be iterated to converge to the optimal horizontal tail area. The centre of gravity was plotted as a function of the leading edge of the mean aerodynamic chord (LEMAC). This led to [Figure 8.5b](#). As it can be seen, by moving the wing aft (increasing LEMAC), the CG range moves forward as it is a function of MAC.

By overlapping, [Figure 8.5b](#) and [Figure 8.5a](#) together, the optimal wing position is found in such way that the yellow line in [Figure 8.5a](#) fits between the red and blue lines in [Figure 8.5a](#) but also between the green line in [Figure 8.5b](#). The lowest S_h/S which fits the CG ranges perfectly is found to be at 0.098606 as plotted in [Figure 8.5a](#). This also includes a 15% safety margin for deep stall purposes, specific to T-tail aircraft but also a 5% margin for stability [43]. The final values after the iteration are summarised in [Table 8.8](#).

Table 8.8: Final Horizontal Tail Value

Parameter	Value	Parameter	Value	Parameter	Value
$\frac{\bar{x}_{ac}}{\bar{c}}$ (Land)	-0.0324	$d\epsilon/d\alpha$	0.15567	C_{L_h}	-0.5833
$\frac{\bar{x}_{ac}}{\bar{c}}$ (Cruise)	-0.0539	l_h	12.7584m	$C_{L_{A-h}}$	2.8833-
$C_{L_{\alpha_h}}$	4.327	V_h/V	1-	x_{LEMAC}	12.53983m
$C_{L_{\alpha_{A-h}}}$	6.5	C_{mac}	-0.25309	S_h/S	0.09861

8.4 Vertical Tail Sizing

In the midterm a preliminary sizing of the vertical tail was already performed. It was decided to design the aircraft with a T-tail configuration. To perform a more detailed aerodynamic design of the vertical tail for lateral stability of the aircraft, the vertical tail is sized on four main requirements. The requirements the vertical must satisfy are [44]:

- The aircraft shall be controllable when flying with a one engine-group inoperative.
- The aircraft shall be controllable when landing with cross winds of 30 knots.
- The aircraft shall be directional stable.
- The aircraft shall be controllable in a spiral manoeuvre.

To determine the size of the vertical tail for flying with one engine-group inoperative, the most critical engine-group failure should be determined. ECHO-1 is an aircraft with distributed propulsion over the wing, whereby the power is supplied to engine groups via separate electric cables for redundancy, as described in [subsection 6.3.2](#). Therefore, one engine-group inoperative is considered as most critical, which is located at the tip of the wing. Failure of an engine-group which is located at the tip of the wing causes the aircraft to yaw and roll due to the differential thrust. To counteract these moments the ailerons and rudder need to be deflected. During this analysis the aileron deflection neglected. The analytical expression can be derived given in [Equation 8.9](#).

$$\left(\frac{S_v}{S}\right)_{Inoperative} = \frac{1}{\eta_v C_{y_{v\alpha}}} \cdot \frac{C_L \frac{Y_e}{l_v} \frac{\Delta T_e}{MTOW} + \beta C_{n_{\beta_{A-H}}} \frac{b}{l_v}}{\tau_v \delta_r - (\beta - \sigma_v)} \quad \left(\frac{S_v}{S}\right)_{Crosswind} = \frac{1}{\eta_v C_{y_{v\alpha}}} \cdot \frac{\beta C_{n_{\beta_{A-V}}} \frac{b}{l_v}}{\tau_v \delta_r - (\beta - \sigma_v)} \quad (8.10)$$

From [Equation 8.9](#) a ratio of $\left(\frac{S_v}{S}\right)_{Inoperative}$ is found. However, some simplification were used, so is the side wash and side wash gradient of the aircraft neglected for the moment. Moreover, is a value for η_v assumed. To get to more accurate result the ECHO-1 must be tested in a wind tunnel. The next step is to size the vertical for crosswind landings, where crosswinds could have air speeds up

to 30 knots, the associate angle of side slip is then equal to 15 degrees. To size the vertical tail for crosswind landing Equation 8.10 can be used. When both ratio's of $\left(\frac{S_v}{S}\right)_{Inoperative}$ and $\left(\frac{S_v}{S}\right)_{Crosswind}$ are determined a range is obtained, the upper limit should selected to verify if the aircraft is directional stable.

To calculate the directional stability coefficient C_{n_β} of an aircraft Equation 8.11 is used. The aircraft is stable when C_{n_β} is larger than zero. Resulting into that the aircraft is turned into the airflow when the aircraft experiences a slide slip angle. When the stability coefficient is smaller than zero the initial requirement is not met. Therefore, is the upper limit of the surface area ratio slightly increased until the requirement is satisfied. During the design of ECHO-1 it was decided that the entire aircraft should at least have $C_{n_\beta} > 0.08$ to have a slight safety margin.

To determine the contribution of fuselage, wing and propellers to directional stability empirical formulas have been used[40]. The contribution of the wing is assumed to be a constant, which has a value of $C_{n_{\beta_w}} = -0.017$. Once again wind tunnel test need to be performed to obtain more accurate values.

$$C_{n_\beta} = C_{n_{\beta_{A-H}}} + \eta_v C_{y_{v\alpha}} \frac{S_v l_v}{S b} \left(1 - \frac{d\sigma_v}{d\beta}\right) \left(\frac{V_v}{V}\right)^2 > 0 \quad (8.11)$$

From the Equation 8.9, Equation 8.10 and Equation 8.11, three values for $\frac{S_v}{S}$ are obtained, which are presented in Table 8.9.

Table 8.9: The Required Surface Area for the Vertical Tail

Surface Area ratio	Value
$\left(\frac{S_v}{S}\right)_{Inoperative}$	0.16
$\left(\frac{S_v}{S}\right)_{Crosswind}$	0.06
$\left(\frac{S_v}{S}\right)_{Directional-Stability}$	0.23

At last, the aircraft should be controllable when accidentally entered in a spiral and the vertical tail is experiencing a airflow of 45 degrees from below. At this point the aircraft is only controllable if the rudder is not in the wake of the horizontal tail and thus experiences some free airflow. Therefore, it is required to have at least one-third of the rudder area to remain outside of the wake of the horizontal tail, when experiencing an angle of attack of 45 degrees. However, for the design of ECHO-1 a T-tail is considered and thus no problems will occur when fulfilling this requirement.

To conclude, from Table 8.9 it can be obtained that directional stability is the most critical case for the sizing of the vertical tail, since the largest area is required. Therefore, is an $\left(\frac{S_v}{S}\right)$ of 0.23 required for the design of ECHO-1. To verify this value windtunnel test need to be performed.

8.5 Landing Gear Sizing

In order to have a stable aircraft on ground, the extended CG from Table 8.5, including the shift due to batteries will be considered for the landing gear design. To make the aircraft also stable when the battery package of the aircraft is replaced. Furthermore, it is worth mentioning that a tri-cycle landing configuration was chosen with the nose wheel below the cockpit and the two main landing gear just aft the wing.

The first step in the design of the landing gear is the determination of nose and main landing gear x-positions. There is a requirement on the nose landing gear that it should not be carrying more than 15% of the MTOW and also not less than 8% of MTOW in order to have enough grip for an efficient

turn on ground. In the end, 15% of the MTOW is carried by the nose landing gear and 85% is carried by the main landing gear. With both the most forward and most aft CG points, the nose landing gear was placed at 1.86 m and the main landing gear at 14.23 m from the nose of the aircraft.

The second step performed was the check if the tip back angle given by the tail configuration is satisfied. This requirement imposes the aircraft not to touch the ground even for a tip back angle of 15° . This requirement was checked for both the end of the aircraft as well as the start of the tailcone. Both requirements were satisfied and led to a height of the aircraft end point of 66.5% of the fuselage outer diameter starting from the belly of the fuselage. Moreover, the height of the fuselage (distance between the ground and the belly of the fuselage) was found to be 1.4705 m. In this step it was also checked whether the main landing gear is placed aft enough from the aft centre of gravity even for the aircraft inclined at the tip-back angle. In other words, it was checked that the angle between the z-direction line from the main landing gear and the line between most aft CG point and main landing gear is higher than 15° . This requirement was met as well.

The third step was focused on the y-position of the main landing gear. The purpose of this positioning is in order not to allow the aircraft to tip when it turns. The main requirement that needs to be met is the tipover angle $\psi < 55^\circ$. This will lead to a y-position of the main landing gear from the CG of 2.33 m. Thus the distance between the main landing gears is 4.66 m. Since the main landing gear is located 0.9 m outside the fuselage on both sides a fearing is required. Whereby, the strut of the landing gear is fixed in the fearing and when retracted the wheels are stored in the belly. Moreover, this step has also been verified by checking if the clearance angle between the main landing gear and the tip of the wing is greater than 5° .

The fourth and last step performed in the landing gear sizing was the design of the wheels. For this, it was found using statistical data that for a MTOW of 20937 kg, a load classification number (LCN) of 24 is required. Moreover, also statistically, it was found that the tire pressure should be 7.12 kg/cm^2 . In order to find the required wheel dimensions, the load on each wheel is required. It was already assumed that the main landing gear does not have to carry more than 92% of the MTOW while the nose landing gear no more than 15% of the MTOW. Moreover, 2 wheels were considered for each gear. Thus, for main landing gear 4 wheels are taken while for nose landing gear, 2 wheels. Those assumptions lead to a main landing wheel load of 5221 kg and to a nose landing wheel load of 1702.5 kg. For sizing of the main landing gear wheels an empirical figure[43] is used. An outer diameter of 0.8382 m, an inner diameter of 0.4064 m and a width of 0.24765 m is required. For the nose landing gear wheels, an outer diameter of 0.4826 m, an inner diameter of 0.2032 m and a width of 0.1524 m is required. To summarise, the most important values of this section are presented in [Table 8.10](#).

Table 8.10: Dimensions for the landing gear sizing

Parameter	Length m	Parameter	Length m	Parameter	Length m
x_{mlg}	1.8564	h_{ground}	1.4705	w_{mlg}	0.24765
x_{nlg}	14.232	$h_{tailcone_{end}}$	3.344	d_{nlg}	0.4826
y_{mlg}	2.3296	d_{mlg}	0.8382	w_{nlg}	0.1524

8.6 Control Surfaces

With all the geometry determined, the design of more detailed systems can start. For the aircraft to yaw, roll or pitch, control surfaces are required. Thus, presenting a preliminary calculation of the dimensions of these surfaces will be done in this section. Firstly, for roll control, the area of the ailerons will be calculated. Secondly, for pitch control the elevator dimensions will be presented and lastly, the same will be done for rudder.

8.6.1 Aileron

The main requirement of the aileron is that it should provide enough roll performance to the aircraft. For medium-weight, low-to-medium manoeuvrability aircraft (Class-II aircraft), the aircraft shall produce a roll of 45° in 1.4s. In order to calculate the roll rate, the following equation is used:

$$P = -\frac{C_{l_{\delta a}}}{C_{l_p}} \delta a \left(\frac{2V}{b} \right) \quad (8.12)$$

where V is the approach speed value of 72.02 m/s as landing is the most critical phase. δa can be set to a maximum value of 30°. However, looking at similar aircraft, and to take into account the aileron reversal effect, a conservative value of 20° will be assumed. Moreover, as differential ailerons are preferred, this value is the average between the right and left aileron deflection angles. The ratio of the deflection angles is usually 0.75[45] so the maximum upward deflection should be 22.86° while the maximum downward deflection should be 17.14°. Also, there are still some parameters in Equation 8.12. $C_{l_{\delta a}}$ is found through:

$$C_{l_{\delta a}} = \frac{2C_{l_{\alpha}}\tau}{Sb} \int_{b_1}^{b_2} (c(y)ydy) \quad (8.13)$$

where $C_{l_{\alpha}}$ is set at 2π and τ at 0.57 for an aileron to wing chord ratio of 0.35[46]. Lastly, the integral is done using the chord length function along the wingspan from the start of the aileron b_1 till its end b_2 . Similarly to the rolling moment coefficient due to aileron, the roll rate also has an influence on the moment coefficient as can be seen below:

$$C_{l_p} = \frac{4(C_{l_{\alpha}} + C_{d_0})}{Sb^2} \int_0^{b/2} (c(y)y^2dy) \quad (8.14)$$

The only new parameter that has been added to this equation is c_{d_0} set at 0.0071. Summing everything up in Equation 8.12 and imposing that the roll rate has to be larger than 45° in 1.4 s, the aileron dimensions can be found. Moreover, by considering the truss connection to the wing, the aileron was assumed to start at 40% of the wingspan. This value was chosen so close to the truss location in order to reduce the possible aileron reversal as this phenomenon is predominantly found especially at wings with high aspect ratios. With this in mind, an aileron span of 26% of the wing span and an aileron area of 4.81862 m² were determined. A redesign might be necessary in the future focused on the structure of the wing. This is mainly in order to check if the aileron surface can be minimised and the aileron moved more to the tip.

8.6.2 Elevator

An analysis of the elevator surface is also required. One of the main reasons for the design is because, compared to other aircraft, the horizontal tail area was found to be very small. Thus a check to see if it complies with the required pitch angular acceleration in order to lift the aircraft for take-off is necessary. According to Al-Shamma et al.[46], the required take-off pitch angular acceleration for a regional aircraft is between 6 and 8 °/s². Moreover, especially for T-tail, the elevator usually spans along the entire horizontal tail and the maximum deflection angle is 25° to avoid flow separation which will lead to horizontal tail stall. The last parameter that can be chosen is the elevator chord to horizontal tail chord ratio. This should not be higher than 0.34 as, otherwise, a full horizontal tail movement might become more beneficial. Therefore, the ratio will be initialised with 0.34 as full tail movement are specific to aircraft with very high manoeuvrability and not commercial aircraft. In order to see how much pitch angular acceleration can the elevator produce with this configuration, the following moment equilibrium equation will be used:

$$M_{wing} - M_W - I_{yy}\ddot{\theta} = L_h(x_{ac_h} - x_{mlg}) \quad (8.15)$$

From this equation, L_h will be calculated to see how much lift can the tail produce. This moment equation is done around the main landing gear as this is the point around which the aircraft must

rotate during landing. Thus all the lengths, for example the aerodynamic centre of the horizontal tail position x_{ac_h} , are reported to this point x_{mlg} . Also, I_{yy} (along the wings) was assumed to be 266967 m^4 which is the value of ATR-72 aircraft¹. In the moment equations, the airspeed should be the rotation speed V_r which was found to be approximately around 1.3 of the stall speed (so it was assumed equal to approach speed)², the lift coefficient is set to design lift coefficient. For the weight moment, the most forward CG point was selected as this will lead to the most critical condition. Last but not the least, the horizontal tail lift was found using the lift formula where the horizontal tail lift coefficient C_{L_h} is found through:

$$C_{L_h} = C_{l_{\alpha_h}} i_h + C_{l_{\alpha_h}} \tau \delta_{e,max} \quad (8.16)$$

In this equation, $C_{l_{\alpha_h}}$ is set to 2π as a symmetric airfoil was chosen, i_h to 0° in order to reduce the aircraft drag and τ to 0.56, for a chord ratio of 0.34. Summing everything up, a pitch angular acceleration of $13 \text{ }^\circ/\text{s}^2$ was determined, for the horizontal tail, which is even more than the interval previously established. However, the calculations are not complete at the moment. As it was seen, only the weight, wing lift and horizontal tail moment were considered. In the future, better results can be found if other forces are also considered like drag or thrust.

8.6.3 Rudder

In order to yaw an aircraft, a rudder is necessary. However, as this control surface is not very critical for an aircraft³ (as the wings have no sweep, the dynamic stability is even less concerning that other commercial aircraft) and the values found in section 8.4 comply with other existing aircraft, it was decided to estimate the rudder dimensions and not enter into too much detailed calculations. Thus, taking the values from [47], a rudder to vertical tail area ratio of 0.2 and chord ratio of 0.25 were imposed. As it was already specified, those values are just some estimated so more detailed design calculations will be required.

8.7 Verification and Validation

In order to check if the code calculates what it should, verification will be done. Validation will be performed in order to test if the model outputs realistic results. Those two steps will be performed as suggested in section 3.5. For verification all the tests passed as can be seen in Table 8.11. Most of them were either input checks or calculation checks. This is because this chapter relies a lot on equation implementation.

¹http://atr.flight1.net/forums/moments-of-inertia_topic5186.html

²<http://www.aerodynamics4students.com/aircraft-performance/take-off-and-landing.php>

³<https://www.tsb.gc.ca/eng/rapports-reports/aviation/2005/a05f0047/a05f0047.html>

Table 8.11: Performed Unit Tests for Geometry Scripts

Nr.	Name	Type	Parameters	Passed
1	Fuselage Dimensions	Hand calculation	$W_{ground}, W_{headroom}, L_{cabin}, L_{Fuselage}, L_2$	Yes
2	Fuselage Parametrization	Hand calculation	$W_{ground}, W_{headroom}, L_{cabin}, L_{Fuselage}, L_2$	Yes
3	Import System Values	Check inputs	$MAC, S, b, \Delta T_e, Y_e, L_{Fuselage}$	Yes
4	Aid Function Calculation	Hand calculation	$x_{cg_{cargo}}, x_{cg_{battery}}, x_{cg_{pax}}$	Yes
5	CG Calculation	Hand calculation	$x_{cg_{fwd}}, x_{cg_{aft}}$	Yes
6	CG Excursion	Hand calculation	$x_{cg_{fwd}}, x_{cg_{aft}}$	Yes
7	Stability & Control Calculation	Hand calculation	$\bar{x}_{ac}, \bar{C}_{L_{\alpha_h}}, \bar{C}_{L_{\alpha_{A-h}}}, C_{m_{ac}}, d\epsilon/d\alpha$	Yes
8	Horizontal Tail Calculation	Hand calculation	$S_h, x_{LEMAC}, x_{cg_{fwd}}, x_{cg_{aft}}$	Yes
9	Vertical Tail Calculation	Hand calculation	$S_v, C_{n_{\beta}}$	Yes
10	Landing Gear Calculation	Hand calculation	$x_{mlg}, x_{nlg}, y_{mlg}, h_{ground}$	Yes
11	Control Surfaces Calculation	Hand calculation	P, θ, S_a, S_e, b_a	Yes

Validation will be performed a little different compared to verification. As most of the values determined during this chapter are found empirically or statistically, there is no software to actual check it. On the other hand, a comparison with similar aircraft like ATR-72 or Embraer ERJ145 will be performed as the empirical formulas used are based on these aircraft's data. However, the results cannot be completely confirmed as there exists no electric commercial truss braced wing aircraft but the differences can be slightly quantified.

For the length of the fuselage, the ERJ145 aircraft was considered as the comparison aircraft. This is because it can carry 50 passengers and they are divided in a 3-seat abreast configuration. The ERJ145 has a fuselage length of 25.7m (compared to ECHO-1 26.63m) and an outer diameter of 2.69m (compared to ECHO-1 2.82m)[48]. The main reason for the overestimated values of ECHO-1 are the Venturi requirements. For example, it was found that the passengers cabin length for ECHO-1 should be 13.23 m while for ERJ145 it was set at 12.6m. Similarly, for the diameter, a ground floor width of 2.22m was calculated for ECHO-1 while for ERJ145 it is 2.03m. Also the fuselage thickness was increased for ECHO-1 from 0.08m to 0.1m.

Regarding the rest of the systems designed in this chapter, they will be compared with the ATR-72 as all the systems depend on the CG and MTOW for whom the values are very similar with ECHO-1. Fortunately, the values were not extremely different. The biggest difference was observed for the horizontal tail. The ECHO-1 had an horizontal tail area of 5.61m² compared to ATR-72's value of 10.76m²[49]. This huge differences is caused by multiple factors. Firstly, for ECHO-1, the tail was optimized as much as possible such that the CG range fits perfectly between the limits. Secondly, the CG range of ECHO-1 is a lot smaller than for the ATR-72. The main reason behind this is that batteries were included in OEW and are not changing the CG range for tail design as fuel is doing for combustion aircraft. Thirdly, the moment coefficient was found to be very small as, its main contributor, the flaps, are not having such a great influence in the end as the ΔC_L needed is small. Thus, the tail size was expected from the beginning to be a lot smaller than other aircraft. For the other parameters, pretty similar values were found. As already said, x_{LEMAC} and the CG range were imposed by the tail sizing, thus an accurate comparison cannot be made with other aircraft. However, the values are still very close[49]. Similarly, the vertical tail area was found to be very close with a value for ECHO-1 of 13.19 m² compared to ATR-72 tail area of 14.08 m²[49]. The smaller value might be caused by the slightly lower influence of the fuselage which is smaller.

Next, the landing gear was compared with ATR-72 and the values were found to be extremely cost. There were 2 parameters that seemed a little bit off. First of them was the y_{mlg} which was positioned

outside the fuselage. The same case was for the ATR-72 where it also brought the necessity of building a fairing. Fortunately, the difference was very close as the y_{mlg} was found to be 2.3 m for ATR-72[49] and 2.33 m for ECHO-1. The second value that seemed unexpected high was the diameter of the main landing gear (ECHO-1 has a value of 0.84m). Again, it was proven that the value was actually realistic as the main wheel diameter of the ATR-72 was found to be 0.86 m[50]. The last system that was considered was the control surfaces. The rudder and elevator dimensions were inputted using recommended values from similar aircraft[46].

8.8 Recommendations

Most of the systems that determine the aircraft geometry have been designed in a detailed way, however there is always room for improvement. Thus, as a future recommendation for design procedure, more detailed formulas will be necessary for better results. For example, for fuselage design, the structure of the aircraft can be taken into account and the dimensions optimised based on this. Similarly, for CG positioning, all the system's centre of gravity (fixed equipment, tail etc.) and weight can be optimised as well. To add, there are assumptions which need to be quantified at a later stage. For example, in the horizontal tail sizing, the effect of the nacelles were ignored. Also, for the vertical tail, the side wash was neglected. To verify the surface-area ratio wind tunnel test need to be performed. Some more detailed insight should be performed for rudder and elevator sizing. At the moment, a lot of assumptions have been made and only some rough calculations have been performed. Moreover, for a better performance, it should be studied if the main landing gear can be aligned with truss.

9

Dynamic Stability Analysis

After the geometry and sizing focused on static stability was performed, one factor that is still critical for an aircraft was not checked. This refers to the dynamic stability, which determines how the aircraft reacts to different inputs. In order to check this important requirement, first the dynamic coefficients of ECHO-1 are found in section 9.1. Next, the eigenvalues of the equations of motions and the behaviour of the eigenmotions will be shown and analysed in section 9.2. Lastly, verification, validation and some recommendations are presented in section 9.3.

9.1 Dynamic Coefficients

Dynamic coefficients are the parameters that describe the 3D air movement and control of the aircraft. These coefficients are usually obtained from the forces that act on the aircraft to different inputs and were taken from a XFLR5 simulation. By inputting the dimensions calculated in chapter 7 and chapter 8, the following values are obtained and summarised in Table 9.1.

Table 9.1: Dynamic stability coefficients of ECHO-1

Coefficient	Value	Coefficient	Value	Coefficient	Value
C_{X_0}	0	C_{Z_0}	-0.56797	C_L	0.565
C_{X_u}	-0.0006776	C_{Z_u}	-8.4089e-06	C_{m_u}	4.1887e-11
C_{X_α}	0.12371	C_{Z_α}	-6.5801	C_{m_α}	-8.3791
C_{X_q}	0	C_{Z_q}	25.438	C_{m_q}	-137.68
C_{Y_β}	-0.59651	C_{l_β}	-0.024631	C_{n_β}	0.20784
C_{Y_p}	-0.020069	C_{l_p}	-0.697794	C_{n_p}	-0.013235
C_{Y_r}	0.45178	C_{l_r}	0.068713	C_{n_r}	-0.15925

9.2 Eigenmodes Analysis

In this table, the coefficients are simply derivatives. The first subscript refers to force or moment as follows: X is the force in x-direction, Y is the force in y-direction, Z is the force in z-direction, l is the rolling moment around the x-axis, m is the pitching moment the y-axis and n is the yawing moment around the z-axis. The second subscript refers to the parameter with respect to which the derivative is made. Thus, α is the angle of attack, u is the speed along the x-direction, q is the pitching velocity and 0 refers to the weight coefficient at initial condition. For the asymmetric coefficients, β is the sideslip angle, p is the rolling velocity and r is the yawing velocity. Moreover, in Table 9.1, also C_L is shown as it will be used later and represents the design lift coefficient. All these values were inputted in the aircraft analytical non-dimensional equations of motion (EOM). Firstly, the symmetric EOM will be presented in the state-space form[51]:

$$\begin{bmatrix} C_{x_u} - 2\mu_c D_c & C_{x_\alpha} & C_{Z_0} & C_{X_q} \\ C_{z_u} & C_{Z_\alpha} + (C_{Z_{\dot{\alpha}}} - 2\mu_c)D_c & -C_{X_0} & C_{Z_q} + 2\mu_c \\ 0 & 0 & -D_c & 1 \\ C_{m_u} & C_{m_\alpha} + C_{m_{\dot{\alpha}}}D_c & 0 & C_{m_q} - 2\mu_c K_{yy}^2 D_c \end{bmatrix} \cdot \begin{bmatrix} \hat{u} \\ \alpha \\ \theta \\ \frac{q\bar{c}}{V} \end{bmatrix} = \begin{bmatrix} 0 \\ 0 \\ 0 \\ 0 \end{bmatrix} \quad (9.1)$$

Most of the coefficients in this equation are already known but some new ones appear as well. D_c is the non-dimensional time derivative equal to $\frac{\bar{c}}{V} \frac{d}{dt}$. μ_c is the non-dimensional mass equal to $\frac{MTOW}{\rho S \bar{c}}$. K_{yy}^2 is the non-dimensional aircraft moment of inertia around the y-direction I_{yy} (set to 266967 m^4)¹. This coefficient is equal to $\frac{I_{yy}}{m\bar{c}^2}$. The state vector also contains new parameters: \hat{u} is the non-dimensional x-direction velocity (divided by flow airspeed), α is the angle of attack, θ is the pitch angle and the pitching velocity q is made non-dimensional. One important observation is that the coefficients with respect to derivative parameters could not be calculated by XFLR5. Thus, the coefficients $C_{Z_{\dot{\alpha}}}$, $C_{m_{\dot{\alpha}}}$ were initialised with 0. Similar to Equation 9.1, the asymmetric EOM can be seen below[51].

$$\begin{bmatrix} C_{Y_\beta} + (C_{Y_{\dot{\beta}}} - 2\mu_b)D_b & C_L & C_{Y_p} & C_{Y_r} - 4\mu_b \\ 0 & -\frac{1}{2}D_b & 1 & 0 \\ C_{l_\beta} & 0 & C_{l_p} - 4\mu_b K_{xx}^2 D_b & C_{l_r} + 4\mu_b K_{xz} D_b \\ C_{n_\beta} + C_{n_{\dot{\beta}}}D_b & 0 & C_{n_p} + 4\mu_b K_{xz} D_b & C_{n_r} - 4\mu_b K_{zz}^2 D_b \end{bmatrix} \cdot \begin{bmatrix} \beta \\ \phi \\ \frac{p\bar{b}}{2V} \\ \frac{r\bar{b}}{2V} \end{bmatrix} = \begin{bmatrix} 0 \\ 0 \\ 0 \\ 0 \end{bmatrix} \quad (9.2)$$

Again, in Equation 9.2 some new parameters appeared. D_b and μ_b are very similar to D_c and μ_c but made non-dimensional using the wing span instead of the wing chord. K_{xx}^2 and K_{zz}^2 are calculated similarly to K_{yy}^2 but again made non-dimensional using the wing span instead of the wing chord. In the equation, I_{xx}^2 is set to 114860 m^4 and I_{zz}^2 to 279890 m^4 , both ATR72 values². K_{xz}^2 is the product moment of inertia related to I_{xz} but it was set to 0 as the aircraft is assumed to be symmetric and more accurate values could not be found. Next, in the state vector, β is the sideslip angle, ϕ is the roll angle, p is the rolling velocity and r is the yawing velocity while the derivatives $C_{Y_{\dot{\beta}}}$ and $C_{n_{\dot{\beta}}}$ are initialised with 0.

In order to analyse the dynamic stability, the derivative coefficients D_c and D_b are substituted by eigenvalues λ_c and λ_b and the determinant is calculated. The solution of the resulting equation leads to the eigenvalues for symmetric and asymmetric EOM, which are specific to different dynamic modes. These are summarised in Table 9.2 where other important parameters (period T , damping coefficient ζ and time to half amplitude $t_{1/2}$) are shown as well.

¹http://atr.flight1.net/forums/moments-of-inertia_topic5186.html

²http://atr.flight1.net/forums/moments-of-inertia_topic5186.html

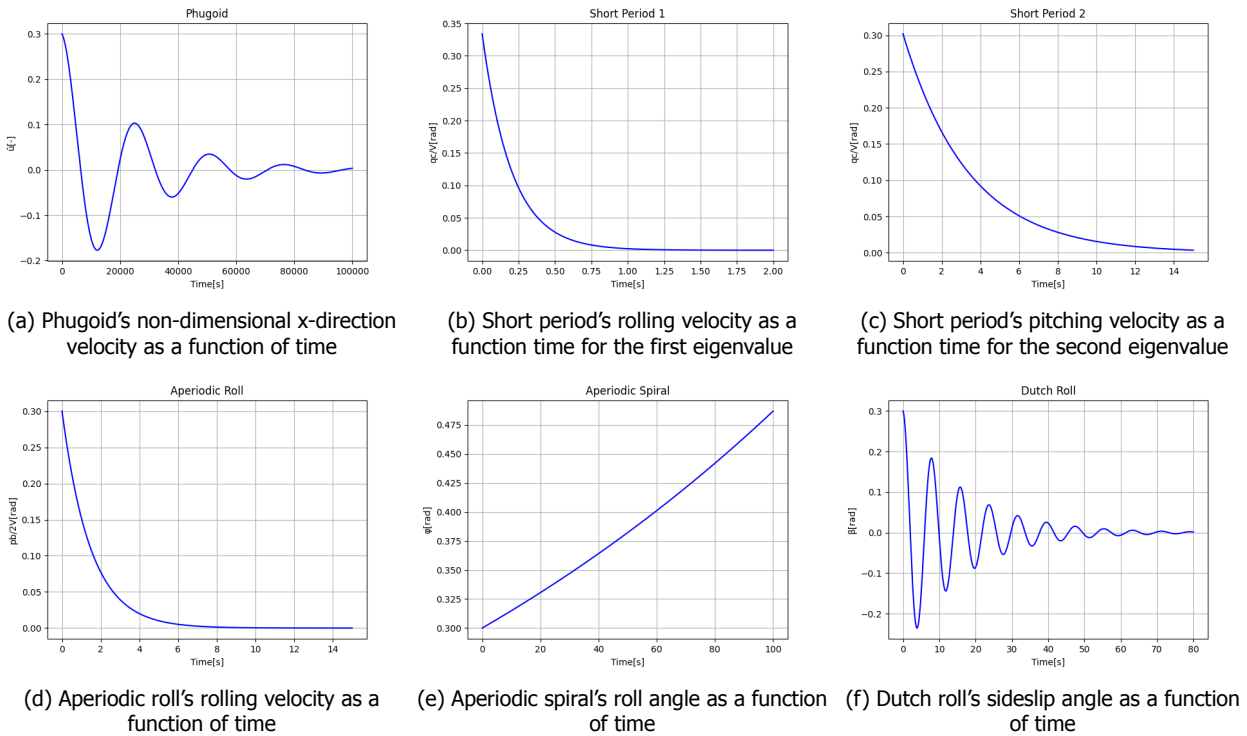


Figure 9.1: Different parameters response to input for the dynamic eigenmodes of an aircraft

Table 9.2: Eigenvalues of the dynamic modes of ECHO-1

Parameter	Phugoid	Short Period	Aperiodic Roll	Aperiodic Spiral	Dutch Roll
Eigenvalue	$-5.08517e-07 \pm 3e-06j$	$-0.07686; -1.28722$	-0.171326	0.001295	$-0.18332 \pm 2.1272j$
$T[s]$	25279	-	-	-	2.93574
$t_{1/2}[s]$	16444	0.1088	4.04492	-	3.78015
$\zeta[-]$	0.16718	-	-	-	0.08586

With the values found, some plots showing the behaviour of the aircraft to different disturbances were drawn. Thus, starting with a fixed input (0.3), plots were made for each eigenmode as seen in Figure 9.1. In order to have a stable aircraft, the real part of all the eigenvalues should be negative. As it can be observed, only one value is not positive and this corresponds to the aperiodic spiral mode. Thus, for this eigenmode, the response will increase in time as it can be seen in Figure 9.1e. Fortunately, because the eigenvalue is very small, the increase in time is also very big (in order to double the roll angle, a time (t_2) of 535s should pass). For this reason, the divergence of this eigenmode is not considered critical as most aircraft usually develop a tightening spiral-dive [52]. However, there are a few ways to solve this problem. In mathematical terms, the problem is that C_{n_β} and C_{l_β} are too high. Thus, by decreasing these values, the aperiodic spiral might become stable. Nonetheless, making it too stable might affect the stability of dutch roll so the changes should be limited. To decrease C_{n_β} , the area of the vertical tail can be decreased or the centre of gravity can be moved aft to increase the influence of the fuselage. In order to decrease C_{l_β} , a positive sweep or dihedral angle can be applied to the wing. However, increasing the sweep angle should also increase C_{n_β} so the effect is neutral. To conclude, a smaller vertical tail and a higher dihedral angle should help.

The other eigenmodes are stable. However, the results might be wrong as a lot of assumptions have been made. At a first glance, the dutch roll and the aperiodic roll values and plots seem correct. On

the other side, phugoid eigenvalues seem too small and the plot time span too large. The reason for these results might be the horizontal tail area which is very small compared to other aircraft and thus, the motion damps for a very long time. Similarly, the short period results do not look correct. The short period should have had an oscillation response (a lot more damped than phugoid) but not a perfect convergence. Thus, complex eigenvalues were expected but 2 real eigenvalues were obtained and a plot was made for each of them. A reason for this behaviour might be the multiple assumptions and neglects made throughout the calculations, for example, neglecting the derivative coefficients or the moment of inertia assumptions. Moreover, XFLR5 dimensions might be as well wrong. The main reason that could lead to the mistakes is the ignorance of the fuselage and truss. The truss could not be inputted in XFLR5 program while the fuselage would give very bad results. This might explain the discrepancy between the empirical value for $C_{n_{\beta}}$ (0.08) and the XFLR5 one (0.20784).

9.3 Verification, Validation and Recommendations

Verification and validation was also considered for this chapter. The code that calculated all the values and plotted the results was verified and validated intensively in the past[53]. Now, minor verification tests were performed mainly to check if the inputs are correctly implemented. Moreover, the dynamic stability coefficients obtained from XFLR5 were already validated. The conclusion stated that all the results are consistent and that the differences are within the error margin expected[54]. However, these results were not confirmed with the empirical estimations, as specified before.

As a recommendation, more refine work should be performed in the future on dynamic analysis and a vertical tail redesign might be necessary for making the aperiodic spiral eigenmode stable. Similarly, XFLR5 data might not be extremely trustworthy. As for $C_{n_{\beta}}$, differences might exist also for other coefficients but could not be quantified at this stage. Thus, a better analysis is required like, for example, the other coefficients can be calculated empirically or values can be taken from similar aircraft. Or, lastly, a better software tool can be used for more accurate values.

10

Structural Analysis

In this chapter the structural design of ECHO-1 will be discussed. For the final design it was chosen to design a truss-braced wing which can achieve an impressive L/D but there are some structural challenges. Modelling and sizing the wing with truss will be discussed in [section 10.1](#). The decision on the materials for the wing box will be made in [section 10.2](#). Furthermore, it will be estimated what the additional mass is due to the batteries in the belly of the aircraft, this will be discussed in [section 8.1](#). To add, a vibrational analysis will be performed in [section 10.4](#). Lastly, the verification and validation of the programs written will be discussed in [section 10.5](#).

10.1 Modelling Wing with Truss

In this section the wing with truss will be modelled and an optimised wing box structure will be computed. This will be done by first indicating all assumptions taken in [subsection 10.1.1](#), then the load cases will be described in [subsection 10.1.2](#). The method used to get an optimised wing box will be explained in [subsection 10.1.3](#). The program that will be used for the analysis is explained in [subsection 10.1.4](#). Furthermore [subsection 10.1.5](#), [Table 10.1.5](#) and [subsection 10.1.6](#) will describe methods to calculate wing box failure modes not covered in the program used.

10.1.1 Assumptions

- It is assumed that the lift force acts in the centre of pressure of the wing.
- The wing is modelled as a beam.
- The weight of the propellers and the electric motors do not add any torque. Since the torque

caused by the weight of the electric motors will counteract the torque due to lift, the total torque on the wing will be slightly overestimated.

- Forces parallel to the flight direction are not analysed.
- Single material is used for the wing box. This assumption was made for simplicity. A wing box could have multiple materials, but, in that case, in the design, the connection between two different materials should be accounted for.
- Shear loads are carried by the spars. This assumption leads to an overestimation of the shear loads in the spar since actually the skins will also carry some of the loads.
- Thin walled assumption is used. Since the thickness is an order of 100 smaller than the height, the thin walled assumption will be used when computing moments of inertia.
- Stringers modelled as point areas. Due to the small size of the stringer, their individual moment of inertia is negligible compared to their Steiner term. With this assumption the actual moment of inertia is slightly underestimated which means that higher stresses are allowed in the wing box. However, this extra stress is very small compared to the other elements.
- For shear and torque calculations, wing box is analysed as a rectangle, this assumption leads to a slight underestimation of the forces. However, the real wing box shape is very close to a rectangle as well, therefore the effects are small.

10.1.2 Load Cases

For the design of the wing with truss, two critical load cases will be analysed, during flight and during on ground operations. The description of the load cases can be found below.

- **Load Case 1:** Manoeuvring the aircraft at MTOW with an ultimate load factor of 3.75 at sea level. Due to this high load factor the wing and truss should be designed to carry the lift force.
- **Load Case 2:** Performing on ground operations at MTOW such as taxiing. Because there is no lift during on ground operations the wing and truss have to be designed to carry only the weight of the wing itself and the engines.

The free body diagrams will be provided for each of the critical load case. The free body diagram for load case 1 is presented in [Figure 10.2](#), and the free body diagram for load case 2 is presented in [Figure 10.3](#).

10.1.3 Method

In order to model the wing with truss, a program will be build to calculate stresses and deflections in the wing and truss. Anastruct ¹ will be used to build a model of the wing. With the use of this program, the wing with truss can easily be modelled using a lot of trusses in Anastruct. Furthermore, different kinds of supports can be chosen and all kinds of loads can be selected. The way the wing has been modelled in Anastruct will be explained in [subsection 10.1.4](#). With the use of build-in functions in Anastruct, bending moments, shear forces, axial forces and deflections can be computed in the complete structure. Although Anastruct can calculate the aforementioned forces and moments, there are also some extra functions written to calculate the actual stresses, moment of inertia, torque, twist angle and buckling behaviour to make the model more complete. These extra functions will be integrated into the Anastruct model. With the use of the complete model, an optimization program will be written to optimise the layout of the wing box, this procedure will be explained in [subsection 10.1.9](#). The optimization will be made for the lightest wing box meeting all the requirements set.

10.1.4 The Model and Anastruct

As said before, the program used to calculate the deflections and thus the stresses in the wing box is Anastruct. Anastruct is a python implementation of a 2D finite element method in order to calculate

¹<https://anastruct.readthedocs.io/en/latest/installation.html>

stresses and deflections in beams and trusses. Anastruct is a discretization of beams which means that it uses the beam theory to calculate bending stresses and deflection for each of the smaller beams. The way Anastruct is set up, is by modelling a structure consisting of various beams which are connected to each other and can thus transfer loads between them. If different connected beams are used for the model of one larger structure, the different beams allow for varying MOI's, material properties and dimensions along the structure. This property of Anastruct is critical for the analysis of the wing box because, in reality, internal moments of the wing box are not constant and thus the wing box must be designed taking this different moments and loads into account to prevent over- or under designing.

The main wing without truss, is modelled as various connected beams with varying MOI along the wingspan. In order to prevent the main wing from transferring massive moments to the fuselage, the connection of the wing and truss to the fuselage is done using pinned connections. It is not beneficial for the fuselage to carry a lot of bending stress and thus the massive bending moments in the wing must not be transferred to the fuselage. Furthermore, in order to prevent bending moments in the truss, this is hinged to the main wing which makes the truss only axially loaded. However, if this hinge is placed in somewhere in the wing, this hinge prevents the transfer of bending moments from the outer to the inner part of the wing. An idealisation was then made by having a little vertical beam going from the end of the truss with a hinge connection, to the main wing with a fixed connection. This idealisation and the dimensions of the truss and wing can be seen in [Figure 10.1](#).

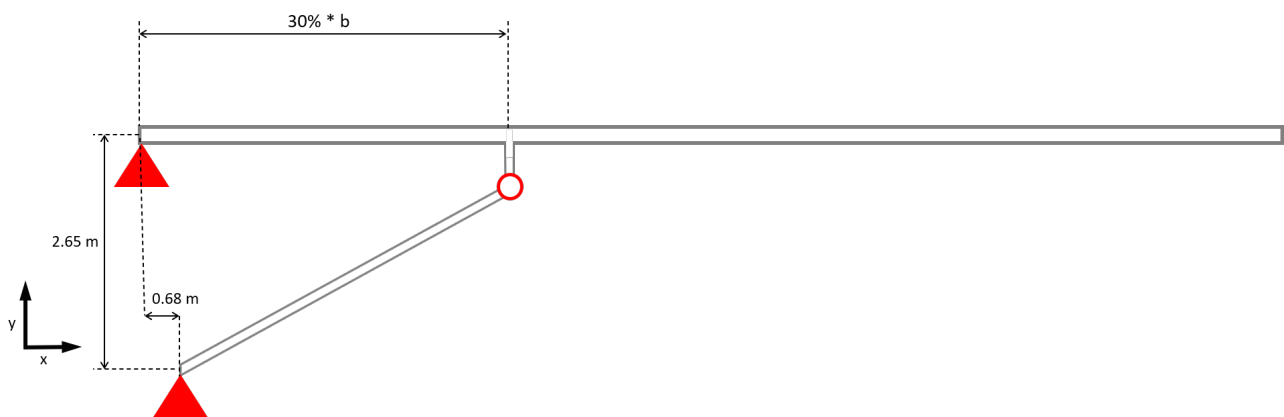


Figure 10.1: Geometric model of the wing and truss used in Anastruct

The FBDs for load case 1 and load case 2 can be seen in [Figure 10.2](#) and [Figure 10.3](#) respectively. In these FBDs, the loads which are analysed can clearly be seen and they are the lift, the weight and the torque of the engines and the weight of the wing itself. Anastruct divides the wing into different smaller beams, called elements, which are connected by nodes. Anastruct can only apply forces on the nodes and no distributed forces on the elements. For this reason, all the distributed loads are modelled as separate forces applied at the nodes at which the initial distributed load was applied. The sum of the magnitude of these separate forces are equal to the sum of the entire distributed load. Additional to these FBD's, one more loading is analysed. This loading is the torsion created by the lift. The centre of pressure of the lift does not coincide with the shear centre of the wing box, meaning that the lift creates torsion around the x-axis.

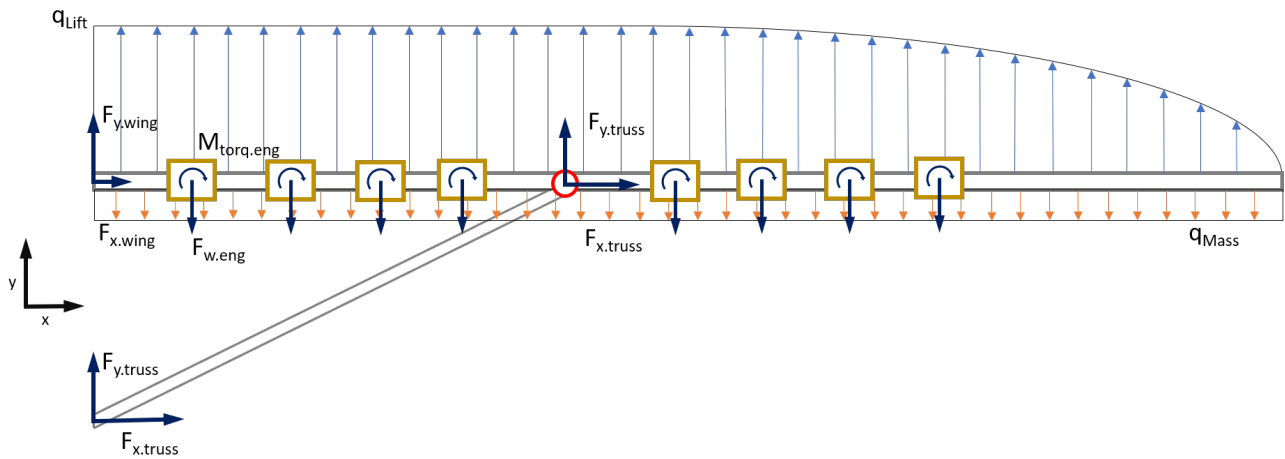


Figure 10.2: Free Body Diagram of the Wing with Truss for Load Case 1

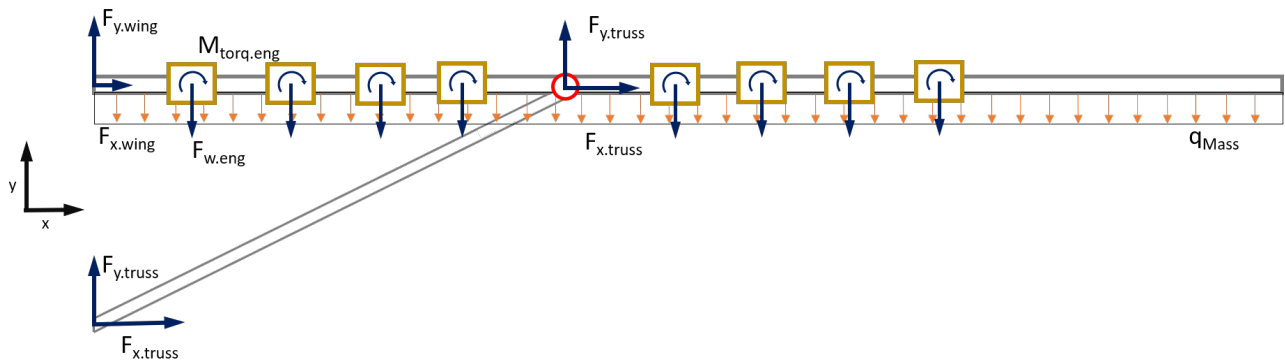


Figure 10.3: Free Body Diagram of the Wing with Truss for Load Case 2

When the geometric model with the added forces is fully setup in Anastruct, the only thing left is the description of the cross section of each beam. In other words, the wing box MOI and areas need to be determined as a function of wingspan. These MOI and areas can then be applied to the various element in Anastruct. These functions are purely dependent on the geometry and design choices of the wing box and the calculations for these can be found in [subsection 10.1.5](#).

10.1.5 Sizing the wing box

Based on the airfoil chosen in [section 7.1](#), the size of the wing box inside the wing box has to be determined. In order to make the wing box as light as possible it is necessary to choose the size and location of the wing box in such a way that it is as high as possible which increases the moment of inertia for bending. The chosen airfoil is the NACA 43014 which (as explained in [section 7.1](#)) has a maximum thickness over chord of 14%. This limits the wing box to have a maximum height over chord of 14% as well. The modelled wing box inside the airfoil is visualized in [Figure 10.4](#).

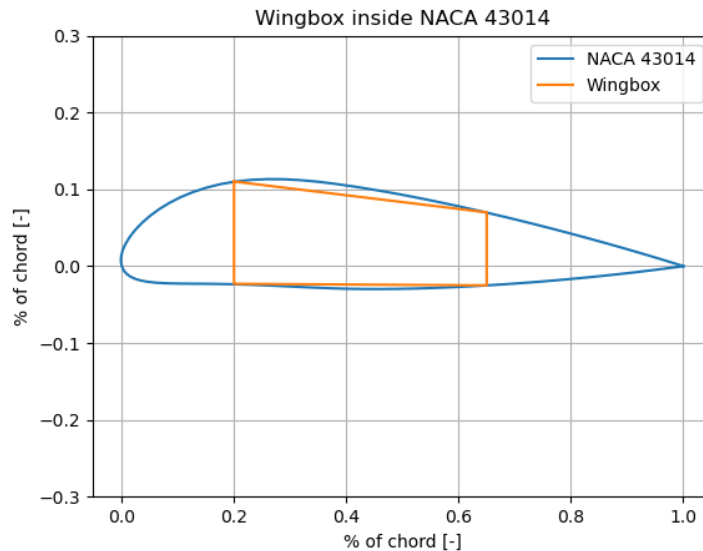


Figure 10.4: Visualization of the wing box inside the NACA 43014

The dimensions of the wing box in terms of the chord are listed in [Table 10.1](#). The dimensions of the wing box scales linearly from the root chord to the tip chord with the use of the taper ratio. It was decided to start the wing box at 20% of the chord for two reasons. First, the thickness of the airfoil is almost at its maximum value at 20% of the chord. Secondly it was not moved to the front because some space should be reserved for the electric motors. To add, the right spar was not moved more aft since that would yield in almost no structural advantage since the top and bottom skin are very close to the neutral axis and therefore will increase the moment of inertia by a very small amount.

Table 10.1: Dimensions of the wing box in terms of the chord

Section	Length/Chord
Top Skin	0.4518
Bottom Skin	0.4501
Left Spar	0.1331
Right Spar	0.095
wing box Width	0.45

Stringers

Stringers will be added on the top and bottom skin in order to increase the moment of inertia of the wing box. It was decided to use conventional I-stringers. The required area and the amount of the stringers needed will be calculated by the optimization program. The stringers will run from the root to the tip and will not change in area or amount in between.

With the amount and size of the stringers known, the area of the cross section and the moment of inertia can be calculated. The area of the cross section will be needed to calculate the weight of the wing box and will be used in torsion calculations. The moment of inertia is a very important parameter in determining the bending and shear stresses.

10.1.6 Torsion and Twist

As Anastruct is a program which models trusses in 2D, torsion and twist are not calculated by it. Therefore a program was written to calculate the torque distribution on the wing. Since it was assumed that the lift acts in the centre of pressure, at each node the lift force will create a torque on the wing box as the centre of pressure does not coincide with the shear centre of the wing box. It was assumed that the shear centre, and centre of gravity coincide since the wing box is almost

rectangular. Additionally, the weight of the electric motors would also create a torque since their centre of gravity is close to the leading edge. However it was assumed that the torque of the electric motors is negligible compared to the torque created by the lift force.

The shear flow due to the torque and the shear force in the spar will be calculated using the following formulas:

$$q = \frac{T_{lift}}{2 * A} \quad (10.1) \quad V_{shear} = \frac{q}{t_{spar}} \quad (10.2)$$

The rate of twist due to the torque can be calculated using the following expression.

$$\frac{d\theta}{dz} = \frac{T_{lift}}{4A^2} \oint \frac{ds}{Gt} \quad (10.3)$$

The torque and angle of twist over the wing are plotted in [Figure 10.5](#) and [Figure 10.6](#). A positive twist angle means the wing twists in such a way that the angle of attack would increase. As can be seen in [Figure 10.6](#), twist at the tip of the wing is only three percent. Therefore, the decision of choosing for a single cell wing box is verified as twist angle is relatively small at the end of the long wing. This small angle of twist can be explained by the fact that the aspect ratio of the wing is very high, and therefore the chord is relatively small. Therefore, the torque due to the lift is small because of the smaller distance to the shear centre. Using [Equation 10.1](#) and the torque, the shear flow can be calculated which can be divided by the thickness to get the shear stress.

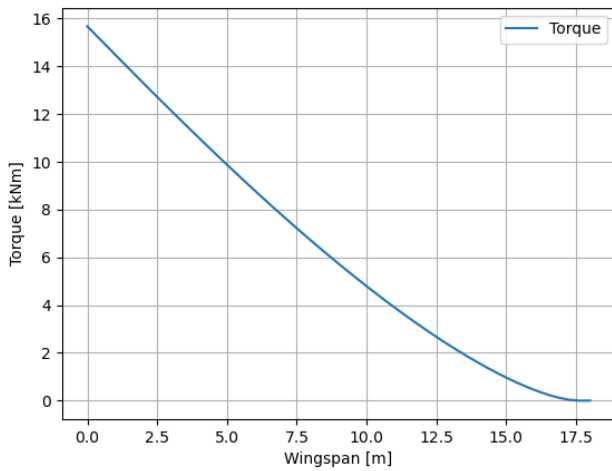


Figure 10.5: Torque distribution along the wingspan

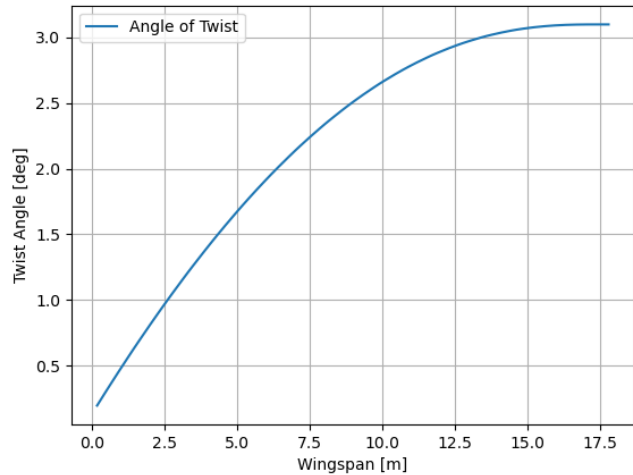


Figure 10.6: Twist angle along the wingspan

10.1.7 Axial and Bending Stress

Since Anastruct can only calculate the bending moments and the axial forces, a function has to be written to convert these moments and forces to stresses. This was done using the following formulas.

$$\sigma_{axial} = \frac{F_{axial}}{A} \quad (10.4) \quad \sigma_{bending} = -\frac{M_{bend} \cdot y}{I} \quad (10.5)$$

Anastruct calculates the axial force and bending moment for each node. As explained in [subsection 10.1.5](#), the area of the cross section and the moment of inertia can be calculated at each node. Integrating these two functions yields the axial stresses and bending stresses at each node.

The truss has also been sized using [Equation 10.4](#) and used in a rewritten form. Since Anastruct outputs the axial force in the truss, and the maximum stress allowed in the truss is known (yield stress), the area needed to carry this axial load can easily be calculated. As explained in [subsection 10.1.4](#), there are no bending moments in the truss so the area needed to carry the loads is only dependent on the axial force in the truss.

10.1.8 Buckling

During the optimization of the wing box design buckling is also taken into account. Two different failures in buckling are taken into account which are top/bottom skin buckling and spar buckling. For both, a buckling stress was calculated. When the stress in the skins is lower than this calculated value, it should not buckle. Determining this allowable stress is different for the skin and spar since the skin will be mainly loaded in bending and the spar mainly in shear.

In order to calculate the allowable stress in the skins, it was assumed that the skin with stringers could be modelled as a panel. The allowable stress in the panel can be calculated by a weighted average of the buckling stress of the skin and the buckling stress of the stringers. The critical buckling stress of the plate is given by:

$$\sigma_{cr} = C \cdot \frac{\pi^2 \cdot E}{12(1 - \nu^2)} \left(\frac{t}{b}\right)^2 \quad (10.6)$$

where C is a constant depending on the boundary conditions of the skin which can be read of from a graph[55].

The crippling stress of flanges in a stringer is given by the following expression:

$$\frac{\sigma_{cc}^{(i)}}{\sigma_y} = \alpha \left[\frac{C}{\sigma_y} \cdot \frac{\pi^2 \cdot E}{12(1 - \nu^2)} \cdot \left(\frac{t}{b}\right)^2 \right]^{1-n} \quad (10.7)$$

where C is again a constant depending on the boundary conditions and α and n are constants set by literature and are taken as 0.8 and 0.6 respectively[55]. [Equation 10.7](#) has to be used for each flange of the stringer. For the wing box optimization, an I-stringer was chosen which means that [Equation 10.7](#) has to be used for five sections. Then, a weighted average is taken to compute the allowable stress in the stringer.

With the buckling stress of the skin and stringer known, another weighted average is taken. The weighted average of the total buckling stress can be computed using:

$$\sigma_{cc_{panel}} = \frac{\sum \sigma_{cc}^{(i)} \cdot A_i}{\sum A_i} \quad (10.8)$$

The maximum allowable stress in the top and bottom skin is plotted in [Figure 10.7](#).

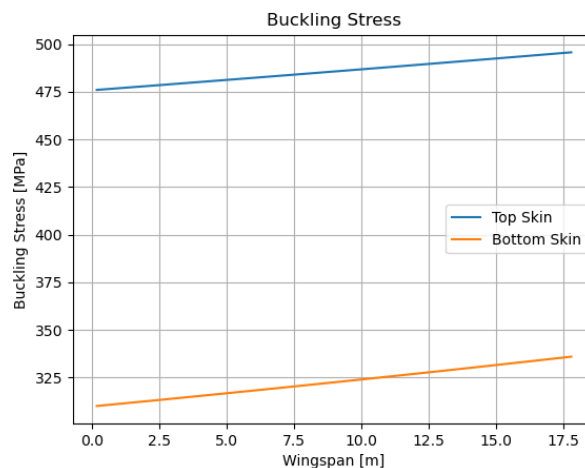


Figure 10.7: Allowed stress in the top and bottom skin before buckling

The buckling stress of the spar is calculated in a slightly different way. For the spar, the buckling stress of the stiffeners is not taken into account. However only the stiffener spacing is considered in the following equation:

$$\tau_{cr} = C \cdot \frac{\pi^2 \cdot E}{12(1 - \nu^2)} \cdot \left(\frac{t}{b}\right)^2 \quad (10.9)$$

where C is again a constant depending on the boundary conditions of the spar.

10.1.9 Optimization

Given a method which is able to compute the maximum stresses in the structure, it is necessary to choose a number of cross-sectional parameters in order to meet material property boundaries while minimising the total mass. As such, an optimization algorithm was used to compute the following cross-sectional properties: skin thickness (assumed to be the same on top and on the bottom of the wing box), spar thickness (the same for the left and right spars, seen from the fuselage), the number of stringers on top, and the number of stringers on the bottom. These four variables were then varied as inputs to an optimization algorithm which would simulate the wing with Anastruct, compute the maximum stresses and compare them to the allowable stresses. This meant that the maximum compressive stress in the top skin and the maximum tensile stress in the bottom skin were then compared to the maximum yield stress of the material, the maximum shear stress was compared to the maximum shear strength and the maximum compressive stress was compared to the maximum allowable buckling stress given by [Equation 10.8](#). This set of four constraints were imposed within the optimization and are described in [Table 10.3](#). The stresses which could be met exactly by sizing their respective elements, such as the shear buckling stress in the spar and the tensile axial stress in the radius, were not included in the optimization. Moreover, normal stress due to axial loads was assumed to be non-critical, but this assumption will be checked with the final design. Since these loads in the wing box are typically most critical for in-flight conditions with the load factor, the optimization was run for the lift loading in flight, and then it was checked that the constraints were met also during ground operations. Moreover, the order of magnitude of the deflections must be sufficient for nominal ground operations, and as such it shall be checked.

In order to aid the optimization (in terms of computational cost) and to ensure a feasible final design, bounds were imposed on the inputs. For example, all thicknesses of the skins must be at least 1 mm for production limits. Moreover, the stringers have to be able to fit within the wing box, as and such, a maximum number of 25 was imposed on them. These bounds are summarised in [Table 10.2](#). As it can be imagined, the optimization was ran to minimise the total mass of the wing box, which was computed by integrating the cross-sectional area along the span of the wing to obtain the volume and multiplying it with the density of the chosen material, whose trade-off and material properties will be outlined in [section 10.2](#). Besides this, the mass of the stiffeners and truss were added, together with an additional 15% margin factor. 8% of this factor accounts for the skin of the wing, the structure between the wing box and the leading edge and other non-sized structures in the cross-section of the wing, while the remaining 7% accounts for the mass of the ribs. Since the sizing was not done in the direction of the drag, and since the buckling loads were able to be fulfilled without the need of ribs, they still have to be taken into account in the wing weight estimation. From statistics of similar aircraft (with similar loads on the wing) a total number of 26 ribs per wing was identified as a good estimate. Also from statistics and engineering judgement, this meant an additional wing weight increase by 7%, resulting in a total of 15% (counting the previously mentioned 8% due to non-sized elements in the wing).

Table 10.2: Optimization bounds on the inputs for the program

Parameter	Minimum	Maximum
Top & Bottom Skin Thickness	0.001m	0.05m
Left & Right Spar Thickness	0.001m	0.05m
Top skin stringers	no. 1	25
Bottom skin stringers	no. 1	25

Table 10.3: Optimization program constraints. Note that here σ is the combination (addition) of axial and bending stresses (σ_{axial} and $\sigma_{bending}$). Moreover, τ is a combination of the shear stresses due to torque and the ones due to shear forces.

Parameter	Constraint
Top skin σ	$< \sigma_y$
Bottom skin σ	$< \sigma_y$
Top panel σ	$< \sigma_{cc}$
Spar τ	$< \tau_y$

An aspect which was considered but is currently not present in the optimization description is the choice for the location of the intersection between the truss and the wing. As it was shown in Figure 10.1, it is located at 30% of the wingspan, but this value was obtained by a further optimization. The wing weight was optimized for a number of locations of the truss, and the location was chosen in a way to minimize the total wing mass. As can be seen in Figure 10.8, the wing box mass is minimal when the truss is located between 30% and 35% of the span. As such, since they are comparably light, the 30% location is chosen in order to have a shorter truss. With this value, the optimization can now be run, and the wing box parameters and values can be obtained.

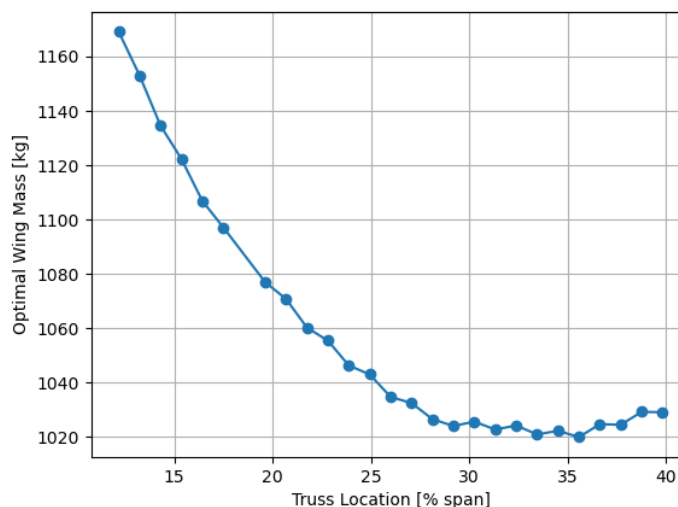


Figure 10.8: Wing mass against truss-wing attachment location as a percentage of the total span.

10.1.10 Results

As previously mentioned, in order to set up the optimization, the internal forces are first computed with the aid of Anastruct, and are plotted in Figure 10.9. It is possible to see how only the shear force and the axial forces are non-zero at the root of the wing. Moreover, it is also interesting to note the effect of the truss (large jump in shear and axial forces, large change in slope in bending moment) and the engines (small irregularities in the shear force due to weight, small irregularities in the bending moment due to the torque). Following the setup of the optimization, it is possible to run it until a converged design is obtained. The final dimensions and parameters are outlined in Table 10.4, together with the tip deflections for the two loading cases. Since the truss is only loaded axially, only its cross-sectional area is outlined in Table 10.4; if this was to be converted into an equivalent solid column it would have a radius of 2.84 cm.

Two other interesting aspects to analyze are the stresses in the wing, and the different failure modes. Since loading case one was assumed to be the most critical (and this will be verified soon), the stress diagrams are plotted for this loading case in Figure 10.10. The maxima of these plots are all compared in Table 10.5. It is possible to see how for loading case 1, the optimized wing box would fail, if loaded beyond the design loads, in four ways nearly simultaneously: shear failure and shear buckling of the spar, compressive buckling of the top skin and compressive yield failure of the truss. An interesting remark would be: is it actually safe to design a wing box which fails so close to the loads applied? In reality, this whole design step assumed a safety factor of 1.5 on the maximum load factor, and as such, the answer to the previous question is most probably yes. Finally, the values for loading case two (on ground) are also analyzed. Since the bottom panel compressive buckling is oversized by 99.53% and the truss Euler buckling is also oversized by 66.42%, it is safe to say that the wing box will not fail in on-ground loads.

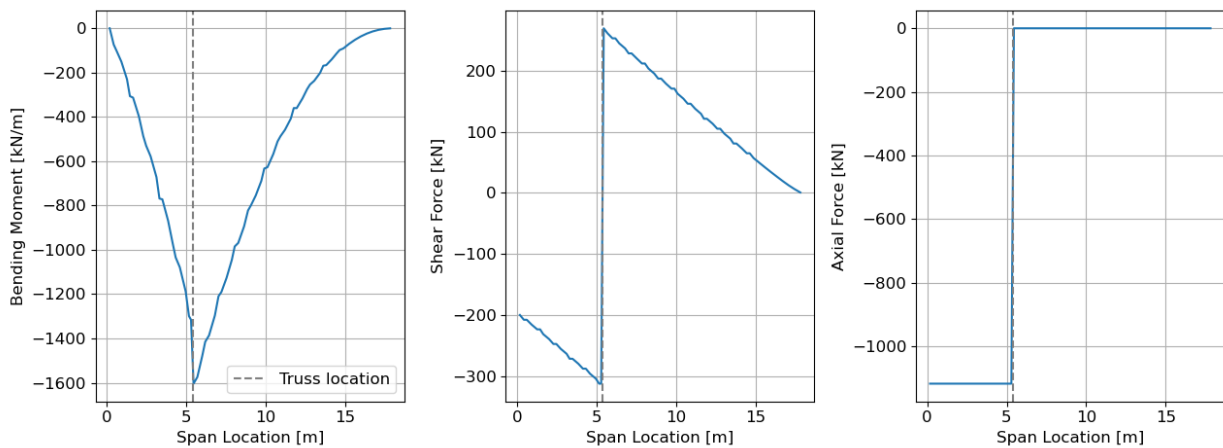


Figure 10.9: Internal force diagrams for loading case one (flight with ultimate load factor).

Table 10.4: Final wing dimensions and parameters.

Parameter	Value
Wing weight	1024.33 kg
Top skin no. stringers	3
Bottom skin no. stringers	1
Leading edge no. stiffeners	52
Trailing edge no. stiffeners	71
Top & Bottom Skin thickness	1.00 mm
Left & Right Spar Thickness	1.78 mm
Top skin stringer area	0.000895 m ²
Bottom skin stringer area	0.000925 m ²
Truss cross-sectional area	0.001938 m ²
Tip deflection for load case 1 (ult. load factor)	2.388 m
Tip deflection for load case 2 (on ground)	0.017 m

Table 10.5: Maximum allowable and actual stresses in the wing box.

Failure type	Max. in structure MPa	Max. allowable MPa	% overdesign
Top skin σ_y	481.34	650.00	25.95%
Bottom skin σ_y	604.18	650.00	7.05%
Top panel σ_{cc}	481.34	481.63	0.06%
Bottom panel σ_{cc}	1.50	317.17	99.53%
Truss σ_y	650.00	650.00	0.00%
Truss σ_{cr}	3.62	10.78	66.42%
Spar τ_y	364.96	365.03	0.02%
Spar τ_{cr}	364.96	364.96	0.00%

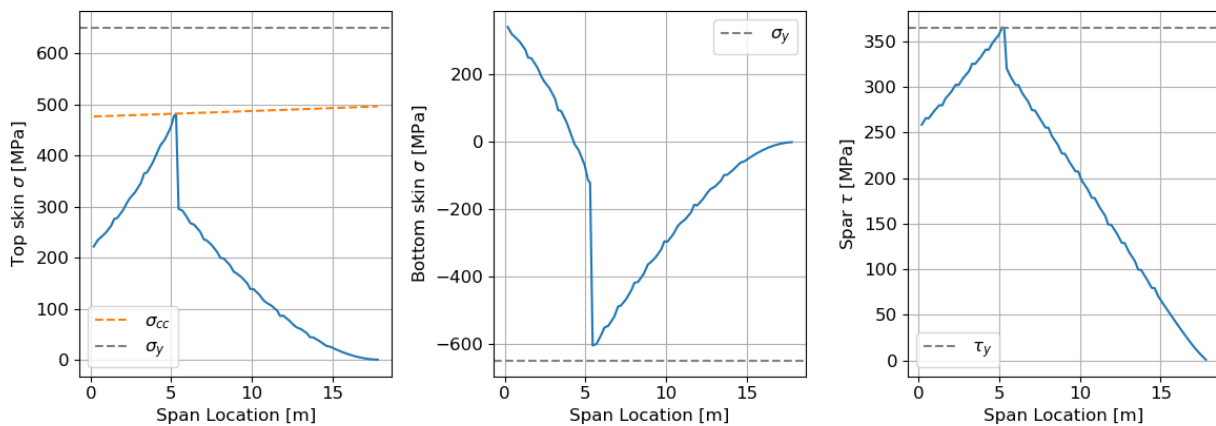


Figure 10.10: Wing box stress diagrams for loading case one (flight with ultimate load factor).

Although the wing box has been designed in quite some detail already, there is always room for improvement to make the wing box even lighter and stronger. First of all, there is a chance that the number of stringers is not optimal in the whole wing box. The amount of stringers have been chosen in such a way that the maximum bending stress would be lower than the yield stress. However, since the bending stress is not at its peak throughout the wing box, the wing box is over designed at places where the bending stress is lower. It is possible to design for this, then the wing box has to be split up in parts and the amount of stringers could be changed between different parts. Furthermore, now it was assumed that the top and bottom skin has the same thickness, as well as the left and right spar. For detailed design it is recommended to have four different thicknesses for these skins and spars as most likely one of them will be over designed now. Another consideration for detailed design of the wing could be to combine all the shear bending and axial stress in the Von Mises stress to size the wing box. To add, it would be recommended to take a more detailed look at the stiffeners: in this design there are a lot of them to make sure the spars will not buckle. However there may be a smarter way to design for this. Also, two loading cases have not been designed for in this analysis: forces in the flight direction and fatigue. For detailed design, it would therefore also be recommended to size the wing box for these load cases. Forces in the flight direction will also allow for determining the exact amount of ribs needed, without the use of statistical estimations.

10.2 Material Selection for Wing Box

In order to select the best material possible for the wing box a trade-off will be performed. This trade-off will not be a common trade-off by weighting different criteria and scoring materials based on this criteria. This trade-off will be performed with the use of a life cycle assessment of the material. This assessment is a quantitative tool to compare the life cycles of different materials. The life cycle of a material is divided in three stages; the raw material phase, the use phase and the end-of-life (EOL) phase. Within each of this phases the materials will be analysed on sustainability and cost.

Sustainability will be taken into account by determining the energy needed for processes in each phase and cost will be considered by determining the price/kg of each process.

In the raw material phase, the production of the material itself will be taken into account. The use phase consists of three qualitative criteria which are ease of manufacturing, ease of maintenance and ease of application. Lastly, in the EOL phase the energy and cost for end-of-life processes will be taken into account.

The materials selected for this trade-off are three types of aluminium and three types of composites. The materials are listed in Table 10.6 with their most important strength properties. These three types of aluminium have been chosen because they are already commonly used in aerospace such as the first two materials listed. The third chosen aluminium is a new high performance alloy which is more and more used in aerospace². Two carbon fibre reinforced polymers (CFRP) have been chosen as composites since CFRP are already commonly used as materials in the fuselage of certain aircraft³. Furthermore, glare has been chosen as a material since it is more often used in aviation. Within this selection of the materials, also technology readiness has been taken into account. All the selected materials could be for the manufacturing of the wing box as of today.

Table 10.6: Materials Selected for Trade-Off

Contenders	Type	Young's Modulus GPa	Yield Tensile Strength MPa	Yield Tensile Strength MPa	Shear Strength MPa
Al-2024 T6	Aluminium	73.85	363	378	283
Al-7075 T6	Aluminium	72.5	445	460	331
Al-7068 T6	Aluminium	73.1	702	600	365
AS4 8552 T6	Composite	144/10.6	2200/81	1500/260	80
AS4 3501-6 T6	Composite	131/8.9	1964/24	1197/200	85
Glare	Composite	58.1	620	267	40

Since the life cycle assessment is a very time-consuming process, one type of aluminium and one type of composite will be taken into account. To determine the best aluminium and best composite material, the properties of the material were used in the optimization program to calculate the weight of the wing. The materials which yield the lowest wing weight will be further analysed. Table 10.7 shows the weight of the optimized wing box for each of the materials. From this table it can be concluded that Al-7068 T6 and AS4 3501-6 will be analysed in the life cycle assessment.

Table 10.7: Materials with the related wing box weight

Contenders	Wing Weight in kg
Al-2024 T6	1037.46
Al-7075 T6	1036.52
Al-7068 T6	1024.33
AS4 8552	515.7
AS4 3501-6	507.27
Glare	888.29

As can be seen in Table 10.8, the two materials that resulted in the lightest wing box are being analysed in three different phases in their life cycle. The raw material and the EOL phase are treated quantitatively and the use phase qualitatively. In the raw material phase it is clear that the composite uses a lot more energy compared to the aluminium for the production and manufacturing which has

²<https://www.aircraftaluminium.com/product/7068-aircraft-aluminum-alloy.html>

³<https://www.compositesworld.com/articles/the-first-composite-fuselage-section-for-the-first-composite-commercial-jet>

a negative impact on sustainability. Next to this, there is also a very big difference between the cost of the two materials. Composites are very expensive per kilogram and will therefore greatly influence the total cost of the wing box.

Within the use phase three qualitative criteria will be used to determine the best material. Ease of manufacturing determines how easy it is to manufacture parts of the wing box and the ease of assembling. The second criteria will determine the ease of maintenance, this included replacing damaged parts and performing checks on the wing box. Lastly, the ease of application is taken into account. This criteria is about how easy it is to actually use the material in a wing box. The use of composites in a wing box could be a problem in terms of application since the allowed stresses in longitudinal and transverse direction are very different (Table 10.6). This means that, in order to make the entire wing box out of composites, every element of the wing box has to be analyzed in terms of load and all fibres in that part should be in the direction of the load to ensure the highest yield strength. Lastly, the EOL phase is treated quantitatively again, by determining the EOL energy. This is the energy needed to properly recycle the product.

Table 10.8: Life Cycle Assessment

	Al-7068 T6	AS4 3501-6
Raw Material Phase		
Production Energy [MJ/kg]	194 [29]	615 [56]
Manufacturing Energy [MJ/kg]	15 [29]	-
Production Cost [€/kg]	8 ⁴	275 [57]
Material Cost [€/kg]	4 [29]	-
Use Phase		
Ease of Manufacturing (1-9)	8	4
Ease of Maintenance (1-9)	7	3
Ease of Application (1-9)	9	3
EOL Phase		
EOL Energy [MJ/kg]	33.3 [29]	50 [58]

From the table above, it is very clear that the aluminium scores are better in each of the life cycle phases. However, Table 10.7 shows that the composite wing box yields a lighter design. In order to properly choose between a composite or aluminium it was decided to assess the life cycle of the material with a higher weight compared to the weight of the wing box. This means that although the composite wing box will be lighter, in terms of sustainability it performs way worse than aluminium. therefore, it was decided that Al-7068 T6 will be the material used in the wing box. It should be noted that this choice is mainly based on the fact that in terms of energy required and cost, the composite will not be used in ECHO-1. This choice was made with the knowledge and technologies that currently are. If, in the future, new technologies would decrease the required energy in the complete life cycle of composites and their recycling capabilities are better, the material choice should be reconsidered.

10.3 Modelling Fuselage Structure for Battery Integration

ECHO-1 gets all its power from the batteries meaning that they need to be very heavy. As explained in chapter 8, the batteries are all housed in the fuselage. This increases the weight of the fuselage significantly. This increase in weight causes a greater stress on the structure of the of the fuselage, meaning that the fuselage structure needs to be reinforced. This reinforcement increases the weight of the fuselage structure by a certain factor. This section aims to calculate that factor. This is done by designing a simplified fuselage with and without batteries. The weight of these two designs are then compared in order to determine the weight increase due to the batteries. In the end, this weight increase is then applied on the Raymer formula for determining the fuselage weight as in

chapter 5

10.3.1 Assumptions

The following assumptions are considered in the calculation of the fuselage weight:

- The skin has zero thickness.
- The fuselage is subjected only to bending.
- The fuselage structure is modelled as only consisting of stringers.
- The stringers are modelled as point areas.
- The connection between parts is assumed to be perfect. This means that rivets are not modelled.
- The fuselage is modelled as a beam.
- The weight of the fuselage is equally distributed over its length.
- Shear is not modelled.

10.3.2 Load Case

Just like the wing box load cases, for the structural design of the fuselage, two load cases will be analysed. One load case is in-flight with the maximum load factor of lift applied and the other load case is the touchdown of the aircraft on ground. Other load cases like the pressurisation of the cabin, side slipping flight and lateral gusts are not considered because it is not likely that the batteries will have an effect on these ones. This means that if these load cases were analysed, the result with batteries will be the same as without batteries.

The first load case is the manoeuvre with gust loads. From previous analyses [1], it has been analysed that the most critical load factor for the aircraft is 3.9. This means that, in the most critical situation, the lift is 3.9 higher than the nominal lift in cruise. This increase in lift will increase the bending stresses in the fuselage. In flight, the bending stress in the fuselage is mainly caused by the weight of every component. The wing carries the fuselage in the air which means that the rest of the fuselage creates a bending moment due to its own weight. This all means that the forces on the fuselage are the lift, the weights of the batteries, the weight of the fuselage with payload and the downforce created by the tail. Moments during the landing load case is considered to be smaller than the moments in the first load case. This means that only the first load case where the load factor of the lift is 3.9 is modelled.[59] [60]

10.3.3 The model

In the model, the fuselage is designed as a beam just as the wing in [section 10.1](#). On this beam, the various forces and loads are applied. These loads are the fuselage weight as a distributed load along the entire beam, the lift which acts as a point load at the centre of pressure of the wing, the down force from the tail which is a force downwards at the location of the tail and finally the weight of the batteries which is modelled as a distributed load on the beam. The FBD of the fuselage can be seen in [Figure 10.11](#). Note, that the loads in this model are not drawn to scale but this figure just functions as a visual aid. In this model, there is a resultant moment at the centre of gravity. This resultant moment is there so that the sum of all moments equals zero. If this is not the case, Anastruct will give errors. In reality, this resultant moment will cause the model to rotate but this is irrelevant because only the static situation is analysed. Besides, this resultant moment will not be too great.

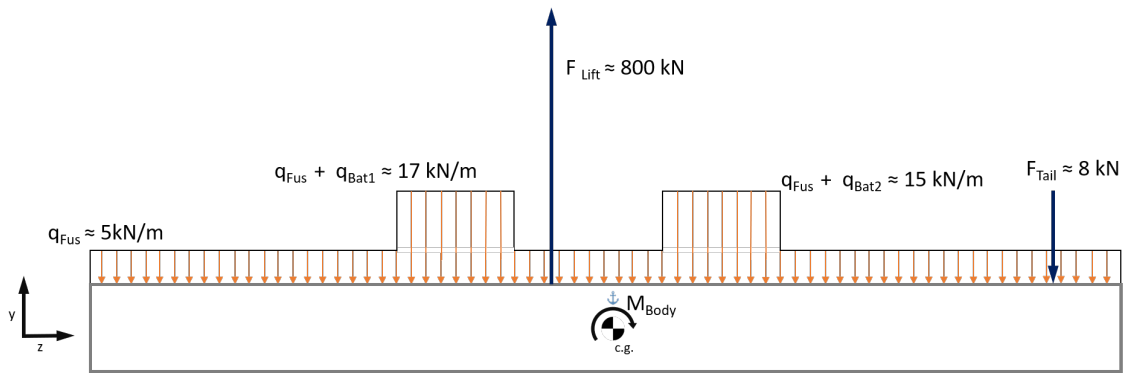


Figure 10.11: FBD of the fuselage model

Logically, the distributed loads from the masses of components of the fuselage point downwards and are equal to their masses times the gravitational acceleration. However, this is only valid if the model does not accelerate. When the load factor is higher than 1, the entire aircraft experiences an acceleration upwards. This acceleration causes an extra bending moment in the fuselage. This extra bending moment can easily be calculated using Newton's second law : $F = m \cdot a$. When a body is in acceleration, this body feels a force equal to its mass times the acceleration. This means that all the distributed loads caused by masses in [Figure 10.11](#) will simply be multiplied by the load factor in order to model the extra loads due to the acceleration.

For the analysis of the fuselage, only the bending stresses are analysed. The shear stress could have also been analysed but due to time constraint this was not done. The shear stress is expected to increase due to the extra batteries. It is assumed that the increase in weight due to shear is the same as the increase in weight due to the bending. From the previous fuselage model, the internal moment distribution can be computed. However, the stresses in the fuselage are needed. These stresses are highly dependent on the cross sectional geometry of fuselage. The model for the cross-section of the fuselage will be a structural idealisation of the fuselage by modelling the stringers as different booms connected with a thin walled skin assuming to not carry any of the axial stress. This means that all the bending stresses will be carried by the booms. This assumption is valid only when looking at the bending stress and shear stress. The model of the cross section of the fuselage for an arbitrary number of stringers can be seen in [Figure 10.12](#).

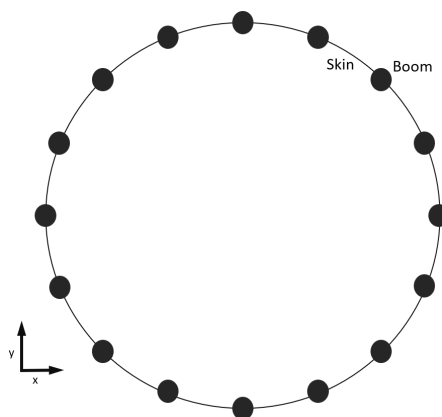


Figure 10.12: Idealised cross section of the fuselage

10.3.4 Sizing of the fuselage

The fuselage operational empty weight will be calculated using the Raymer empirical method just like in the class II weight estimation [61]. This equation gives the weight for the fuselage based on the fuselage outer dimensions. If there were no batteries present in the fuselage, the fuselage could have been made less strong because the weight of the batteries is removed. This removal of the batteries

does not change the dimensions of the fuselage and thus the Raymer equation will give the same weight for a fuselage with as without batteries. This is simply wrong, as the batteries require the fuselage to be stronger and thus an increase in weight. One method for estimating the fuselage weight with batteries is by calculating the relative weight increase of a fuselage with added batteries. This increase factor will be applied to the class II weight estimation, making it more accurate for ECHO-1. This means that two fuselages will be designed, one with batteries and one without batteries.

For each moment along the fuselage, the required MOI of the fuselage can be calculated using:

$$\sigma_z = \frac{M_x * y}{I_{yy}} \quad (10.10)$$

The moment of inertia of the fuselage is dependent on the amount of stringers and the area per stringer. This means that there are two unknown variables with only one equation. Therefore, the required area per stringer was computed for various amount of stringers ranging from 6 to 60 stringers in steps of 2 with a limitation that the area per stringer can not be smaller than 0.0012 m². This resulted in approximately 25 different configurations for which the total area was calculated. In the end, the configuration with the lowest area was considered as the best. The total fuselage was divided into 4 different sections in order to prevent over designing. For each of these sections the amount of stringers and stringer area was computed as described above. In the end the total mass of the entire fuselage was computed. The total mass of the fuselage with batteries and without batteries can then be compared.

From this comparison, the increase in fuselage weight with batteries versus without can be calculated. In the end, the final goal is to calculate the weight of the fuselage. This is done using the empirical Raymer formula multiplied with this extra factor. This resulted in an increase of fuselage weight of 4.192%.

10.4 Vibrational Analysis

During flight, an aircraft is subjected to vibrations. These vibrations cause an increase in the internal loads on the structure of the aircraft. For this reason, a vibrational analysis of the wing is performed. For the assessment of the vibrations of the wing, the natural frequency of the wing system is computed. This natural frequency is a property of a system and gives insight if the system will resonate during operation. The natural frequency is the frequency at which a system will amplify a certain motion. If the wing is subjected to an external force or motion which is close to its natural frequency, the system will amplify this motion and thus increase the stresses within the beam.

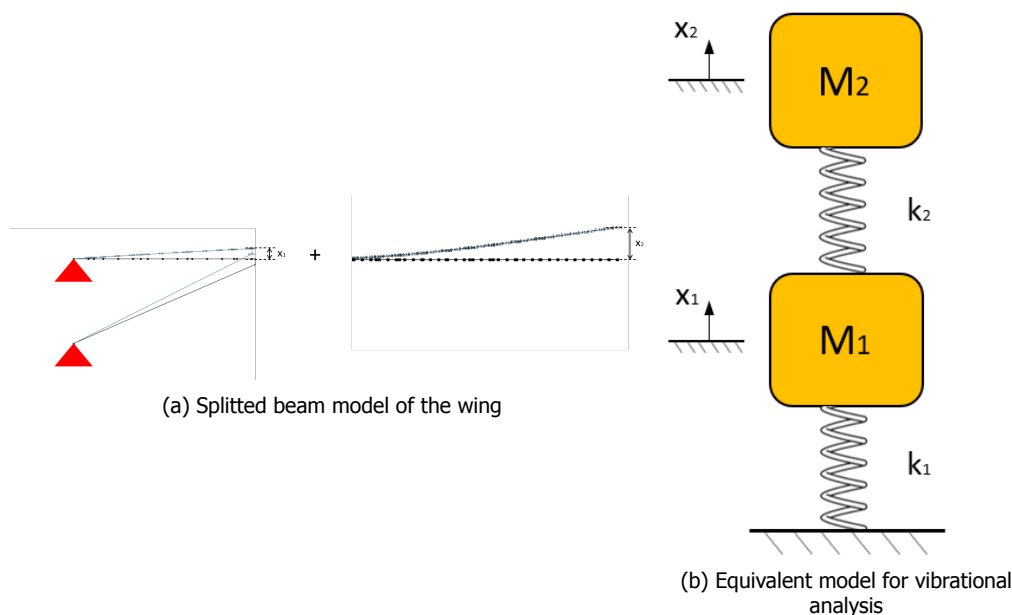


Figure 10.13: Vibrational model of the wing

In order to determine the natural frequency of the system, the system is modelled like [Figure 10.13](#). In this model, the initial wing is splitted into two parts, one part up until the beam connection and one from that connection until the end of the wing. These two parts can then be combined into a two degrees of freedom system as seen in [Figure 10.13b](#). Two degrees of freedom mean that the system will have two natural frequencies. The spring constants of the system can be calculated using [Equation 10.11](#). This equation calculates the spring constant based on the deflection of the beams when subjected to a certain load. From these spring constants, the natural frequencies can be computed given in [Table 10.9](#). With the deflection of the wing known due to a certain load, the natural frequency can be computed.

$$k = \frac{F}{\delta} \quad (10.11)$$

Table 10.9: The natural frequencies of the wing model

Part	Natural frequency in Hz
Root	69.6
Tip	169.0

The system is not sensitive to vibrations if its natural frequency is higher than the frequency of the forces or motion to which it is subjected. Lowest natural frequency of the wing box structure is about 69 Hz, which is relatively high. This means that vibrations are not an issue for the wing structure.

10.5 Verification and Validation

Verification and validation is an important aspect of the structures optimization. These two processes must be performed in order to make sure that your results are correct and valid. The general procedure for verification and validation is described in [section 3.5](#). All the unit test which were performed for verification can be found in [Table 10.10](#). The main purpose of these unit tests is that the calculations in python were correctly used and filled in.

Nr.	Name	Type	Parameters	Passed
1	Max shear test	Hand calculation	$MOI_{xx}, t_{top}, t_{bot}$	Yes
2	Buckling test	Hand calculation	$\sigma_{cc_{top}}, \sigma_{cc_{bot}}$	Yes
3	Stringer area test	Hand calculation	A_{string}	Yes
4	Torque test	Hand calculation	$T_{reaction}, \theta_{max}$	Yes
5	Fuselage MOI test-I	Hand calculation	$MOI_{fus}, x_{loc_{boom}}$	Yes
6	Fuselage MOI test-II	One test	MOI_{fus}	Yes
7	Required stringers check	Hand calculation	n_{string}, A_{string}	Yes
8	Percentage check	Hand calculation	$m_{bat}, m_{no-bat}, m_{tot}, f_{struc}$	Yes
9	Vibration test	Hand calculation, one test	f_{nat}	Yes

Table 10.10: All the unit test performed on the python script for the structural analysis

However, besides these unit tests, more systems tests were performed. One of which is the discretization test. The discretization test assesses if the discretization or amount of nodes is correct in computational methods. As explained previously, Anastruct splits one beam up into several smaller beams or elements. The amount of elements must be chosen correctly to give accurate results and to limit the computational time of the method. The maximum deflection of the tip of the final wing

box tip for various number of elements can be found in [Figure 10.14](#). From this graph, it can clearly be seen that after a certain amount of points, the deflection diverges to 2.37 m. In order to limit the computation time of the program, a grid of 50 points was selected to be enough to give accurate results, while still obtaining fast computational time.

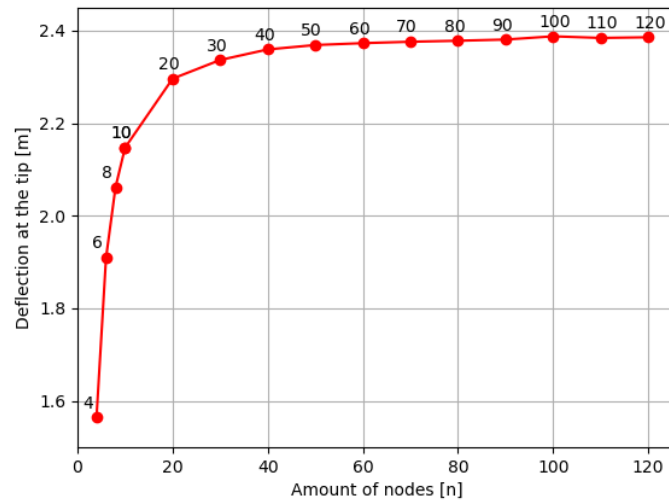


Figure 10.14: Deflection of the wing box tip with different meshes at load case 1

Anastruct is validated using a very simplified model as input in the program and comparing the deflection with experimental data. If Anastruct is a valid program for analysing deflections and stresses, the structural program is validated. The simplified model will be a simple cantilever beam with a point load at the end of the beam. This means that, on the beam, two loads are applied: the point load at the end of the beam and a distributed load because of the mass of the beam. The results of Anastruct are compared to the results of an identical experiment [62]. These results can be seen in [Table 10.11](#). It can clearly be observed that the experimental deflection and the deflection in Anastruct are almost identical. This means that Anastruct represents reality accurately and thus it is a valid program to use.

Table 10.11: Validation Results

Part	Anastruct	Experimental Results
Weight	0.554 N	0.554 N
I_{xx}	1.2e-12 m ⁴	1.2e-12 m ⁴
Point load	3.92 N	3.92 N
δ_y	0.127 m	0.128 m

11

Battery Integration

Since ECHO-1 will use electric propulsion, the battery subsystem is a critical subsystem. The battery system is required to both deliver the power output or voltage required by the electric motors and it should be able to hold all the energy needed for an entire flight including loiter and diversion. In this chapter, [section 11.1](#) will derive the architecture of the various battery modules used and how these architectures were derived. [section 11.2](#) will show and visualise the packaging of these various

battery modules into the fuselage of ECHO-1. Finally [section 11.3](#) will describe the way the aircraft will manage the temperature of the batteries at various operating conditions.

11.1 Battery Architecture

To arrive at the battery architecture of a pack it is important to first understand how the batteries in ECHO-1 will be build up. In total there will be 2 big batteries, called battery packs, each providing 1200 V to the electric motors on each wing. Each of these big battery packs is made up of a number of modules and each module in turn is made up of a number of cells. The cell which will be used as a reference cell will be the Tesla 2170 cell. This cell has a diameter of 21 mm, a height of 70 mm and currently have an energy capacity of 21.275 Wh at an energy density of 322.3 Wh/kg (E_{cell}^*) at the cell level and having a nominal cell voltage of 4.2 V. These cells were choosing since they are currently the best available Li-ion cells on the market. ¹

Since the ECHO-1 will operate from 2035 and on wards the energy density of the cell will increase. Currently it was assumed that the battery will have a energy density of 575 kg/Wh at the pack level end of life so including pack efficiency loss and degradation. For all following calculations a degradation of 15% at end of life and a energy loss of 20% from cell to pack are assumed [1]. In order to find the total number of cells required in the batteries, first the total required energy at the pack level at end of life needs to be calculated. This can be done using [Equation 11.1](#). Since this is the energy at pack level end of life it needs to be converted to the energy at start of life at the cell level. This can be done by multiplying the found number with η_{pack} (1.2) and η_{deg} (1.18). This multiplication needs to be done since the cells need to be designed for the beginning of life. So they should hold more energy then required at the pack level end of life since they will both degrade and lose energy due to efficiency losses. If these are not accounted the aircraft would not be able to complete its full mission.

$$E_{tot} = M_{bat} E_{pack}^* \eta_{pack} \eta_{deg} \quad (11.1)$$

Next it is required to determine the energy capacity of the Li-ion cell in 2035. The capacity found was the capacity in 2020. To find the capacity in 2035 it is assumed that the energy density will go up. This allows for a linear scaling of the energy capacity of the cell. The energy density at cell level start of life in 2035 can be found using [Equation 11.2](#). With this new energy density the capacity in each cell in 2035 can be calculated using [Equation 11.3](#). To find the total number of cells required the energy can simply be divided by the energy capacity of each cell. This resulted in a total of 104832.7 cells. This number was round up to 104840 so that the cells could be more easily divided over the various modules.

$$E_{cell_{2035}}^* = 575 \eta_{pack} \eta_{deg} \quad (11.2) \quad E_{cell_{2035}} = 21.275 \frac{E_{cell_{2035}}^*}{322.3} \quad (11.3)$$

With the total number of cells known it becomes possible to size and design the battery modules. It was decided that the same type of architecture as used by Tesla would be used. This architecture puts 6 Li-ion cells in series in a string in each module and an x number in parallel. With the 6 cells in series each module will have an output voltage of 25.2 V. The electric motors require an operating voltage of at least 1200 V. This requires for at least 1200/25.2 (=48) modules to be put into series. Since the design decision was made to use 2 batteries, 1 for each wing, a total of at least 96 modules will be necessary. The number of parallel strings (x) can now be determined by dividing the total required number of cells by the total number of cells in series. This resulted in a number of strings in parallel of at least 174.7 strings this was rounded up to 175 strings since there cannot be a 0.7 string.

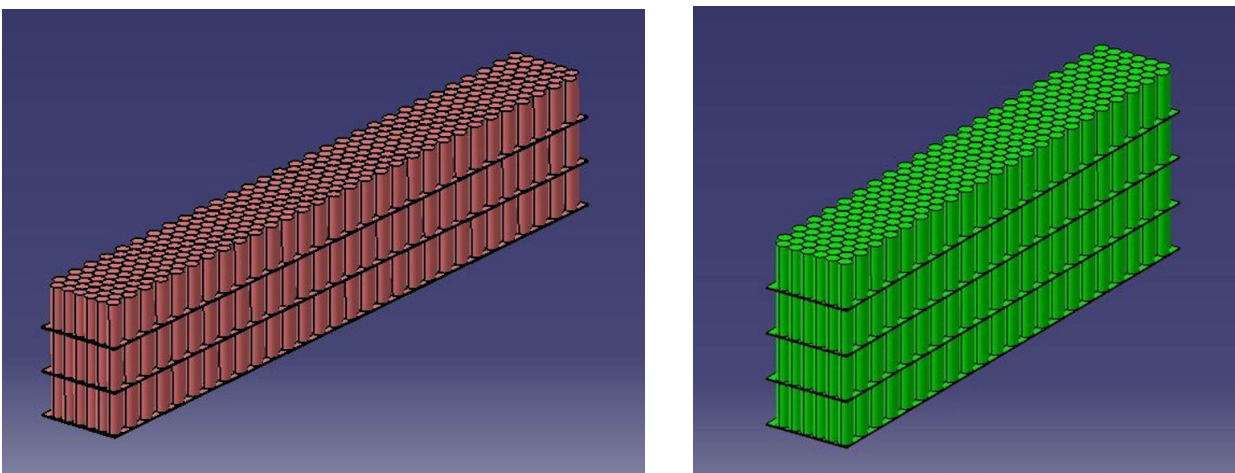
¹https://www.reddit.com/r/teslamotors/comments/65pt0k/tesla_2170_battery_cell_specifications_calculated/

11.2 Battery Packaging

With the number of cells in series and parallel known, it is now important that these cells are arranged in such a manner that they will make the best use of space available for the batteries in the fuselage. In [section 11.1](#) it was found that the battery modules required 6 cells in series and at least 175 strings in parallel. If there would be a module of 1 row high, all these parallel cells would be ordered behind each other resulting in a module length of 3.68 m. This is a very long module which would make it very difficult to handle during maintenance and ground operations.

To overcome this issue it was decided to 'cut' the battery module at various places along the length and stack these sliced pieces on top of each other in the vertical direction. Since the battery compartment only had enough vertical space to accommodate 7 vertical rows of cells it was decided to make two types of battery modules. The first module would be 3 layers of 1 cell high. This would result in a module having a length of $174.7/3 (=58.23)$ strings. This number was rounded up to 60 since there cannot be 0.23 string. It was rounded to 60 since for cooling reasons the amount of strings in longitudinal direction always has to be a multiple of two to allow for coolant to flow between the cells as will be described in more detail in [section 11.3](#). The resulting module would have a length x width x height of 60 x 6 x 3 cells which can be seen graphically in [Figure 11.1a](#). Do note that the wiring of the battery module is still 6 cells in series and for the 3 module $60 \times 3 (=180)$ strings in parallel. It is assumed that the wiring between the layers and of the battery cells can make this possible irrespective of the actual geometry of the battery module. All 3 layers with the 60 strings will be wired together in parallel. Between each two rows of cells there is some margin between the cells as can be seen in [Figure 11.1a](#). This is done since the batteries will be fully submerged in coolant which needs to flow between the rows of cells in order to be able to properly cool the battery. The thermal management system will be discussed in more detail in [section 11.3](#)

The second designed module is a 4 row high module. With the 4 rows each module would have a length of 43.68 cells. This number was rounded up to 44 cells for the same reasons as described with the 3 high module. This module now has a length x width x height of 44 x 6 x 4 cells. The module can be seen graphically in [Figure 11.1b](#). Again some space is left between each two rows of cells to allow for the coolant to flow between the cells and all 4 rows with 44 strings in parallel are wired together in parallel.



(a) A 3 High Battery Module

(b) A 4 High Battery Module

Figure 11.1: The Two Types of Battery Modules

With the types of battery modules designed as it is, it is now time to place these modules into the available space as efficiently as possible. This process was started by looking at the cross section of the available battery space and placing in as many of the modules as possible. In [Figure 11.2a](#), the green modules correspond to the 4 high (4H) modules and the pink ones are the 3 high (3H) module. Since the actual wiring of the modules together in a proper way would be outside the scope and detail

level of this DSE, it was decided to simply see if the needed amount of modules to achieve the required total cell count would fit. This does not take the practicality or accessibility of the wiring of modules together into account. In [Figure 11.2a](#) it can be seen that 11 of the 4H modules were placed and 8 of the 3H modules. It can also be noted that on the lower sides of the battery compartment and on the flat bottom two types of modules are placed but not yet described. These modules are a variant of the 4H modules but simply with each row not stacked vertically on top of each other but rearranged in an L shape or plate shape respectively. This was done to be able to maximally utilise the empty spaces remaining in the battery compartment. In total the cross sectional of the battery compartment can fit 8 of the 3H modules and 11 of the 4H modules as can be seen in [Figure 11.2a](#).

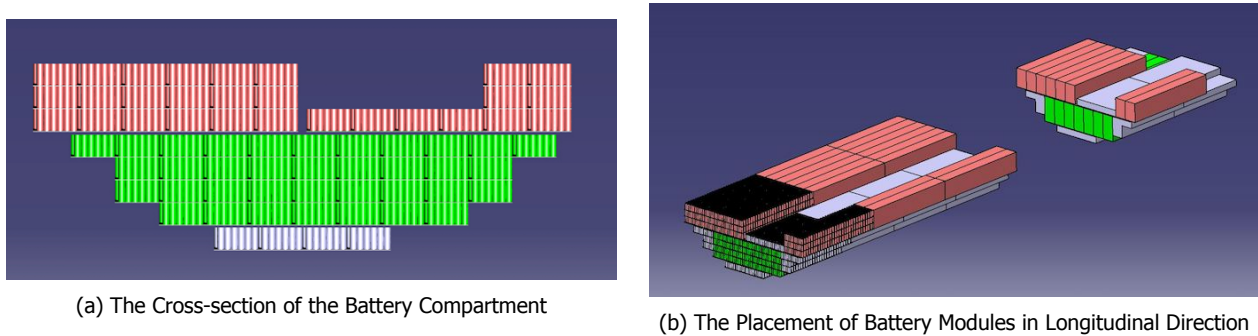


Figure 11.2: The Battery Placement

In longitudinal direction, the front battery compartment is able to fit 3 of the 3H modules in length and 4 of the 4H modules. The aft battery compartment is able to fit 1 of the 3H modules and 2 of the 4H modules in longitudinal direction. The resulting number of modules in each compartment and corresponding number of cells can be seen in [Table 11.1](#) and visually in [Figure 11.2b](#).

Table 11.1: The Number of Modules in Each of the Battery Compartments

Compartment	Cross 3h	Cross 4h	Long 3h	Long 4h	Total Cells
Front	8	11	3	4	72384
Aft	8	11	1	2	31827

The number of modules in series in each battery pack equals 48. With a module voltage of 25.2 V this gives an operating voltage for each of the battery packs of 1235 V. This is well above the required 1200 V and so allows for a small drop in voltage. This drop in voltage occurs when the battery discharge since Li-ion batteries have a slight voltage drop as they lower state of charge. At this stage of the DSE, quantifying the drop in voltage with the discharge would go into too much depth. As a recommendation for future work, it would be worth investigating how much the voltage would drop with a higher state of discharge and see if this 35 V margin is enough to account for it. Adding up to total amount of cells the number 104211 is found. This is slightly below the required 104840. This problem is overcome by placing 1 battery module of 25.2 V in the nose of the aircraft which could be used to provide power to the avionics systems in the cockpit. This would bring the total battery cell count in the aircraft up to 105291 which is above the required 104840.

Next to the analysis into the voltage drop in the batteries, when discharging it would be worth while to investigate if the assumption that the battery modules can be wired according to the previously described geometry holds. It could be that wiring the battery modules in the way described in [section 11.1](#) would impose a number of performance penalties on the batteries or that the weight of the required wires would be high. It is recommended to do this investigation in collaboration with an electrical engineer since more in depth knowledge on batteries would be required.

11.3 Thermal Management

Lithium-Ion batteries have a very significant drawback: they have a very tight operating range in terms of temperature, i.e. between 15 and 35°C [63]. At temperatures below 15°C, the efficiency of the battery drops significantly. At above 35°C, the battery experiences a drop in efficiency as well, but with the added risk of thermal runaway, in case the temperature continues to rise. The optimal operating temperature is considered to be 25°C. It is the job of the battery thermal management system (BTMS) to maintain this temperature, i.e. to both cool down the battery doing normal discharge, as well as heat it up to prepare it for charging before landing.

11.3.1 Heat Produced

The thermal management system includes the battery and the electric motors on the wing. In terms of heat produced, for the battery only the Joule effect heating was taken into account. The Joule effect refers to the heat being produced due to the internal resistance of the batteries. The heat flow generated by this effect is shown in Equation 11.4. Although there are other forms of heating that occur within the battery such as the energy of electrochemical reactions within the cells, these represent less than 1% of the total heat being produced [64] and were, therefore, not taken into account.

$$\dot{Q}_{battery} = I_{cell}^2 * R_{cell_{int}} \quad (11.4)$$

The heat flow being produced by the motors is considered to be equal to the efficiency losses of the motors as a percentage of the total power being drawn by the motors from the battery at any moment. This is shown for cruise conditions in Equation 11.5. The efficiency of the motors is 92.9 %.

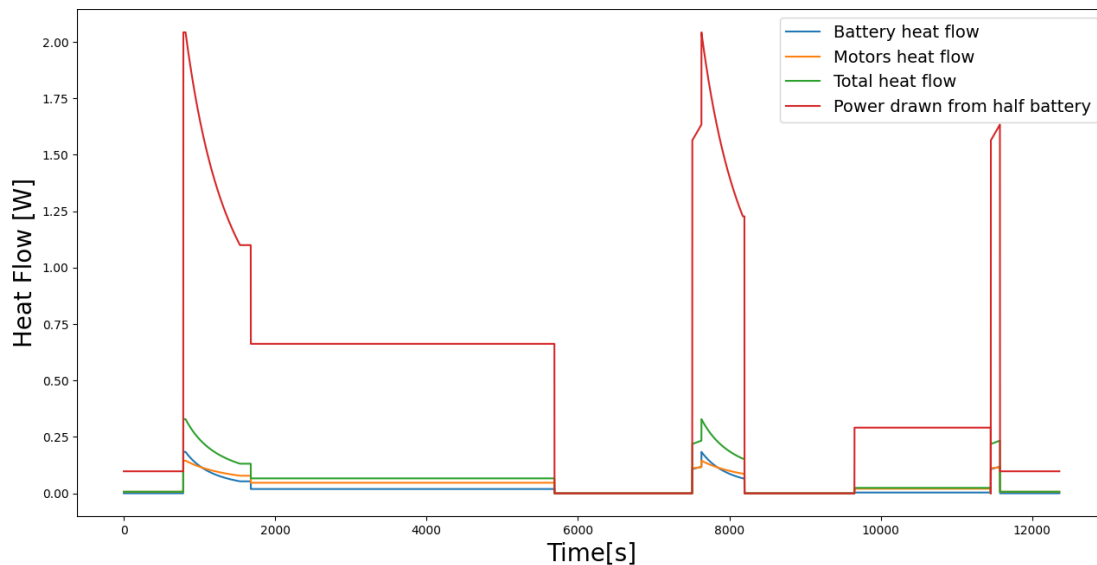


Figure 11.3: Heat Flow and Power Drawn Over the Mission Profile

11.3.2 Cooling system type and architecture

The BTMS will be a liquid-cooling system as these can provide adequate cooling for high-power systems, it can be packaged tightly in the aircraft and can be used for the cooling of the electric motors as well. A cooling system based on pulling air through the battery packs would not work because of multiple reasons. One is the lack of packaging space that would not allow for such volume in between the cells in the belly of the aircraft. Another one is the lack of efficiency as the air just does not have the thermal capacity necessary to cool down the batteries. Also, because of the length of battery compartments that would slow down the airflow which would lose energy before reaching the end of

the batteries.

The battery cells will be effectively submerged in coolant or the liquid filling in all the gaps in between. The coolant will be pumped through 2 circuits, one for the right and another for the left side of the aircraft. Each of these 2 circuits will include the modules from that side's battery, the electric motors on that side of the aircraft, 1 aluminium heat exchanger and 1 pump driving the coolant. This whole architecture can be seen in [Figure 11.4](#). The heat exchangers and pumps will be placed on the side of the aircraft in the bulbous fairings that house also the landing gear. The heat exchanger and pump assembly is represented by the box that has red (hot) coolant input and blue (cold) coolant output. Cooling pipes will run to the motors up in the wings through the truss structure, as can be seen by the pipes showing coolant heat up (blue -> yellow -> orange). Note that when cooling is not required anymore, for example during the descent phase, the air inlet to the heat exchangers will be narrowed, decreasing the frontal area of the heat exchanger and insuring that the battery stays at nominal temperature before landing and is preconditioned for charging.

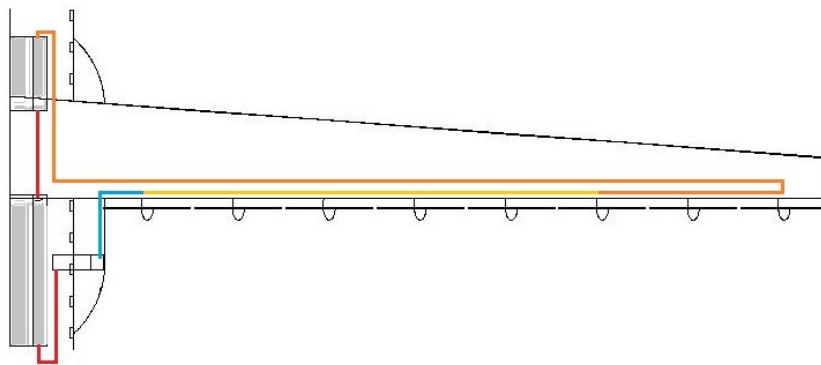


Figure 11.4: BTMS Architecture

11.3.3 Thermal Management Strategy

In order to understand what the BTMS needs to be sized for, it is interesting to understand how the temperature of the battery evolves over the course of the mission profile if there is absolutely no cooling. For this, it was assumed that the battery is completely isolated and all the heat generated goes back into heating the battery and the coolant just resting inside it. The parameters taken into account such as the masses of coolant, battery and their specific heat capacities are shown in [Table 11.2](#).

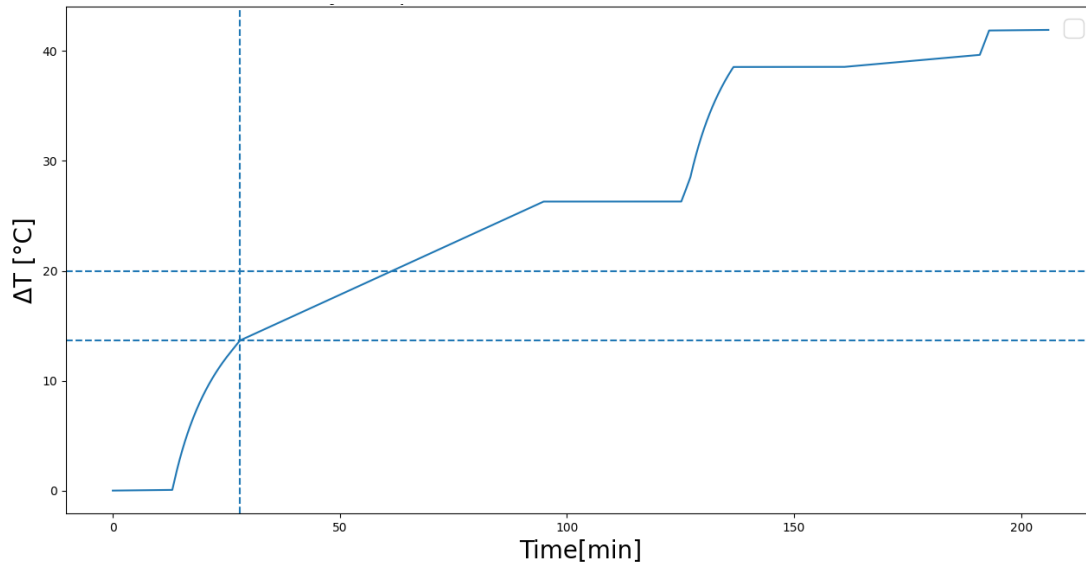


Figure 11.5: Battery ΔT Over the Mission Profile

Figure 11.5 shows that in these conditions, the temperature would increase by 13.7 °C until the start of cruise. The start of cruise is after 28 minutes and that is the point where the power is decreased and the heating is slower. In terms of strategy, this means that precooling the batteries to 15°C before taking off, the cooling system can be sized for only the continuous power being drawn from the battery at cruise when the battery needs to maintain the nominal 25°C. The temperature would increase by 13.7°C until the start of cruise, i.e. up to 28.7°C which is below the maximum temperature allowed. In fact, although sized for cruise power, the cooling system can be started in-flight way before actually reaching cruise. While it will not be able to maintain the battery at 25°C, it is able to create a more significant margin to the maximum allowed temperature.

11.3.4 System Sizing

Having established that the cooling system has to be sized for cruise, the actual sizing can begin. Coolant mass flow is obtained from the equations:

$$\dot{Q}_{cruise} = \dot{Q}_{battery} + \dot{Q}_{motors} = I_{cellcruise}^2 * R_{cellint} + 0.071 * P_{cruise} \quad (11.5)$$

$$\dot{Q}_{cruise} = \dot{m}_{coolant} * C_{coolant} * \Delta T \quad (11.6)$$

The ΔT of the coolant over its travel through the circuit from Equation 11.6[65] was initially assumed to be 25 °C. That is because the battery is to be kept at 25°C and the coolant was assumed to reach 0°C after passing through the heat exchanger, considering that at cruise, the outside temperature is approximately -20°C. It is necessary to check if this assumption of ΔT would actually satisfy the requirement. For that, using the previously computed mass flow, the density of the coolant, and the smallest cross-sectional area of the cooling circuit in-between two cylindrical cells, the velocity of the coolant fluid was computed. Using that and the length of the battery circuit, as well as the length of the electric motors circuit on one wing, one can compute the time a certain "control volume" of coolant spends within the circuit. Afterwards, from the time spent in the circuit and the heat flow, the heat that is transferred to a fixed mass of coolant is computed. From this heat and mass, the required ΔT was computed and the value is for coolant that passes through both linked circuits is approximately 20°C. Applying a 1.25 safety factor gets exactly to the initially assumed value.

11.3.5 Heat Exchanger Sizing

One of the most important components of the BTMS is the heat exchanger, also known as the radiator. The importance lies with the fact that it defines the frontal area that needs to be exposed to the flow, as well as a significant mass component that needs to be taken into account for the mass estimation of the full aircraft. The approach that was taken for sizing the heat exchanger is based on the method of Dragan Kožulović from his paper "Heat Release Of Fuel Cell Powered Aircraft" [9].

The heat exchangers will be made from aluminium, as this is used for similar applications in aviation and motor sports that require high power and low weight. First of all, the geometric parameters of the radiator are initialised. The radiator is assumed to have cross-flow, i.e. the coolant passes in tubes that are perpendicular to the airflow. The airflow tubes have a triangular cross-section, as can be seen in Figure 11.6.

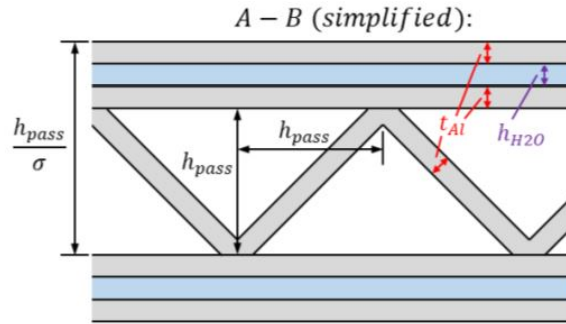


Figure 11.6: Heat Exchanger Frontal Geometry [9]

After determining the cross-sectional dimensions of the tubes, a relation between the number of said tubes n_{tubes} and the depth of the heat exchanger, l_{tube} is set up. The coolant mass flow is split between the respective number of tubes, as can be seen in Equation 11.7. Then, the length is calculated using Equation 11.8. The F_{size} is a safety factor of 1.2 applied on the size of the heat exchanger, as recommended in the method of the paper [9], to account for possible inaccuracies. The ratio of fluid temperature change over local temperature change is shown in the paper, for a similar scenario, to be 0.4, therefore this value is also used in the current calculation. The α_{HE} is the heat transfer coefficient between coolant and aluminium and is also taken from the paper, although that method used water instead of the water and ethylene glycol mix of the current design. The ethylene glycol mix is used because it has a freezing point below 0°C and the coolant risks dropping below that temperature in cruise conditions.

$$\dot{m}_{tube} = \frac{\dot{m}_{coolant}}{n_{tubes}} \quad (11.7)$$

$$l_{tube} = F_{size} * \frac{c_{coolant} * \dot{m}_{tube}}{e * \alpha_{HE}} * \frac{\Delta T_{fluid}}{\Delta T_{local}} \quad (11.8)$$

$$A_{frontal} = \frac{n_{tubes} * h_{pass}^2}{\sigma} \quad (11.9)$$

$$m_{HE} = n_{tubes} * l_{tube} * e * t_{Al} * \rho_{Al} \quad (11.10)$$

Changing the number of tubes gives the same mass for the heat exchanger every time, but different pairs of frontal area, that is computed with Equation 11.9 and depth of the radiator. These pairs can be visualised in the graph below Figure 11.7.

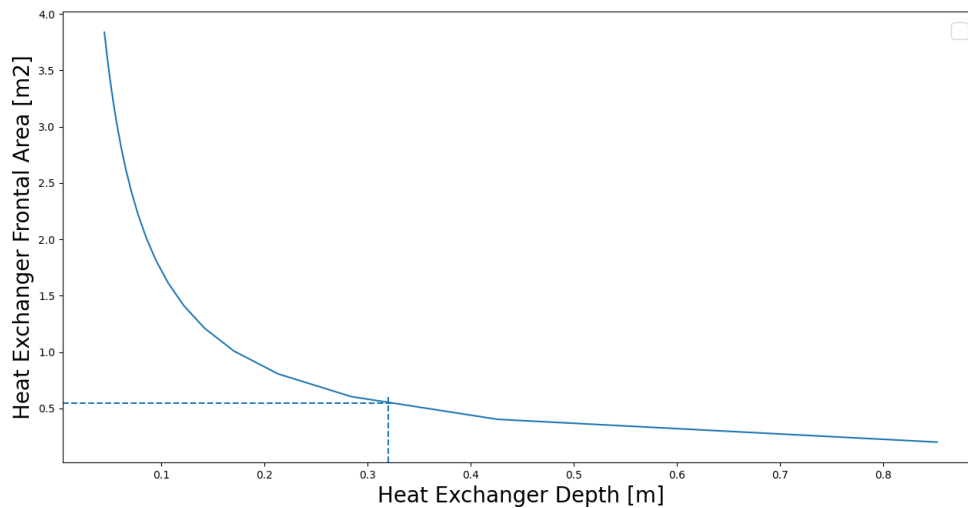


Figure 11.7: Heat Exchanger Frontal Area vs. Depth

The actual selection of this pair is based on being able to package the heat exchanger in the fuselage belly fairing that is used for storing the main landing gear. The final pairing consists of using heat exchangers of 0.55m^2 frontal area and 32cm depth, placed in the fairing, as can be seen in the rendering below [Figure 11.8](#). In a further, more detailed design, such a decision should be taken based on the drag penalty imposed by the respective frontal area and shape of the air inlet, which is not estimated in this phase of the design. Also, the power required is not estimated in this current sizing, as from literature it was found to be less than 1% of the total power consumed by the aircraft [\[66\]](#), but it should be included in a more detailed design down the road.

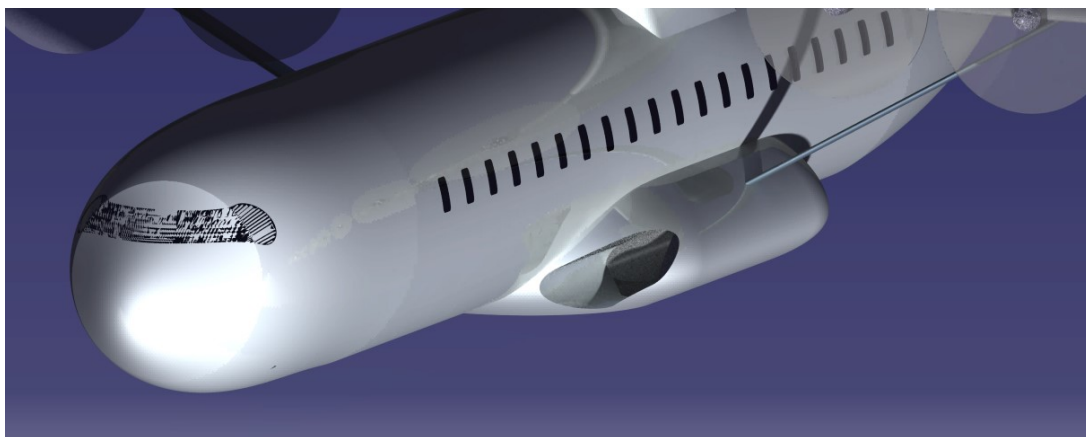


Figure 11.8: Heat Exchanger and Air Inlet in Fuselage Belly Fairing

The final values and all the parameters used are presented in the [Table 11.2](#). The final component masses for 1 cooling circuit (i.e. for one side of the aircraft, one battery) are presented in [Table 11.3](#). Note that the coolant inside the battery is contained within the total battery mass. Only the coolant in the pipes is taken into account as added BTMS mass.

Table 11.2: BTMS Parameters and Results Table

Parameter	Value	Unit
$R_{cell-internal}$	37e-3	Ω
$m_{coolant-battery}$	310	kg
$C_{coolant}$	3473	J/kg*K
$\rho_{coolant}$	1040	kg/m ³
$\dot{m}_{coolant}$	2.76	kg/s
α_{HE}	112	W/m ²
h_{pass}	10	mm
e	48.284	mm
σ	0.495	-
t_{Al}	0.1	mm
ρ_{Al}	2700	kg/m ³
n_{tubes}	3000	-
l_{tube}	0.32	m
$A_{frontal}$	0.55	m ²
$m_{heat-exchanger}$	11.1	kg

Table 11.3: BTMS Components Mass Overview

Component (for 1 battery i.e. 1 side)	Mass
Coolant in Battery Packs	310 kg
Coolant in Pipes	10 kg
Heat Exchanger	11.1 kg
Pump	15 kg
Coolant Lines and Control Units	12 kg
Total per Side (coolant in the battery NOT included)	48.1 kg

12

Converging to Final Design

Different subsystems of the aircraft were designed by different departments, whilst their inputs and outputs were interrelated. Therefore, it was crucial to combine all calculations and connect the inputs and outputs everywhere. In order to reach an optimal design, iterations were necessary. This is the topic of this chapter. The process of combining and iterating the code is presented in [section 12.1](#). The final design itself is presented in [section 12.2](#). In order to see whether the requirements have been met, a compliance matrix is presented in [section 12.3](#). In [section 12.4](#), a sensitivity analysis is presented to see how changes in the major requirements compare. Finally, in [section 12.5](#), the outcomes of this sensitivity analysis are compared to the outcomes from the Class I sensitivity analysis and the resource allocation in the midterm and baseline reports.

12.1 Iterative Process Description

In order to setup the iteration process, a number of steps were taken. Initially, it was crucial to identify inputs and outputs for each department. The Design N2 chart, which was previously made in the Midterm report, shown in [Figure 12.1](#), was particularly useful for this task. From each of the Python scripts that were written for the subsystems of the aircraft, variables that change with iterations were collected. These variables include, amongst others, the fuselage length, MTOW, wing area, horizontal tail size and many more. In every iteration, these were updated and used as inputs in the subsystem calculations. Besides these, there were also a number of parameters which were kept constant throughout the iterations. These included the wingspan, the cruise altitude, the cruise speed, battery energy density, among others.

The iteration loop was designed in a way to minimise its impact on computational cost while maximising the strictness of its convergence criteria. In order to do this, the computationally expensive calculations had to be identified. After a run of the code, two computations were identified: the calculation of the induced drag (which involved an XFLR5 simulation, which was not automated) and the structural optimisation of the wing box (which takes around 10 minutes). Since the induced drag (for a fixed wingspan) is not bound to drastically vary within iterations, and the same can be said for the fraction of wing weight over MTOW, these were kept constant during a first round of iterations,

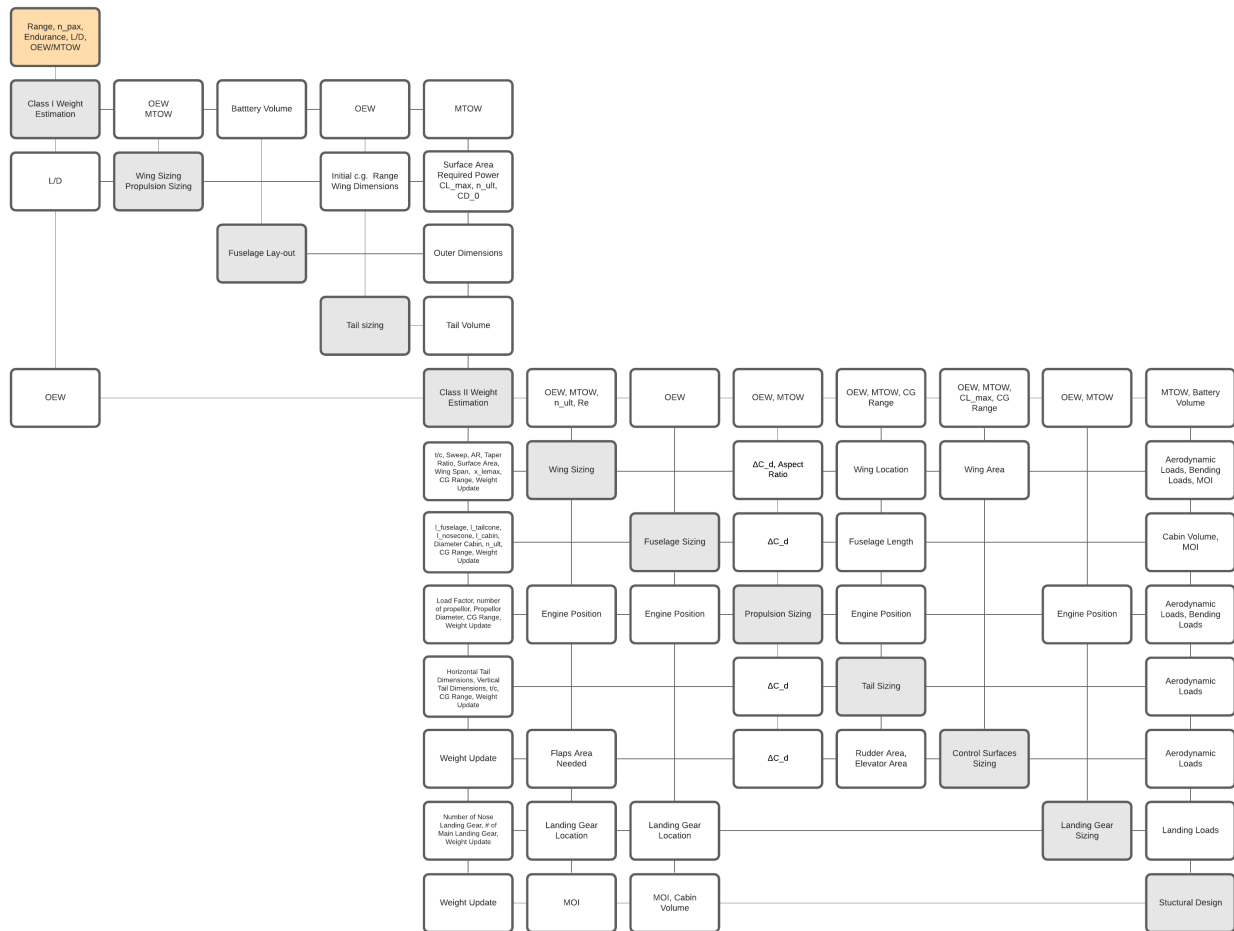


Figure 12.1: Design Process N2 Chart

and then updated only when the design converged. Then, the new induced drag and wing weight fraction values were updated, and the initial, inner iteration loop was repeated. This process in itself is represented by another, outer iteration loop. For both the inner and the outer loops, stopping criteria must be correctly set to define convergence. For the MTOW, a difference (ϵ) between successive inner iterations of 0.1% was set, while for the outer iterations 1% was used. On the other hand, for the wing weight and induced drag, an error of 1% was used. A stricter criterion was imposed on the MTOW since it is typically defined as the main convergence parameter in the aircraft design iteration loop [32]. The whole process, with the inner (yellow blocks) and outer iteration loops, is visually outlined in Figure 12.2.

After it is set up, the iteration loop can be run to convergence. With initial estimates as the values given in the midterm report[1], the iteration loop was initiated. After three outer iterations, for a total of 18 iterations, the design converged. The most important, general final values are all given in section 12.2, while the more specific ones are all given in the previous subsystem chapters. In order to see how the MTOW changed with iterations, it was plotted against the iteration number in Figure 12.3, alongside the C_{D_i} and the wing weight fraction, $W_w/MTOW$. From Figure 12.3, it is also possible to observe how, as explained in the previous paragraph, between outer iterations, only $W_w/MTOW$ and C_{D_i} were changed, before rerunning the inner iteration loop to convergence. This meant that a number of other parameters needed to be used as estimates at the start of each outer iteration, such as the structural efficiency f_e . For simplicity, these were always kept the same as the estimates from the midterm report[1] (for f_e this was 0.5, far from the final 0.403). This was done for simplicity (since changing all the estimated parameters would take a lot of time) under the assumption that, if the variation between the input and the final parameters is small enough, the system would converge to the same point. This is predicted to be a valid assumption, since f_e is

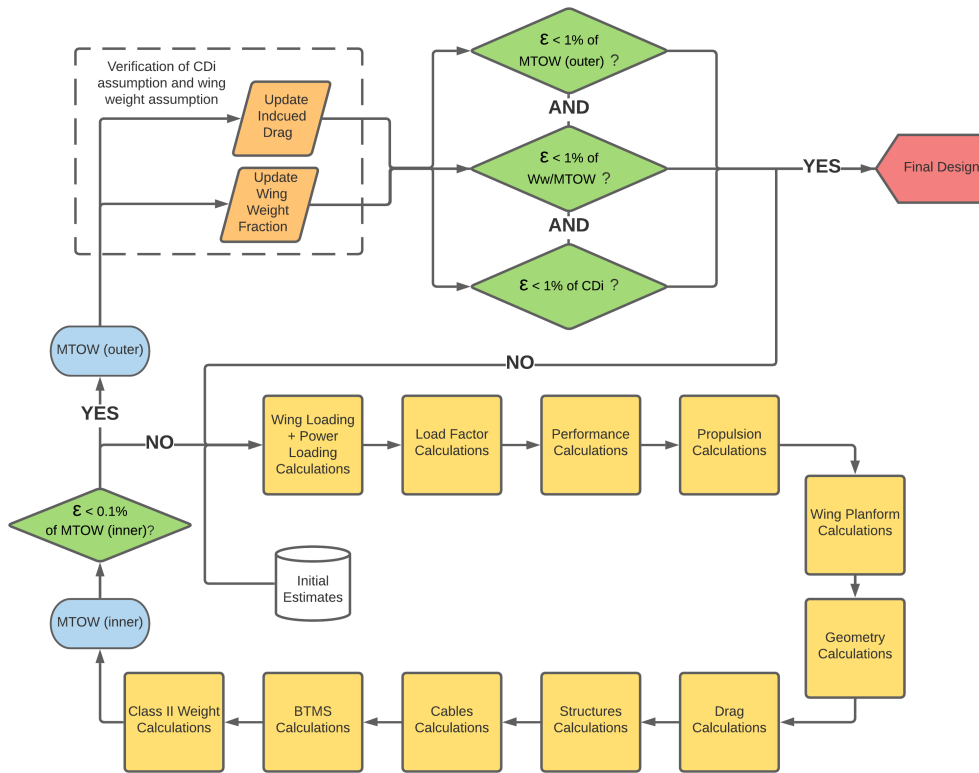


Figure 12.2: Iteration Process Flowchart

recomputed at each iteration, together with many other parameters. This assumption is then verified in the sensitivity analysis of the iteration loop, presented in subsection 12.1.1, by changing the f_e estimate and seeing the effect on the final, converged value.

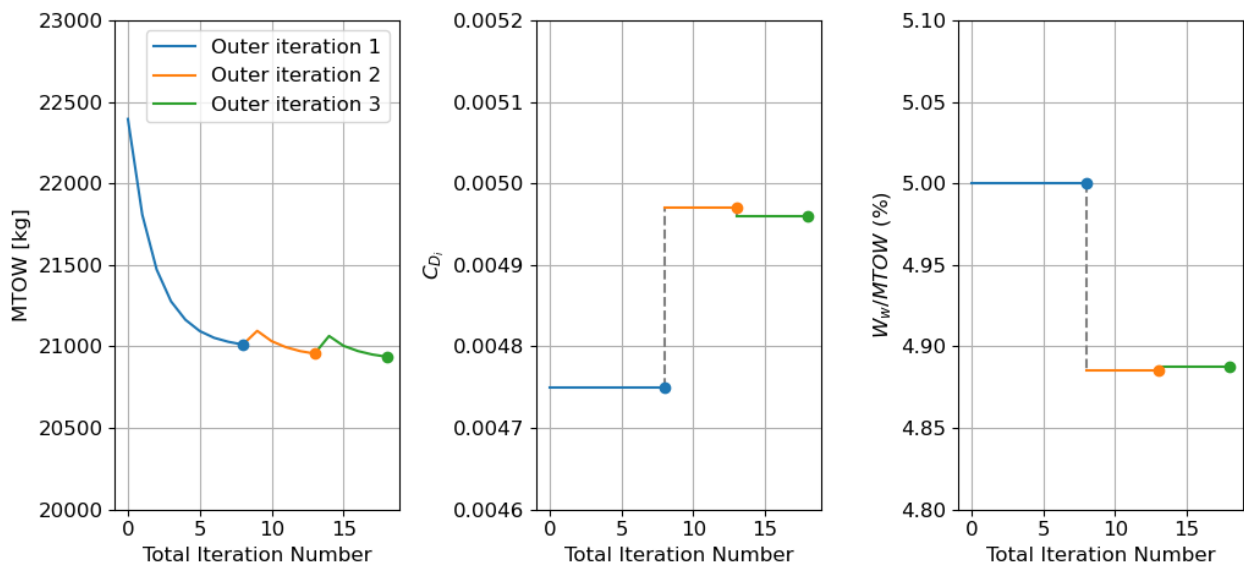


Figure 12.3: Iteration and convergence overview for the MTOW, C_{Di} and wing weight fraction.

12.1.1 Iteration Initial Estimates Sensitivity Analysis

To evaluate the sensitivity to the initial estimates for the iteration loop, the first outer iteration in Figure 12.3 was chosen as a focus. The initial estimate for MTOW was varied and the effect on the final convergence value was observed. This can be analysed with the use of Figure 12.4, which shows the original, blue estimate also used in Figure 12.3, alongside four other input graphs. A black line

is drawn for the originally converged MTOW value, with a 0.1% margin on it, which corresponds to the criterion set within the inner iteration loop, as outlined in Figure 12.2. As can be seen, there are three lines which converge (the blue, orange and green ones), while the other two enter an oscillatory mode which appears to not converge. This is due to the choice mechanism for the number of engines: even though it is based on efficiency, in this case they keep oscillating between 18 and 16. If this was to happen in the iteration loop, it would be wise to fix the number of engines to one of the two numbers, check the converged result and compare it to fixing the other number. Fortunately, the estimate for MTOW for the design was consistent with the other input parameters, and as such, this type of oscillation did not occur. In short, it is important to have consistency between input parameters for a fully convergent design.

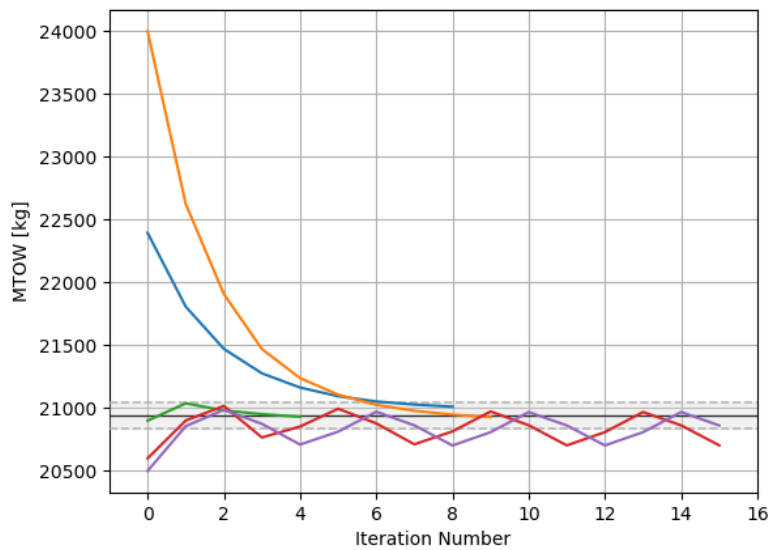


Figure 12.4: Effect of changing the initial MTOW estimate on the first outer iteration in Figure 12.3. For the red and purple lines, the iterations were truncated after 15.

As mentioned in section 12.1, the sensitivity to the structural efficiency f_e is important for the verification of the outer-inner-iteration loop. This is because f_e was kept at the initial estimate on the second iteration loop, rather than being updated. As such, the first outer iteration was repeated with varying estimate values of f_e , ranging from 0.2 to 0.6, but no change was identified in the convergence of this iteration. Not only the final value was the same, but also the rate of convergence. This is probably because f_e in itself only influences a parameter which very slightly affects the convergence, and since it is recomputed for every inner iteration, this has little to no effect overall. As such, the iteration method described in section 12.1 is considered verified.

A final interesting aspect to analyse are the two kinks present in Figure 12.3, at the start of the second and third iteration. Originally, it was thought that these were affected by f_e , but since it has been proven that this has little to no effect both on the rate of convergence, it must be another parameter which is set as an inaccurate initial estimate. Since the graph jumps back down (as expected, this is also probably a parameter which is re-computed at every iteration, and as such, it probably does not influence the final converged value. Nevertheless, having more accurate estimates at every intermission of outer iterations would have eased the computational cost of this iterative process, since the kink would have probably not been there.

12.2 Final Design

A converged design was achieved after the differences between the $MTOW_{outer}$, CD_i and $\frac{W_{wing}}{MTOW_{outer}}$ were smaller than 0.1%, 1% and 1% of their previous values respectively, as described in section 12.1.

The numbers and figures that were used in the previous chapters (chapter 5 through chapter 11) are the ones that were obtained from the final design. To avoid ambiguity on the final design numbers, all the values throughout the report correspond with the final design. The most important parameters, including the ones that varied between iterations are again presented in this section. The final performance values are presented in Table 12.1, the final structures and weight values are presented in Table 12.2, the final aerodynamics values are presented in Table 12.3, the final propulsion values are presented in Table 12.4 and the final geometry and stability values are presented in Table 12.5.

Table 12.1: Performance Final Design Parameters

Performance		
$RC_{max_{sl}}$	13.05	m/s
$R_{nominal}$	800	km
$R_{diversion}$	185	km
T_{loiter}	30	min
h_{cruise}	6000	m
V_{cruise}	138.89	m/s
$V_{approach}$	72.02	m/s
$S_{standing}$	1500	m
$S_{take-off}$	1500	m

Table 12.2: Structures/Weight Final Design Parameters

Structures / Weight		
$W_{wingstructure}$	1024.06	kg
$W_{fuselage}$	3077.19	kg
OEW	8429.45	kg
$W_{battery}$	6919.92	kg
$W_{passenger+luggage}$	106.00	kg
$W_{additionalcargo}$	500.00	kg
$W_{payloadtotal}$	5588.00	kg
$MTOW$	20937.37	kg

Table 12.3: Aerodynamics Final Design Parameters

Aerodynamics					
AR_{eff}	22.80	-	e	0.93	-
b	36	m	$h_{winglet}$	0	m
C_{D_0}	0.0165	-	L/D	28.24	-
C_D	0.0221	-	MAC	1.68	m
$C_{L_{cruise}}$	0.5955	-	S	56.85	m ²
$C_{L_{max, clean}}$	1.75	-	Λ_{LE}	0	deg
$C_{L_{max, landing}}$	2.3	-	λ	0.4	-

Table 12.4: Propulsion Final Design Parameters

Propulsion		
N_{engine}	16	-
D_{prop}	1.907	m
$T_{st, engine}$	3.6	kN
RPM setting	1809	rpm
Q_{engine}	1026	Nm
P_{engine}	194.6	kW
Take-Off Run	1101	m

Table 12.5: Geometry/Stability Final Design Parameters

Geometry / Stability					
n_{PAX}	48	-	AR_{hor}	5	-
$D_{fuselage_{outer}}$	2.82	m	AR_{vert}	1.3	-
$l_{fuselage}$	26.63	m	$\Lambda_{horizontal}$	8	deg
l_{cabin}	16.03	m	$\Lambda_{vertical}$	25	deg
$l_{nosecone}$	4.51	m	$S_{aileron}$	4.82	m ²
$l_{tailcone}$	7.33	m	$S_{elevator}$	1.91	m ²
$S_{horizontal-tail}$	5.61	m ²	S_{rudder}	2.64	m ²
$S_{vertical-tail}$	13.19	m ²	$T_{differential}$	2252.97	N
$S_{horizontal-tail}/S$	0.0986	-			

Furthermore, the fuselage cross-section was presented in Figure 8.1. The top view of the three-abreast configuration was shown in Figure 8.2. The technical three-view drawing of ECHO-1 is presented in Figure 12.5.

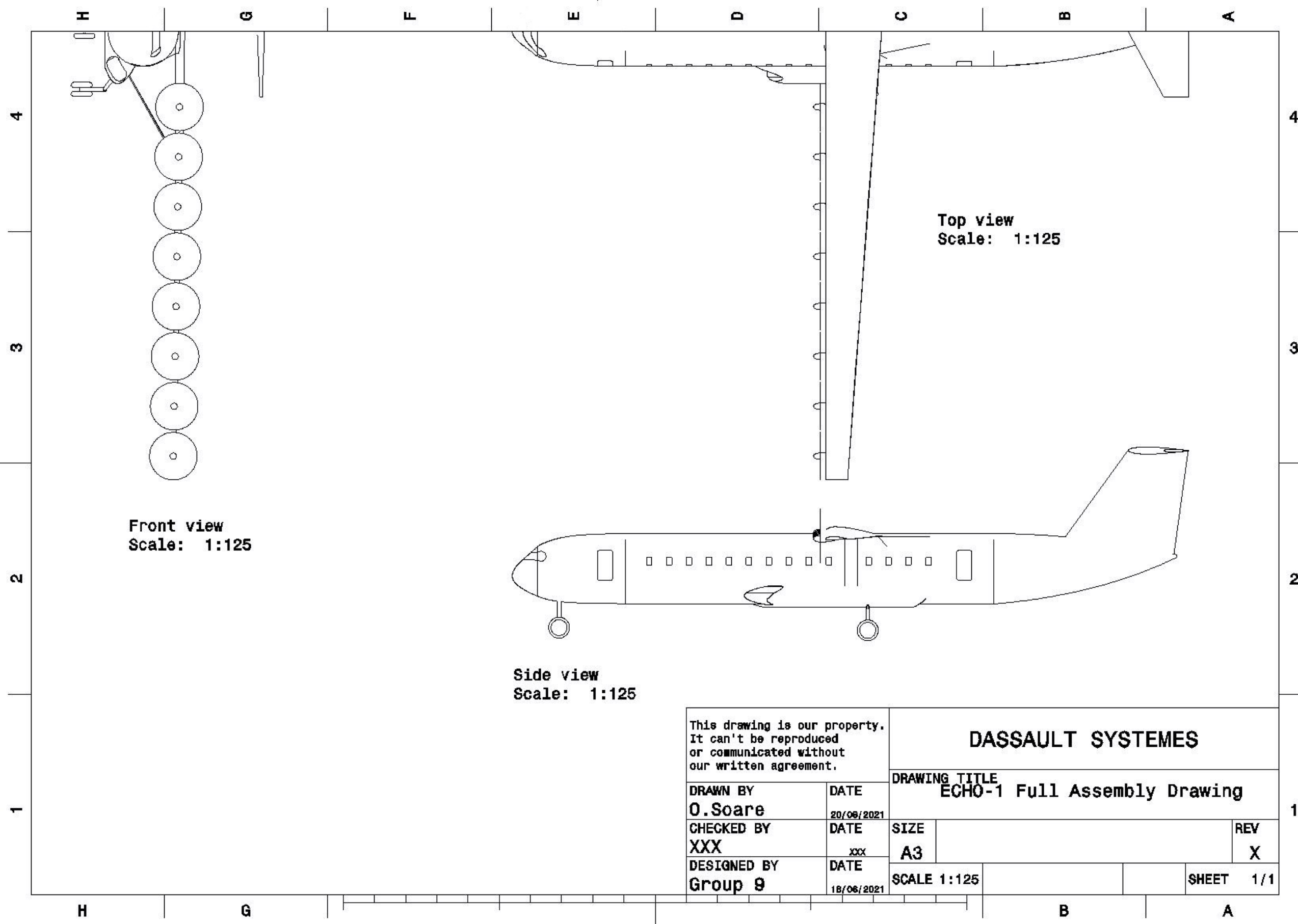


Figure 12.5: ECHO-1 Three-View

12.3 Compliance Matrix

In this section the compliance matrix that shows if the requirements have been met will be presented. All the requirements that have been used for the design along with their status are shown in [Table 12.6](#). A number of requirements that were presented in the Baseline Report were reevaluated as being redundant at some point in the design phase. These have been left out of the current compliance matrix. If, in the status column, the cell is green, the requirement is met. Otherwise, if red, the requirement is not met. Note that requirements that bear an ID with a ".1" at the end have been changed since the midterm report[1].

It is also important to note that 4 requirements have not been met. Requirement SUB-POW-3 that refers to the necessity of redundancy of electrical wiring is not met because the cables that link the motors to the batteries add extra weight and doubling their number would lead to quite large increase in mass. Furthermore, redundancy regarding engine-inoperative cases or battery cell failures is already built into the system through the battery architecture and the motor grouping, so there is not necessarily need for redundancy in the cables. Requirement SUB-PROP-10 regarding reverse thrust was not met because it was discovered during the design process that this capability is not actually needed for any flight phase and therefore the propulsion system has not been designed for it. Requirement SUB-OPS-3 is not met because in passenger configuration, the standardised cargo containers are too big to fit in the allocated cargo compartment cross-section in the belly of the fuselage.

Table 12.6: Compliance matrix

Req. ID	System Requirements	Status
SYS-PERF-1.1	The aircraft shall be able to carry a payload of 48 passengers in passenger transport configuration.	
SYS-PERF-2.1	The aircraft shall be able to carry 5588 kg of cargo in cargo configuration.	
SYS-PERF-3.1	The aircraft shall have a range of 800 km at maximum payload.	
SYS-PERF-4	The aircraft shall have a cruise speed of 500 km/h.	
SYS-PERF-5	The aircraft shall have a mission block time of 2.5 hours.	
SYS-SR-1	The aircraft shall be compliant with current EASA CS25 regulations.	
SYS-COST-1	A battery life-cycle financial plan shall be made if the battery life cycle is affecting the direct operating cost.	
SYS-LIFE-1	The aircraft shall have a minimum lifespan of 10 years.	
SYS-OPS-1	The aircraft's wingspan shall be smaller than or equal to 36m.	
SYS-OTHER-1.1	Adequate technology parameters and technology readiness levels shall be considered to forecast an Entry Into Service in 2035	
SUB-AERO-AC-1.1	The aircraft shall have a lift-over-drag ratio (L/D) larger than 28 in cruise configuration.	
SUB-AERO-AC-3	The aircraft shall be laterally stable in any flight configuration or phase.	
SUB-AERO-AC-4	The aircraft shall have a negative $C_{m\alpha}$ to achieve longitudinal stability in any flight configuration or phase.	
SUB-AERO-AC-5	The aircraft trimmed for straight flight at a speed selected by the pilot, shall not be at a speed less than 1.13 of the stall speed. (CS25.107 (b))	
SUB-AERO-AC-12	In clean configuration and perfect working conditions, the aircraft shall fly during landing with a speed of at least 1.23 of the stall speed (CS25.125)	
SUB-AERO-AC-16	The aircraft shall be able to withstand a load factor of not less than 2.5g and not more than 3.8g (CS25.337)	
SUB-AERO-AC-17	The aircraft shall be able to withstand a load factor of not less than -1.0g (CS25.337)	
SUB-AERO-AC-19	The aircraft shall be able to meet the trim requirements at the controllable speed set in SUB-AERO-AC-23 (CS25.161)	
SUB-AERO-AC-20	The airspeed shall return to within 10% of the original trim speed for the climb, approach and landing conditions when the control force is slowly released from any stable speed (CS25.173)	
SUB-AERO-AC-21	he airspeed shall return to within 7.5% of the original trim speed for the cruising condition when the control force is slowly released from any stable speed (CS25.173)	
SUB-AERO-AC-22	Any oscillation occurring between 1.13 of the stall speed and maximum allowable speed appropriate to the configuration of the airplane shall be heavily damped with the primary controls (CS25.181)	
SUB-AERO-AC-25	The aircraft shall have the cruise speed of not more than 0.8 of the dive speed (CS25.335(b))	
SUB-AERO-AC-26	The aircraft shall have a maneuvering speed of at least stall speed times the squared root of the load factor (CS25.335(c))	
SUB-AERO-WING-1	The wing shall provide a minimum lift coefficient $C_{L_{cruise}}$ of 0.550 in cruise.	
SUB-AERO-WING-2	The wing shall have a maximum lift coefficient $C_{L_{max}}$ larger than <TBD> in clean configuration.	
SUB-AERO-WING-4	The wing shall have a minimum aspect ratio of 21.	
SUB-AERO-WING-5	The wing root shall stall before the wing tip.	
SUB-AERO-AIRF-1	The airfoil shall provide a minimum lift coefficient $C_{L_{cruise}}$ of 0.575 in cruise configuration.	
SUB-AERO-AIRF-2	The airfoil shall not have a sudden drop in the $C_{L\alpha}$ curve after $C_{L_{max}}$ in order to have a predictable stall behaviour.	
SUB-AERO-AIRF-3	The airfoil shall have a maximum thickness-to-chord ratio larger than 14.	
SUB-AERO-HLD-1	The HLD shall increase the $C_{L_{max}}$ of the wing by a value of 0.3 .	
SUB-AERO-HLD-2	The HLD shall be easily accessible and inspectable for maintenance.	
SUB-AERO-HLD-3	The HLD shall be as simple as possible, to mitigate the risk of mechanical failure.	
SUB-AERO-AIL-1	The ailerons shall provide a roll performance of 45 deg in 1.4 s in clean configuration, according to Class II aircraft specifications.	
SUB-POW-1	The power subsystem shall deliver an output power of 3.1 MW in take-off configuration.	
SUB-POW-2	The power subsystem shall keep all power requiring systems powered during nominal flight operations.	
SUB-POW-3	All electrical wiring connections shall have 1 or more redundant replacements in case of an electrical failure.	
SUB-POW-BAT-1	The power subsystem shall use batteries with a battery energy density that ensures a minimal MTOW.	
SUB-POW-BAT-2	The power subsystem shall use electrical batteries as its sole form of energy storage.	
SUB-POW-BAT-3	The Depth of Discharge of the batteries shall not be more than 5%, taking into account both battery life and reserve energy required.	
SUB-POW-BAT-4	The required battery life shall be sufficient to ensure minimal recharge procedure operational costs during the aircraft's whole lifetime.	
SUB-POW-BAT-5	The battery maintenance shall ensure a minimal replacement of batteries during the whole aircraft's lifespan.	
SUB-POW-BAT-6	The battery shall be insulated in such a way that its thermal excursion does not hinder its required power outputs during all stages of flight and ground operations.	
SUB-POW-BAT-7	The battery shall be insulated in such a way that its thermal excursion does not cause long-term degradation in any way.	
SUB-POW-BAT-8	The battery capacity shall not drop below 85% of its original value before being replaced.	
SUB-POW-BAT-9	A battery life-cycle financial plan shall be made when the battery life cycle is affecting the direct operating cost.	
SUB-POW-BAT-10	The battery should be kept between 15 deg C and 35 deg C.	
SUB-POW-OPS-3	The power subsystem output voltage shall match the voltage level required by the sub-systems it supplies power to.	
SUB-POW-OPS-4	The aircraft shall have enough reserve battery energy for loitering.	
SUB-POW-OPS-6	The power system shall keep the battery temperature in the temperature range as specified by the battery manufacturer.	
SUB-POW-OPS-7	Safe cell temperatures and pressures must be maintained during any probable charging or discharging condition (CS25.1353(c))	
SUB-POW-OPS-10	The power system shall keep the battery cells operating voltage in the operating window specified by the manufacturer at all times.	
SUB-POW-LOG-2	The power subsystem shall allow for easy access for battery replacement.	
SUB-POW-LOG-3	The power subsystem shall allow for a safe and logistically simple battery recharge procedure.	
SUB-SMG-STR-1	No flight condition shall induce vibrations with frequency equal to the natural frequencies of the structure parts.	
SUB-SMG-STR-4a	The structure must be able to support limit loads (the maximum loads to be expected in service) without detrimental permanent deformation. At any load up to limit loads, the deformation may not interfere with safe operation.	
SUB-SMG-STR-4b	The wingbox maximum shear stress during flight with ultimate load factor should be below the maximum allowable shear stress of the material	
SUB-SMG-STR-4c	The wingbox maximum bottom skin normal stress during flight with ultimate load factor should be below the maximum allowable yield stress of the material	
SUB-SMG-STR-4d	The wingbox maximum top skin normal stress during flight with ultimate load factor should be below the maximum allowable yield stress of the material	
SUB-SMG-STR-4e	The truss maximum normal stress during flight with ultimate load factor should be below the maximum allowable yield stress of the material	
SUB-SMG-STR-4f	The wingbox maximum top skin compressive stress during flight with ultimate load factor should be below the maximum allowable buckling stress of the top panel	
SUB-SMG-STR-4g	The truss maximum compressive stress on ground should be below the maximum buckling stress of the truss (<10.8 MPa)	
SUB-SMG-STR-4h	The wingbox maximum shear buckling stress during flight with ultimate load factor should be below the maximum allowable shear buckling stress of the side panels	
SUB-SMG-STR-4i	The wingbox maximum bottom skin compressive stress on ground should be below the maximum allowable buckling stress	
SUB-SMG-STR-4j	The tip deflection during on-ground operations shall be small enough to allow for safe operations.	
SUB-SMG-STR-12	The aircraft's nose landing gear shall carry a load between 8% and 15% of the total weight of the aircraft.	
SUB-SMG-STR-14	At least 80% of the structure of the aircraft shall be recyclable after the end-of-life.	
SUB-SMG-STR-17	The aeroplane must be protected against catastrophic effects from lightning (CS25.581(a))	
SUB-SMG-STR-18	Non-destructive inspection aids shall be used to inspect structural elements where it is impracticable to provide means for direct visual inspection (CS25.611(a))	
SUB-SMG-STR-19	Manufacturing cost shall be kept as low as possible.	
SUB-SMG-STR-22	The battery integration design choices shall account for minimal additional mass in the surrounding structure.	
SUB-SMG-STR-26	The truss shall only be loaded axially	
SUB-SMG-STR-27	The wingbox shall meet all SUB-SMG-STR-4 requirements for on-ground operations as well as during flight	
SUB-SMG-STR-28	The fuselage weight shall account for the additional structure required for the batteries with respect to the Raymer fuselage weight estimation methods	
SUB-SMG-STR-29	Emissions and energy required shall be considered in the material selection for the structural components of the aircraft	
SUB-SMG-GEO-4	There shall be at least four exits, one of which must be a type I exit on each side of the fuselage (CS25.807(g))	
SUB-SMG-GEO-5	The aisle width shall be at least 51 cm (CS25.815)	
SUB-SMG-GEO-6	The seat width shall be at least 48.26 cm	
SUB-SMG-GEO-7	The armrest width shall be at least 5.08 cm	
SUB-SMG-GEO-8	The aisle height shall be at least 190 cm	
SUB-SMG-GEO-9	There shall be 40 seats in Economy class and 10 seats in First/Business class	
SUB-SMG-GEO-10	The seat pitch for Economy class shall be at least 81.28 cm	
SUB-SMG-GEO-11	The seat pitch for First/Business class shall be at least 88.9 cm	
SUB-SMG-GEO-12	There shall be at least 3 m ³ of volume for in the overhead luggage bin	
SUB-SMG-GEO-13	There shall be at least 2 lavatories	
SUB-SMG-GEO-14	There shall be at least 1 galley	
SUB-SMG-GEO-16	The aircraft shall be controllable when flying with one engine-group inoperative.	
SUB-SMG-GEO-17	The aircraft shall be controllable when landing with cross winds of 30 knots.	
SUB-SMG-GEO-18	The aircraft shall be directional stable.	
SUB-SMG-GEO-19	The aircraft shall be controllable in a spiral manoeuvre	
SUB-SMG-GEO-20	The aircraft shall be controllable at a speed of at most 1.3 of the stall speed (CS25.145 and CS25.147)	
SUB-SMG-GEO-21	The aircraft shall be stable at cruise speed	
SUB-SMG-GEO-22	The aircraft shall allow for a tip back angle of 15 degrees	
SUB-SMG-GEO-23	The aircraft shall have a tip over angle of no less than 55 degree	
SUB-SMG-GEO-24	The elevator shall make the aircraft have a pitch angular acceleration of at least 6 °/s ²	
SUB-SMG-GEO-25	The aircraft cargo holds shall be able to accommodate at least 500 kg of cargo	
SUB-SMG-GEO-26	The aircraft cargo hold shall be able to store the required battery package	
SUB-SMG-GEO-27	The aircraft cargo hold shall be able to store the landing gear	
SUB-PROP-1	The propulsion system shall provide a minimum static thrust of 57 kN at sea level	
SUB-PROP-2	The propulsion system shall not consume more than 3.1 MW of electrical power	
SUB-PROP-4	The propulsion system shall not have a negative influence on the aerodynamic performance of the aircraft	
SUB-PROP-6	The propulsion systems shall use electricity supplied from a battery as its energy form.	
SUB-PROP-7	The propulsion system shall be lighter than the systems found on conventional aircraft with similar and comparable missions.	
SUB-PROP-10	The propulsion system shall allow for reverse thrusting	
SUB-PROP-11	The propulsion system shall be able to have deicing capabilities	
SUB-PROP-12	The propulsion system shall maintain the optimal internal temperature of -40°C - +60°C as indicated by the engine manufacturer	
SUB-PROP-13	The propulsion system shall have a propulsive efficiency greater than 80%.	
SUB-PROP-15	The propulsion system shall be able to operate in an ambient temperature range of -56.5°C - +37.8°C . (CS25.1521 d) [10]	
SUB-PROP-16	The propulsion system shall be able to control its thrust output	
SUB-PROP-18	The propulsion system architecture shall be symmetrical with respect to the center line of the aircraft.	
SUB-OPS-1	The turnaround time of the aircraft shall be at most 30 minutes.	
SUB-OPS-2	The aircraft shall be able to operate in a C/D ICAO Aerodrome Code Letter airport.	
SUB-OPS-3	The aircraft shall be loaded with <TBD> ULD container type cargo.	
SUB-OPS-4	The recharge procedure of the battery subsystem of the aircraft shall take at most 30 minutes.	
SUB-OPS-5	The battery subsystem recharge procedure shall not interfere with the boarding of passengers and cargo loading.	
SUB-OPS-7	The charging airport infrastructure installation shall not be invasive or detrimental to the nominal airport operations.	
SUB-OPS-9	The aircraft shall have a competitive maintenance cost with respect to similar aircraft on the market.	
SUB-OPS-10	The aircraft shall have a competitive direct operating cost with respect to similar aircraft on the market.	
SUB-OPS-11	The aircraft shall be able to fly at least 2000 cycles on one battery package	
SUB-OPS-12	The recharge procedure of the battery subsystem of the aircraft shall take at most 29 minutes until a battery degradation of 10% has reached and loitering energy is not included for charging.	
SUB-OPS-13	The Charging cables shall not require any ground personnel	
SUB-OPS-14	The Battery Package shall be able to recharge at the power of the charging cables, without any consequence	
SUB-OPS-15	The voltage of the chargers shall match the voltage of the batteries	
SUB-OPS-16	The charging platform shall be able to obtain a sufficient amount of power from the electricity grid	
SUB-OPS-17	The aircraft shall be safe while operating	
SUB-OPS-18	The airport shall be supply the electricity power needed for recharging multiple electric aircraft.	
SUB-SUS-EM-1	The aircraft shall be operated with zero COx emissions.	
SUB-SUS-EM-2	The aircraft shall be operated with zero NOx emissions.	
SUB-SUS-EM-3	The aircraft shall be operated with zero SOx emissions.	
SUB-PERF-TO-1	The aircraft shall be take off from a runway of 1500 m, MTOW, ISA sea level conditions	
SUB-PERF-TO-2	The aircraft shall be land on a runway of 1500 m, MTOW, ISA sea level conditions	
SUB-PERF-CL-1	The aircraft shall be able to achieve a climb rate of 9.4 m/s at sea level, MTOW, ISA standard atmosphere	
SUB-PERF-CL-2	The aircraft shall be able to achieve a climb rate of 1.5 m/s at cruise altitude, MTOW, ISA standard atmosphere	
SUB-PERF-CL-3	The aircraft shall be able to climb to climb to FL170 in 762 seconds, MTOW, ISA standard atmosphere	
SUB-PERF-APP-1	The aircraft shall have an approach speed of 140 kts, MTOW, ISA sea level conditions	
SUB-PERF-RES-1	The aircraft shall have enough battery energy to divert for 185 km as well as loiter for 30 min. on top of the nominal mission mission range	
SUB-PERF-APP-1	The aircraft shall have an approach speed of 140 kts, MTOW, ISA sea level conditions	

12.4 Final Design Sensitivity Analysis

This section will present the sensitivity of the final design to certain main driving requirements. For a number of these driving requirements, different combinations of payload and range were checked for convergence. This has been done for the battery energy density in [subsection 12.4.1](#), for the landing and take-off distances in [subsection 12.4.2](#) and for the cruise velocity in [subsection 12.4.3](#). The effect on the MTOW is presented for each combination. For each sensitivity analysis, 250 payload-range combinations were tested for convergence. These 250 points make up a grid which has 25 range-inputs (between 350 km and 1400 km) and 10 number of passenger-inputs (between 42 and 69 passengers), as can be seen in the plots. This grid was considered for each of the iterations. For each combination of payload and range, the inner loop of the iteration tool discussed in [section 12.1](#) was run. A number of outcomes are possible:

- Converged
- Too few propellers (*converged*)
- Too many propellers (*diverged*)
- Winglet too large (*diverged*)
- Power too low (*diverged*)
- Too many iterations (*diverged*)

A design still converges if the program states that there are too few propellers. The software tool only prints this to indicate that the number of propellers is significantly lower than for the final design, but in fact it is not a problem, so a design would still converge. Too many propellers would be the case if a design needs more than 24 propellers. This is deemed too large of a number of propellers in order to be operationally competitive. If a design requires winglets that exceed a height of 2 meters, the tool design will also not converge. Finally, if the power available is too little with respect to the required power, the tool will also not converge. Additionally, if too many iterations are required to end up at a converged solution, the program will abort that calculation as it will most likely not end up at a desired outcome.

12.4.1 Sensitivity to Payload, Range and Battery Energy Density

In order to determine the sensitivity of the final design to the battery energy density, for five different battery energy density values (525, 550, 575, 600 and 625 Wh/kg), the sensitivity tool was run. For the final design of ECHO-1, in [Figure 12.6](#), the outcomes are presented, showing a clear distinction between converged designs (green) and diverged designs (red). A similar type of plot was made for each of the other four energy densities. The boundary between converged and diverged designs is shown in [Figure 12.7](#). For these lines, the most right green grid points were used. The lines were created using linear regression on the 10 data points, where R^2 -values of at least 0.995 were achieved since the 250-point grid is discrete, hence the points are not exactly on the line. It can be observed that, as is to be expected, with increasing energy density, higher passenger range combinations can be achieved.

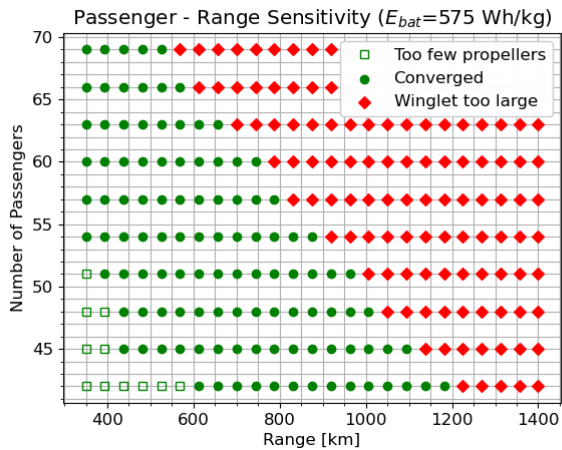


Figure 12.6: Design convergence sensitivity to various passenger and range combinations, with a 575 Wh/kg battery energy density.

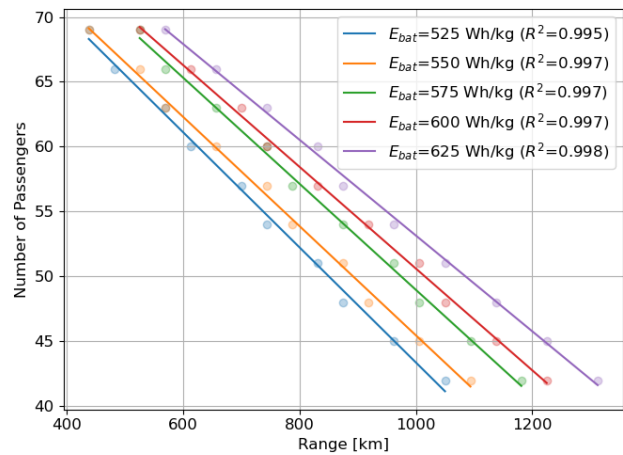


Figure 12.7: Overview of the convergence boundaries for various battery energy densities.

For the baseline energy density (575 Wh/kg) and the two most extreme tested energy densities (525 Wh/kg and 625 Wh/kg), the MTOW of each converged design has been plotted in [Figure 12.8](#), [Figure 12.9](#) and [Figure 12.10](#) respectively. It is clearly visible that MTOW increases with increasing payload-range combinations. For each energy density, the MTOW boundary is approximately 24000 kg, whereas a design for 350 km and 42 passengers would only have a weight of 17000 kg. This can be explained from the fact that a higher energy density allows a plane of the same mass to fly further, since essentially the "snowball" does not start to roll. The same mass of batteries only provides more energy, hence a longer range to be flown or a higher number of passengers to be carried. Another explanation that proves a line of constant mass at the boundary is that for a given MTOW value, using the design point (W/S), a wing area is obtained. From this wing area and the wingspan, the geometric aspect ratio is found and to increase this to the desired 22, a winglet is needed. This winglet height however is constrained such that indirectly, whether a design converges or not is constrained by the MTOW, which in this case is 24000kg for the baseline. Whenever the boundary shifts to the left, the maximum MTOW will decrease. Whenever the boundary shifts to the right, the maximum MTOW will increase. A last thing that can be noticed from the graphs is that for every row of three passengers that is removed, the range can increase for 73 km. Similarly, for every 1 Wh/kg that is added to the battery energy density, the range would be able to increase with 2 km.

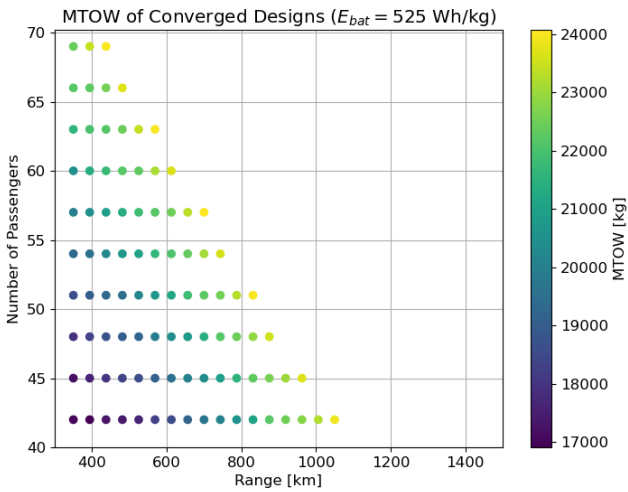


Figure 12.8: MTOW of converged designs at energy density of 525 Wh/kg

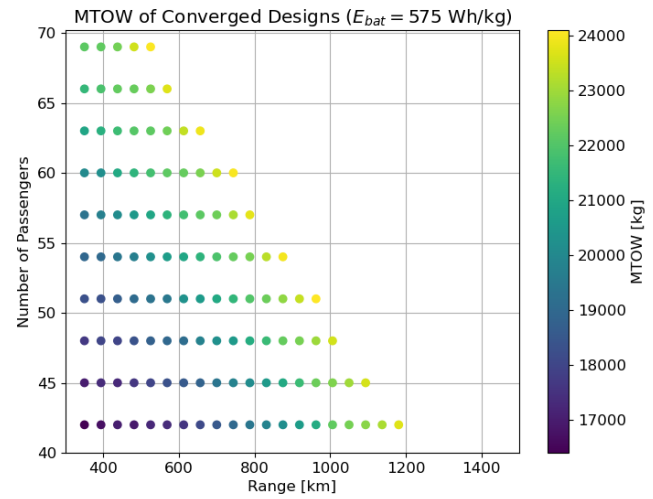


Figure 12.9: MTOW of converged designs at energy density of 575 Wh/kg

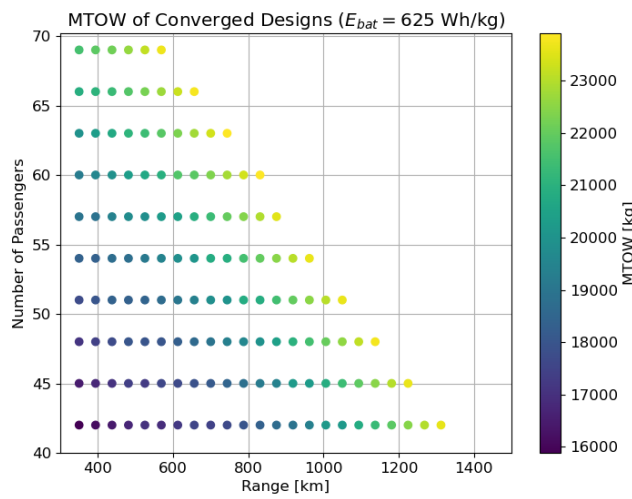


Figure 12.10: MTOW of converged designs at energy density of 625 Wh/kg

12.4.2 Sensitivity to Payload, Range and Landing and Take-off Distances

Similarly to what was done for various battery energy densities, the take-off and landing distance of ECHO-1 was varied. An analysis was performed for a runway length of 1400 meter, as well as for 1600 meter. Figure 12.11 shows how these runway lengths compare to the baseline runway length of 1500 meter of ECHO-1. In contrast to varying the battery energy density, it can be seen that when changing the runway length the effect is not linear. It is interesting to see that reducing the runway length with 100 meters decreases the range with approximately 15% for a 50 passenger configuration. Increasing the runway length with 100 meters, however, only increases the range with approximately 4%. Regarding the MTOW values, similarly to what was found in subsection 12.4.1, the MTOW values are constant over the boundary lines.

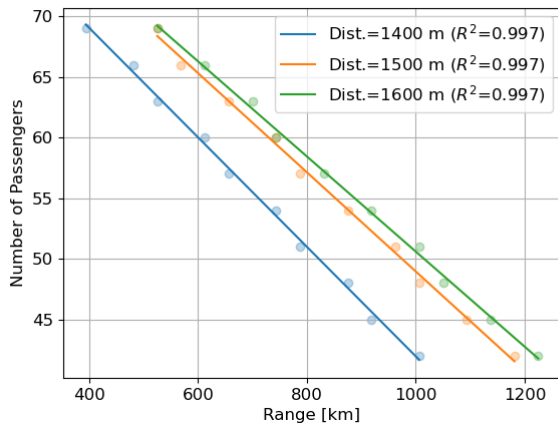


Figure 12.11: Overview of the convergence boundaries for various landing and take-off distances.

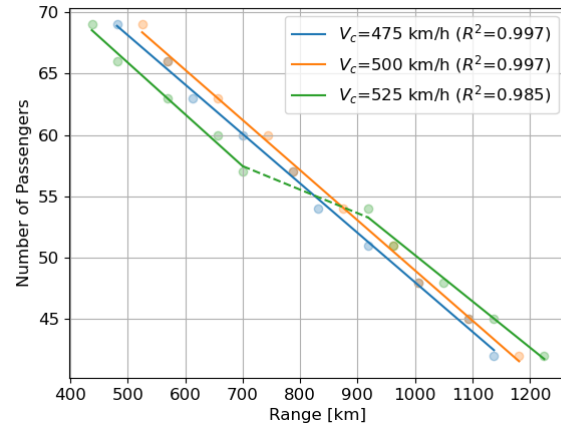


Figure 12.12: Overview of the convergence boundaries for various cruise speeds.

12.4.3 Sensitivity to Payload, Range and Cruise Speed

Finally, the cruise velocity of ECHO-1 was altered to see the effect on the possible payload range combinations. These results are presented in a similar fashion to the previous sensitivity analyses in [Figure 12.12](#). Cruise velocities of 475 km/h and 525 km/h were compared to the baseline cruise velocity of 500 km/h. It can be observed that flying at a slightly lower cruise velocity of 475 km/h, as expected, translates the line to lower payload range combinations. Interestingly, for a slightly higher cruise velocity of 525 km/h, a shift occurs at a design that can house 57 passengers compared to a design that can house 54 passengers. This can be attributed to the fact that for 57 passengers, the reason of not converging is no longer an unacceptable winglet height but the number of propellers. With increasing velocity, the propeller efficiency goes down and following from this, more propellers are required. Since the iterating tool depends on a large number of variables, it is not exactly evident why this shift occurs but this is most likely caused by a shift in number of propellers. Regarding the MTOW values, similarly to what was found in [subsection 12.4.1](#), for the analysis of 475 km/h and 500km/h, the values are constant over the boundary lines. For the 525 km/h boundary, this is not the case, which can be explained using the shift that was discussed before. After having compared the sensitivity to the battery energy density, the runway length and the cruise velocity, it can be noticed that the design is most sensitive to a decrease in runway length, as this largely decreases the feasible payload range options.

12.5 Resource Allocation and Class II Comparison

It is interesting to compare the sensitivity analysis that was performed in [section 12.4](#) to the sensitivity analysis that was performed on the Class I Weight Estimation in the midterm report[1] and to the resource allocation of the baseline report[13]. For the midterm report, the payload-range diagram was presented for energy densities of 500 and 550 Wh/kg, since at that point of the project, the entry into service requirement was not yet delayed to 2035. Additionally, at that point in time, the 36 meter wingspan requirement was not yet determined.

Looking at the payload-range diagram from the midterm report, illustrated in [Figure 12.13](#), it is interesting to see that the effect of increasing the energy density by 10% from 500 to 550 Wh/kg yields a range increase of 100 km, from 1000 km to 1100 km. When looking at [Figure 12.7](#), for a configuration of 51 passengers when increasing the energy density by 8.7% from 575 to 625 Wh/kg, the range extends with 8.4%. This shows that even though the absolute values differ a bit between the two sensitivity analyses, the sensitivity of the range when the battery energy density is altered hardly changes.

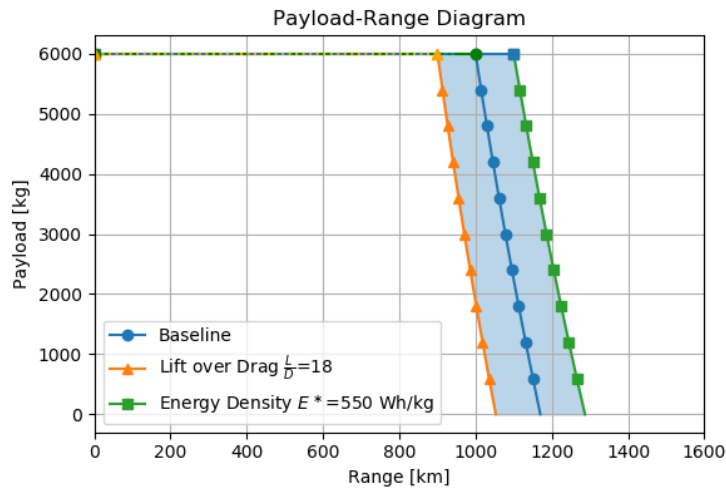


Figure 12.13: Payload-Range Diagram from Midterm Report Values

Secondly, for the baseline report, resource allocation with contingency management was performed. There, technical budgets were determined for the most important parameters and using the contingency allowance for the final design, this section will determine whether those allowances have been met. The four most important parameters and their contingency margins for the final report estimates have been checked, presented in Table 12.7. As can be seen, these four contingency margins were easily met. This is mostly because at the baseline report, the only calculations that had yet been performed were those based on reference kerosene aircraft. These aircraft are much less aerodynamically optimised than ECHO-1 and some of them were a bit larger than ECHO-1. The main conclusion that can be drawn from Table 12.7 is that the initial estimate was quite far off. Fortunately, the direction in which the initial estimate was off was the desired one as in the end, the actual ECHO-1 values are lower than the values that were estimated.

Table 12.7: Contingency Check with Baseline Report Values

Parameter	Estimated Value	Contingency Final Design ECHO-1	Maximum Allowed Value Final Design ECHO-1	Actual Value ECHO-1	Met?
MTOW	70325 kg	11%	78061 kg	20937 kg	✓
Energy	47.24 GJ	10%	51.96 GJ	14.32 GJ	✓
Wing Loading	595.61 kg/m ²	14%	679.00 kg/m ²	368.29 kg/m ²	✓
Power Loading	0.3165 kW/kg	10%	0.3482 kW/kg	0.1485 kW/kg	✓

13

Sustainability Analysis

Climate change is a global problem of rapidly increasing importance, and polluting industries such as aviation play an undeniable role through the emission of greenhouse gases. It is clear that aircraft must be designed to operate in a sustainable manner. Due to its electric propulsion infrastructure and efficient design, ECHO-1 can contribute greatly to a reduction in aviation emissions.

For this project, sustainability is defined as "the ability to meet stakeholder requirements without

compromising the ability to do so in the future” [1]. Stakeholders are entities which are influenced by ECHO-1, which in the case of sustainability is the global environment. Environmental sustainability is specifically concerned with ensuring that the environment is not impacted negatively by ECHO-1. The financial sustainability of ECHO-1 is described in [chapter 16](#).

Throughout the course of the DSE, sustainability of the design has been ensured in the design selection trade-off and in further design decisions, such as air-frame material selection. This chapter serves to quantify the sustainability of the ECHO-1 and compare it to a traditional kerosene aircraft.

Section [13.1](#) describes the method used to analyse sustainability of the aircraft. Section [13.2](#) describes the life-cycle sustainability analysis. Further use of degraded batteries is proposed in [section 13.3](#). Lastly, recommendations for future work are given in [section 13.4](#)

13.1 Methodology

In order to assess the sustainability of ECHO-1, the full aircraft life-cycle was analysed, which includes production, the use phase and end-of-life. During each of these phases, sustainability was considered by three metrics: the energy required, the materials required and the greenhouse gases emitted. The emission of greenhouse gases is calculated using CO₂ equivalents (CO₂e) for a fair comparison between polluting processes [67].

The generation of greenhouse gases is considered in two ways. Firstly, certain processes such as the recycling of batteries or the combustion of kerosene produce emissions directly. Values for direct CO₂e emission were obtained from literature. Secondly, many processes in the aircraft life-cycle require energy. This energy must be generated, during which greenhouse gases are emitted. To compensate for this, a value of 0.15 kg CO₂e/kWh of generated energy is used [68]. The indirect CO₂e emissions are thus a result of the energy required for a process. Both the direct and the indirect CO₂e emission have been calculated for each phase and are shown in the following sections.

To provide context to the values found for ECHO-1, a similar analysis was performed on the ATR 42-600, a regional aircraft which is capable of carrying 48 passengers. This aircraft has a comparable OEW and flies similar range missions ¹.

For the main structure of the aircraft, a full aluminium structural weight equal to the OEW was considered. This is a simplification, because the aircraft OEW includes components made of plastic, steel or composites, and even the flight crew. However, since both aircraft have a similar OEW and carry the same number of passengers, it is not expected that this assumption will produce large inaccuracies.

Since the batteries are still at a state of health of 85% when they are retired, they do not need to be recycled immediately, but can be used as is proposed in [section 13.3](#). Still, a battery is generally retired after its state of health reduces to about 50%. Therefore, the battery use for flight missions contributes 30% to the need for recycling. This correction factor is used when calculating the amount of battery that needs to be produced and recycled.

13.2 Life-Cycle Analysis

Using the method as described above, the full life-cycle of the aircraft was analysed. Many values on sustainability of materials were obtained from literature, after which a calculation was performed to compare the aircraft. The three life-cycle phases are described in [subsection 13.2.1](#), [subsection 13.2.2](#) and [subsection 13.2.3](#). After this, a conclusion is provided in [subsection 13.2.4](#).

13.2.1 Production

During production, materials must be processed for use in the aircraft. For this analysis, it was considered that the materials required for the ATR 42-600 were aluminium, with a weight equal to

¹https://1tr779ud5r1jjgc938wedppw-wpengine.netdna-ssl.com/wp-content/uploads/2020/07/Factsheets_-_ATR_42-600.pdf (accessed on 17 June 2021)

the OEW. For the ECHO-1, not only the structure but also production of batteries had to be considered. As previously described, the batteries must be replaced every 2000 cycles, which means a total of 10 battery sets must be produced. This leads to a large mass of batteries, which require a significant amount of energy for production [69]. The process for their production also emits a large amount of CO₂e [70]. All relevant values are shown in Table 13.1.

Table 13.1: Sustainability characteristics for production

Parameter		ECHO-1	ATR 42-600	Unit
Electric Energy		3 876	176	GJ
Materials	Aluminium	8 430	11 700	kg
	Batteries	20 760	-	kg
CO ₂ e	Direct	871 400	-	kg
	Indirect	161 500	7 300	kg
	Total	1 033 000	7 300	kg

13.2.2 Use Phase

The use phase presents the largest difference between ECHO-1 and conventional kerosene aircraft. Whereas traditional aircraft consume enormous amounts of fuel for propulsion, ECHO-1 only uses electric energy.

For both aircraft, a total operational lifetime of 20 years was considered, with 1000 flights per year and an average mission range of 800km, following from a discussion with Venturi Aviation. For the ECHO-1, the total energy required for all flights was 231.2 TJ (terajoules). For the ATR 42-600 the total kerosene fuel consumption was first calculated to be 21.42 million kilograms². This equates to a chemical energy consumption of 942.5 TJ [71], which is over 4 times as much energy as the ECHO-1 consumes. The high energy efficiency of the ECHO-1 can be explained mostly by its excellent aerodynamics and improved propulsive efficiency, which together more than make up for the slightly higher MTOW.

Besides the lower energy consumption, there is another factor at play. Electric energy generation at large power facilities produces 2.53 times less CO₂e than energy generation from kerosene [72]³. It can be seen in Table 13.2 that ECHO-1 produces almost ten times less CO₂e than conventional aircraft during operation. The ATR 42-600 produces CO₂e directly from combustion of kerosene, whereas the ECHO-1 CO₂e emissions are an indirect result of the energy requirement.

Table 13.2: Sustainability characteristics for use

Parameter		ECHO-1	ATR 42-600	Unit
Electric Energy		231 172	-	GJ
Materials	Kerosene	-	21 419 600	kg
CO ₂ e	Direct	-	85 280 600	kg
	Indirect	9 632 200	-	kg
	Total	9 632 200	85 280 600	kg

13.2.3 End-of-Life

During retirement of the aircraft, the aircraft must be dismantled in order to reuse its materials. Since ECHO-1 will begin operation around 2035, the first aircraft are expected to retire around 2055. It is estimated that nearly 100% of aluminium retired by the transport sector will be recycled from 2050 onwards [73]. For the ATR 42-600 this means that the full aluminium OEW must be recycled. For the

²Extrapolated from flight data on https://1tr779ud5r1jjgc938wedppw-wpengine.netdna-ssl.com/wp-content/uploads/2020/07/Factsheets_-_ATR_42-600.pdf (accessed on 16 June 2021)

³https://www.epa.gov/sites/production/files/2015-07/documents/emission-factors_2014.pdf (accessed on 16 June 2021)

ECHO-1, also the batteries must be recycled. This is reflected in Table 13.3 by the negative masses of materials required.

Current battery recycling technologies are capable of reaching 91% recovery rates by combining mechanical- and hydro-metallurgical treatment [74] [75]. It is assumed that this technology will be improved in the coming decades, and recycling will thus produce negligible amounts of waste products. This is of large importance, because batteries use rare materials such as lithium and cobalt.

The sustainability characteristics for retirement can be seen in Table 13.3. Note that no energy consumption or greenhouse gas emission has been considered for the recycling of batteries. This is done because these values are orders of magnitude smaller than those for production of batteries [76], and realistic values of recycling energy and waste are virtually impossible to predict for batteries recycled in 2055 [77].

Table 13.3: Sustainability characteristics for end-of-life

Parameter		ECHO-1	ATR 42-600	Unit
Electric Energy		281	390	GJ
Materials	Aluminium	-8 430	-11 700	kg
	Batteries	-20 760	-	kg
CO ₂ e	Direct	-	-	kg
	Indirect	11 700	16 200	kg
	Total	11 700	16 200	kg

13.2.4 Life-Cycle Conclusion

To provide a clear image of the sustainability of the ECHO-1 compared to the ATR 42-600, the most important information is concluded in this subsection.

Since a near-complete recycling of the aluminium and batteries is assumed, the most important metrics for sustainability is the CO₂e emitted. As stated previously, the energy required for a certain phase has already been considered by calculating the CO₂e that is emitted when generating this energy.

The need for battery production means that the ECHO-1 has more upfront material requirements and greenhouse gas emissions. Still, this is more than compensated for by the incredibly efficient operation of the aircraft. Specifically, ECHO-1 consumes less than one fourth of the energy an ATR 42-600 consumes per flight, due to the greatly improved aerodynamics and propulsive efficiency.

The total CO₂e emission of the ECHO-1 is 10 676 800 kg, whereas that of the ATR 42-600 is 85 304 200 kg. This means that the ECHO-1 emits 87.4% less CO₂e than a comparable kerosene aircraft. This tremendous reduction in greenhouse gas emissions is possible in part due to the lower energy consumption, and in part due to the cleaner production of energy compared to kerosene.

13.3 Further Use of Batteries

The batteries of ECHO-1 will be replaced once they have degraded by 15% compared to their beginning of life capacity. At this stage, the state of health of the battery is not enough to support the aircraft in performing its mission. However, the batteries might still be useful for other applications where energy density is less of an important factor. Re-using the batteries in this way prolongs the battery life, therefore reducing its environmental impact. If used well, the batteries can even help to make energy consumption less environmentally harmful. In this section, the promising application as back up energy storage will be discussed in more detail.

Using batteries as back up energy storage for households and industrial consumers is already done

by Tesla with their Powerwall⁴ and Powerpack⁵. The battery packs of ECHO-1 would be great for this purpose due to their large size. The stored energy could be used as a back up electricity source for power outages, but also to reduce the reliance on grid power and increase the effective use of solar power. For stationary electricity storage, energy density is much less important than for aircraft, so the batteries of ECHO-1 are still able to provide plenty of use in this case. Furthermore, in this application, a much lower charge-discharge frequency as well as potential lower depth of discharge is needed. Both of these aspects lead to significantly reduced battery degradation and thus prolonged battery life. Tesla sells their Powerwalls with 10 years of warranty, with a capacity retention of at least 70% at the end of these 10 years. It can be assumed that very similar lifetimes can be expected for the ECHO-1 batteries if they would be used for this purpose. This is especially true if effort is made to ensure that the battery pack SOC stays within a degradation friendly range.

13.4 Recommendations

The sustainability analysis described in this chapter is only preliminary, and serves to show the difference between ECHO-1 and conventional kerosene aircraft broadly speaking. A more detailed analysis should be performed in the future, but this was considered beyond the scope of this project. A special emphasis should lie on determining the practical recyclability of batteries, as well as obtaining a better estimate of the material composition of ECHO-1. Lastly, it is advised to gather more accurate information about the battery state of health before retirement.

14

Operational Analysis

After a design of a novel aircraft, an operational plan is made to determine the operational procedures of the aircraft. In this chapter, the operational plan for ECHO-1 is written. Since ECHO-1 is a battery powered aircraft, special attention is given to determining the turnaround time and maintenance of the batteries.

This chapter is divided into three main sections, in [section 14.1](#) the required airport infrastructure is determined. The ground handling procedures of ECHO-1 are determined in [section 14.2](#). The RAMS characteristics are discussed in [section 14.3](#). At last some recommendations for further research are given in [section 14.4](#).

14.1 Airport Infrastructure

In order to accommodate an electric aircraft, some new infrastructure should be built to make airport electric aircraft proof. Therefore, the aim of this section is to describe the steps which should be taken such that airport can accommodate electric battery powered aircraft such as ECHO-1. The required steps are described in [subsection 14.1.1](#), [subsection 14.1.2](#) and [subsection 14.1.3](#)

14.1.1 Airport Requirements

ECHO-1 is a fully battery powered aircraft running on nothing but electricity. This means that the airport must be able to provide this electricity during ground operations. Currently, almost no airport has a recharging station for aircraft, especially for aircraft with the size of ECHO-1. If a turn around time requirement of 30 minutes needs to be fulfilled, the aircraft needs to be charged with an huge amount of power. The airport must be able to provide that power via chargers. This means that each airport on which ECHO-1 aims to land at, needs to have state-of-the-art charging facilities at the gates.

⁴https://www.tesla.com/en_eu/powerwall (accessed on 17 June 2021)

⁵<https://www.tesla.com/powerpack> (accessed on 17 June 2021)

The charging is done by the Megawatt Charging System (MSC) developed by CharIN ¹. One MSC charger can produce 4.5 MW of charging power. These MSC chargers will be connected primarily to the CCS (Connected Charging System). This CCS system is essentially a standard for electric charging of vehicles. This standard is the primary standard in Europe and in North America ². This standard provides for good charging communication and speed for charging electric vehicles. Currently, other charging standards are used in Asia. For example, Japan uses the CHAdeMO ³ standard and in China there is not a lot of charging infrastructure yet. However, the charging systems can be connected to the electrical if there is the right infrastructure for it. This infrastructure will be further discussed in subsection 14.1.2. This means that if there is an electrical grid, a MSC charger could be made there if the right modifications are made.

The MSC charger charges up to 1500 V and 3000 A, however, the batteries of ECHO-1 are designed for 1200 V. This means that at optimal charging speed, ECHO-1 can be recharged with 1200 V and 3000 A and thus at most with 3.6 MW per charger. Taking this charging power into account and considering the total battery capacity of 14.3 GJ (from chapter 11), the charging progress of ECHO-1 during the turnaround can be seen in Figure 14.1a. In this graph, the charging rate for 1, 2 and 4 chargers can be seen. Furthermore, Figure 14.1b shows the power output of every configuration over time. It has been assumed that a SOC of about 95% would be sufficient in the 30 min turnaround time. A higher charging power could deteriorate the batteries and thus 4 MSC chargers at 75% current and power will be used during the turnaround in order to recharge ECHO-1. This results in a SOC of the batteries of 94.1% with the possibility of recharging to 98.0% when operating the chargers at full power for extraordinary flight requirements.

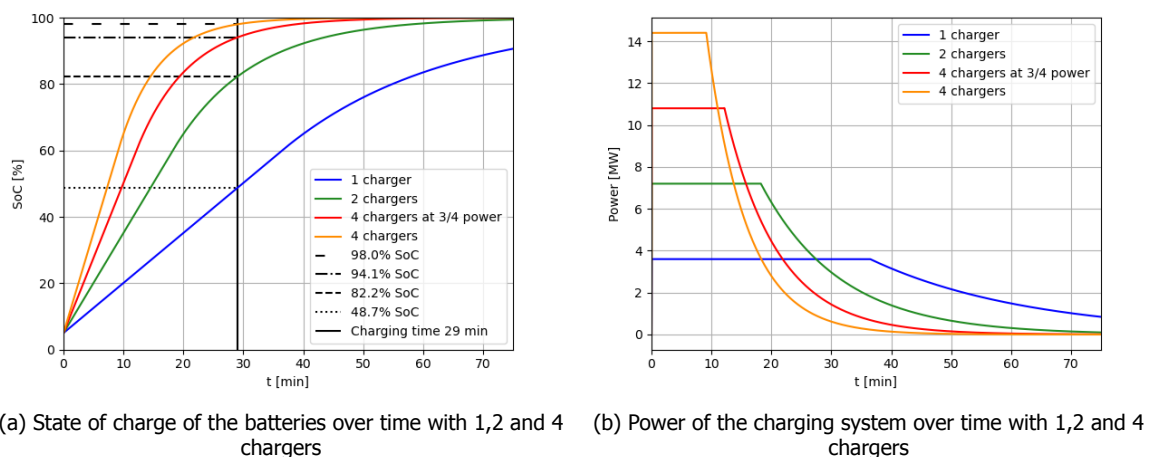


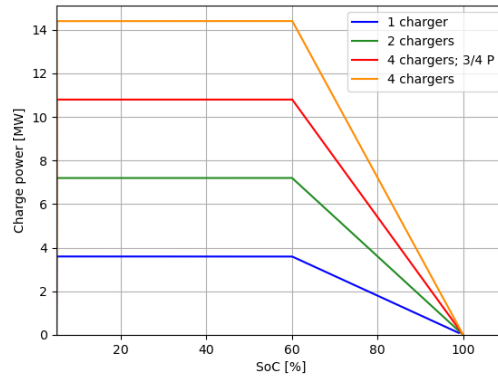
Figure 14.1: Charging performance of various charging setups

In Figure 14.2a and Figure 14.2b, the charging power versus the SoC can be seen for both ECHO-1 and current electric cars as reference. The curves for the electric cars first start with constant power until the battery hits a SoC of about 40% - 50%. Thereafter, the power starts to deteriorate approximately linearly or with steps. These steps are similar to the linear curves regarding nominal power. The linear curves in this graph are used as model for modelling the charging of ECHO-1. In Figure 14.2a the curve also starts with constant power until SoC of 60%. This number is slightly higher than the reference curves because it is expected that the chargers and charge capability of the battery will be improved when ECHO-1 will be produced. Furthermore, the best performing line of the Audi e-tron starts to drop only after 80%. After this dropping point, the curve for ECHO-1 goes down linearly which means that for every increase of SoC, the power decrease is the same until the SoC is 100% and the power is decreased until 0 W.

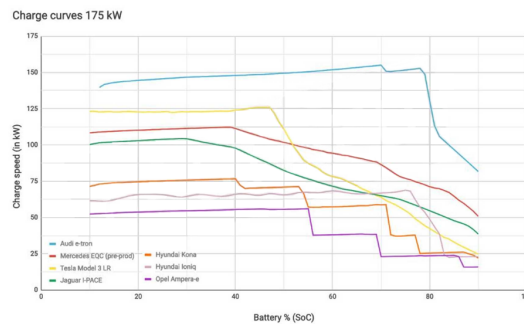
¹<https://www.charin.global/technology/mcs/>

²<https://www.charin.global/technology/dashboard/>

³<https://www.chademo.com/about-us/fast-charger-maps/japanese-map/>



(a) Power and SoC of 1,2 and 4 chargers



(b) Power and SoC of various reference electric cars for validation ^a

^a<https://insideevs.com/news/343587/quickest-charging-electric-cars-compared-at-175-kw-charger/>

Figure 14.2: Power against State of Charge graphs

During charging, the batteries heat up. This increase in temperature has an effect on the battery charging performance. The battery recharges optimally between a certain temperature range between 15 and 30 °C. However, during recharging the battery heats up and the ambient temperature at the ground may be higher than 30 °C. This means that during recharging, the temperature of the battery must be maintained at about 20°C. The amount of current in the batteries is higher during recharge than discharge. This means that the heat generated is also higher during charging and that will cause the temperature of the batteries to increase beyond the operational limit. This means that a cooling system is needed. The cooling system in the aircraft can not cool at lower temperatures than the ambient temperature which can be higher than the required battery temperature. The main reason for this is that the internal cooling system of ECHO-1 uses a radiator. This means that an external battery coolant pump is needed in order to cool the batteries during charging.

One problem that might arise when charging with 4 chargers is that the charging power is too much for the batteries to handle. If the power and current into the battery is too high, significant heating and ionisation problems will occur. As seen in Figure 14.2a, the maximum power that 4 chargers can charge with is 14.4 MW and 75% is at 10.8 MW. This corresponds to a C-rate of 3.6 and 2.7 respectively. As a reference, the Tesla Model 3 has C-rate of 1.8 when charging from 10% to 80%.⁴ Comparing this with Figure 14.2b, this means that the peak C-rate of the Tesla Model 3 could reach about 3 at the constant power stage. This means that the C-rate required of 2.7 for ECHO-1 is achievable with current battery technology. However, the batteries are not able to charge with 4 chargers at full power. This is because charging with 4 chargers at full power would obtain a C-rate of 3.6, which is too high. The battery and charging technology will be improved such that batteries are able to recharge with 4 chargers at full power. One problem that might arise, is that the batteries of

⁴<https://www.drivingelectric.com/tesla/model-3/range>

ECHO-1 can not achieve a very high C-rate, because they are not designed for charging. This could mean that the cell configuration in the battery can not handle the amount of current. For now it is assumed that both the external cooling system and the improved charging technology will allow for a turnaround time of 30 min.

14.1.2 Platform Charging station

To accommodate electric aircraft, a new charging station must be build for the aircraft at the gate. This charging station will consist of 4 MSC chargers, two for each side. The batteries are split over two big packs, one in front of the wing and one slightly behind the wing. This means that the positions of the MSC chargers are at both sides of the aircraft, directly in front and behind the wing. The MCS chargers can not simply be put in the aircraft by ground personal due to their weight. The charge arms will be provided by ROCSYS⁵. These robot arms will automatically put in the heavy MCS chargers when ECHO-1 has arrived at the gate. These robot arms must be able to be relocated before and after the charging in order to make room for ECHO-1 to taxi out of the gate. The MSC chargers draw a lot power from the electrical grid. This means that an extra electric infrastructure must be placed at each gate which will be transformed into an electric gate.

One other big component is the external water cooling system. This system provides the coolant during recharging and makes sure that the battery system is properly cooled during charging. Depending on the needed size of this cooling system, the coolant can also connect to ECHO-1 via the same ROCSYS robotic arms used in charging. However, it is expected that a significant cooling system is required. For this reason one separate cooling system with plug will be connected to ECHO-1 on the right.

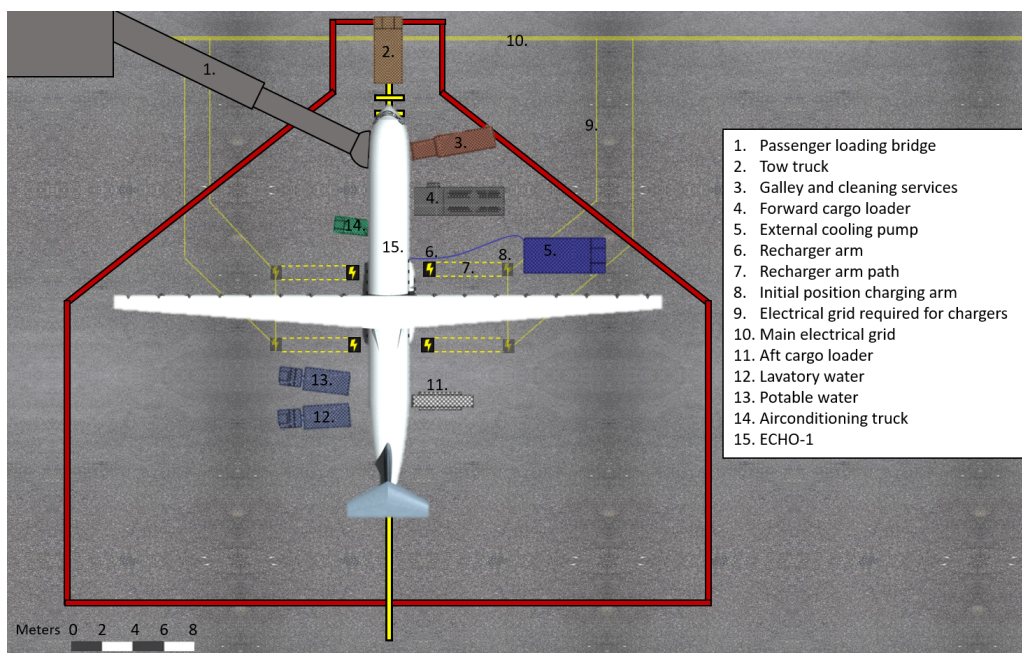


Figure 14.3: Schematic overview of a possible aircraft stand for ECHO-1, icons coming from [10]

A preliminary design for a possible charging platform for ECHO-1 can be seen in Figure 14.3. Most of the ground operations are similar to those of conventional aircraft [10], this is presented in more detail in section 14.2. Like explained before, there are two unique aspects of this aircraft stand. First of all, there are four MCS chargers connected via a new electrical grid to main electrical grid. The aircraft must be able to move in and out of the stand without colliding into anything. This means that the chargers must be able to move from their initial position to the aircraft and back. A second reason for this moving charger system is that the chargers must not interfere with a non-electrical aircraft. This means that this aircraft stand can also be used by non-electric aircraft. The second

⁵<https://www.rocsys.com/industry>

distinct difference is that a big external cooling system is required in order to cool the batteries. This cooling system is large so it must be able to move out of the way if the aircraft taxis.

14.1.3 Energy Supply

One big issue is the amount of power that ECHO-1 draws from the electricity grid. One recharge of the aircraft draws approximately 14 GJ of electric energy with at a nominal rate of about 10 MW. If multiple ECHO-1's simultaneously recharge at one airport, this may give energy supply issues. For this reason, an extensive electrical charging grid which can supply a lot of power locally without issues is needed. Not all countries or remote regions have the infrastructure or capital for such a grid. An alternative to an electrical grid is an electric buffer which stores electricity if in a short period a lot is required.

14.2 Ground Handling

For solid operations, a ground handling plan should be set up. The ground handling of the aircraft consist out of multiple stages, such as tasks to be performed before landing, the turnaround itself. Each of these tasks will be discussed in their respective sections.

During the day of operation, the operations control centre of the airliner is monitoring the aircraft. In the operational control centre of the airliner, the operational control centre performs a pre-operational analysis, whereby flight times will be checked, the weather queues will be resolved and any time discrepancies will be discovered. Moreover, do they also write operational reports every day. The operational control centre is also responsible for the coordination of flights, maintenance and allocation of crew to day operations. For ECHO-1, control centre need to put an emphasis on schedules for recharging the aircraft and how the charging can be improved.

14.2.1 Pre-Turnaround

Before the aircraft has arrived at an airport or at the gate, the ground handling procedures have already begun. The required ground handling equipment is determined and set in place. Data regarding the on-load and off-load have already been obtained and dealt with. Furthermore, the amount of the passengers are determined and the required personnel is briefed to minimise the turnaround time. The groundcrew is assigned to on-loading and off-loading of the cargo, a part of the groundcrew is assigned to the charging of the aircraft. To load the cargo into ECHO-1 the groundcrew requires special training, because the cargohold is shallow. At last, the flight crew is also determined beforehand. After these steps are taken the airport is ready for arrival of the aircraft.

14.2.2 Turnaround

When the aircraft has landed, the aircraft will taxi to the assigned gate. When arrived at the gate, the race against the clock has started to prepare the aircraft for the next flight. Venturi Aviation set a requirement that the aircraft shall have a turnaround time of 30 min. Over the course of the project Venturi Aviation extended their requirement to 40 min. Therefore, it is decided to aim for a turnaround time of 30 min, because the cost for an airliner will increase if they require more time and thus a longer stay at the gate. Moreover, airlines want to maintain their schedules to increase the fleet utilisation and maximise the revenue.

To optimise the turnaround time, a clear overview of the activities which are independent of each other and which activities are performed in sequence has to be made. Any delay in an activity which is performed in sequence could yield in a departure delay and thus extra cost for the airliner and unsatisfied passengers. To give a schematic overview of the activities which are performed during a turnaround a work flow diagram is made, which is presented in [Figure 14.4](#). From the workflow diagram it can be seen that there are four main paths, the battery operations, safety operations, internal and external fuselage operations. In [Table 14.1](#), the time allocation for each activity is given.

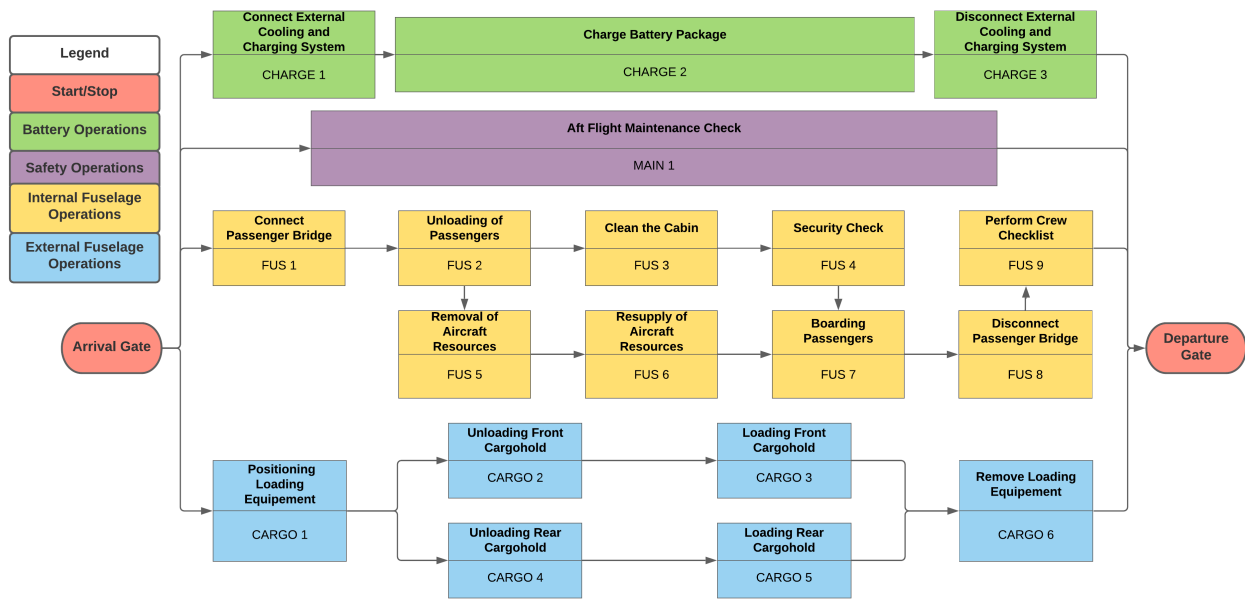


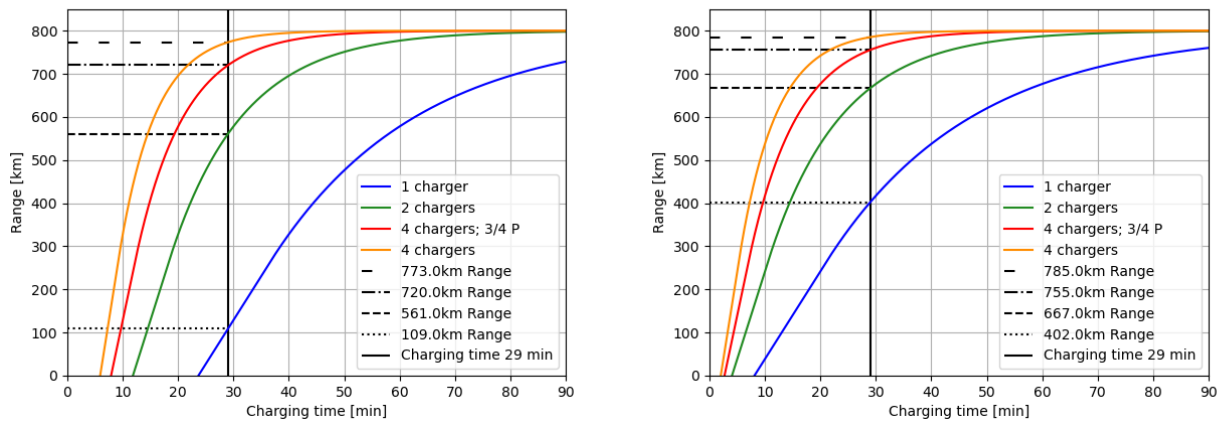
Figure 14.4: Work Flow Diagram of the turnaround of ECHO-1

Table 14.1: Time allocation of the activities performed during a turnaround

ID	Time Allocation in min	ID	Time Allocation in min
CHARGE 1	0.5	FUS 1	1
CHARGE 2	29	FUS 2	7
CHARGE 3	0.5	FUS 3	5
MAIN 1	25	FUS 4	3
CARGO 1	1	FUS 5	4
CARGO 2	14	FUS 6	4
CARGO 3	14	FUS 7	10
CARGO 4	14	FUS 8	1
CARGO 5	14	FUS 9	3
CARGO 6	1		

To prevent any delay the time, allocation for the dedicated activities should be strictly followed. During a turnaround discrepancies could occur internal fuselage operations, to mitigate any time delay, the ground crew should try to make up the time in another activity. Moreover, to manage and model turnaround activities, a project evaluation and review technique (PERT) can be utilised [78]. The aim of the PERT technique is to improve efficiency by evaluation operational procedures and by improving the efficiency of the resources allocation of the ground crew.

Furthermore, for electric battery powered aircraft the main difference in turnaround operations is the recharging of the battery package. When the aircraft is parked, the 4 charger cables and cables for the external cooling system are immediately connected to aircraft as described in section 14.1. After the cables are connected the charging process is started. During charging the batteries will increase in temperature. To keep the batteries on a constant charging temperature an external cooling system is required. Moreover, is it also required to cool the batteries to temperature of 15 °C at departure, to prepare the battery packages for take-off.

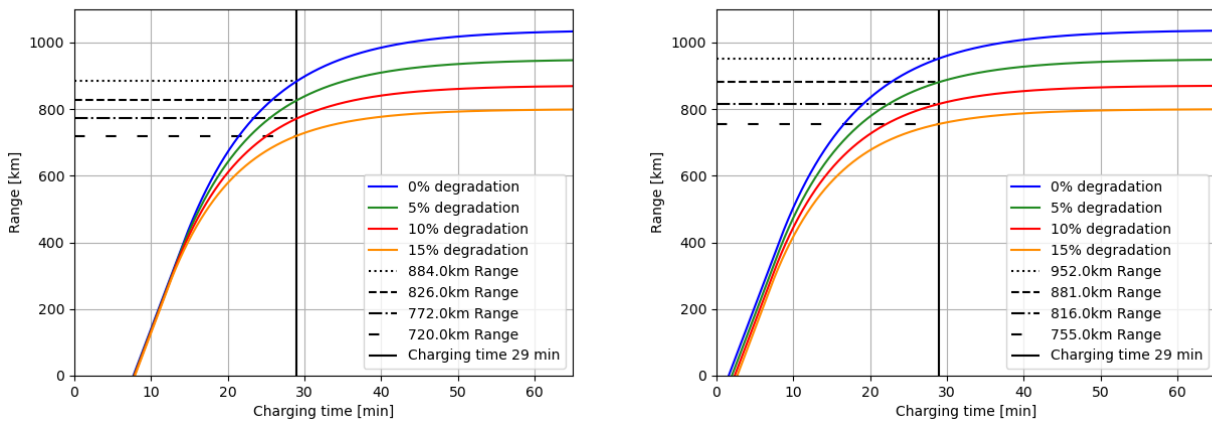


(a) The Range which can be achieved in an turnaround time of 30 min using multiple chargers starting from 5% SoC (b) The Range which can be achieved in an turnaround time of 30 min using multiple chargers starting from 28% SoC

Figure 14.5: The Respective ranges which can be achieved when charging for 29 min.

When using 4 chargers the aircraft is able to charge up to 94.1% SOC in 29 min at end of life. Resulting into that the aircraft is able to fly 720 km and thus the 800 km range requirement is not met anymore. To achieve the full 800 km of range at end of life a longer charging time is required, if the battery is fully discharged during operations. The required turnaround time for a specific range can be found in [Figure 14.5a](#). However, during operations the aircraft will not always fly at maximum range resulting in a lower discharge of the battery package. A lower discharged battery will also be charged faster, resulting that the turnaround constraint can be met in general. The charging is even more reduced when taking into account that loitering and diversion will not occur frequently and thus the state of SOC of the battery after landing will more or less be equal to 28 %. In that case the charging time and their respective ranges are presented in [Figure 14.5b](#). To conclude at the end of the battery life a turnaround of 30 min is in general achievable, and when the battery is fully discharged it should be charged for longer. Airlines can take this into account when making a planning for their flights.

However, at begin of life (BOL) more energy can be stored in the battery package of ECHO-1. For this reason the aircraft is able to achieve a range of 1035 km, when the battery package is fully recharged. However, to keep flying at maximum range over the life time of the batteries, a system should be made which could determine the state of health of the battery package at each point in time. Besides the aircraft has to be certified to constantly fly at maximum range. The downside of flying at maximum range at each lifetime is that the battery degradation will be faster, because the battery is fully charged. Furthermore, the required charging time is longer when the airliner will maximise the range, which can be obtained from [Figure 14.6a](#). On the other hand the aircraft is able to achieve a range of 800 km in a turnaround time of 30 min at begin of life when the battery is fully discharged. An overview of the degradation of the battery and their respective range ,when charging for 29 min and when the aircraft did not loiter or divert during flight, is given in [Figure 14.6b](#).



(a) The degradation of the battery package and their respective range when turnaround time is 30 min using multiple chargers starting from 5% SoC

(b) The degradation of the battery package and their respective range when turnaround time is 30 min using multiple chargers starting from 28% SoC

Figure 14.6: The ranges which can be reached when charging for 29 min at begin and end of life

To Further reduce the turnaround time for begin or end of life, the power output of the 4 charging cables can be increased. Moreover, the charging cables are producing 75% of their maximum power. In the future the full power of the chargers can be utilised if the battery technology allows it. Furthermore, is the full power of the charger not used to improve battery life. Because the faster a battery is charged, the faster it will degrade, the battery package needs to be replaced more often, resulting in increased cost.

14.2.3 Deployment of the ECHO-1

Next to a plan for the turnaround procedures, a plan will be made for the daily operations of the ECHO-1. However, this is really dependent on the airliner since at the end of the day, they will make the flights schedules. Nonetheless, advice on how to operate ECHO-1 will be given. ECHO-1 is an aircraft which is designed to fly at least 2000 cycles on an battery package. After 2000 cycles the battery package of the aircraft is replaced. The replacement of the battery package will occur every two years, resulting into that 1000 flights a year are performed. Therefore, an aircraft is scheduled for on average 3 flights a day. At what time these flights are performed and the range which is flown is entirely up to airliner. On the other hand, it is advisable to fly longer flights in the morning, because the aircraft can than charge longer over night. Furthermore, does charging over the night has the benefit that charging with a lower power will improve battery life.

In addition, when 3 flights a day are performed, then it generally gives more space to charge the plane, resulting into slow charging of the battery package, which indeed improves the battery live again. However, ECHO-1 has only a mission block time of 2.5 hours, therefore it is most likely that airliners will perform more flights a day resulting in a faster replacement of the battery package. The number of flights a day and the battery replacement time is given in [Table 14.2](#)

Table 14.2: The flights a day based on the battery replacement time

Battery Replacement in years	Flights a Year	Flights a Day
2.00	1000	2.7
1.75	1143	3.1
1.50	1333	3.7
1.25	1600	4.4
1.00	2000	5.5
0.75	2667	7.3

The major downside of flying more often per day is that the degradation of the battery package will increase, since charging of the battery is becoming more critical resulting into charging with higher powers. Moreover, the battery packages are charged more frequently. Nonetheless to constantly achieve the maximum range, it is useful to alternate long-haul flights with short flights in order to minimise charging times.

14.3 RAMS Characteristics

The RAMS characteristics specify about an aircraft how safe should be flown but also how much maintenance or repair time is required. Even though these parameters are hard to be quantified, a comparison will be made with another regional aircraft namely ATR72-600. Using this aircraft, some numbers can be given along with an estimation of how good an electric aircraft is compared to an internal combustion one. The acronym RAMS stands for Reliability (subsection 14.3.1), Availability (subsection 14.3.3), Maintenance (subsection 14.3.2) and Safety (subsection 14.3.1).

14.3.1 System Reliability

The first step in the RAMS analysis is determining and addressing the reliability of the various sub-systems in the aircraft. With the reliability assessment and the scheduled maintenance established, the availability of the aircraft can be determined. In order to see how ECHO-1 behaves regarding reliability, it will be compared to other regional turboprop aircraft that can be found on the market. For Bombardier Q400, it was found a reliability of 99.4%⁶ while for ATR 72-600 a reliability of 99.7%⁷. The higher reliability for ATR 72-600 might be caused by the fact that this aircraft was launched later than Q400. Thus, for comparison, a value of 99.7% for reliability will be used. This value will also be used as a starting point for ECHO-1. The main differences compared to ATR72-600 are the wing structure, propulsion system and the batteries which will be quantified separately.

Wing Structure

The wing structure reliability is very hard to be quantified[79] and no data was found for turboprop regional aircraft. However, a qualitative analysis can still be made. Comparing to ATR72-600 which has only one critical point that is liable to maximum stress (where the wing is cantelivered), the ECHO-1 wing structure would have 3 critical points (2 more from the truss). Those points for a truss-braced wing are not linked in parallel (if one fails, the other ones are not a back-up) so the reliability of the wing should be cubed. Thus regarding the structures, the ECHO-1 should have a lower reliability. Fortunately, the wing structure of the aircraft does not usually lead to unscheduled maintenances (below 1 out of 100⁸) so this system is usually very reliable. Thus, assuming for the ATR72-600 a reliability of the wing system of 0.99997, for the ECHO-1 a reliability of 0.99991 can be considered.

Propulsion system and batteries

The propulsion system and battery elements were grouped together as the most numbers that were found, were for both systems combined. For example, for a turboprop engine, including the propeller, combustion engine and the fuel system, a reliability of 13.8 FPMH (Failures Per Million Flights) was found[80]. Thus, for a 2 propeller aircraft, the failure rate would be of 27.6 FPMH and the reliability of 0.9999724. For an electric distributed propulsion, the system is formed of multiple components, each with its own reliability. For example, the propeller was required to have a failure rate of less than 0.1 FPMH by FAA[81]. For the electric motor, a failure rate of 5.93 FPMH[82] was found including bearing, winding, shaft, gear and housing and for the inverter a failure rate of 4.49 FPMH[82] can be considered. As the propeller, electric motor and inverter are present for each of the 16 engines, a combined failure rate of 168.32 FPMH can be determined. The battery failure rate was calculated knowing that the failure rate of one cell is 2.63 FPMH[82]. Thus for 175 cells in parallel and 300 cells in series, a battery failure rate of 4.509 FPMH was found. As two batteries in parallel are used, a battery total failure rate of 9.018 FPMH is found. By putting it in series with the engines, an electric

⁶<https://theflyingengineer.com/aircraft/proud-to-fly-a-turboprop-q400-vs-atr72/>

⁷<https://aviationvoice.com/atr-continues-to-dominate-commercial-turboprop-market-2-201708311056/>

⁸<https://www.maintworld.com/R-D/Aircraft-Reliability-Programme>

failure rate of 177.34 FPMH is found which translates to a reliability of 0.9998227. The reliability is lower compared to ATR72-600. The main cause for it is the distributed propulsion system where each propeller has its own high risk.

Final Reliability Results

The 2 components that changed the reliability of ATR72-600 were the truss-braced structure and the electric propulsion system. The reliability of ECHO-1 was found by taking the reliability of ATR72-600 and dividing by the contribution of the 2 systems considered and then multiplying back with the ECHO-1 contributions. Thus, a reliability of 99.679% is found which means that a failure might appear each 311.6 hours.

14.3.2 System Maintenance

In order to keep the aircraft functioning for a long period of time, maintenance checks have to be performed regularly. These are important to be determined at this stage in time in order to forecast the availability of the aircraft for a more accurate cost estimation. However, at the moment, there are no electric aircraft that are certified with CS-25. Thus, it is difficult to estimate how often maintenance is required and how long the check should last [83]. For this reason, the standard "ABC" maintenance schedule and procedure as suggested by FAA will be imposed. Those check are divided in 4 types: an A check which is done most often and verifies visually the structure for damage, corrosion or missing parts but also the lubrication, leaking, landing gear and the engines. The B check is usually ignored by most airliners and integrated in A checks instead ⁹. The C checks are more labour intensive and time consuming as, now, each part of the aircraft is more seriously inspected. Lastly, there should be a D check as well, where the aircraft is completely disassembled, each part is thoroughly check and then the aircraft is assembled back. Apart from those checks that are performed in specialised hangars, day-to-day checks, called line maintenance, also have to be performed. These are usually done during the turnaround time or at the beginning of the day in order to check visually if the aircraft has any flaws and it can fly safely.¹⁰ As they depend on aircraft schedule, those checks are hard to be accurately planned. On the other hand, the ABC checks should have a clear schedule but as it is hard to forecast it for an electric aircraft, the times will be taken from one of our main competitors ATR-72 and inputted in Table 14.3.

Table 14.3: "ABC" check interval and duration

Check type	Interval ¹¹	Duration ¹²
A	750 flights	6-24 hours
C	5000 flights	3 weeks
D	2/4/8 years	2 months

The times presented in Table 14.3 are a rough estimation of the maintenance of a commercial aircraft as they refer to conventional fuel combustion aircraft. For an electric aircraft it was found that assessing the difficulty of maintenance depends from aircraft to aircraft and an accurate estimation cannot be made. Moreover, in the same paper[83], it was suggested that motors used in distributed electric propulsion can be rapidly replaceable when a maintenance issue is encountered. This is mainly because of its small size and small weight. Electric motors, different to the internal combustion ones, require less maintenance and also causes less vibration to the structures. Thus, for an electric motor less maintenance should be required. On the other hand, more maintenance might be necessary because of the batteries. These might require a completely different type of inspection and repair protocols than the one already used in aviation which will necessitate special training for the aircraft mechanics. Also, thermal damage of the batteries and cables are always possible which could result in performance loss. As a conclusion, the maintenance time might decrease because of the benefits of electric motors and distributed propulsion or might increase due to battery regulations issues. Thus,

⁹<https://simpleflying.com/aircraft-maintenance-checks/>

¹⁰<https://www.aircraftengineer.info/aircraft-line-maintenance/#gsc.tab=0>

as a safety measure, it was decided to stick to the "ABC" check interval and duration of ATR-72 even though the values might still slightly change.

14.3.3 System Availability

The availability of the aircraft is extremely important for an airline as, the more it operates, the more money it can make. This characteristic should be obtained from the previous 2 characteristics. In other words, the only time the aircraft cannot fly is when maintenance is performed. For this reason, an estimation of the time spent in hangars can be made. Regarding the reliability, it was found that each 311.6 hours of flight, a failure might appear. For solving this, a type A check of 15 hours was considered to be enough to solve the failure. On the maintenance side, the average time spent in hangars can be simply taken from Table 14.3. This can be done by considering that there will be around 6 flights per day and that one A check will last 15 hours and one D check will be made once in 4 years. By not overlapping the checks (if type C and type A times coincide, only type C will be considered), 87.25 days will be necessary for maintenance each time a D check is performed. The availability is obtained using the following formula:

$$Availability = \frac{FailureTime}{TotalTime} \quad (14.1)$$

Thus, for ECHO-1 aircraft, combining both the reliability and the maintenance results, an availability of 89.2% can be found. As a comparison, with the same inputs, ATR72-600 will have an availability of 89.5% caused by reliability differences.

14.3.4 System Safety

The system safety relates to the ability not to harm any people or assets during its life cycle. This general safety requirement includes two main safety issues. First of all, none of the components must break or fail during operation of the aircraft. The failure of components can cause a lot damage to nearby parts or even humans. The prevention of failure is already mainly addressed when looking at reliability and maintenance of the aircraft.

The other safety requirement is during operations where the systems must not cause a dangerous environment. This means that there are certain rules and safety regulations for the various systems in the aircraft. Those measures refer mainly to operations risks which were already addressed in Midterm Report[1] and in Baseline Report[13].

As a short conclusion of this section, some preliminary values were found for the RAMS characteristics. Compared to a close competitor, ATR72-600, ECHO-1 will have worse reliability because of the high number of engines and thus also worse availability and even safety. Regarding the maintenance, the mandatory checks were hard to schedule exactly at this design stage, so the same check schedule as ATR72-600 aircraft was implemented even though improvements might arise due to electric motors.

14.4 Recommendations

The operations of ECHO-1 described in this chapter, are all still preliminary. The main focus on this report and DSE is not the operational aspect of ECHO-1. For this reason, recommendations for further research and design will follow in this section. In order to improve the accuracy of the all the charging graphs in this chapter, a final battery with its performances must be chosen. In this chapter, the some of the performances of the battery, like C-rate, was estimated and were not fully accurate. Secondly, the achievable C-rate of the battery must be taken into account when designing the internal lay-out of the batteries. Regarding the charging platform, more research on the charging arm, electrical grid and their capabilities can be done. Similarly, all the RAMS characteristics require further in depth analysis as, at the moment, most of the values were taken and slightly adapted from similar aircraft.

Post-DSE Activities

This chapter aims to describe the activities that are to take place after the DSE is finished. This includes the execution of the preliminary design as well as the detailed design. Furthermore, certification and production belong to the activities that are to be carried out after the DSE. This chapter first provides an outlook on the detailed design and certification in [section 15.1](#). Secondly, in [section 15.2](#), a timeline is presented for all activities that are due in future time. Finally, [section 15.3](#) presents the production plan for ECHO-1.

15.1 Project Design & Development Logic

This section presents the design process of the ECHO-1 aircraft. The design process can be split up into two main parts: a part that is to be completed within the Design Synthesis Exercise (DSE) and a part that could be completed afterwards. Following from what was indicated in the project guide, this chapter solely focuses on the latter part.

The preliminary design consists of detailed technical analysis with the use of advanced computational tools, as well as wind tunnel testing. Furthermore, special emphasis should be laid on executing verification and validation procedures. The detailed design phase mainly consists of finalising subsystem calculations, after which the assembly and part design can start. Furthermore, the manufacturing facilities and manufacturing tools are designed during this design phase. Finally, detailed drawings are produced to assemble a prototype aircraft which is used for a test flight.

The certification phase consists mostly out of demonstrating compliance with requirements. This includes ultimate load tests, structural static tests, flight tests and safety assessments. Finally, before an airworthiness certificate is obtained, a detailed issue of approval must be established. A timeline will be presented that allocates time for each of the post-DSE activities in [section 15.2](#).

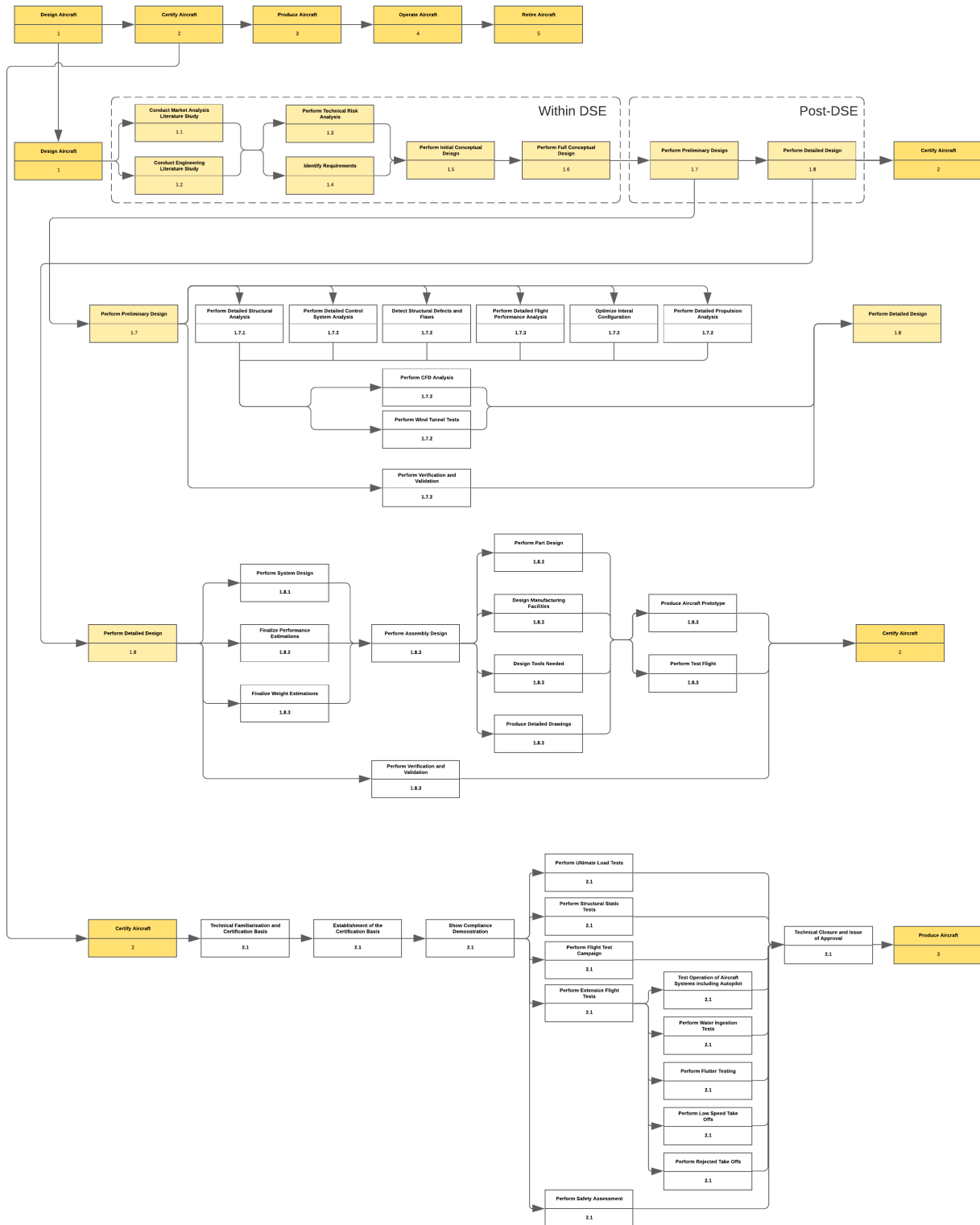


Figure 15.1: Project Design And Development Logic[1]

15.2 After DSE Project Gantt Chart

Using a Gantt Chart for the post-DSE activities, an indication is given for the required time that is necessary for the activities that were illustrated in section 15.1. It should be noted that the time indications are given in weeks and years, as the separate tasks are divided to such an extent that it is not realistic to indicate times in days or hours. The Gantt Chart is presented in Figure 15.2.

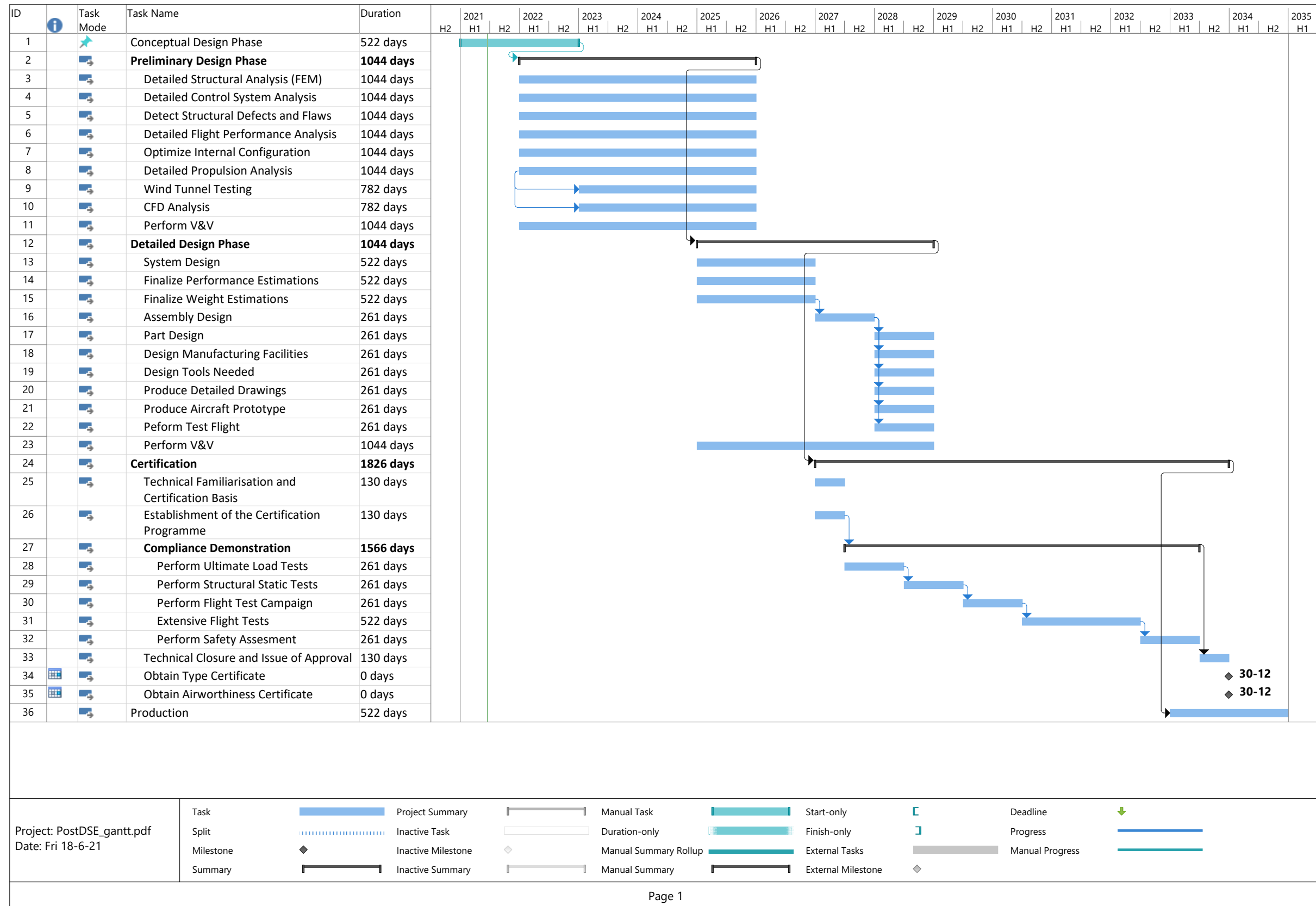


Figure 15.2: Post DSE Gantt Chart

15.3 Production Plan

In order to be able to go efficiently from the prototyping phase into the series production of the aircraft it is important that some thought has already gone into the way the aircraft will be produced in the future. The aim of this section is to provide that insight into the production with the use of a production plan. The production plan as seen in Figure 15.3 will provide a broad overview on what the production of the ECHO-1 could look like. The choice was made to split ECHO-1 up in various subsystems which can be produced and assembled in parallel. This saves time since if everything is planned efficiently and no delays occur each of the subsystems can be assembled together at the same time and at the same assembly plant into the full aircraft.

The aircraft will be assembled on an assembly line. On this assembly line all subsystems such as the wing, fuselage and empennage will be assembled. As can be seen in Figure 15.3 each of these subsystem will be constructed and assembled on separate smaller assembly lines. Each of these lines will either merge with the main assembly line or if the production of a subsystem is happening at a different location that subsystem will be transported to the main assembly line.

The decision was made to mount the electric motors, thermal management system and batteries at the very last stage of assembly. This is done since these systems will be delivered by an external supplier. The delivery by an external supplier has a higher change of a certain subsystem not being on time since there will be no control over the manufacturing of these components. There will also be full dependency on this supplier to deliver. If for some reason the supplier is not able to deliver on time the air-frames can still be assembled up until the final point and then temporarily stored until the motors, batteries and thermal management become available. The only requirement is that there is a space available to store the partly assembled air frames but the assembly line can still keep moving up until the final point where the electrical subsystems will be installed.

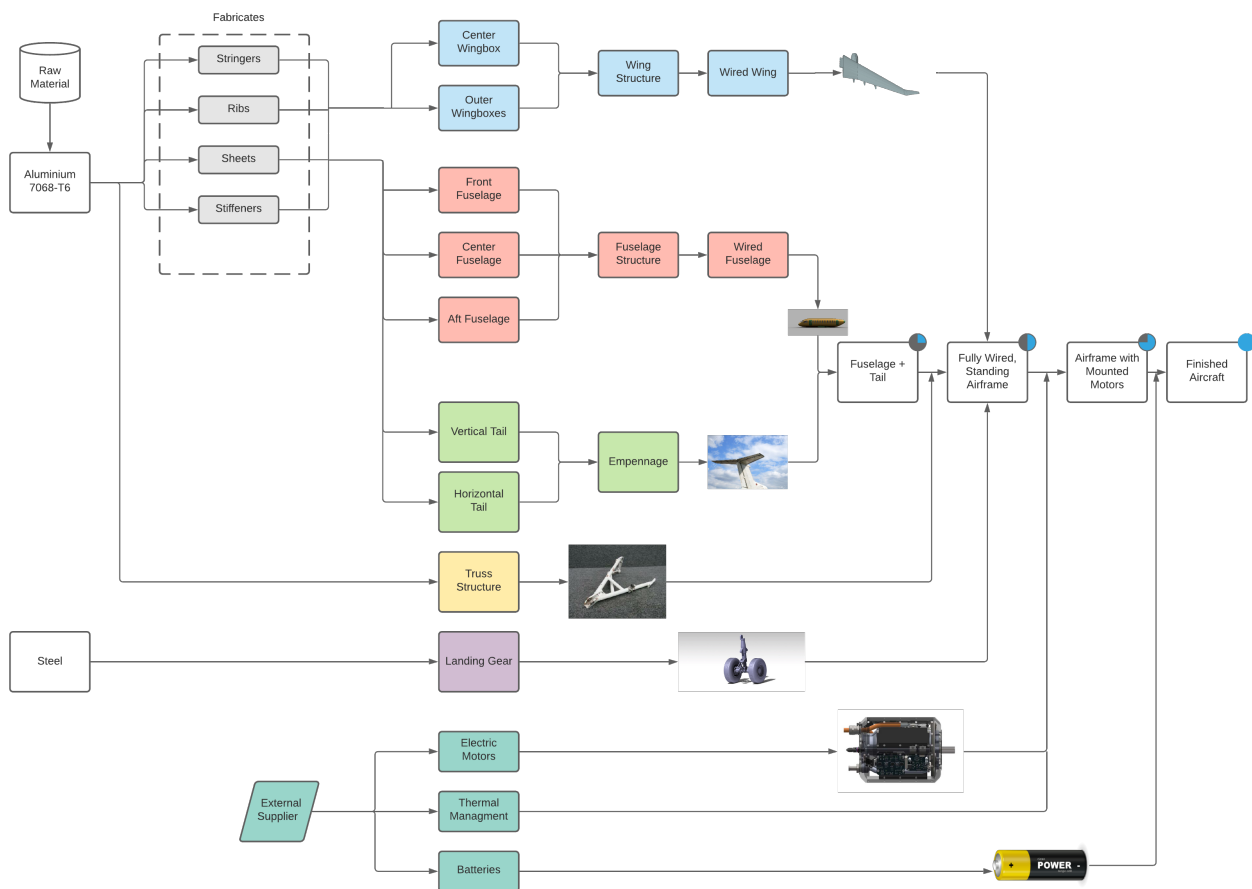


Figure 15.3: The Production Plan for ECHO-1

Economic Analysis

This chapter presents the economic analysis that was performed for ECHO-1. After having presented all the technical details of the aircraft, this section illustrates why ECHO-1 could be a great addition to the market. First, in [section 16.1](#), an overview of all the costs related to ECHO-1 are presented. Following from that, in [section 16.2](#), the return on interest and a break even analysis are discussed. A market analysis is performed in [section 16.3](#), from which a business case is explained in [section 16.4](#).

16.1 Cost Break-Down Structure

In this section a cost analysis will be presented for ECHO-1. This cost estimation is made using Roskam Part VIII [84]. Although the book is already quite old, at this moment it is the most complete way of estimating the costs of an aircraft, as it includes very detailed equations to cover all costs related to aircraft. When computing the cost, inflation was accounted for to get accurate estimation. It was decided to make a cost estimation for the current year 2021 since this cost analysis will also be used to compare operational costs of current conventional aircraft. Furthermore, due to new developments in the future, the costs to develop and produce an aircraft may change, which is currently unknown. The cost estimation is divided into several parts which are development cost, manufacturing cost and operating costs (both direct and indirect). Resulting from this cost estimation, the return on investment, break-even point and unit price of the ECHO-1 will be computed.

16.1.1 Research and Development Cost

The development costs are the costs during the development, research, test and analysis phase. Following from Roskam, the costs have been divided as shown in [Table 16.1](#)[84]:

Table 16.1: Research and Development Cost

Research and Development Cost in M€			
Airframe Engineering and Design	120.9	Test and Simulation Facilities	162.3
Development Support and Testing	15.2	Financing RDTE Phases	81.1
Flight Test Airplanes	345.1	RDTE Profit Margin	81.1
Flight Test Operations	5.7		

The total costs for the research and development phase are calculated to be 811.4M€. The costs of the different parts are depicted in the circle chart in [Figure 16.1](#)

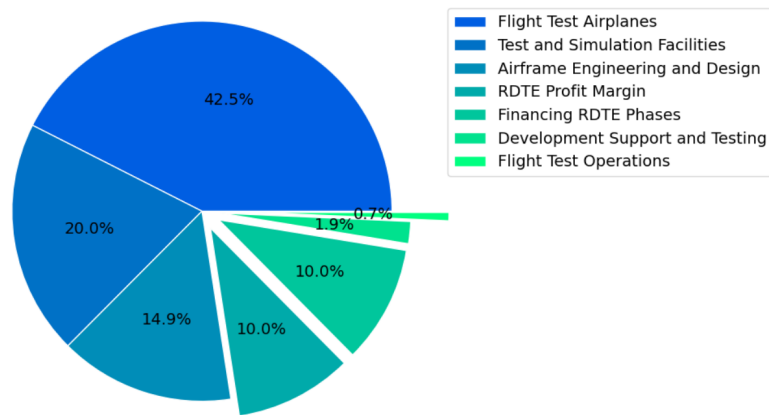


Figure 16.1: Research, Development, Test and Evaluation Cost

16.1.2 Manufacturing and Acquisition Cost

The costs for the manufacturing phase have also been split up in several parts which are listed below in Table 16.2. The costs of the production phase are mainly dependent on how many aircraft will be produced. From Venturi data, it was decided to calculate the production costs taking into account a total of 400 aircraft that will be produced.

Table 16.2: Manufacturing and Acquisition Cost

Manufacturing and Acquisition Cost in M€			
Airframe Engineering and Design	149.4	Production Flight Test Operation	41.2
Airplane Production	3254.7	Financing Manufacturing Program	430.7
Manufacturing Profit Margin	430.7		

The total costs for this phase has been calculated to be 4306.7M€. The division of the costs among the different parts can be seen in the pie chart in Figure 16.2.

With the costs for the development and the production for ECHO-1 known, the unit price can easily be calculated. The total costs in these two phases combined is 5118.1 M€. If a total of 400 aircraft will be produced, this yields a unit price of 12.8 M€. Furthermore, the price of the batteries should also be accounted for. Assuming that the batteries should be replaced every two years, in twenty year they have to be replaced ten times. After a meeting with Venturi, it was clear that the predicted price of batteries would be 50€/kWh by the year 2035. The total cost for the batteries required for 20 years in operation is 1.6 M€. Therefore, the total unit price of ECHO-1 is 14.4 M€when accounting for all batteries. This calculation does not account for the fact that batteries that are 15% degraded, and therefore not useful for ECHO-1 anymore, can possibly be sold again for other purposes. Since it is currently impossible to know if in 2035 the batteries can be sold again for re-usability, this was not taken into account. This means that in the end, the unit price of ECHO-1 could be lower than calculated.

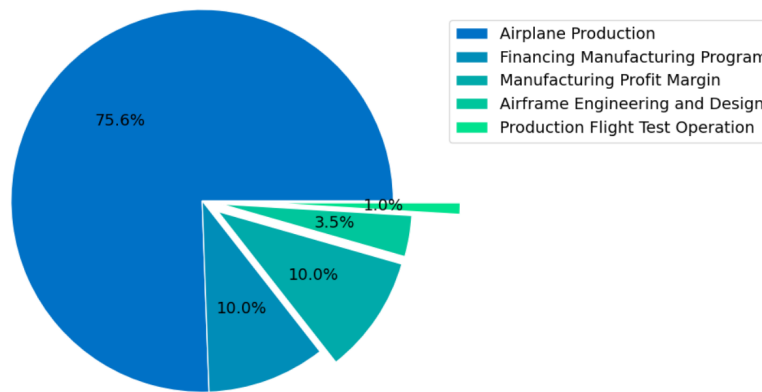


Figure 16.2: Manufacturing and Acquisition Costs

16.1.3 Operating Cost

Operating costs are first divided in direct and indirect operating costs where indirect operating cost is a ratio of the direct cost. Operating costs are calculated in €/km. The direct costs are divided in the following parts.

Table 16.3: Operating Cost

Operating Cost in €/km			
Fleet	1.36	Landing/Navigation/Registry Fees	0.11
Maintenance	1.13	Financing	0.26
Depreciation	0.87		

The total direct operating costs are calculated to be 3.73€/km. The indirect costs are estimated to be 1.1 times the direct operating costs which yields 7.84€/km for the total operating costs[84]. The division of the direct and indirect operating costs is depicted in Figure 16.3. In the estimation of the operational cost, the price of charging the aircraft has been taken into account by multiplying the required energy by the price of 1kWh. For these calculations it was assumed that the price of electricity is 0.116€/kWh, as this is the current price per kWh in the Netherlands and a good average estimate for worldwide. In the calculation of the operating costs, the cost of infrastructure needed for charging has not been taken into account. After a meeting with Venturi, it was concluded that the infrastructure needed for charging will not be provided by the airline but either by the operating airport or another company.

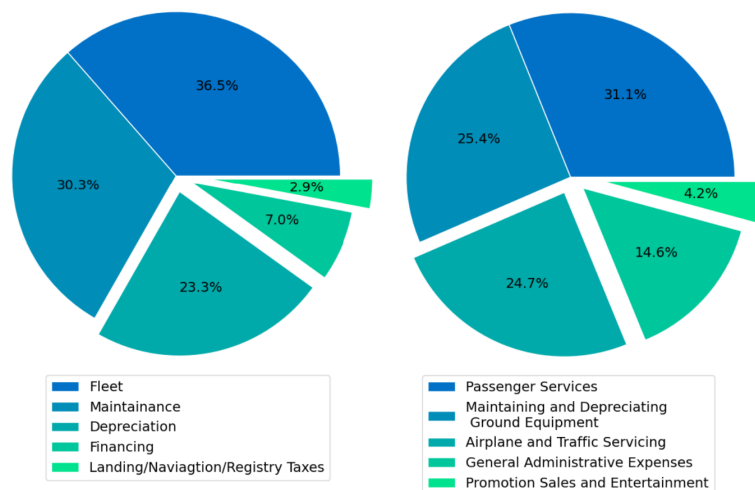


Figure 16.3: Direct Operational Costs (left) and Indirect Operational Costs (right)

16.2 Return on Investment and Operational Profit

The return on investment is a way of measuring the probability that a return will be gained from an investment. Yielding a positive value means the investor will benefit from the investment. A higher value means a greater benefit. The return on investment can be calculated as in Equation 16.1 [84].

$$ROI = \frac{(Rev_{km} - DOC - IOC) \cdot V_{bl}}{AEP \cdot (1 - TR_{inv})} \cdot (1 - TR_{rev}) \cdot U_{bl} \quad (16.1)$$

With the use of the costs calculated in section 16.1, the return on investment is calculated to be 8.75%.

The operational profit can be calculated by considering the cost of the aircraft, the cost of replacing the batteries every 2 years, the operational costs and taking a total lifetime of 20 years. The total costs for the lifetime of the aircraft are 139.9M€. Assuming the aircraft will fly a total of 1000 flights per year, this yields a revenue per flight required of approximately €7000 to break even after 20 years. Including a profit margin of 10%, the revenue of one flight will be €7700 and this will yield a break even point after 10 years as can be seen in Figure 16.4. The operational profit will be €700 per flight. With the revenue of €7700 per flight, the average ticket price will be €160 assuming flights with 48 passengers. Assuming that the business passengers pay six times the price of what the economy passengers will pay, yields a ticket price of €82 for an economy ticket and €496 for a business class ticket. These ticket price are below the ticket prices of KLM flights on routes of equal distance¹ The relation between the profit margin and the break even point for a profit margin of 10% can be seen in Figure 16.4.

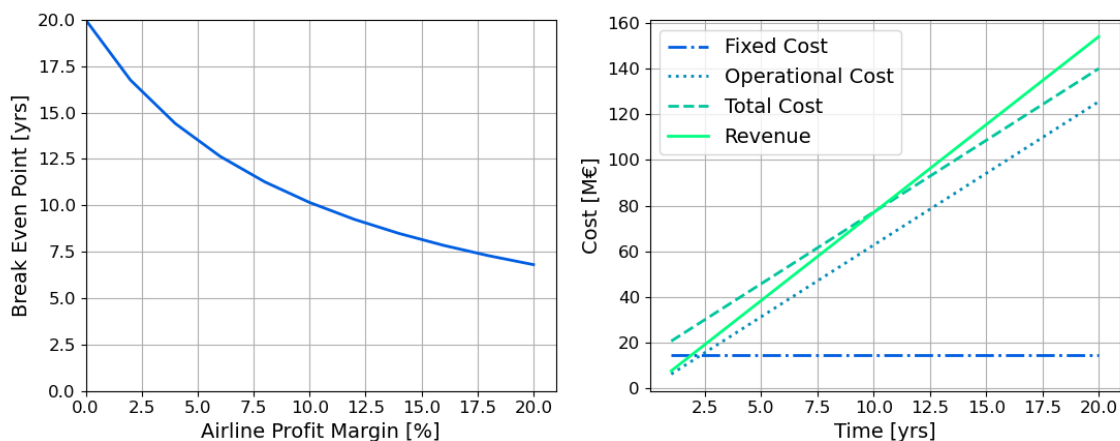


Figure 16.4: Break Even Point Point (left) and Break Even Analysis (right)

16.3 Market Analysis

Based on the market analysis presented in the Baseline Report[13], it can be concluded that there is a growing market for electric flight. In this market analysis it was not specified which type of air transport would be the most promising, long haul, short haul or regional. Based on [3] it can be concluded that there is a promising market in regional air transport. As described in the article, 58% of the worldwide regional air routes were created between 2003 and 2018, showing increasing demand. More 50-passenger aircraft allow for connecting smaller routes and destinations with smaller passenger amounts or cargo volumes. To add, smaller planes also allow more connections per day if the demand allows this, which means a denser transport network [3]. However, due to the low passenger volume, the direct operating costs must be competitive in comparison to other transportation modes or other airlines. This is where ECHO-1 can gain ground. Due to the fact that ECHO-1 is fully electric, highly efficient and very reliable, its direct operating costs are significantly

¹www.klm.nl/search

lower and therefore ECHO-1 is market competitive. The comparison of the direct operating costs will be discussed in [section 16.4](#).

According to Eisenhut et al., there are some top-level requirements an aircraft should adhere to in order to be competitive in this upcoming market. These are requirements which belong to different categories relating to for example; environment, market, operations and regulations[3]. In [Table 16.4](#) below, some top level requirements set by Eisenhut et al., are listed, as well as whether ECHO-1 meets the requirement.

Table 16.4: A selection of top level requirements to be competitive in the regional market[3]

Requirement	Value	ECHO-1
Reduction of CO2 emissions	≥75% vs. ATR-42	✓
Reduction of NOx emissions	≥90% vs. ATR-42	✓
Number of Passengers	≤50	✓
Cargo Capacity	≥500 kg	✓
Direct Operating Costs	Competitive with ground transport	✓
Wingspan	≤36m	✓
Turn-around time	≤25min	✗
Design cruise speed	450-550 km/h	✓
Maximum payload	≤5800 kg	✓
Maximum range	≤800 km	✓
Diversion reserve	185 km	✓
Loitering reserve	30 min	✓
Take-off field length	≤1000 m	✗
Landing field length	≤1000 m	✗
Rate of climb	≥9.4 m/s	✓
Rate of climb at top of climb	≥1.5 m/s	✓
Time to climb to FL170	≤12.7 min	✓

As can be seen in [Table 16.4](#), ECHO-1 meets most of the requirements to be competitive in the regional market. The turn-around time and the take-off and landing field length requirements are not met, however, this should not be the reason why ECHO-1 will not be a success. The turn-around time is still quite uncertain as explained in [chapter 14](#). Turn-around time is strongly dependent on the chargers available in 2035. Regarding the field lengths, although ECHO-1 requires a take-off and landing distance of 1500m this would not mean that it cannot fly on regional or short-haul routes anymore, as only a few airport are ruled out. There are still a lot of airport to fly to, which will be explained in [section 16.4](#). Lastly, the possibilities with regards to the available 800 km range will also be discussed in the next section.

16.4 Business Case

Following from [section 16.3](#), it can be concluded that a market exists for regional air transport. From Eisenhut et al., it can be noticed that a large percentage of all existing flight routs is within the 800 km range of ECHO-1[3], as seen in [Figure 16.5](#). Worldwide, many regional airlines exist that fly most of their routes within this 800 km range, including Wideroe (Norwegian), QantasLink (Australian), SATA Air (Portuguese) and Binter Canarias (Spanish). The aforementioned airlines currently have fleets existing of Bombardier Dash 8 and ATR72 aircraft. Additionally, many larger airlines also serve short regional routes with slightly larger aircraft; examples of this are Lufthansa Regional (German), Air Nostrum (Spanish), HOP! (French) and CityJet (Irish). Therefore, one can conclude that there are already many airlines providing regional and short-haul flights.

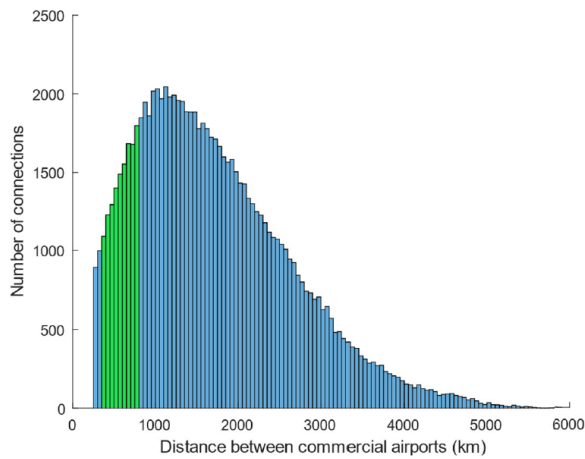


Figure 16.5: Distribution of flight distances worldwide[3]

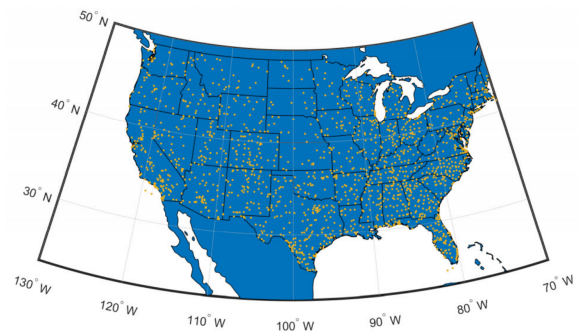
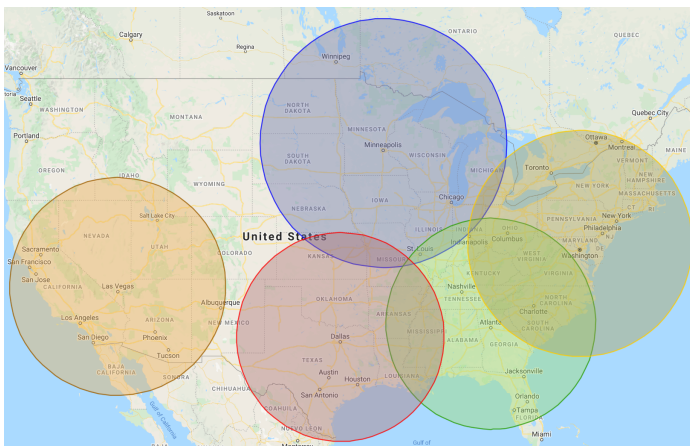


Figure 16.6: US airports with runway length over 1500 m[11]

To illustrate the use case of ECHO-1, Figure 16.7a and Figure 16.7b show possible route opportunities for regional air transport in the United States and Europe. As illustrated, operating ECHO-1 from Las Vegas would allow connections to San Francisco, Los Angeles, Phoenix and Albuquerque, as well as many more smaller regional airports. Similarly, operating from Dallas, Minneapolis, Washington D.C., Atlanta, Madrid, London or Budapest would allow for plenty of feasible routes to be flown with ECHO-1, also in other continents like Asia and Oceania. Moreover, ECHO-1 is capable of landing and taking-off on a 1500 m runway. As can be seen in Figure 16.6, there are at least 10 airports in every US state where ECHO-1 would be able to operate from, leaving many feasible routing options for the airlines[11].



(a) Feasible routes using ECHO-1 in the United States



(b) Feasible routes using ECHO-1 in Europe

Figure 16.7: Feasible routes using ECHO-1

As explained above, there is definitely a practical use case for ECHO-1. For airlines, however, a route is only interesting to operate if it can generate profit. In order to determine how ECHO-1 scales with respect to main competitors on the regional air transport market, Table 16.5 shows key indicators comparing the aircraft. Although usually airlines lease their aircraft, for this comparison, each aircraft was considered to be bought by the airline and amortised linearly. This cost was included in the yearly total fixed cost. The yearly total variable cost arise from the fleet cost, maintenance cost, financing costs and landing, navigation and registry taxes. In order to compare the aircraft, it was calculated how much profit would be made using the ATR72-500, Bombardier Q300 and Embraer ERJ145 when making zero profit per passenger per flight with ECHO-1. The "Revenue for Break Even ECHO-1" value was corrected for the number of passengers for each aircraft since more passengers can bring in more revenue. Clearly, for each of the three other aircraft, an airline would make losses, whereas with ECHO-1, it would break-even. Therefore, it can be concluded that ECHO-1 is more cost-effective

than each of the competitors. It should be noted that the difference in profit per passenger per flight is very small between the ECHO-1 and the ATR72-500. This can mainly be attributed to the fact that the aircraft price for ECHO-1 is currently higher because of the development cost for ECHO-1. If ECHO-1 would sell more and more, the average development cost per aircraft would go down, meaning a lower yearly total fixed cost, hence a higher profit per passenger per flight. One other thing to note is that governments could reward airlines that fly fully electric through subsidies. This would favour the choice of ECHO-1 over all of its competitors, hence increasing operational profits. Especially in the near future, when the transition to electric flight has to occur, this subsidy might make a great difference. Looking at the previous analysis, it can thus be concluded that the direct operative costs are competitive with current direct operating costs, meeting requirement **VEN-TOP-COST-1**.

Table 16.5: Financial breakdown comparing ECHO-1 to main competitors

	ECHO-1	ATR72-500²³	Bombardier Q 300⁴⁵	Embraer ERJ145⁶⁷
Yearly Total Fixed Cost	€ 722,012.20	€ 1,352,339.08	€ 1,696,894.06	€ 1,752,561.40
Yearly Total Variable Cost	€ 2,987,479.56	€ 4,252,028.00	€ 3,659,865.00	€ 6,078,163.08
Total Cost	€ 3,709,491.76	€ 5,604,367.08	€ 5,356,759.06	€ 7,830,724.48
Revenue for Break Even ECHO-1	€ 3,709,491.76	€ 5,564,237.64	€ 4,327,740.39	€ 3,864,053.92
Number of Passengers	48	72	56	50
Number of Flights per Year	1000	1000	1000	1000
Profit per Passenger per Flight	€ 0.00	€ -0.56	€ -18.38	€ -79.33

The difference in variable costs can mainly be attributed to two things. Firstly, ECHO-1 is more energy efficient than main competitors, as was presented in [chapter 13](#). Secondly, the prices for electricity and kerosene differ quite a bit. Following from ATR42-600 data, it can be found that for a similar range as ECHO-1, a total of 1322.2 liters of kerosene is required⁸. Using the current average kerosene price of €0.68 per liter⁹, a total energy price of €899.10 is found. ECHO-1 has 6920 kilograms of batteries that can store 575 Wh/kg at end of life. This accounts to a total of 3979 kWh of capacity. Multiplying this amount with the current average electricity price of €0.116 per kWh¹⁰, one obtains a total energy price of €461.56. These values (€437.54 difference) are only for one flight, hence they show a great advantage of flying electric.

Table 16.6: Kerosene and electricity cost comparison

	ECHO-1	ATR42-500
Kerosene Price	-	€ 0.68 per L
Electricity Price	€ 0.116 per kWh	-
Liters of Kerosene	-	1322.2
Number of kWh	3979	-
Fuel Price of Flight	€ 461.56	€ 899.10

⁸https://1tr779ud5r1jgc938wedppw-wpengine.netdna-ssl.com/wp-content/uploads/2020/07/Factsheets_-_ATR_42-600.pdf

⁹https://www.globalpetrolprices.com/kerosene_prices/

¹⁰https://www.globalpetrolprices.com/Netherlands/electricity_prices/

To conclude, for many regional airlines, the purchase of ECHO-1 would mean lower costs per passengers, resulting in higher profits. ECHO-1 can serve a large number of routes as was shown in [Figure 16.5](#), [Figure 16.7a](#) and [Figure 16.7b](#). Furthermore, the required runway length of 1500 m will not drastically limit the routing options for airlines. With increasing number of ECHO-1 aircraft sold in the future, the aircraft purchase price may go down even more to assure even lower total costs in the future. As was calculated in [section 16.1](#), in order for the airline to make 10% profit, it would have to sell the tickets of €82 for economy seats and of €496 for business class seats. Moreover, since flying eco-friendly is becoming more desirable, passengers might be willing to pay a premium for flying on ECHO-1. Furthermore, it was verified that these ticket prices are lower than KLM prices on routes of similar distances¹¹. Should the aircraft purchase price go down in the future, this would allow for reduction in ticket prices to be even more attractive to customers.

¹¹www.klm.nl/search

Conclusion and Recommendations

17.1 Conclusion

The initial goal of this project was to "Design a fully electric transport aircraft, focused on achieving zero emission flight, flying at 500 km/h for 1000 km, whose payload volume can be easily reconfigured for both passenger transport (50 passengers) or cargo transport (6000 kg)". Over the past 10 weeks the 10 students of DSE group 9 have worked full time to achieve this goal, ending up with the design of their aircraft: ECHO-1.

From the start of the project it was already known that the final design would tend towards the boundaries of E-flight. Before proceeding into the detailed design phase, a boundary was already found. The initial requirements set by Venturi seemed unrealistic and after a proper discussion the requirements were adjusted to 48 passengers, 800km range and an EIS in 2035, which increased the design space. Furthermore, Venturi added another main requirement on the wingspan at a later stage which decreased the design space significantly. Before even starting the detailed design, the boundaries were already defined. Therefore, it was of utmost importance to minimize the energy required in flight, minimize the OEW, maximize the L/D and maximize the propulsive efficiency in order to meet the new requirements set. To achieve this, a truss braced wing with distributed propulsion was selected, which is a perfect fit for minimizing and maximizing the above mentioned parameters. All these subsystems were designed and analysed in more detail to work towards these goals.

The subsystem design calculations were integrated in an iteration program to arrive at a converged final design. Some of the most important values of the final design of ECHO-1 include a MTOW of 20937.37 kg, a lift-over drag ratio of 28.24, a wing area of 56.85 m^2 and a battery mass of 6919.92 kg. This program did not only allow for finding the final design values within the given requirements. It was also used to visualise the actual boundaries of E-flight with a sensitivity analysis. The iteration program showed that convergence occurred only for a certain range of input values. The boundaries of convergence, in terms of payload and range were determined for different battery energy densities (525-625 Wh/kg), runway distances (1400-1600 m) and cruise speeds (475-525 km/h). From this analysis it was found that the design of ECHO-1 is first mainly bounded by the 36 meter wingspan and after that by the amount of propellers, the aspect ratio and the amount of power.

Finally the economic analysis of ECHO-1 showed that a profitable business model exists and that there is a growing market in regional air transport. So there is a justified incentive to continue the design of ECHO-1. From this project it can be concluded that the boundaries of E-flight have been identified and that they are one step closer to being reached.

17.2 Recommendations

For this project, the aim was to perform a feasibility study on an electric air transport vehicle. This has led to a number of conclusions presented in [section 17.1](#), but the road to flying electric does not stop there. Over the previous weeks, a number of design steps were not executed to the full extent due to various constraints. Additionally, some challenges were only on the table in late design phases, therefore these could not be executed in a lot of detail. Some recommendations were already presented in their respective chapters, however for the sake of completeness, an overview is presented below:

- The concept of having cables running through the truss could be worked out into more detail, as the cables would have to fit through the truss, but also the cables should be accessible for maintenance. The latter could cause troubles if the truss should be a rigid load-transferring

structural element. It is therefore recommended to look into this matter in more detail should the project be continued.

- For the detailed weight estimation of the aircraft, the Raymer method was used for the conventional aircraft components and more detailed methods were used for the mass estimation of specific subsystems like the distributed propulsion and the truss. For more detailed design phases, it is recommended to use more subsystem-specific weight estimations.
- Currently, for the estimation of the power that is required for subsystems that are not related to propulsion (e.g. environmental control), a rough estimation was made for this exercise. For further work, it is recommended to look into this calculation in more detail.
- For further design phases, it is recommended to look into the aero-propulsive interaction in more detail. The effect the distributed propulsion has on the aerodynamic performance has been calculated on in the DSE, but there is definitely room for improvement. It is recommended to look especially into the local lift change over the wing as a result of a rotating propeller in front.
- For the dynamic stability of the aircraft, a verified and validated Python program was used. This program heavily depended upon inputs from XFLR5. For more detailed and more reliable dynamic stability analysis, it is recommended to obtain these inputs from a test flight or a wind tunnel test.
- For the structural sizing, as a result of time constraints, it was not possible to size for fatigue and crack propagation, as well as loads in the flight direction. For further work, it is recommended to look at these load cases.
- For the structural sizing, the wing structure, wing box structure and fuselage were sized. Some major aircraft elements like the empennage were not structurally sized since these elements were deemed less important for the conceptual design since they are comparable to regular kerosene aircraft. For later design phases, it is recommended to look into these structural elements in more detail.
- In order to be more certain of the validity of the code, it is recommended to perform more extensive verification and validation on the Python code. This could yield more confidence in the obtained results.
- It would be worth investigating how much the voltage would drop with a lower state of charge of the battery and see if this 35 V margin currently in place is enough to account for this. If this is not the case a battery redesign would be necessary.
- For the battery design it is worth while to investigate if the assumption that the battery modules can be wired according to the geometry described in [section 11.1](#) holds. It could be that wiring the battery modules in the way described in [section 11.1](#) would impose a number of performance penalties on the batteries or that the weight of the required wires would be high. It is recommended to do this investigation in collaboration with an electrical engineer since more in depth knowledge on batteries would be required.
- For battery thermal management system, it would be worth including the other types of heat being produced by a battery besides Joule effect heating and do a generally more accurate thermal modelling of the heat transfer. For the heat exchanger sizing and positioning, a proper CFD analysis should be conducted in order to determine the best pairing of depth and frontal area, as well as the drag penalty that this induces. Finally, the power consumption of the BTMS should be evaluated in further design.
- One interesting topic for further investigation is the design and performance of the recharging procedure of ECHO-1. The analysis in this report was not highly accurate because the information about the battery performance was not too extensive. This means that the recharging ability of the batteries could not have been accurately assessed. Furthermore, the design of the battery lay-out did not take into account the fast charge capability of the battery. Additionally, more research on the actual feasibility and possibilities of the charging platform should be performed in the future in order to ensure that ECHO-1 can be integrated into existing airports.

17.3 Errata

Some errors were found at a really late stage of the project, such that it was not possible anymore to rewrite the code and most of the text in this document. The group did feel obliged to report these errors in a separate section of the report. The aim of this section is to indicate what were the flaws that were found too late in the design process and to quantify their effect on the final converged design. This will be done by first enumerating the (minor) errors that were found, then running again the iteration file with the errors corrected. This will allow to reproduce Figure 12.3 with the corrected values, converging again to a final design. Additionally, the sensitivity to payload and range will be checked again, in the same fashion as was done in Figure 12.6. It is recommended to read chapter 12 before reading this chapter to have an understanding of the method of converging to a final design. The errors are summarized below:

- In the program for the energy calculations, one of the inputs was the propeller blade area and the number of blades per propeller. By accident, propeller blade area was multiplied with the number of blades per propeller twice, ending up at a feathering drag that was 4 times too high (since there are 4 propellers per engine).
- When adding the mass of the electric motors, the value was divided by the gravitational constant, ending up at a mass that was 9.80665 times too low.
- When taking into account the zero lift drag coefficient contribution of the wing twist, instead of 4 drag counts per degree twist, 0.4 drag counts were added per degree of wing twist.
- For the iteration loop, a Python dictionary was used to which all variables were appended. Unfortunately, a coding error restricted the drag calculation to run with updated values, which accounts for a small offset in the drag calculations for each iteration.
- For running the file that provides the sensitivity plots, a coding error ensured that the fuselage length was not a variable, hence it was not changing if the number of passengers changed.
- For the battery sizing, a factor of 1.2 was used to calculate the required number of battery cells. This should have been a factor of $1/0.8 = 1.25$. Even though this difference is only 4%, it was an error and should be corrected in later design phases (*This error was not part of the iteration loop*)

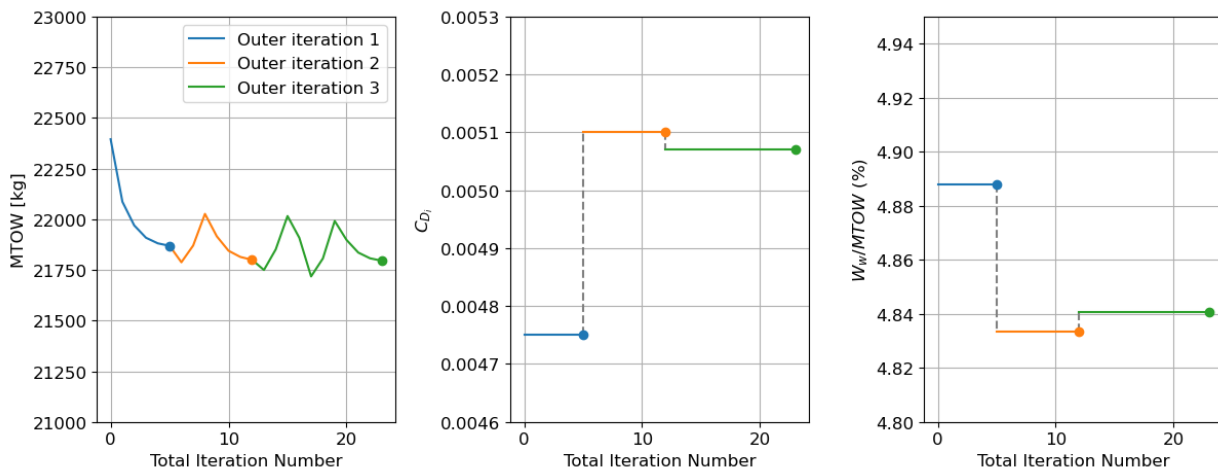


Figure 17.1: Final design convergence post-errata

Most interesting is to see what is the effect of implementing these changes in the code to the final design. The convergence plot, as was done before in Figure 12.3, is now presented in Figure 17.1, with the errors listed above resolved. As can be seen, the final MTOW now converges to 21795 kg which is 4.1% more than the 20937 kg that was calculated in the report. Furthermore, the newly performed payload range sensitivity is illustrated in Figure 17.2. What differs with respect to Figure 12.6 is can be seen in Figure 17.3, which shows a difference in the slope of the boundary line; in stead of 73 km, given the post-errata results, each row of 3 passengers equals an additional range of 85km. This

can be explained by the fact that for the sensitivity study, the length of the fuselage did not change due to a coding error. It can be concluded that the errors resulted in a significant weight increase of 4.1%, but still allow the design to converge.

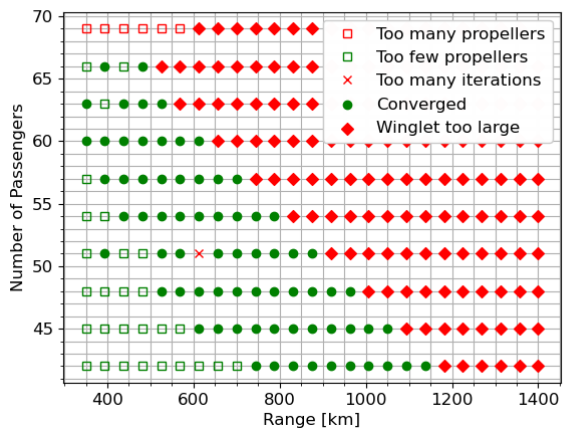


Figure 17.2: Final design sensitivity post-errata

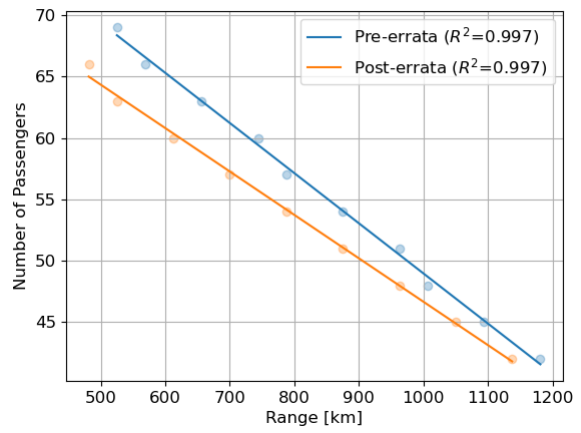


Figure 17.3: Comparison sensitivity pre-errata and post-errata

Bibliography

- [1] DSE Group 9. Towards the boundaries of e-flight - ae3200: Midterm report, 2021.
- [2] B.T.C. Zandbergen R. Vos, J.A. Melkert. *ADSEE-I The Design of the Fuselage*. Technical University of Delft (FPP), Delft, The Netherlands, 2019.
- [3] D. et al. Eisenhut. Aircraft requirements for sustainable regional aviation. *Aerospace*, 8:61–84. doi: <https://doi.org/10.3390/aerospace8030061>.
- [4] Reynard de Vries, Malcom Brown, and Roelof Vos. Preliminary sizing method for hybrid-electric distributed-propulsion aircraft. *Journal of Aircraft*, 56(6):2172–2188, dec 2019.
- [5] A. K. Kundu. *Aircraft Design*. Cambridge, Cambridge University, 2010.
- [6] Hamilton Standard. *Generalized Method of Propeller Performance Estimation*. U.A., Windsor Locks, Connecticut, 1961.
- [7] G.J.J. Ruijgrok. *Elements of airplane performance*. VSSD, Delft, 2009.
- [8] N. Nørmark Sørensen J. Johansen. Numerical analysis of winglets on wind turbine blades using cfd. 2007.
- [9] Dragan Kozulovic. Heat release of fuel cell powered aircraft. 2020. doi: 10.33737/gpps20-tc-99.
- [10] Marnix R. Beudeker. Reallocating aircraft stand capacity. Master thesis, Delft University of Technology, aug 2015.
- [11] I. Geiß and A. Strohmayer. Operational energy and power reserves for hybrid-electric and electric aircraft. *Deutscher Luft- und Raumfahrtkongress*.
- [12] Michiel Huijgen. The potential effects of passenger car electrification on co2 and pollutant emissions. Master's thesis, University of Amsterdam, Bloys van Treslongstraat 42-III; 1056 XC Amsterdam, jun 2017.
- [13] DSE Group 9. Towards the boundaries of e-flight - ae3200: Baseline report, 2021.
- [14] Martin Hepperle. Electric flight – potential and limitations. sep 2009.
- [15] B Song and S Kang. A Method of Assigning Weights Using a Ranking and Nonhierarchy Comparison. *Advances in Decision Sciences*, 2016:1–9, 2016. doi: 10.1155/2016/8963214.
- [16] J. Roskam. *Part V: Component Weight Estimation*. DARcorporation, 120 East 9th Street, Lawrence. Kansas, 1 edition, 1985.
- [17] R.H.Daugherty. A study of the mechanical properties of modern radial aircraft tires. *Langley Research Center, Hampton, Virginia*, 2003.
- [18] E. Van Baaren. The feasibility of a fully electric aircraft towing system. Master's thesis, TU Delft, Aerospace Engineering, 2019.
- [19] M. Voskuijl P. Roling. *AE2230-I Flight & Orbital Mechanics, Climb and Descent*. Technical University of Delft (FPP), Delft, The Netherlands, 2019.
- [20] T. Sinnige et. al. Aerodynamic performance of a wingtip-mounted tractor propeller configuration in windmilling and energy-harvesting conditions. 2019.
- [21] D. Erzen. An optimal propeller design for in-flight power recuperation on an electric aircraft. 2018.
- [22] A. Filippone. Options for aircraft noise reduction on arrival and landing. *Aerospace Science and Technology*, 60, 2017.
- [23] International Civil Aviation Organization. *Annex 6 to the Convention on International Civil Aviation—Operation of Aircraft—Part I—International Commercial Air Transport—Aeroplanes*. ICAO, Montreal, QC, Canada, 11 edition, 2018.
- [24] HENDRIK SCHEFER. Discussion on electric power supply systems for all electric aircraft. *Technische Universität Braunschweig*, 2020.
- [25] P. Olexa M. Špák. Enhancement of the diversion airport selection methodology. *Transportation Research Procedia*, 51, 2020.
- [26] L.L.M. Veldhuis. *Propellor Wing Aerodynamic Interference*. Technical University of Delft, Delft, 2019.
- [27] B.J. German M.D. Patterson. Simplified aerodynamics models to predict the effects of upstream propellers on wing lift. *53rd AIAA Aerospace Science Meetings*, 53, 2015.
- [28] C.E. Lan J. Roskam. *Airplane Aerodynamics and Performance*. DARcorporation, 120 East 9th Street, Lawrence. Kansas, 1 edition, 1997.
- [29] *EduPack*. Ansys, 2021. URL <https://www.ansys.com/products/materials/granta-edupack>.
- [30] Dr. F. Oliviero. *Aircraft Design 2 - Lift & Drag Estimation*. Technical University of Delft (FPP), Delft, The Netherlands, 2019.
- [31] J.A. Melkert R. Vos. *A/c preliminary sizing*. Aerospace Design and Systems Engineering Elements I, Lecture 3, 2019.

- [32] R. Vos and J. Melkert. *Lecture 6 - Wing and Propulsion System Design*. Technical University of Delft (FPP), Delft, The Netherlands, 2018.
- [33] N. El Haddad. Aerodynamic and structural design of a winglet for enhanced performance of a business jet. Master's thesis, Embry-Riddle Aeronautical Engineering, 2015.
- [34] T. T. Moore. The effect of winglet twist and toe angle on the drag of a high aspect ratio wing. 2019.
- [35] O. Gur, W.H. Mason, and J.A. Schetz. Full-configuration drag estimation. 2010.
- [36] N. Van Oene. Landing gear design integration for the tu delft initiator. Master's thesis, TU Delft, 2019.
- [37] Ira Herbert Abbott and Doenhoff A E Von. *Theory of Wing Sections*. Dover Pubns.
- [38] Friedrich Wilhelm Riegels. *Aerofoil sections: results from wind-tunnel investigations, theoretical foundations / F.W. Riegels*. Butterworths, 1961.
- [39] Vincenzo Di Lecce, Cataldo Guaragnella, Dario Rita, and Tiziana D'Orazio. Smart postural monitor for elderly people. *19th IMEKO TC 4 Symposium and 17th IWADC Workshop Advances in Instrumentation and Sensors Interoperability*, jun 2013.
- [40] Dr. F. Oliviero. *Design for Lateral-directional aspects and for ground operations*. Technical University of Delft (FPP), Delft, The Netherlands, 2021.
- [41] R. Vos and J. Melkert. *Lecture 7 - Landing Gear and Empennage Design*. Technical University of Delft (FPP), Delft, The Netherlands, 2018.
- [42] Dr. F. Oliviero. *Requirement Analysis and Design principles for A/C stability & control (Part 2)*. Technical University of Delft (FPP), Delft, The Netherlands, 2021.
- [43] Dr. F. Oliviero. *Requirement Analysis and Design principles for A/C stability & control (Part 1)*. Technical University of Delft (FPP), Delft, The Netherlands, 2021.
- [44] E Torenbeek. *Synthesis of subsonic airplane design*. Delft University Press, dec 1982.
- [45] Dr. F. Oliviero. *Aircraft Design 3 - Mobile Surfaces*. Technical University of Delft (FPP), Delft, The Netherlands, 2019.
- [46] Omran Al-Shamma, Rashid Ali, and Haitham S. Hasan. An instructive algorithm for aircraft elevator sizing to be used in preliminary aircraft design software. *Istrazivanja i Projektovanja za Privredu*, 15(4):489–494, jan 2017.
- [47] H. Hasan O. Al-Shamma, R. Ali. An educational rudder sizing algorithm for utilization in aircraft design software. 2018.
- [48] Regional Aircraft Bombardier Aerospace. Bombardier q300. 123 Garratt Blvd Downsview, Ontario, Canada M3K 1Y5, jun 2006.
- [49] Mihaela Florentina Niță. *Aircraft Design Studies Based on the ATR 72*. PhD thesis, Hamburg University of Applied Sciences, aug 2008.
- [50] Pieter-Jan Goderis. Conceptual design of fuselages, cabins and landing gears, methods, statistics and tool setup. Master thesis, Hamburg University of Applied Sciences, jul 2008.
- [51] J.A. Mulder, W.H.J.J van Staveren, J.C. van der Vaart, E. de Weerd, C.C. de Visser, A.C. in 't Veld, and E. Mooij. *Flight Dynamics*, 2013. Accessed: 22-06-2021.
- [52] Courtland D. Perkins and Robert E. Hage. *Airplane Performance, Stability and Control*. John Wiley and Sons, first edition, jan 1949.
- [53] Tudor Avarvraei, Andrada Gheorghe, Nico Gheorghe, Alexandru Iancu, Crina Mihalache, and Octavian Soare. Simulation plan - flight dynamics. Technical report, Technical University of Delft, 2021.
- [54] A. Deperrois. Modal analysis and experimental validation. Online, feb 2011.
- [55] J.A. Melkert C. Rans. *AE3521-I Structural Analysis and Design*. Technical University of Delft (FPP), Delft, The Netherlands, 2020.
- [56] US Department of Energy. Bandwidth Study on Energy Use and Potential Energy Saving Opportunities in U.S. Carbon Fiber Reinforced Polymer Manufacturing . 2017.
- [57] S.R. Naqvi. A critical review on recycling of end-of-life carbon fibre/glass fibre reinforced composites waste using pyrolysis towards a circular economy. *Elsevier*, 2018.
- [58] F. Meng. Environmental and cost analysis of carbon fibre composites recycling. *Univeristy of Nottingham*, 2017.
- [59] I. Sen. Aircraft fuselage design study. Master thesis, Delft University of Technology, dec 2010.
- [60] Q.P.D. van Keymeulen. Design of a modular fuselage for commercial aircraft. Master thesis, Delft University of Technology, sep 2010.
- [61] Daniel Raymer. *Aircraft Design: A Conceptual Approach*. American Institute of Aeronautics and Astronautics, 2006.
- [62] A. Beléndez T. Beléndez, C. Neipp. Large and small deflections of a cantilever beam. *European Journal of Physics*.
- [63] Jaewan Kim, Jinwoo Oh, and Hoseong Lee. Review on battery thermal management system for electric vehicles. *Applied Thermal Engineering*, 149, 2019. doi: 10.1016/j.applthermaleng.2018.12.020.

- [64] P.C. Bhatia. Thermal analysis of lithium-ion battery packs and thermal management solutions. 2013.
- [65] Ivan Kasatkin, Mikle Egorov, Evgeny Kotov, and Evgeny Zakhlebaev. Cooling of a battery pack of a car, working on renewable energy. *MATEC Web of Conferences*, 245, 2018. doi: 10.1051/mateconf/201824515003.
- [66] Jonathan M. Rheaume, Malcolm Macdonald, and Charles E. Lents. Commercial hybrid electric aircraft thermal management system design, simulation, and operation improvements. *AIAA Propulsion and Energy 2019 Forum*, 2019. doi: 10.2514/6.2019-4492.
- [67] Report of the conference of the parties on its nineteenth session, held in warsaw from 11 to 23 november 2013. *United Nations Framework Convention on Climate Change*, 2014.
- [68] IEA. Carbon intensity of electricity generation in selected regions in the sustainable development scenario, 2000-2040. 2020.
- [69] Chris Yuan, Yelin Deng, Tonghui Li, and Fan Yang. Manufacturing energy analysis of lithium ion battery pack for electric vehicles. *CIRP Annals*, 66, 2017.
- [70] Hans Melin. Analysis of the climate impact of lithium-ion batteries and how to measure it. 2014.
- [71] K. Seeckt and D. Scholz. Jet versus prop, hydrogen versus kerosene for a regional freighter aircraft. 2009.
- [72] Study on actual ghg data for diesel, petrol, kerosene and natural gas. *European Commission DG Ener*, 2015.
- [73] David Laner, Helmut Rechberger, and Johann Fellner. Future raw material supply: Opportunities and limits of aluminium recycling in austria. *Journal of Sustainable Metallurgy*, 2015.
- [74] Omar Velázquez-Martínez, Johanna Valio, Annukka Santasalo-Aarnio, Markus Reuter, and Rodrigo Serna-Guerrero. A critical review of lithium-ion battery recycling processes from a circular economy perspective. 5(4), 2019. ISSN 2313-0105. doi: 10.3390/batteries5040068. URL <https://www.mdpi.com/2313-0105/5/4/68>.
- [75] Jędrzej Piątek, Semih Afyon, Tetyana M. Budnyak, Serhiy Budnyk, Mika H. Sipponen, and Adam Slabon. Sustainable li-ion batteries: Chemistry and recycling. 2020. doi: <https://doi.org/10.1002/aenm.202003456>. URL <https://onlinelibrary.wiley.com/doi/abs/10.1002/aenm.202003456>.
- [76] A.G. Daimler. Environmental certificate mercedes-benz b-class electric drive. 2014.
- [77] L. Ellingsen and C. Hung. Research for tran committee - battery-powered electric vehicles: market development and lifecycle emissions study. 2018.
- [78] A. El-Raouf Badawi M. Abd Allah Makhloof, M. Elsayed Waheed. Real-time aircraft turnaround operations manager. 01 2012.
- [79] Wei Tao Zhao and Da Qian Zhang. Discussion of reliability analysis for aircraft wing box structural system. *Advanced Materials Research*, 118–120:236–240. doi: 10.4028/www.scientific.net/amr.118-120.236.
- [80] R.A. DeLucia, D.T. Salvino, and B.C. Fenton. Statistics on aircraft gas turbine engine rotor failures that occurred in u. s. commercial aviation during 1985. Final report, FAA Technical Center, Springfield, Virginia 22161, jul 1989.
- [81] Michael C. Romanowski. Advisory circular- certification of propellers. Technical report, U.S. Department of Transportation Federal Aviation Administration, nov 2018.
- [82] Fabrizio Gaspari, Lorenzo Trainelli, Alberto Rolando, and Igor Perkon. *D1.1: Concept of Modular Architecture for Hybrid Electric Propulsion of Aircraft*. MAHEPA, dec 2017.
- [83] Ryan P. Naru and Brian J. German. Maintenance considerations for electric aircraft and feedback from aircraft maintenance technicians. *2018 Aviation Technology, Integration, and Operations Conference*, jun 2018. Georgia Institute of Technology, Atlanta, GA, 30332.
- [84] J. Roskam. *Part VIII: Cost Estimation*. DARcorporation, 120 East 9th Street, Lawrence. Kansas, 1 edition, 1985.